Univerzita Karlova v Praze
Přírodovědecká fakulta

Université de Strasbourg
EOST

Doktorát pod dvojím vedením
Thèse en cotutelle

Studijní program: geologie (P1201)

Mgr. Martin Staněk

Strukturní a petrofyzikální charakterizace granitu vhodného pro ukládání radioaktivního odpadu

Structural and Petrophysical Characterisation of Granite Intended for Radioactive Waste Stocking

Doctoral Thesis

Školitelé/Supervisors:
Yves Géraud
Ondrej Lexa

Praha 2013

Prohlášení:

Prohlašuji, že jsem závěrečnou práci zpracoval/a samostatně a že jsem uvedl/a všechny použité informační zdroje a literaturu. Tato práce ani její podstatná část nebyla předložena k získání jiného nebo stejného akademického titulu.

V Praze, Martin Staněk

Název práce: Strukturní a petrofyzikální charakterizace granitu vhodného pro ukládáni radioaktivního odpadu

Autor: Mgr. Martin Staněk

Katedra: Ústav strukturní geologie a petrologie

Vedoucí disertační práce: Yves Géraud a Ondrej Lexa

Abstrakt: Byla provedena studie stavby a fyzikálních vlastností žulového masívu se zaměřením na stavby ovládající přenosové vlastnosti horniny. Stavba masívu byla upřesněna na základě rozsáhlého souboru údajů zahrnujících AMS a terénní měření duktilních a křehkých staveb. Za účelem zobrazení magnetických staveb a systému trhlin byly sestaveny mapy a stereogramy. Systém fraktur byl popsán dvěma hlavními a dvěma vedlejšími sety puklin a zlomy tvořícími se reaktivací puklin nebo méně často střižnými trhlinami. Naměřené petrofyzikální údaje byly použity k charakterizaci vlivu frakturace a alterace na geometrii pórového prostoru stejně tak jako na propustnost, tepelnou vodivost a elastické vlastnosti studované žuly. Odlišné petrofyzikální vlastnosti byly rozpoznány pro zdravou žulu, pro frakturovanou čerstvou žulu a také pro frakturovanou žulu alterovanou oxidy železa, chloritem a jílovými minerály. Vztahy mezi měřenými petrofyzikálními vlastnostmi byly vysvětleny ve smyslu vývoje pórového prostoru. Podrobná mikrostrukturní studie kombinovaná s měřením rychlosti P-vln v mnoha směrech za vysokého omezujícího tlaku a s analýzou AMS byla provedena na vzorku Lipnické žuly se šlíry. Tato studie ukázala, že za nízkých omezujících tlaků je anisotropie VP ovládána intergranulárními mikrotrhlinami propojujících štěpnosti slíd a živců subparalelních se šlíry, a v křemeni, který nemá štěpnost, mikrotrhlinami subparalelními s exfoliační trhlinou. Značné uzavírání mikrotrhlin pro žulu se šlíry a hloubku méně než 500 metrů bylo interpretováno ve smyslu stlačení mikrotrhlin odrážejícího se rychlým nárustem VP s omezujícím tlakem.

Title: Structural and Petrophysical Characterisation of Granite Intended for Radioactive Waste Stocking

Author: Martin Staněk

Departments: Institute of Physics of the Globe of Strasbourg, Institute of Petrology and Structural Geology of Prague

Supervisors: Yves Géraud and Ondrej Lexa

Abstract: Structural and petrophysical analysis have been conducted within the Melechov massif with focus on structures controlling the porosity, permeability and thermal conductivity of the rock. The structure of the massif has been constrained based on extensive dataset including AMS and field structural measurements of ductile and brittle structures. Maps and stereograms have been constructed to display the magnetic fabrics and the fracture system of the studied massif. The fracture system of the massif has been described by two principal and two supplementary sets of joints and by faults formed mainly by joint reactivation or less frequently formed as shear fractures. The measured petrophysical data have been used to characterize the effect of fracturing and alteration on pore space geometry and in turn on permeability, thermal conductivity and elastic properties of the studied granite. Distinct petrophysical properties have been identified for pristine granite, for fractured fresh granite as well as for fractured granite altered by Fe-oxide, chlorite and clay minerals. Relations between the measured petrophysical properties have been explained in terms of evolution of the rock pore space. A detailed microstructural study combined with multidirectional P-wave velocity measurements at high confining pressure and with AMS analysis has been conducted on a schlieren bearing sample of Lipnice granite. The study has shown that the granite VP anisotropy at low confining pressure was controlled by intergranular cracks interconnecting schlieren-subparallel cleavage cracks in micas and feldspars and by exfoliation fracture-subparallel intra- or trans-granular cracks in cleavage-free quartz. Major closing of the crack porosity linked to the schlieren granite below depth of 500 m has been interpreted in terms of crack compliance reflected by rapid increase in VP with confining pressure.

"It is not because things are difficult that we do not dare,
it is because we do not dare that things are difficult."

Seneca

Contents

Acknowledgements

Thanks to you all who smile often and particularly to those who supported me at the origin, during and mainly in the final of that interesting challenge to investigate what is worth writing a book and to write a book on what is worth investigating. Thanks to my parents, who initiated me into the world and motivated me to search the horizons of knowledge. Thank you Stano for indicating me the right directions. Thank you Yves for speaking few and meaning lot. Thank you Marc for being available when the others were not. Thank you Ondro for your generosity. Very special thanks to Alexandra for being always sunshining even if the storm was all around. Special thanks to Matěj Machek for providing ground-based reflections to my scattered ideas throughout my PhD. Thank you Aleš, Lenka, Prokop, Zuzka, Jirka, Mr. Uličný and all the good people at the GFU that accepted me among them and made for me the job there much more valuable than just a job. Glory to Mr. Pros for having constructed a unique and powerful machine that makes people wonder.

The Czech Radioactive Waste Repository Authority (RAWRA/SÚRAO) is thanked for allowing us to sample the MEL-5 borehole core.

Chapter I:

Introduction

1. Motivation, approach and aim of the study

The present study demonstrates the use of data acquired by structural and petrophysical analysis of a granitic massif for the purpose of search and characterization of suitable sites for deep geologic repositories of radioactive waste.

The motivation to work on such a subject arises from the recent demand for data, methodology and personal capacities applicable within the scope of repository projects where the related challenges are numerous and not yet satisfactorily reflected by adequate technologies. Indeed, no deep repository of high activity and long lived (HALL) radioactive waste has been constructed or run in Europe to date despite the effort of many European countries during the past decades. Nevertheless, stocking of HALL radioactive waste in deep underground facilities is nowadays favored by countries with massive nuclear power and waste production and its feasibility is supported by data from subterranean laboratories run by the research-field leaders. Several European countries including Czech Republic have chosen granite as the intended repository host rock owing to its abundance and commonly low inhomogeneity and porosity.

For safe and sustainable stocking the host rock must be highly impermeable, be able to retain contaminants and be able to extract the radioactive heat of the waste to prevent thermal cracking of engineered and geologic barriers. In this scope, the main geologic challenge related to waste repositories is the description of structures controlling the rock transfer properties. In granites, i.e. rocks highly impermeable in the majority of the volume, ubiquitous fractures represent localized conduits delimiting rather impermeable blocks of pristine rock and the fracture walls represent the principal rock-fluid interaction interface. In domains with low fracture density or where fractures are healed or sealed, the rock transfer properties are controlled by the rock matrix microstructures such as grain boundaries, mineral cleavages and microcracks. In this scope, macro- and micro-structural analyses coupled with direct experimental measurements represent a convenient multi-method approach when evaluating site suitability for nuclear waste repository. In addition, this methodological approach finds application in other actual geo-engineering applications where the rock transfer properties play a key role such as in energy production by exploitation of the terrestrial heat, geologic CO_2 sequestration or ultimately in hydrocarbon production from basement rocks.

Within this study, a set of techniques of structural and petrophysical analysis has been applied on the Lipnice granite in the Melechov massif, Czech Republic. This granitic massif has been previously subject to numerous studies since early 1990' when the Czech

authorities choosed it as a testing site analogous to granitic massifs actually prospected for the final repository of HALL radioactive material. Related geological reports recorded since then were in part focused also on the structural and petrophysical characteristics of the granitic massif including detailed analyses of the massif deformation history and also several focused and rather descriptive sets of petrophysical data. However, the available structural data have not been recently compiled and yet no study provided a complex set of petrophysical measurements representing the principal structures encountered within the massif. Hence, we have compiled the available and acquired new structural data in order to define the principal structural framework of the massif and we have measured many petrophysical parameters related to the magmatic structures, fracturing and alteration. The elementary goals of the structural analysis were to describe the magmatic fabric and the fracture system of the massif and to explain their origin and interplay during the massif deformation history. The elementary goals of the petrophysical measurements were to characterize various fracturing and alteration facies of the granite in terms of porosity, permeability, thermal conductivity, density and elastic properties and to explain relations between these quantities with focus on the rock pore space geometry.

2. Deep geologic repository of nuclear waste

The actual concept of deep geologic repository consists in isolation of HALL radioactive material within the geosphere in locations where it is expected to be stable over a very long time. In practice, time spans up to 10^4 to 10^5 years are considered. The idea of underground stocking of radioactive waste became important with the increasing use of nuclear energy for energetic and scientific purposes during the second half of the 20^{th} century and with the consequent necessity to isolate the spent nuclear fuel or other man-treated radioactive material (waste) from the environment. Since then, provisory disposals have been run either in superficial facilities within or close to the nuclear power stations or in geologic facilities such as abandoned mines adapted for the purpose. However, none of these accommodated HALL radioactive material, which is the most technologically exigent also due to the important heat production, though some have been used for stocking of either high activity or long lived radioactive waste (Rempe 2007).

As a consequence of international convention prohibiting export of nuclear waste, the choice of the repository host-rock is constrained by available homogeneous and impermeable rock massifs on territory of countries disposing with nuclear material. Actual research-leading countries intend to dispose the HALL waste in welded volcanic

tuff (USA), claystone (Belgium, France, Switzerland), granite (Sweden, Finland, Japan) or salt (Germany, USA) (IAEA 2009). Underground laboratories for testing and building confidence in disposal technologies have been built in all types of potential host rocks. The Swiss authorities have decided to prefer claystone formation instead of granitic massif after having considered both the possibilities and supporting the decision by the clay creep self-sealing property. In addition to the primordial considerations on the initial rock transfer properties, attention is actually also paid to enhancement of the excavation technologies with focus on reduction of the related host rock damage and contamination. Regarding the projects schedules, insertion of first HALL material waste packages to long-term deep repositories should take place within the next two decades. However, the projects may be delayed or abandoned due to the increasing safety accent but also due to changes in social, economic and political acceptance.

In Czech Republic, treatment of radioactive material has a long tradition mainly owing to the availability of significant uranium ore deposits. The actual governmental plans include increasing of nuclear power production and underground long-term stocking of the related HALL material. Recent progress in prospection for a suitable site has been marked by negative reaction of the public which resulted in convergence of candidate sites towards remote ancient army bases hardly contestable by the civil public. Actually 8 sites are considered and should be reduced to the two most suitable between 2018 and 2020 and then to the final one in 2025. Detailed study by surface methods should then first evaluate the best localizations for deep research boreholes allowing further site suitability analysis and iteration of the best position for an underground laboratory leading ultimately to construction of the final stocking facility. The schedule of the Czech repository project suggests construction of the underground laboratory by 2030, construction of the repository by 2050 and the beginning of accommodation of nuclear material by 2065 (SUJB 2011; ÚJV 2013).

3. Structures controlling transfer properties of granite

The ability of rock to transfer liquids, gases as well as thermal or mechanical energy varies primordially with volume and interconnectivity of the rock pore space. In granites, average porosity typically below one per cent is localized in non-homogeneously distributed fractures and to them related microfractures. In the prevailing volume unaffected by fracturing, the transfer properties are controlled by earlier, mostly magmatic structures manifested by organization of grain boundaries, mineral cleavages or ultimately crystal

lattices or defects. The distribution of these elementary structural features is supposed to be systematic and to reflect the superposed past deformation processes related to the granite deep origin in the ductile crust, to its uplift to the brittle upper crust and to its final exhumation and weathering on outcrop. In turn, deciphering the principal processes leading to the actual structural pattern and unraveling their mutual interplay is necessary to predict the distribution of the elementary structural features in the rock volume inaccessible for direct measurements. Structures in granite result from a sequence of physical-chemical processes involving partial melting of a source rock, segregation and ascent of granitic melts or magmas (melt + solid), their emplacement to the brittle crust and fracturing and later (near) surface weathering.

3.1 Generation and segregation of granitic magma

Granite forms by solidification of magma derived by partial melting from lower to middle crust or less usually from mantle or by mixing of magmas of both the sources (Chappell & White 1974, 2001; Wall et al. 1987; Clarke 1992; Clemens 2003; Clemens et al. 2011; Sawyer et al. 2011; Clemens & Stevens 2012; Brown 2013). In addition to the prevailing I- and S-granites with typical lower crust meta-igneous mafic to middle crust meta-sedimentary felsic protoliths, respectively, supplementary classes have been proposed to account for granites in dissimilar geologic settings (e.g. A- and C-granites, Clemens et al. 1986; Kilpatrick & Ellis 1992). The variability within granite suites has been explained in terms of crustal restite-unmixing (Chappell et al. 1987), magma mixing (Collins 1996; Keay et al. 1997) or entrainment of peritectic minerals (Clemens et al. 2011; Clemens & Stevens 2012). Due to lack of comprehensive systematization, the extended granitic alphabet was partly disputed, abandoned or modified, although the original idea of I- and S-granites remains recognized (Frost 2001; Clemens 2003; Bonin 2007; Ghani et al. 2013). In the original concept the two, mainly geochemistry-based granite types were correlated with important differences of associated structures. While the I-granites preserve mostly magma flow structures and are associated with sharp intrusive contacts marked by thermal aureole, the S-granites often comprise partially molten blocks of wall rocks recording similar thermal peak conditions (Chappell & White 1974; 2001; White et al. 1999).

The S-granites are spatially and genetically associated with voluminous meta-pelites or meta-greywackes (paragneisses to migmatites) within high-grade zones of orogenic belts affected by regional crustal anatexis providing the granitic melt (Sawyer 1996; Milord et al. 2001) which is a scheme plausible also for granitoids in the broader area of the present study (Finger et al.1997; Gerdes 2003; Schulmann et al. 2009; Žák et al. 2011). In this scheme,

different evolution stages between the protolith and the granite can be understood as a consequence of prograde high-grade metamorphism including melt-poor metamorphic processes as well as melt-rich metamorphic or magmatic processes of the granitisation in broad sense. The largest structures on the scale of the metamorphic-magmatic complex are thus represented by domains recording different degree of partial melting (Mehnert 1971; Brown 1973; Sawyer 1998).

Within the domains, the degree of partial melting dictates the resultant structures as it controls the overall rock rheology which may be associated to rock strength variations of up to sixteen orders of magnitude from the wet granite to the granitic melt (Cruden 1990; Paterson et al. 1998; Petford et al. 2000; Mecklenburgh & Rutter 2003; Petford 2003; Rosenberg 2001; Rosenberg & Handy 2005). The incipient partial melting is associated with progressive decrease of the rock strength by ca. one order of magnitude at melt fraction ~ 0.1 (van der Molen & Paterson 1979; Rutter & Neumann 1995) which corresponds to the "melt connectivity transition" (Rosenberg & Handy 2005). The low partial melting stages are characterized by redistribution of the melt along grain boundaries coupled with intracrystalline deformation (Dell'Angelo et al. 1987; Rosenberg 2001) and may be preserved in field as low degree migmatites. Strength drops of several orders of magnitude were observed for granitic material at melt fractions between 0.1 and 0.4 defined as "rheologically critical melt percentage" (Arzi 1978; van der Molen & Paterson 1979) or "solid to liquid transition" (Rosenberg & Handy 2005) characterized by breakdown of the solid network and change from grain-supported to suspension flow (Paterson et al. 1998). Although beyond the "critical melt fraction" (0.3 - 0.35, van der Molen & Paterson 1979) comprehensive experimental data are lacking, focused experiments on granitic material at melt fraction ~ 0.5 (Bagdassarov & Dorfman 1998) and on Mg-Al silicate alloys at melt fractions 0.4 - 0.6 (Lejeune & Richet 1995) point to little strength dependence on the increasing melt fraction as expected by empirical laws for suspensions (Roscoe 1952; Pinkerton & Stevenson 1992; Spera 2000). At such high melt fractions the melt is likely to segregate which may lead to scattered pattern of isolated unmolten protolith aggregates within highly interconnected melt network as observable in high-grade migmatites (Sawyer 1999; Brown 2001).

3.2 Ascent and emplacement of granitic magma

Given that the liquid melt is less dense and more mobile than the magma (melt + residuums) which in turn is less dense and more mobile than the solid protolith, buoyancy and deviatoric stress may induce differential ascent velocities within the system (e.g. Petford et al. 2000; Sawyer et al. 2011). In such a scheme, three end-member possibilities may arise:

the melt segregates from and travels through the solid, the melt does not segregate and moves as a part of the magma, or both melt segregation and magma mobility induce relative displacement of the melt within the magma and of the magma within the surrounding unmolten rock (Sawyer 1996).

Two contrasting end-member models prevail among many specific processes accompanying the crustal scale upward transfer of granitic melt or magma and its emplacement, i.e. arrest of the transfer within the crust. Forceful diapiric rise model supported by laboratory hot-stoke experiments is associated with distributed melt flow and grain flow within usually circular or elliptical intrusion and with concentric fabric in the host rock due to ballooning effect (Price 1975; Pitcher 1979; Ramberg 1980; Ramsay 1989; Patterson & Fowler 1993; Paterson & Vernon 1995; Weinberg & Podladchikov 1995; Connolly & Podladchikov 1998; Miller & Paterson 1999). In contrast, permitted diking mechanism implies incremental pluton growth by subsequent multiple (sheeted) dike and sill injections fed by localized subvertical conduits connected to deeper magma chambers (Pollard 1973; Clemens & Mawer 1992; Hutton 1992; Petford et al. 1993; Petford 1996; Clemens 1998; Engvik et al. 2005). The thermally driven vertical ascent may cease and switch to lateral emplacement typically in case of the diking model (Clemens et al. 1997) whereas the ascent and emplacement stage is regarded as essentially the same in case of diapiric rise (Miller & Paterson 1999). Phenomena related to both diapirism and diking may contribute to construction of a pluton in different stages of its evolution or during the same stages but at different depths and hence at different P-T conditions. The common treats are an early or deep rising of diapir deformed by ductile shear bands and ductile fractures localizing the melt and a late or shallow brittle-elastic opening-mode fracturing (Weinberg 1996; Solar et al. 1998; De Saint-Blanquat et al. 1998; Brown 2007; Závada et al. 2007; Weinberg & Regenauer-Lieb 2010). Stoping is another important emplacement mechanism related to disintegration of the magma chamber roof by thermal cracking and consequent sinking of its blocks down the magmatic chamber (Bouchez et al. 1997). This mechanism has been attributed only little volumetric importance though recognized as widespread (Paterson & Miller 1998), claimed not to exist or unlikely to occur (Coleman et al. 2004; Glazner et al. 2004; Clarke & Erdmann 2008; Glazner & Bartley 2008), demonstrated to affect large volumes of some batholiths (Žák et al. 2006; Pignotta & Paterson 2007; Paterson et al. 2008) and interpreted to be initiated by intrusion of sills and dikes disrupting the batholith roof (Žák et al. 2012).

3.3 Fractures in granite

Fracture is an irreversible macroscopic failure of solid which nucleates and grows by formation and coalescence of microfractures, also called cracks or micro-cracks. During fracture growth, elementary tensile microfractures form in the fracture process zone before and around the tip of the propagating fracture (Scholz 1968; Scholz et al. 1993; Vermilye & Scholz 1999). Three modes of fracture propagation are distinguished based on the relative displacement of the material on opposite sides of the fracture. In mode I extension fracture grows perpendicular to the displacement, in mode II shear fracture grows parallel to the displacement and in mode III shear fracture grows perpendicular to the displacement (Twiss & Moores 2007). Fractures may become interconnected into large-scale discontinuities such as major faults or fault zones (Vermilye & Scholz 1999; Townend & Zoback 2004; Mitchell & Faulkner 2009) that have been shown to control the transfer properties at the scale of the crust or lithosphere (Caine et al. 1996; Faulkner et al. 2010, 2011). From genetic point of view, microfractures in rock form generally in response to differential stress which can be provoked by larger-scale fractures propagation (Lespinasse & Pêcher 1986; Scholz et al. 1993; Faulkner et al. 2010), thermally induced volumetric changes (Géraud 1994; Chaki et al. 2008) or volumetric changes due to phase transition (Angerer et al. 2011; Lachassagne et al. 2011).

Brittle fracture system of a granitic massif may progressively develop throughout the solid-state history of the granite. Development of fractures in plutons and its genetic relation to the pluton magmatic structures has been a subject of discussion since the pioneering works of Cloos (1925) and Balk (1937) reminded and revisited elsewhere since then (e.g. Berger & Pitcher 1970; Price and Cosgrove 1990; Paterson et al. 1998; Bahat et al. 2003; Žák et al. 2009). The original work on "granittektonik" presents a concept of on an ideal elongated dome-shaped intrusion with developed linear and planar "primary" flow fabrics (magmatic lineation and foliation) and to them systematically oriented four sets of "primary" joints. "Cross" joints form perpendicular to both the flow structures due to continuing stretching parallel to the elongation direction of the pluton or due to drag of magma flowing in the mobile pluton core against the solid roof or wall rock. "Longitudinal" joints form perpendicular to magmatic foliation and the cross joints and thus parallel to the magmatic lineation and are due to cooling contraction of slabs delimited by the cross joints. "Parallel" joints form near the intrusion roof perpendicular to both the cross and longitudinal joints, i.e. parallel to both the magmatic lineation and foliation, and their formation is driven by vertical stress drop due to cooling shrinking or due to pluton roof unloading causing their orientation to be coupled with that of the pluton

roof. Finally, "diagonal" shear fractures form diagonally to the cross and longitudinal joints to accommodate the lineation-parallel stretching. In contrast to the original concept of Cloos (1925) relating the "primary" magmatic and brittle fabric to the pluton shape and to the magma flow orientation, magmatic fabric may reflect strain from various processes including regional tectonic deformation unrelated to the magma flow or the pluton shape (Paterson et al. 1998; Žák et al. 2007). Furthermore, joints in granite have been shown to form in regional stress field (Bankwitz & Bankwitz 1994; 1997) and prior (Bahat et al. 2003), during (Bahat & Rabinowitch 1988) or after the pluton uplift (Holzhausen 1989; Bahat et al. 1999; Lachassagne et al. 2011). Faulting of the pre-existing joints or formation of new mode shear fractures, which is less common due to higher activation energy, represent deformation structures that may systematically develop on the massif-scale during and after the massif uplift and exhumation (Wilkins et al. 2001). Depending on the faulted fracture wall roughness and on syn-faulting fluid activity, various secondary structures may develop and modify the fracture surface and consequently the fracture (wall) permeability (Wilson and Will 1990; Engelder et al. 2004). In addition, in favorable cases the structures serve as fault kinematics indicators (Price & Cosgrove 1990; Twiss & Moores 2007).

4. Geological setting of the Melechov Massif

The Melechov Massif (MM) represents the northernmost part of the Central Moldanubian Pluton (CMP), which belongs to the deeply eroded high grade orogenic root of the eastern European Variscan orogen, the Moldanubian Zone (MZ), within the Bohemian Massif (BM), Czech Republic. The rocks of the MM cover an area of about 110 km^2, reach to a depth of 15 km and form a cylindrical subvertically prolate magmatic body (Šrámek et al. 1996). The columnar batholith of the MM consists of four types of peraluminous two-mica granite disposed in a concentric manner (Procházka et al. 1998; René 2001; Procházka & Matějka 2006). From the center outwards these are the Stvořidla, Melechov, Kouty and Lipnice granites (Fig. 1). In comparison with other moldanubian granitic rocks the types Stvořidla and Melechov fit the best the Eisgarn type, the Kouty type fits the type Čímě̌ř, whereas the type Lipnice does not have any close equivalent in the Moldanubian with the principal deviatory parameter being the high Th content on the order of tens of ppm (Procházka et al. 1998; Breiter 2006).

The majority of the study area (N, E and S of the massif) belongs to the middle-crustal Monotonous group of the MZ (Vrána 1988; Vrána et al. 1995) and is formed by

paragneisses and derived migmatites. The highest-degree migmatites are present at the SE limit of the massif close to the principal part of the CMP further south (CGS geologic map, 2013). Here, the contact between the granites and the country rock is spatially diffuse with commonly observed sharp or gentle transitions between numerous small (~ 10^2 m^2) bodies of granitic and metasedimentary rocks. Delimited from the Monotonous group by a major fault (Mitrenga et al. 1979), the host rock west of the massif belongs to the upper-crustal Varied group and is dominantly composed of paragneisses with numerous, intercalations of marble or erlan.

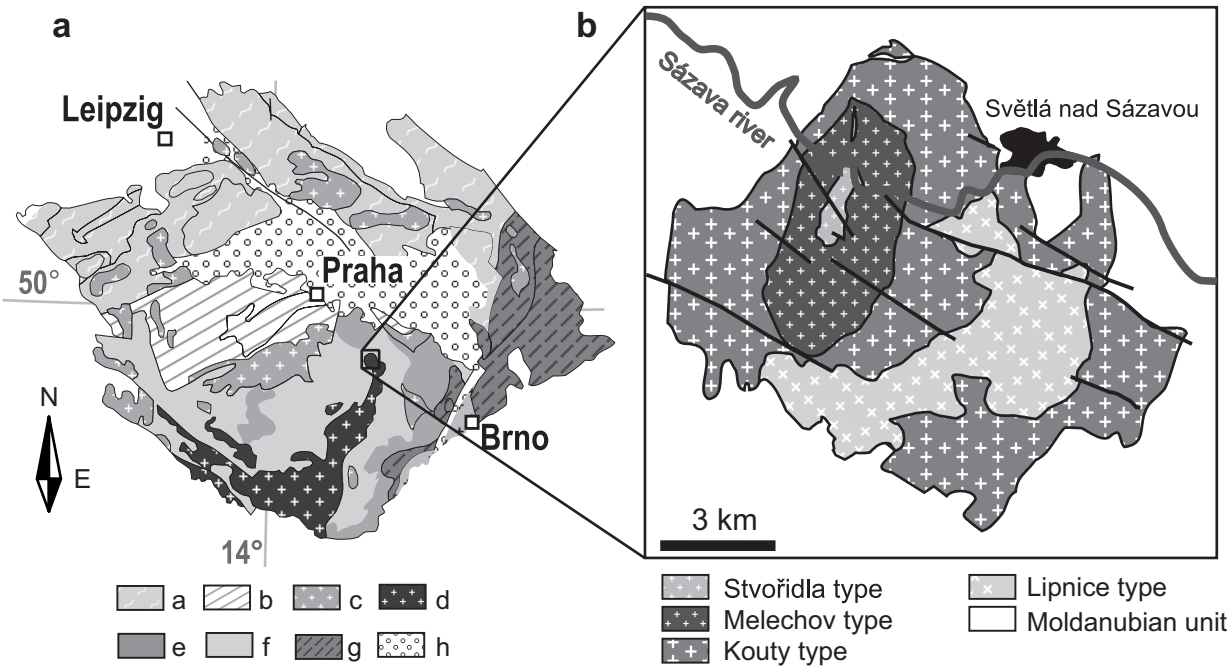

Figure 1. (a) Simplified geological map of the Bohemian Massif showing the location of the studied Melechov massif, (a – Saxothuringian and Lugian, b – Teplá-Barrandian, c – Variscan granitoids, d – Central Moldanubian Pluton, e – Gföhl unit, f – Varied and Monotonous unit, g – Brunovistulian, h – Cretaceous sedimentary cover), (b) Geological map of the Melechov massif showing the extent of the four granite types (modified after Machek 2011).

4.1 Metamorphism and deformation in the host rock

A detailed petrologic and structural description focused on the present study area is given in Schulmann et al. (1997), which was later compiled with other related reports in Procházka et al. (1998). Three domains featuring different mineral associations and crystallization evolutions have been described, with the lowest-grade rocks in the Varied group W of the massif, intermediate degree-rocks in the Monotonous group NE of the massif and the highest-grade rocks in the Monotonous group SE of the massif.

The peak metamorphic conditions of the Varied group containing dominantly biotite-paragneisses and subordinary marbles and metamorphic Ca-silicate rocks were estimated to 500 MPa and 600 °C. Structures observed in this domain have been interpreted

in terms of four phases of deformation. The oldest recognized foliation S_1 is defined by alternating layers with contrasting composition: paragneiss- and erlan-rich layers in layered paragneisses, Ca- and feldspar-rich layers in the Ca-silicate rocks, felsic and biotite-rich domains in metagreywackes and layers with different content of quartz or feldspar and with different grain size in marbles. The S_1 dips moderately to the W-SW and no orientation is recorded for rarely developed lineation L_1 defined by weak organization of biotite aggregates in paragneisses. Locally developed isoclinal folds V_1 affect erlan layers in layered paragneisses, where locally developed axial cleavage is subparallel to the S_1. D_2 structures are represented by dm to m scale recumbent, open to tight folds with NNE or SSW gently plunging fold axes and S_1-parallel W-SW dipping fold axial planes and by W-dipping shear bands and W-NW plunging elongation or contraction axes of mineral aggregates. ESE dipping D_3 aplite veins crosscut V_2 folds and are crosscut by S_1-parallel planes. Joints and faults crosscutting the former structures represent the latest D_4 deformation. For the sillimatnite-biotite paragneisses and low degree migmatites NE of the MM the peak conditions were estimated to 400 – 800 MPa and 650 – 750 °C and available records show NE-dipping S_2 defined by alternation of migmatites leucosome and melanosome. For the cordierite +/- sillimanite medium to high grade migmatites in the SE vicinity of the MM the peak conditions were estimated to 350 – 600 MPa and 700 – 800 °C. Three phases of deformation were defined for this domain. Orientations of scarce D_1 structures correlate with folded foliation in unmolten paragneiss relics passively rotated during the high-degree anatexis and feature no stable orientation. The orientation of the migmatite S_2 foliation is locally highly variable and disrupted in domains with increased melt fraction. At places with stable orientations the S_2 is steep to subvertical and strikes NE-SW. The S_2 is folded by V_3 open to tight folds and kink-bands with S-plunging fold axes and S- and SE-dipping fold axial planes. Shear bands sub-parallel to the V_3 fold axial planes are locally developed. It has been interpreted that the D_1 was earlier than the regional anatexis in both the Varied and Monotonous group. Extensive regime persisted in the Varied group during D_2 and D_3, whereas in the Monotonous group D_2 was associated with compression and D_3 with extension. Furthermore, it has been concluded that an initial E-W compressive regime led to steep fabrics in the structurally deeper Monotonous group and that a following extensional regime acted on the semi-brittle Various group at the same time the Monotonous group was suffering normal movements at ductile conditions.

4.2 Magnetic fabric

The results of analyses of magmatic susceptibility (AMS) of rocks within the study area can be found in several previous works (Schulmann et al. 1997; Procházka et al. 1998; Lexa & Schulmann 2006). The data from the eastern part of the Lipnice granite indicate highly variable, dominantly oblate to weakly prolate shape and weak, granite boundary-concentric magnetic fabric. Towards the core of the MM the AMS degree increases in association with higher degree of the granite recrystallization. Anticlinal magmatic structure revealed in the older granite intrusions (Lipnice and Kouty) close to and on the opposite (NE and SW) sides of the younger ones (Melechov and Stvořidla) were interpreted in terms of perturbation of the initially concentric fabric by the intruding and heating younger granites. Within the Melechov granite, concentric lineations and flat foliations were interpreted in terms of magmatic flow within the intrusion including interaction of successive magma pulses.

4.3 Fracture system

Brittle structures within the MM were studied within well exposed quarries (Coubal 1994; Schulmann & Lexa 2000), boreholes (Lexa & Schulmann 2005), on the scale of the polygons related to the RAWRA testing site (Lexa & Schulmann 2004) and are synthetized in Lexa & Schulmann 2006. Recognized were: mutually perpendicular ESE-WNW and NNE-SSW striking joints of sets 1 and 2, respectively, supposed to be related to the primary post-magmatic system and latterly reactivated; moderately NE or SW dipping joints of set 3; tectonic N-S to NNW-SSE trending striking joints or faults of set 4 and a fifth set represented by exfoliation fractures. Three-stage reactivation has been suggested to affect the joint sets 1, 2 and 3 with the first related to NW-SE maximum stress resulting in transcurrent strike-slip movements, the second related to NE-SW maximum stress resulting in transcurrent movements on set 4 and 2 and in formation of new, set 2-parallel joints, and the third related to ESE-WNW minimum stress reactivating set 3 joints.

4.4 Constraints on age of emplacement

Based on granite-host rock cross-cutting relationships and on interference between the distinct granite intrusions, the succession of the MM poly-phase magmatic activity began by the Lipnice granite and was followed by Kouty, Melechov and Stvořidla granite with relative age decreasing towards the massif core. It is suggested that the older intrusions of the Lipnice and Kouty granite are autochtonous and related to in-situ granitisation and assimilation of the surrounding paragneisses (Schulmann et al. 1998; Rajlich 2001; Procházka

2005, Procházka & Matějka 2006) and that the younger geochemically similar Melechov and Stvořidla granites intruded the former granites as alochtonous and fractionated melts segregated from a common deeper crustal source (Procházka & Matějka 2006). On the basis of microprobe-measured content of Th, U, and Pb in monazites from within the distinct intrusions Breiter and Sulovský 2005 suggest that all the granites solidified in a short time span 318 to 313 Ma with estimated intrusion ages 318 ± 7 Ma to 317 ± 17 Ma for the Melechov granite, 313 ± 15 Ma for the Kouty granite and 315 ± 23 Ma to 313 ± 14 Ma for the Lipnice granite recording also another thermal event at 308 ± 13 Ma. Based on high-resolution U-Pb monazite dating Gerdes (2003) suggests intrusion of late-Variscan CMP two-mica (Eisgarn-like) granites between 319 and 315 Ma. Using the same method the migmatitisation and granite intrusion in the northern part of the CMP has been recently dated to 329 Ma and 327 Ma, respectively, suggesting rapid migmatite exhumation from depth of ~ 21 km and subsequent intrusion of the S-granites into the migmatites at depths < 9 km (Žák et al. 2011). According to the concepts recently put forward to explain the structure of the Bohemian Massif (Schulmann et al. 2005, 2009; Lexa & Schulmann 2006; Guy et al. 2011; Maierová et al. 2012) and in particular the exhumation of the Variscan orogenic middle and lower crust (Štípská et al. 2004; Racek et al. 2006; Lexa et al. 2011; Žák et al. 2011) the CMP magmatic rocks together with their paragneiss-migmatite host rocks (called as a whole "the Pelhřimov Complex" in the latter work) was uplifted to shallower crustal levels during and shortly after the Variscan peak metamorphism, i.e. between c. 340 and 325 Ma.

Chapter II:

Structural Characterisation of the Massif

1. Introduction

Structural analysis of the granitic massif and its country rock is a first step to constrain the distribution of structures controlling fluid permeability and heat transfer on the scale of the massif.

In massifs of crystalline rocks featuring generally low porosity, such as granite, the system of fractures represents the fundamental network of conduits within otherwise massive and highly impermeable rock. In this context, the primary task of the presented structural analysis was to acquire data on distribution of the fractures present within the massif. In practice, the totality of fractures in a rock volume on the order of 10^2 - 10^3 km^3 cannot be entirely described and usually local outcrop, quarry or borehole data are extrapolated. The extrapolation is usually based on observation and consequent assumption that the fractures group into fracture sets characterized by proximate fracture size, orientation, fracture spacing, clustering and structural position within the massif. On surface, such data can be acquired by field structural measurements, whereas for direct acquisition of data on the interior of the massif borehole drilling and consequent logging are necessary. For integral description of the massif fracture system, the origin of the fractures has to be explained in terms of stress field coeval with their formation as such notion may imply further constrains on the fracture distribution in the massif volume inaccessible for direct measurements. The record of regional stress relative to pre-, syn- and post-emplacement stages of the granitic massif may be in favorable case preserved within the country rocks. In contrast to the granites of the studied massif, which are often weakly anisotropic, the metasedimentary country rocks are strongly foliated and folded. This implies the folding-related structures as the primary targets of the country rock structural analysis, though the fractures, which are substantially less abundant here than in the massif, are important for deciphering the deformation history of the study area.

In this chapter, a large set of structural measurements acquired both within the granitic massif and the surrounding metasedimentary rocks is presented. Using orientation diagrams and maps, the structural pattern of both the magmatic fabrics and the fracture system are constrained on the scale of the massif and discussed in terms of deformation processes leading to their formation and variability in distribution. Within the scope of the present study, the established structural framework serves mainly to support the petrophysical and microstructural measurements presented in Chapter III and IV which are focused on the effect of the magmatic structure, fracturing and alteration on the transfer properties of the granite.

2. Data acquisition and processing

The structural database processed here contains data acquired during previous RAWRA (Radioactive Waste Repository Authority of the Czech Republic) studies concentrated on the Melechov Massif and new data we have acquired during field work in the frame of the present study.

2.1 Compilation of available structural data

Several RAWRA reports present data on the anisotropy of magnetic susceptibility (AMS) and the fracture system of the MM and in a lesser extent also on structures in the massif host rock (Schulmann et al. 1997, Schulmann & Lexa 2000, Lexa & Schulmann 2004, Lexa & Schulmann 2006). The first step of the present study consisted of gathering, organisation, formatting and georeferencing of data available in these reports as well as of data measured during the previous studies but not published as yet (Lexa, pers. comm.). As a result, 2387 structural measurements acquired on 150 sites have been compiled. Given the various formatting and sources within the data (.txt, .dbf, .xls, .mdb, .shp, paper maps and texts) the compilation process began by unification of the data format and consecutive data merging into a single structural database facilitating further data export and treatment. For this purpose the PySDB (Python Structural Database, http://petrol.natur.cuni.cz/~ondro) software suited for stocking and management of numeric structural data was used. For few sites where the only source of their position was a non-georeferenced, usually raster map, the coordinates were extracted via georeferencing and subsequent calculation of the raster data point position using ESRI ArcGIS software.

2.2 Field work

The field work was based on preliminary evaluation of the map extent of the compiled structural data and was focused on blank spots in the otherwise extensive record within the massif and on some proximate or remote country rock domains where structural data was not available or spatially discontinuous. In both the cases the field work consisted in measurement of orientation of geologic structures on outcrops using geological compass and in recording of the site positions using a GPS apparatus. The new field structural data were added to the structural database containing the compiled previous data.

2.3 Primary structural database

The resulting database contained information on sites (name, geographic coordinates, unit) and on structural measurements linked to these sites (structure, dip

direction / plunge direction, dip / plunge). The structures recognized in the database comprise magnetic fabric (AMS ellipsoid principal axes), veins (aplite, pegmatite, quartz), fractures and fracture surface features (joints, exfoliation joints, faults, fault lineations, relative displacement indicators) and ductile structures in the country rock (foliations, fold axial planes, fold axes).

2.4 Cluster analysis and Jelínek statistics analysis

Within the primary database, the number of measurements per site varies from one to c. 150, with the least populated sites typically corresponding to a single fracture or foliation measurement on small and poorly exposed outcrops and the most populated representing several detailed fractographic and AMS studies executed in well exposed quarries. For the purpose of creation of structural maps on the scale of the massif such data were inappropriate as they would show too much information on detriment of the map clarity. The first goal of the data treatment was thus to prepare a secondary database containing simplified structural data representative of the primary database.

In cases of single measurement per structure and site the records were duplicated to the secondary database. For multiple measurements the data was subject either to cluster analysis in SpheriStat software for the field structural measurements or to the Jelínek statistics analysis in AniSoft software for the AMS data. For a minor (9/64) part of the AMS sites (LX01 – LX04, LX10 - LX15) the original AMS measurement files (.ran / .poo) were missing. However, results of analyses of specimens from these sites were available (.xls) and the mean orientation of the principal axes of the AMS ellipsoid was therefore calculated via cluster analysis in SpheriStat software using all the available specimen data.

Except for brittle structures, the primary data featured rather site-unimodal distributions and were approximated by one mean orientation per structure and site. Concerning the orientation of joints, field observations as well as previous studies indicate that the granitic massif joint system can be divided into two principal mutually subperpendicular sets of dominantly subvertical joints developed on the scale of the massif (set 1 and 2), two locally developed sets of steep and moderately to shallowly dipping joints (set 3 and 4, respectively) and a fifth set represented by shallowly dipping to subhorizontal exfoliation joints. The latter set, which is presumably not developed at depths below 200 m, was not treated in this study as it is assumed insignificant for the repository depths of c. 500 m. For the other joints, mean cluster orientations calculated separately for each site were given an attribute corresponding to one of the four treated joint sets, assuming that the joints of the set 1, 2 and 3 show regular mutual orientation with dominant ESE-WNW,

NNE-SSW and N-S strike, respectively, and that the set 4 is represented by moderately to shallowly dipping joints with dip directions variable at the scale of the massif. These observations and assumption have also been taken into account when clustering all the joint orientations into the sets.

2.5 Spatial averaging of orientation of structures

The spatial averaging was used to visualize trends of structures for which numerous and wide-spread measurements were available: foliations and fold axes in the country rock, magnetic foliation and lineation and joints within the massif. Except the joints, the procedure was used only as an auxiliary step supporting the choice of representative measurements intended for structural maps display (described later). For joints, the clustered and set-attributed data were used as input for inverse-distance-weighed spatial averaging of orientation using the SpheriStat software. The averaging was done using the moving circle method with circle diameter 5000 m for joints sets 1 and 2, 2000 m for joint set 3 and 1000 m for joint set 4. The preset circle diameter also defined the extrapolation distance from the closest measurements of orientation of joints attributed to the respective joint set. For all the sets the treatment resulted in grids of averaged orientation data points with regular spacing between 250 and 300 m. The resulting grids partly overlapped the granitic massif boundary and were clipped by the Melechov massif polygon extent using the clip function within data management toolbox of the ESRI ArcGIS software.

2.6 Interpolation of structure dips and of AMS parameters

Similarly to the application of the spatial averaging, inverse distance weighing interpolation using the spatial analyst toolbox within ESRI ArcGIS software was independently applied on inclination values of the same datasets (foliations and fold axes in the country rock, magnetic foliation and lineation and the four joint sets within the massif) plus on the AMS parameters (P and T shape parameters and Km – the mean magnetic susceptibility) in order to display their spatial variation in a continuous fashion by means of raster datasets.

The applied algorithm was the same for all the features and its variable parameters were adjusted specifically for each of them due to the differing spatial extent (c. 30 x 30 km for the country rock and c. 15 x 15 km for the granitic massif) and spatial density of the feature source datasets (e.g. c. 0.5 and c. 7 measurements per square km for the foliation and for the AMS values, respectively). Given the irregular spatial distribution of the input features, in all cases the variable data point distance option was used, with input data point number fixed to approximately 1/20 of the total count of input features. Another

adjustable variable of the interpolation algorithm was the power parameter controlling the measure of influence of distant features on the resulting pixel value. In practice, a series of values between 0.5 and 2.0 of the latter parameter were tested for each of the interpolated feature datasets. For the final image a compromise between scattered pattern with little bias and homogeneous pattern with large bias was aimed and supported by comparison of value histograms of the input and the output data sets to avoid oversimplification. Another important setting of the procedure was the definition of polyline barriers in order to restrain the algorithm search for neighboring input data to the appropriate definition range. Thus, the interpolation within the country rock was bounded by limits of the complement of intersection of the maximum rectangle data extent with the extent of non-country rocks and the interpolation within the massif was bounded by the massif external boundary.

The final step of the interpolation procedure consisted in classification of the output values and definition of symbology look-up-tables (colour ramps) for the classification display. For all the interpolated inclination raster data sets, 9 classes of 10° and the same multi-colour ramp was used in order to facilitate comparison between the different features. For the other group of interpolated raster datasets showing the values of the AMS parameters, the classes corresponding to multiples of standard deviation based on the dataset statistics calculated within the ESRI ArcGIS software were used and a bi-colour ramp was applied to highlight differences with respect to the mean value of each dataset.

2.7 Reduction of displayed data for sake of clarity

One type of results of this study are maps showing structural symbols representing mean orientations based on the cluster analysis (foliations, fold axes, magmatic foliations and lineations) with the interpolated inclination raster in the background. Despite the site-based cluster analysis simplification, the maps would have locally featured overlapping symbols representative of spatially close, though different sites if no further treatment had been done. In order to improve the clarity of the maps, some of the symbols at the overdensified spots must have been deleted. To execute this reduction and at the same time to preserve the primary data information, the results of the above mentioned spatial averaging and interpolation were used as a supporting criterion throughout the exclusion process. Another criterion concerned only the country rock ductile structure data and arose from the fact that the structural record on sites was often incomplete in terms of measurements of the three principal structures (foliation, fold axial plane, fold axis), i.e. at least one of the structures had not been represented by any measurement. In such situations the measurements at sites with complete record were preferred to be displayed.

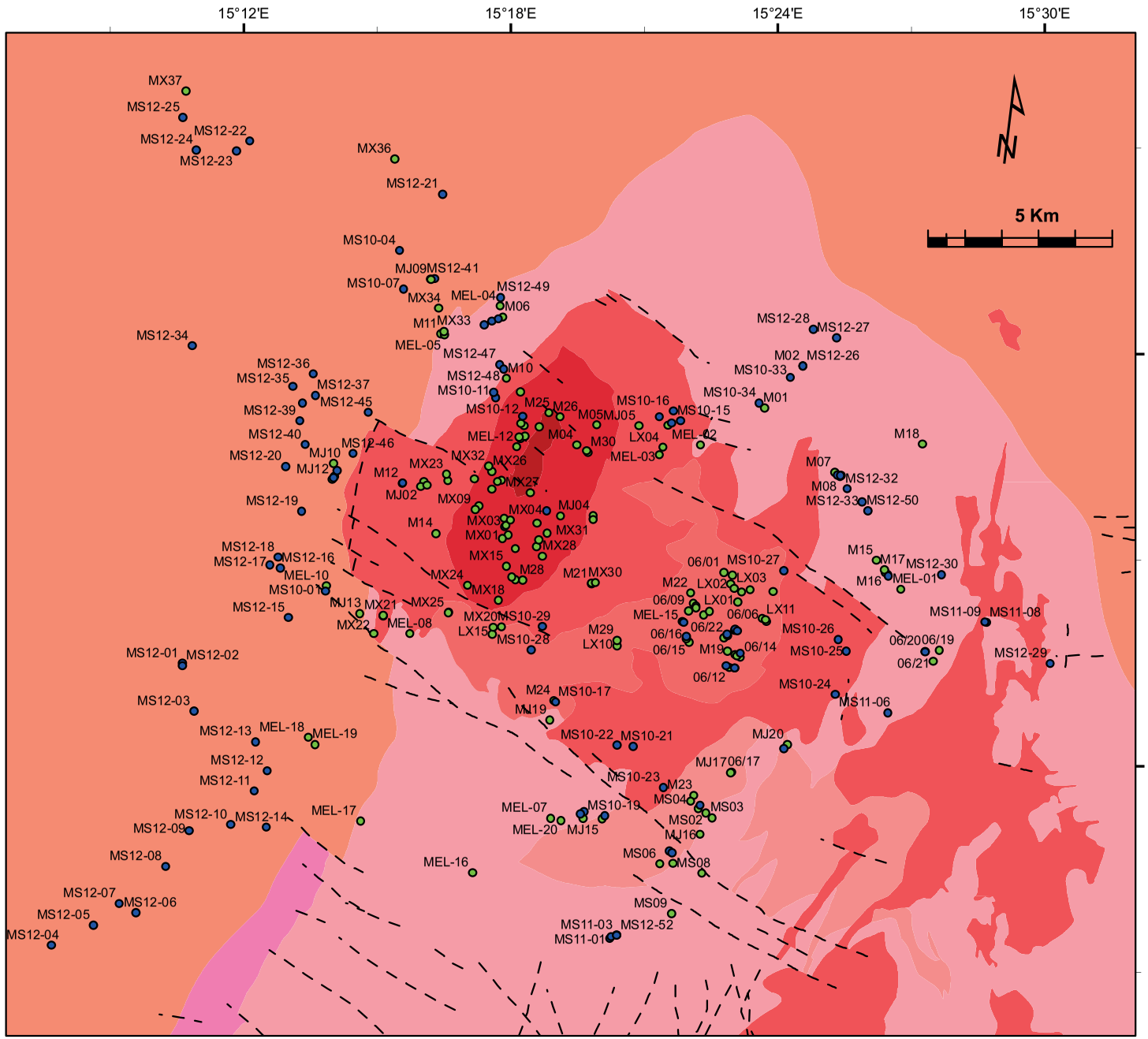

Figure 1. Geologic map of the study area showing position of data sites. The points correspond to the position of data sites recorded in this study (blue) and in previous studies (green). The geologic map shows the extent of the four granite types within the Melechov massif and of granites of the Central Moldanubian Pluton, high grade anatexites and paragneisses of the Monotonous Group (M), paragneisses of the Varied Group (V), unassigned orthogneiss and major faults (simplified based on CGS 1:50000 map 2013).

3. Results

The position of the sites included in the structural analysis can be seen on a geologic map of the study area in Fig. 1. The treated data density distribution is displayed in Fig. 2 for all the treated data, for the data acquired within the present study and for the data acquired in previous studies.

3.1 Structures in the massif host rock

3.1.1 Definition of structural domains

Three different structural domains in the massif host rock have been defined based on the lithology, metamorphic grade and overall structural pattern.

The rocks of the Varied group (VG) west of the massif represent the lowest grade domain (domain W) with the dominant foliation defined by disjunctive foliation within the prevalent paragneisses. The paragneisses outcropping on majority of the sites within this domain are in the northern part intercalated by cm to several m thick layers of erlan or marble defining compositional foliation which is subparallel to the one in the paragneisses. The dominant foliation is folded by metric to decametric gentle to tight asymmetric folds with the largest ones developed in paragneisses in the southern part and in the competent thick layers of marbles in the northern part. In addition, in the northern part centimetric isoclinal intrafoliation folds subparallel to the dominant foliation are rarely preserved.

The rocks of the Monotonous group (MG) northeast of the massif represent the medium grade domain (domain NE) with the foliation defined by disjunctive foliation in paragneisses which locally prograde into low degree migmatites with foliation defined by alternation of leucosome and melanosome. Both the disjunctive and the migmatitic foliation are folded by decimetric to metric gentle to close asymmetric folds.

The rocks of the MG southeast of the massif represent the highest grade domain (domain SE) with the foliation defined by alternation of leucosome and melanosome in medium to high degree migmatites. A variety of fold styles is represented in this domain by open and round to close and angular cm-dm symmetric and asymmetric folds. The overall high degree of partial melting in this domain is demonstrated by locally melt-disrupted folded migmatite foliation and by frequent granitic dikes or melt pockets.

3.1.2 Orientation of ductile structures in the domains

The orientations of the dominant foliation and of fold axes and axial planes have been plotted on stereograms in Fig. 3 separately for each of the defined structural domain.

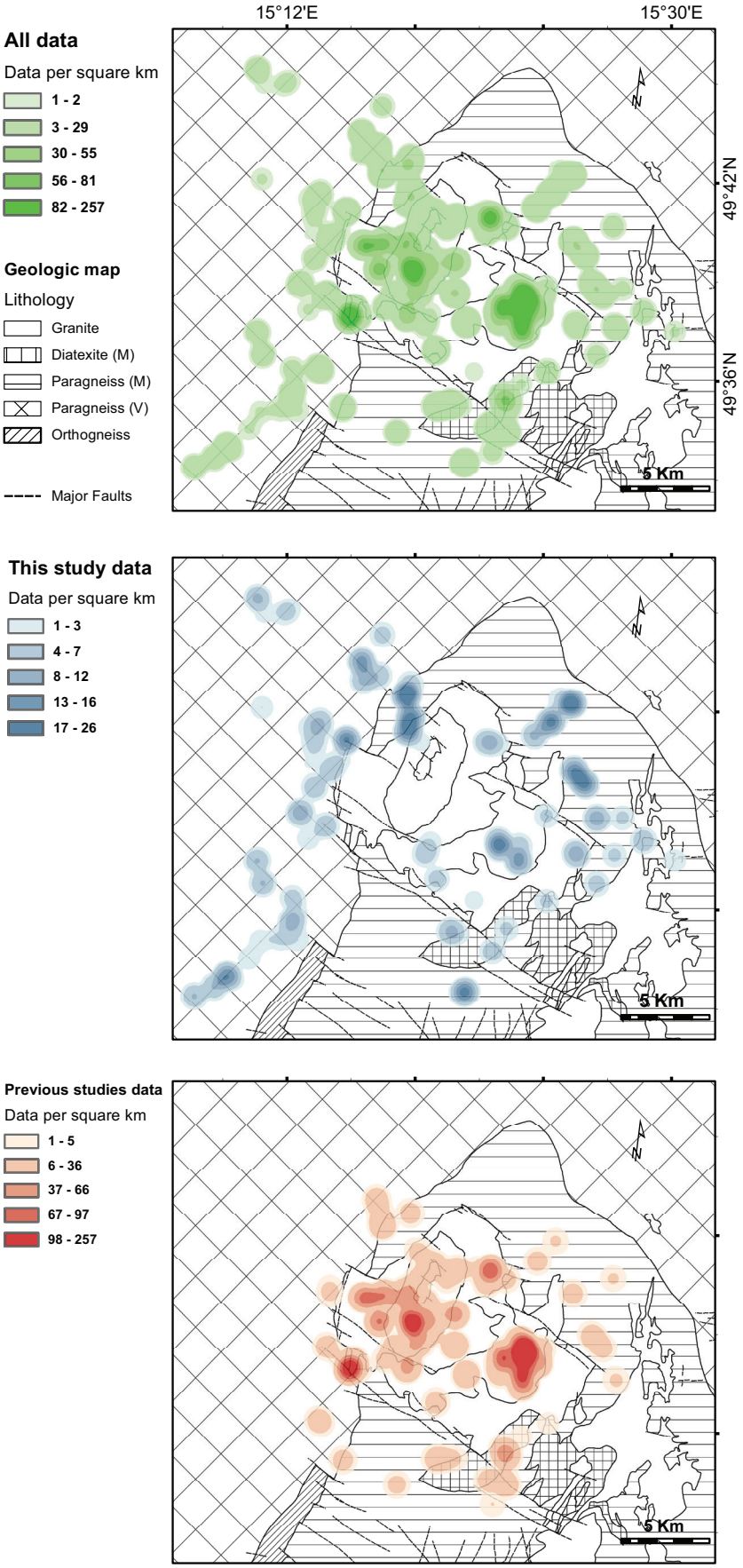

Figure 2. Data density distribution within the study area. Maps showing values of interpolated distribution of all data included within the structural analysis (top), of data acquired within the present study (middle) and of data from previous studies (bottom). The geologic map legend is common to all the maps.

In domain W (Fig. 3a) the foliation and the long limbs of the folds dip moderately towards W-NW, the fold axial planes show similar W-NW dip directions as the foliation though with more gentle, up to subhorizontal dips and the fold axes plunge gently towards WSW. In addition to these dominant orientations the stereograms reveal girdle distribution of poles to foliations and of fold axes. The directions of poles to foliations are distributed along a great circle with the pole approximately coinciding with the dominant cluster of fold axes directions oriented c. 250/30. Inversely, the directions of fold axes are girdle-distributed along a great circle with the pole approximately coinciding with the dominant cluster of poles to foliations oriented c. 115/50.

In domain NE (Fig. 3b) the foliations and the long limbs of the folds dip steeply to moderately towards N to NE, the fold axial planes dip steeply towards N subparallel to the principal orientation of foliation and the fold axes plunge gently to moderately towards

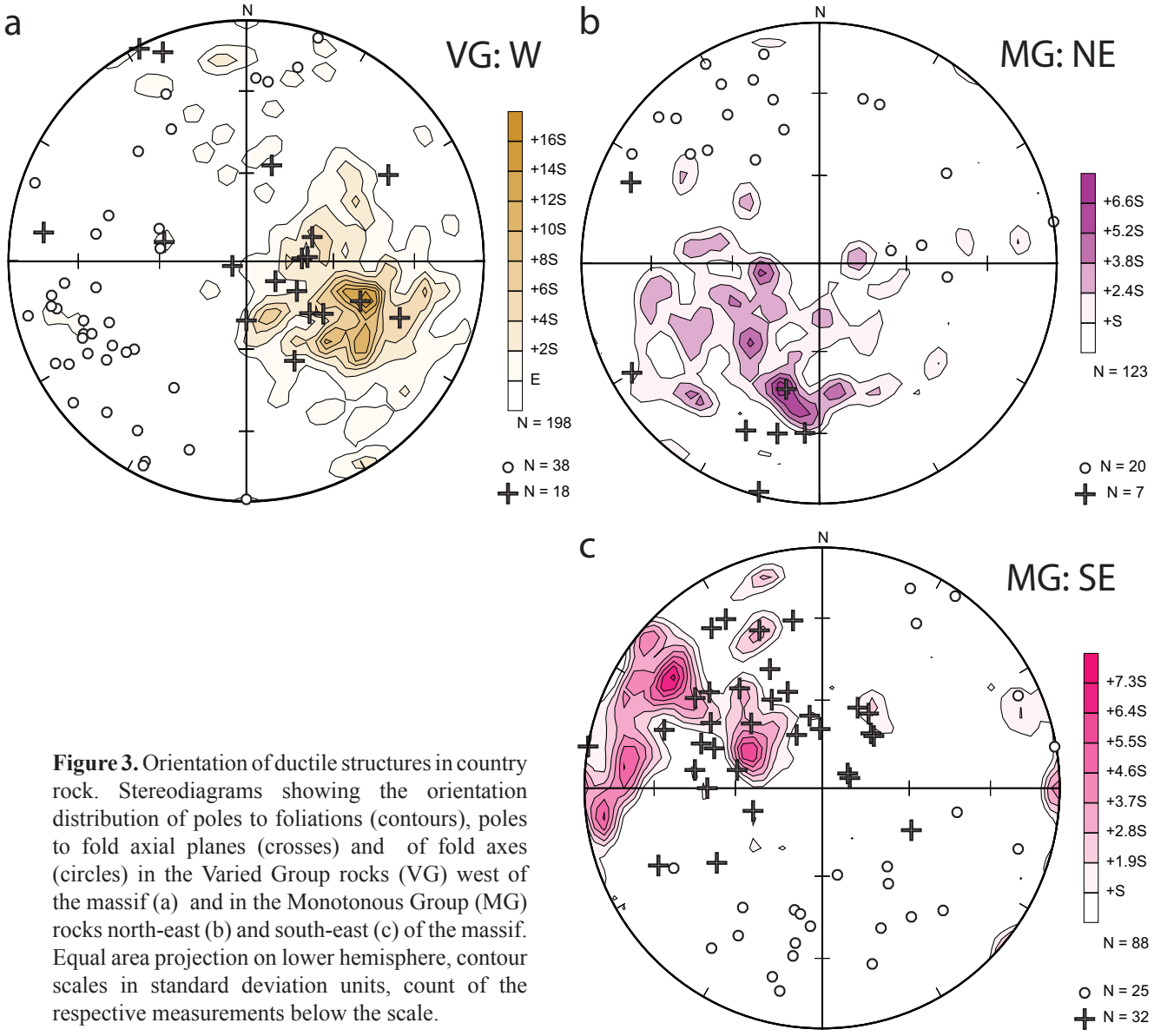

Figure 3. Orientation of ductile structures in country rock. Stereodiagrams showing the orientation distribution of poles to foliations (contours), poles to fold axial planes (crosses) and of fold axes (circles) in the Varied Group rocks (VG) west of the massif (a) and in the Monotonous Group (MG) rocks north-east (b) and south-east (c) of the massif. Equal area projection on lower hemisphere, contour scales in standard deviation units, count of the respective measurements below the scale.

NNW to NW. In addition to these dominant orientations the stereograms reveal girdle distribution of poles to foliations and of fold axes with the great circle poles oriented c. 50/55 and 210/60, respectively.

In domain SE (Fig. 3c) the foliations dip steeply to moderately towards ESE to E, the fold axial planes dip moderately to gently towards E to SSE and the fold axes plunge gently to moderately towards S or SSE. Whereas the poles to foliations and to fold axial planes feature rather clustered distribution with the latter being in between the submaxima of the former, fold axes show girdle distribution with the great circle pole oriented c. 315/45, i.e. subparallel to poles to both the planar structures.

3.1.3 Spatial variation of orientation of the ductile structures

In addition to the stereograms the distribution of orientation of the foliations and of the fold axes within the study area is documented on maps in Figs. 4 and 5 by means of discrete structural markers showing strike and dip directions accompanied by spatially interpolated values of dip.

In domain W the foliation strikes dominantly NNE-SSW subparallel to the large-scale discontinuity represented by boundaries of the VG with either the MG or the MM and the foliation dip increases northward from gentle dips in the south, moderate in the central part and steep in the north. On the domain scale the foliation strike varies along with variations in strike of the major lithological boundaries and on a smaller scale may be deviated from the general NNE-SSW strike to E-W or NW-SE strikes in association with steepening of the dip. The latter situation can be seen in the northern part of the domain several km away from the massif as well as in the very vicinity of the massif near its WSW limit. Finally, the outermost measurements either in the NW or SW extremity of the study area show coherently the general NNE-SSW strike and gentle to moderate WNW dips. Similarly to the foliation the fold axes show northward increasing subhorizontal to moderate plunge and somewhat more scattered trend of generally NNE-SSW direction with local deviations to E-W or NW-SE trends.

In domain NE the foliation strikes WNW-ESE or E-W at moderate dips north of the massif and deviates to N-S strike at steep dips east of the massif. In addition, the highest dip values appear in the vicinity of the massif, whereas the lowest dip values appear in the more remote part of the domain. The fold axes orientation is rather stable in the northern remote part of the domain with NW-SW trend and gentle plunge and deviates to N-S or NE-SW trends associated with steeper, up to moderate plunges in the vicinity of the massif.

In domain SE the foliation strikes NNE-SSW at steep dips in association with the high degree migmatites and deviates to WSW-ENE or W-E strike at moderate dips further west. The trend of fold axes varies coherently with the foliation strike, i.e. NNE-SSW deviating to WSW-ENE or W-E towards the west, and the plunge is moderate in the vicinity of the massif and gentle farther away (~ 3.5 km) from it.

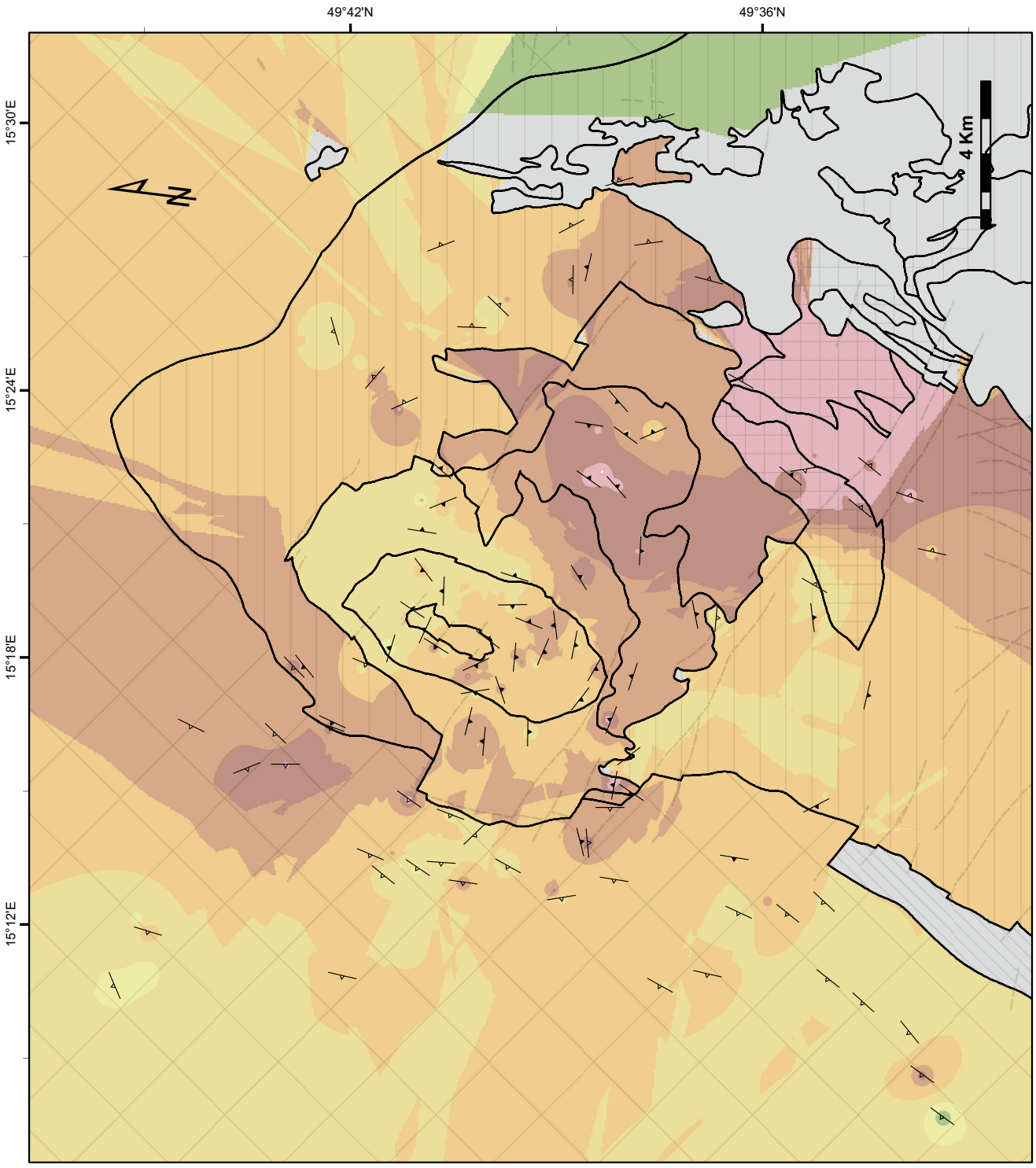

Figure 4. Map showing orientation of macroscopic foliation in the metasediments (empty symbols) and of magnetic foliation in the granitic massif as well as in the metasediments (full symbols). The raster background shows interpolated dip values with common scale for both the structures. Gray colour represents no dip data.

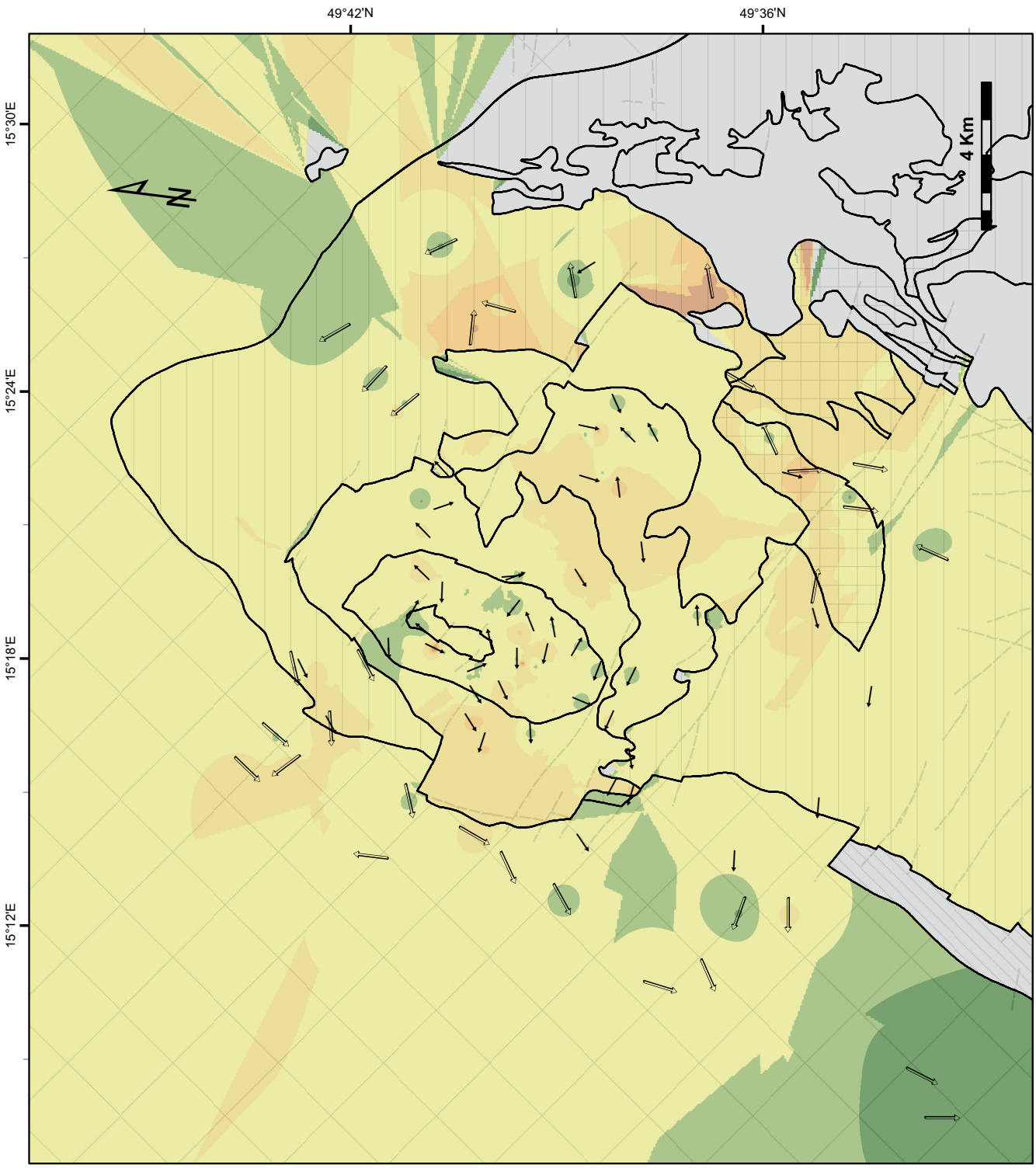

Figure 5. Map showing orientation of fold axes in the metasediments (empty symbols) and of magnetic lineation in the granitic massif as well as in the metasediments (full symbols). The raster background shows interpolated dip values with common scale for both the structures. Gray colour represents no dip data.

3.1.4 Veins, joints and faults

The orientation of pegmatite, aplite and quartz veins within the host rock is displayed on stereogram in Fig. 6. The pegmatite veins dip gently to moderately mainly towards S, the aplites are subhorizontal and the quartz veins are subvertical to moderately dipping to the E (from SE to NE).

The orientation of joints within the host rock is displayed on a stereogram in Fig. 7 (f). Three sets of dominantly steep joints can be distinguished commonly for the VG and the MG. The most populated set comprises subvertical joints striking WNW-ESE, the intermediately populated set comprises steep joints striking NNW-SSE and the least populated set comprises steep to moderately to gently dipping and NW-SE striking joints.

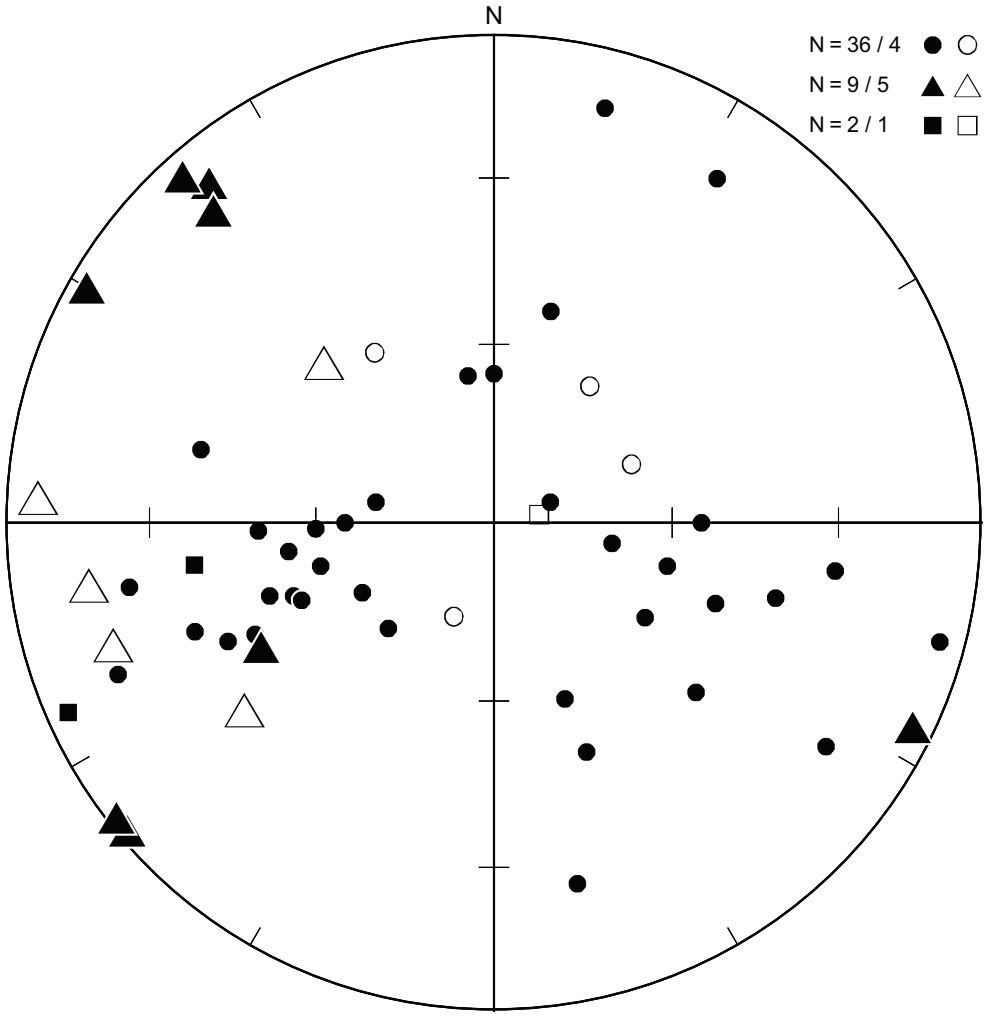

Figure 6. Orientation of veins in the study area. Stereodiagram showing the orientation distribution of poles to pegmatite veins (circles), to quartz veins (triangles) and to aplite veins (squares) in granite (full symbols) and in country rock (plain symbols). Equal area projection on lower hemisphere, count of the measurements at top right.

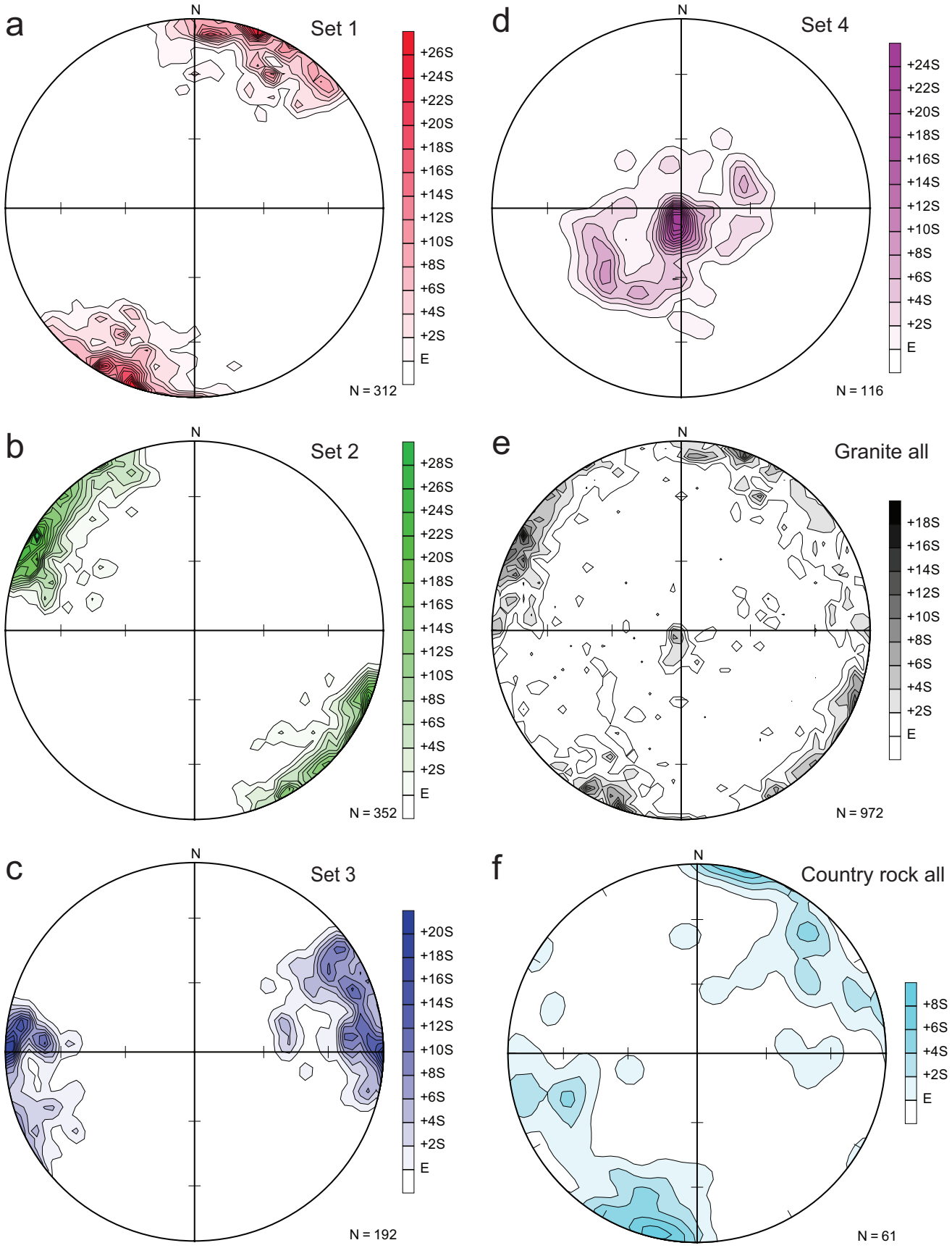

Figure 7. Orientation of joints in the study area. Contoured stereograms showing the orientation distribution of poles to joints in granite for set 1 (a), 2 (b), 3 (c), 4 (d) and for all of them (e) and for all the joints in country rock (f). Equal area projection on lower hemisphere, contour scales in standard deviation units, count of the measurements at bottom right.

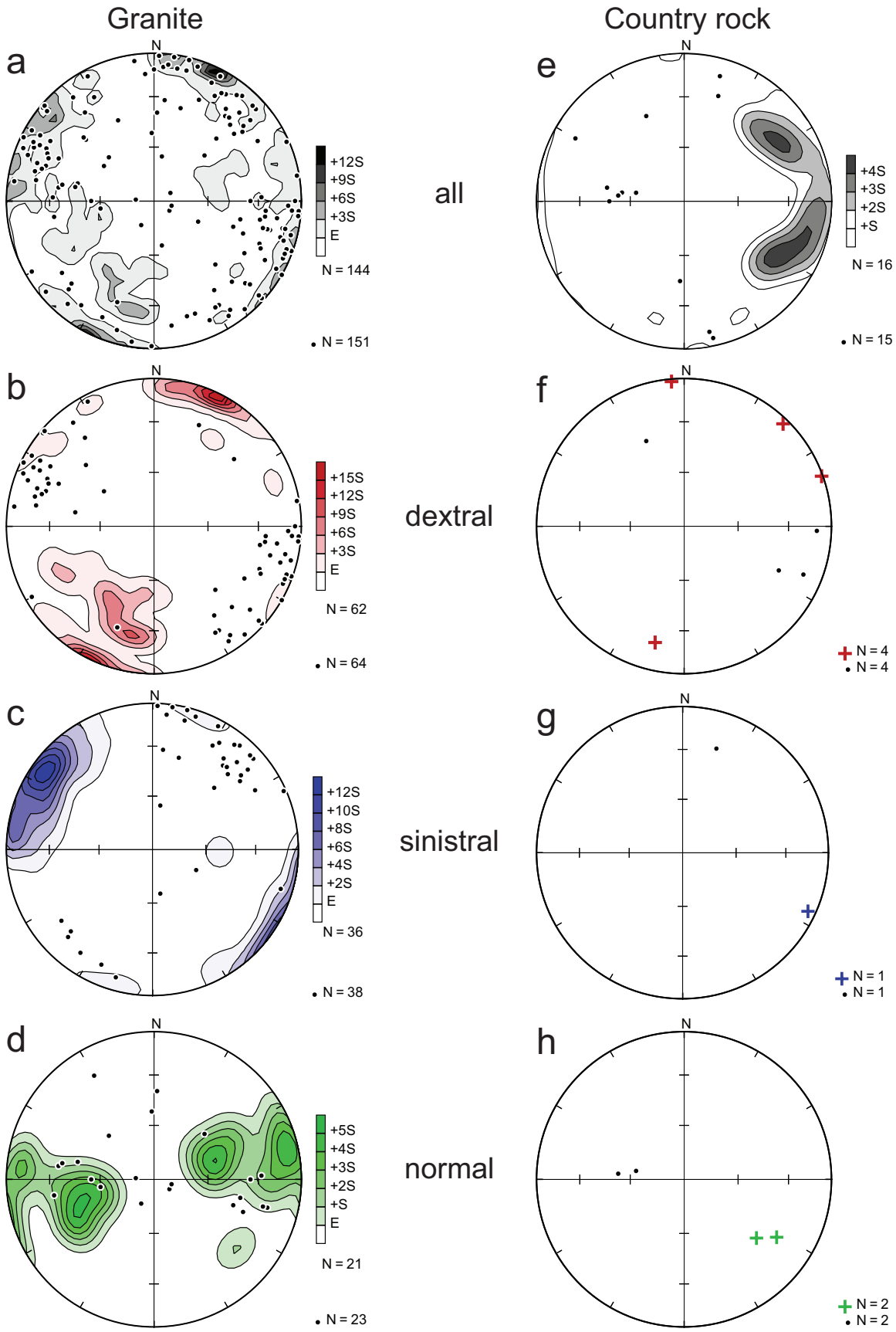

Figure 8. Orientation of faults and striations in the study area. Stereodiagrams showing the orientation distribution of poles to fault planes (contours and crosses) and striations (dots) in granite (a-d, left column) and in country rock (e-h, right column) for all (a, e), dextral (b, f), sinistral (c, g) and normal (d, h) faults. Equal area projection on lower hemisphere, contour scales in standard deviation units, count of the measurements at bottom right.

The orientation of faults and related striations within the host rock is displayed on a stereogram in Fig. 8 (e-h) distinctively for all, dextral, sinistral and normal faults. Taking into account all the faults, i.e. also the ones with unknown sense of relative displacement, two sets of steep faults with comparable population can be distinguished with NW-SE and NNE-SSW strikes. The dextral faults are subvertical to steep and strike WNW-ESE or W-E and bear striations gently to moderately plunging to the WNW or ESE. The sinistral fault is subvertical, strikes NNE-SSW and bears striations gently plunging mainly towards NNE. The normal faults dip steeply to moderately towards WNW and bear striations steeply plunging towards W. Important characteristic of the fault distribution within the host rock is the absence or unclear character of fault displacement sense indicators on fault planes recorded in the MG, whereas for most of the faults in the VG the sense could have been identified. In addition, the NNE-SSW striking faults are absent in the MG.

3.2 Structures in the granitic massif

3.2.1 Magnetic fabrics

The following results are based on AMS measurements executed during the previous studies on 651 specimens from 60 sites within the granitic massif.

The mean magnetic susceptibility (k_m) ranges from 16 to 414 x 10^{-6} SI. The magnetic anisotropy degree parameter P ranges from 1.010 to 1.197 and the shape parameter T varies between -0.892 and 0.967, suggesting prolate to oblate susceptibility ellipsoids (Fig. 9). The accompanying histograms show uneven distribution of values of both the parameters within the given ranges. The majority of P values lies between 1.03 and 1.09 with a clearly dominant peak between 1.06 and 1.08 and little populated values above 1.13. The majority of T values is concentrated in positive values and four peaks can be discerned from the most to the least populated, which are also ordered from the most positive (oblate) towards the most negative (prolate) T values: 0.85 to 0.6, 0.5 to 0.2, 0.15 to -0.15 and -0.3 to -0.55. A correlation between the two parameters can be seen with the least anisotropic shapes (low P) being the most prolate ones (low T) and the P values above c. 1.11 being almost exclusively linked to positive T values, i.e. to oblate shapes.

The distribution of values of k_m, P and T within the granitic massif can be seen on maps in Fig. 10 showing results of distance-weighed interpolation based on the unique specimen values. The k_m distribution shows a rather simple pattern with low values prevailing in the NW part of the massif and concentrated on the Melechov granite and with high values in the SE part concentrated on the Lipnice granite and on a positive peak localised on the triple point between the host rock and the Lipnice and Kouty granites. The

P values distribution reveals the generally low anisotropy below c. 1.08, i.e. below 8 per cent, and higher values concentrated within the northern part of the Melechov granite and to the southern part of the Lipnice granite including the already mentioned triple point Lipnice-Kouty-host rock. The T values feature scattered distribution with diametric changes over the site-to-site distances, i.e. on the order of hundreds of meters. Nevertheless, the low values prevail within the Melechov granite and in an E-W trending band in the southern part of the Lipnice granite and the high values are concentrated to the northern part of the Lipnice and the Kouty granite and to several sites along the southern massif-host rock boundary. Regarding the conventional classification into prolate, transitional and oblate

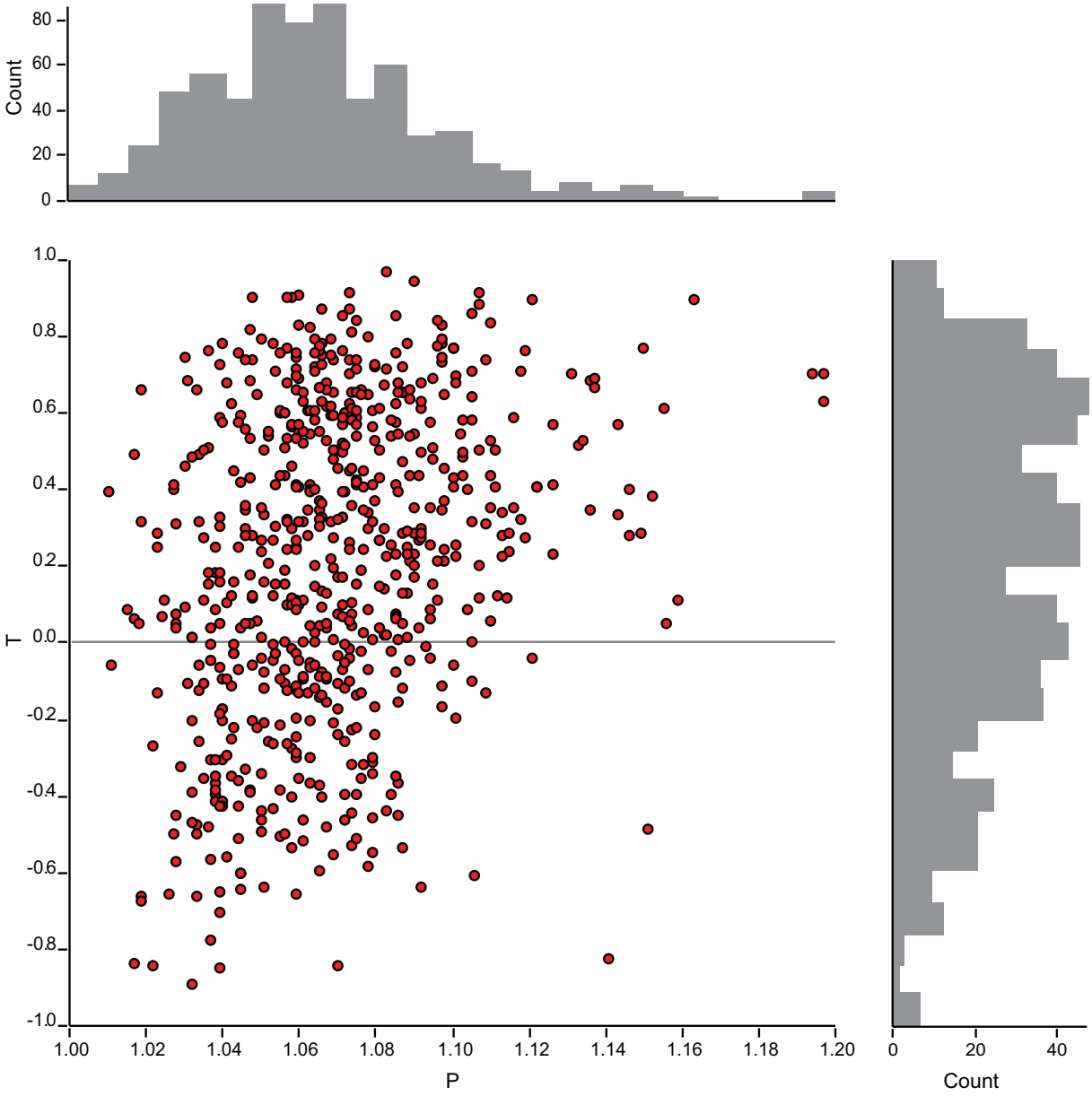

Figure 9. Shape and degree of anisotropy of magnetic susceptibilitty (AMS) ellipsoids of specimens of granite. The principal XY chart shows the P parameter (proportional to degree of anisotropy) and the T parameter (shape of anisotropy, prolate for negative, oblate for positive). The histograms show distribution of the P parameter (top) and of the T parameter (right).

shapes, it can be seen that the massif as a whole shows triaxial to oblate AMS ellipsoid with localized tri-axial to prolate ellipsoids mainly within the Melechov granite and at several sites in the Lipnice granite.

The orientation of the granite magnetic foliation, i.e. plane perpendicular to the minimum principal susceptibility direction k_3, and magnetic lineation, i.e. line parallel to the maximum principal susceptibility k_1, is displayed on maps in Figs. 4 and 5 by means of discrete structural markers showing strike and dip directions accompanied by interpolated dip value rasters. The foliation is steep to moderately dipping within the majority of the Lipnice granite, moderately dipping within the majority of the Kouty granite and moderately to gently dipping within the Melechov granite. At the scale of the massif the foliation flattens northward and eastward, the steepest foliation is related to the Lipnice granite including its western tip and the nearby Kouty granite and the lowest dips converge towards the northern part of both Kouty and Melechov granite. The foliation within the eastern core of the Lipnice granite strikes dominantly NNE-SSW and towards its western extremity turns progressively to WNW-ESE strike. This trend appears also in the Kouty granite. In addition, the strike of foliations within the latter two granites co-varies with strike of the granite-granite or granite-host rock boundaries. Within the Melechov granite the foliation strikes dominantly WNW-ESE and is deviated towards NNE-SSW strikes close to boundaries with both the outer Kouty granite and the inner Stvořidla granite. The lineation dips gently in the majority of the massif with local steepening to moderate dips mainly within the Lipnice and Kouty granite. The lineation trend is dominantly subparallel to the strike of the foliation and only rarely deviates towards foliation down-dip direction for the highest plunges.

3.2.2 Veins

The veins recorded within the massif include 36 pegmatite, 2 aplite and 9 quartz veins with each of the category showing distinct orientation pattern (Fig. 6). The most numerous pegmatite veins show dominant N-S strike associated with gentle to moderate dips towards E or W and NNW-SSE or NNE-SSW strike associated with moderate to steep dips towards ENE or WNW. About a fifth of the recorded pegmatites deviates from the given general pattern and shows approximately E-W strikes at gentle to moderate dips. The two aplite veins show N-S and NNW-SSE strikes at moderate to steep dips towards E and ENE-WSW, respectively. The majority of the quartz veins is subvertical and strikes NE-SW (including two different ones with the same orientation 138/75) and a minor part with subvertical to moderate dip shows NNW-SSE strike.

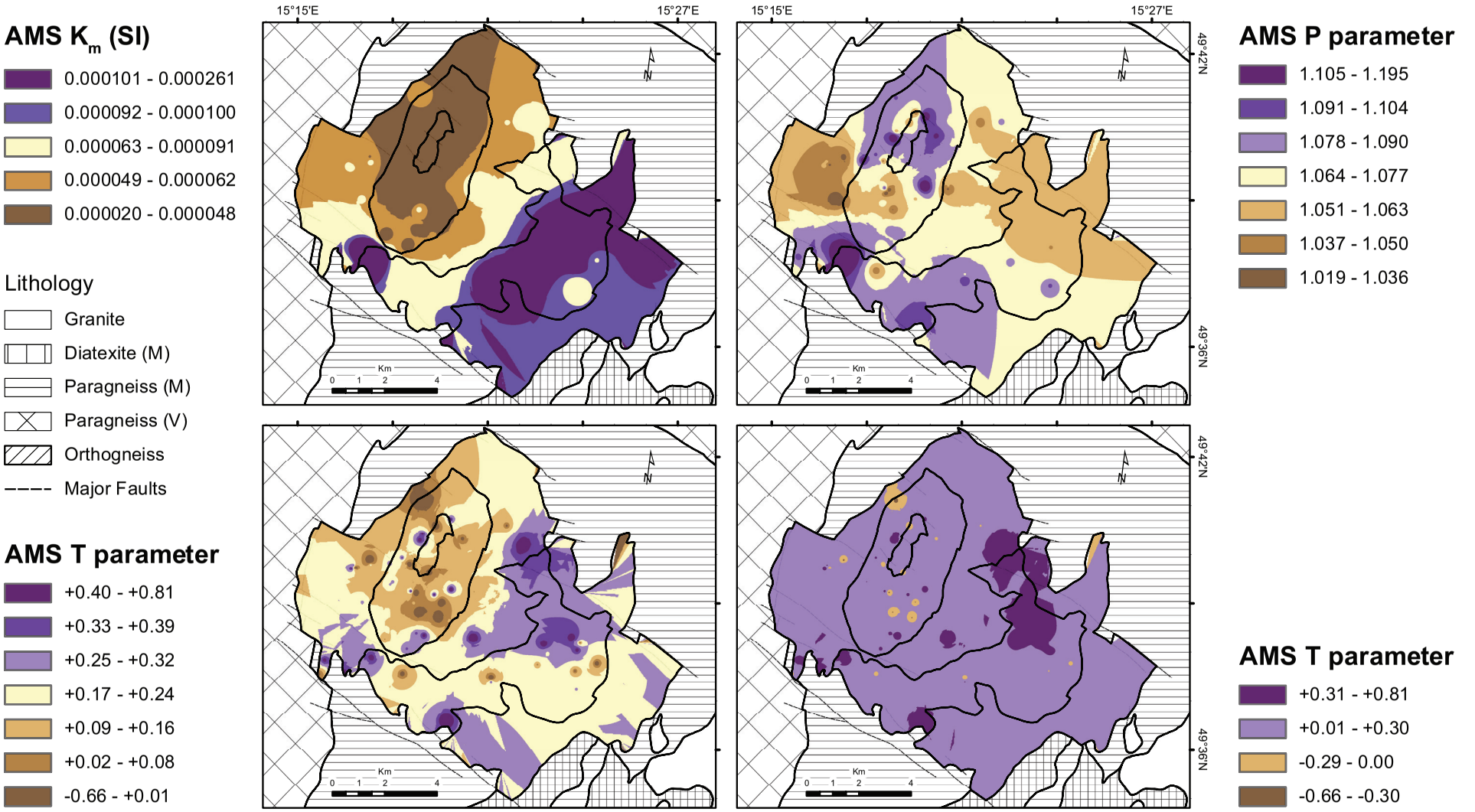

Figure 10. Distribution of values of mean magnetic susceptibility (Km) and of the degree (P) and the shape (T) of anisotropy of AMS ellispoids. The distribution of the T parameter is shown both with standard deviation-based classification (left) and with AMS ellipsoid shape-based classification (right). The legend to lithology and the coordinates are common to all the maps.

3.2.3 Joints

The total of 972 joints recorded within the massif has been divided into four sets characterized by different orientation and arrangement as observed in the field and described in the previous data-source studies. The orientation density distributions of the four joint sets are plotted on stereograms in Fig. 7. Joints of set 1 represent the most abundant, the largest and the most loosely spaced joints observed in field on the majority of sites. Observed joints of the other sets usually terminate on the set 1 joints. The set is characterized by size of tens of meters, spacing on the order of meters, subvertical or steep to exceptionally moderate dip and dominant WNW-ESE to subdominant E-W or NW-SE strike (Fig. 7 a). Joints of set 2 are developed on the majority of sites and range from several meters to ten meters in size, meters to decimeters in spacing, are subvertical to steep and strike dominantly NNE-SSW to ENE-WSW (Fig. 7 b). In addition, the set 2 joints often appear in clusters spaced by one to several tens of meters, with each cluster containing joints with cm–dm spacing. Joints of set 3 are locally developed with similar size and spacing characteristic as the set 2 and strike dominantly N-S to subdominantly NNW-SSE at subvertical to moderate dips (Fig. 7 c). These joints show similar clustering pattern as the set 2 joints and terminate on both the precedent sets of joints. Joints of set 4 are developed rarely as dominantly flat, curved and upward steepening joints of metric to decametric size, spacing on the order of meters and NW-SE strike for the subdominant moderate dips (Fig. 7 d).

The variation of orientation of the four sets is displayed on maps in Figs. 11-14 by means of spatially averaged strike trajectories superposed to interpolated dip value rasters. Joints of set 1 are subvertical in the majority of the massif and steep to rarely moderately dipping on its southern and northern extremities (Fig. 11). The strike trajectories show a sigmoidal pattern with alternating WNW-ESE and E-W strikes. The majority of the Lipnice and Kouty granite shows the dominant WNW-ESE strike which deviates to E-W near the southern granite-host rock contact and to a lesser measure also in the center and at the western and eastern extremity of the massif. In addition, both the northern and the southern dip anomaly is associated with dip directions towards the massif center. Within the Melechov granite the joints are subvertical and E-W striking except its NE extremity marked by WNW-ESE strike and steep dips. Joints of set 2 are mainly subvertical with lower though very steep dips (> 70°) localized near the granite-host rock limits (Fig. 12). The dominant NNE-SSW strike is very stable in the Lipnice granite and in the eastern and northern extremity of the massif. With respect to the dominant direction, the strike is slightly (< 10°) shifted towards N-S strike in the central and western part of the Kouty

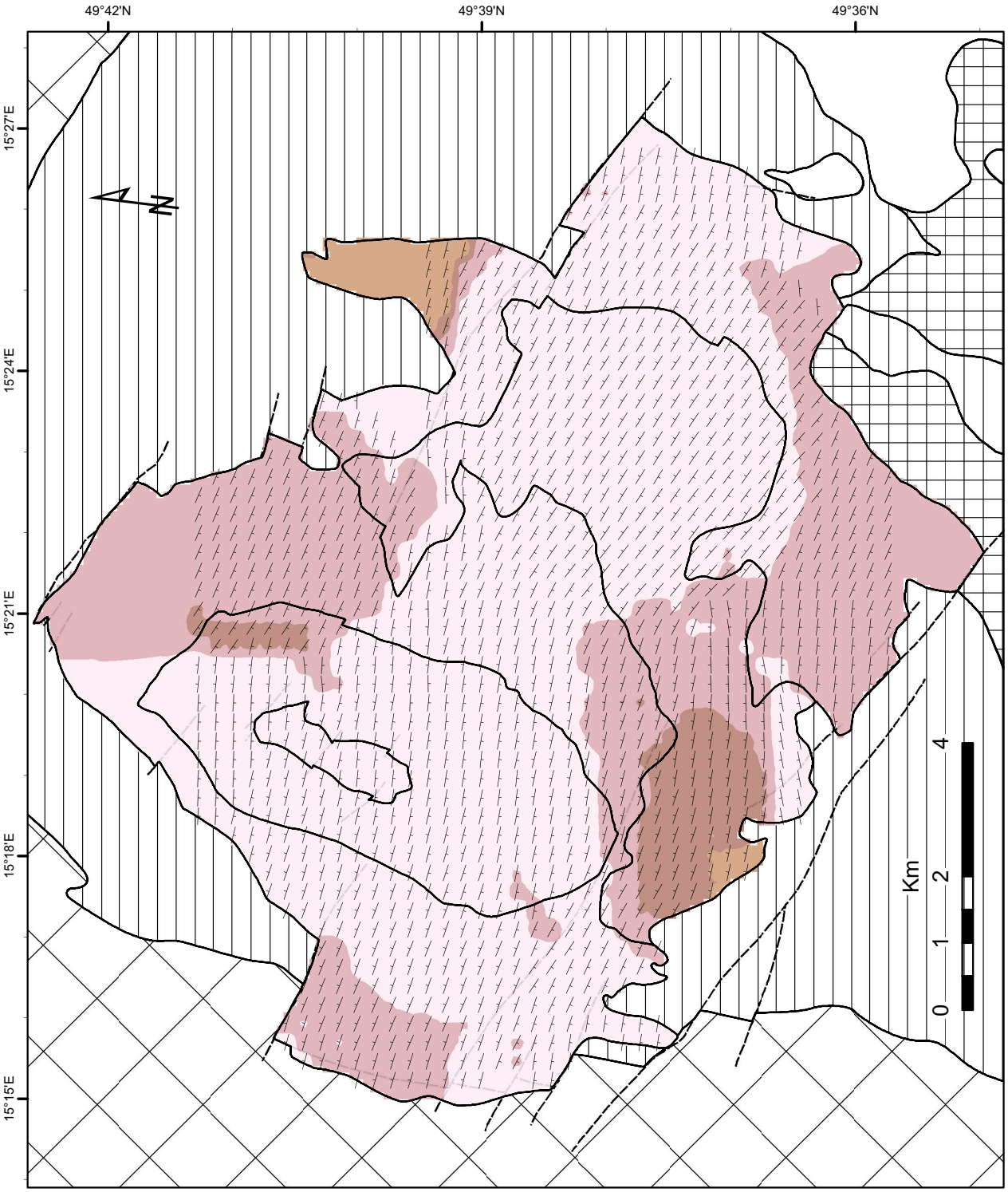

Figure 11. Map of set 1 joints trajectories. The structural symbols represent spatially averaged orientation values based on field measurements. The raster background shows interpolated dip values.

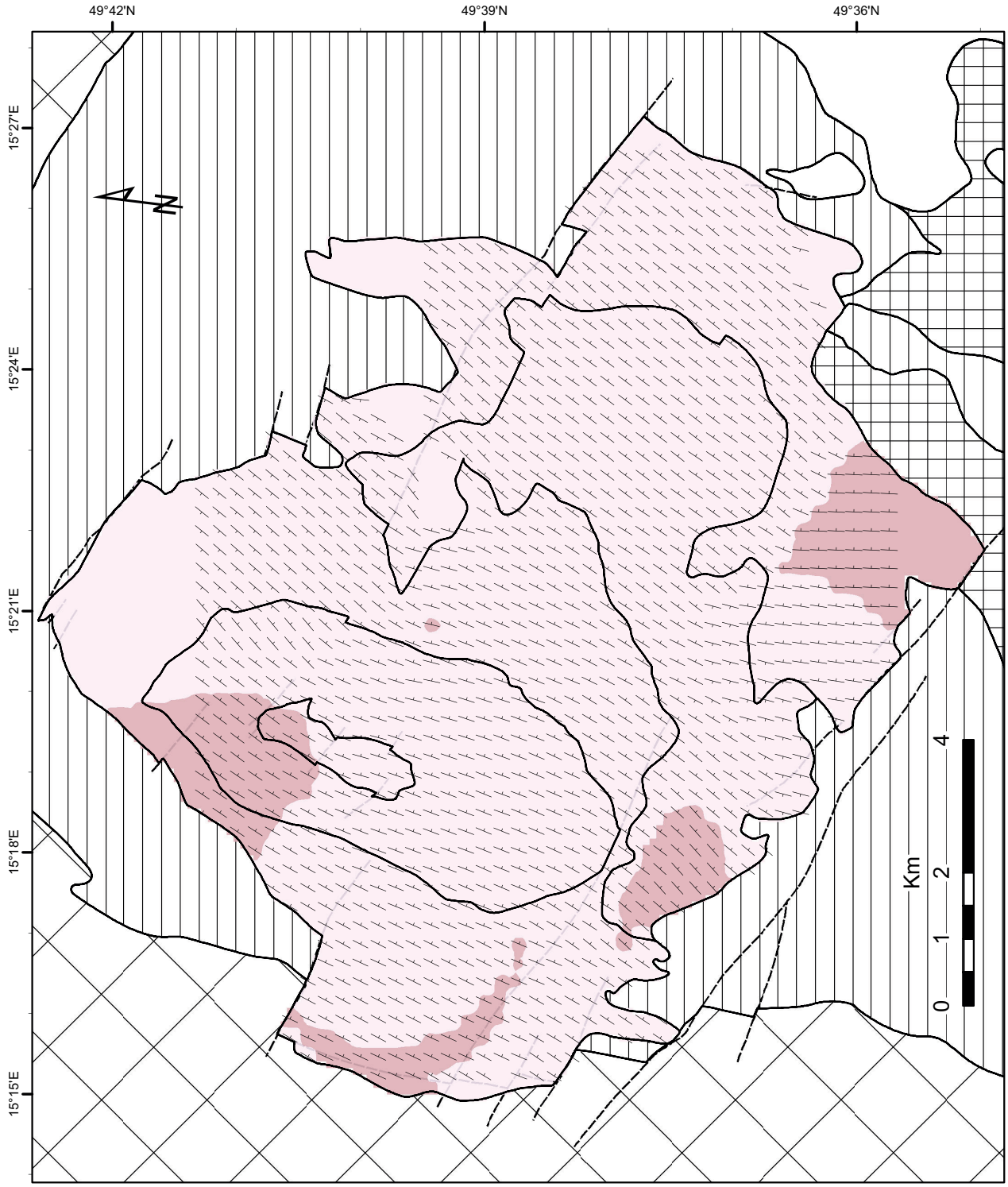

Figure 12. Map of set 2 joints trajectories. The structural symbols represent spatially averaged orientation values based on field measurements. The raster background shows interpolated dip values.

granite and progressively more in the central part of the Melechov granite. Joints of set 3 show subvertical dips within the central part of the massif and locally variable dominantly N-S strike (Fig. 13). The locally steep to moderate dips at the SW and the NW massif limits and in the NW part of the Melechov granite are associated with NNW-SSE strike. The rare joints of set 4 are subhorizontal to gently dipping in the Lipnice and Melechov granite as well as in the northern part of the Kouty granite (Fig. 14). In the eastern part of the Kouty granite the joints strike WNW-ESE to NW-SE at moderate dips.

3.2.4 Faults

The faults in the study area comprise the largest fractures of typically decametric to hectometric size and at places probably exceed these dimensions corresponding to the largest outcrops or quarries. For a minor part of the recorded faults the sense of relative displacement is unknown due to unclear or lacking kinematic indicators. The orientation density distributions of all the 144 recorded faults and of therein included dextral, sinistral and normal faults are plotted on stereograms in Fig. 8 (a, b, c, d), respectively, together with orientations of the associated striations. The dextral faults strike dominantly WNW-ESE at subvertical to moderate dips, the sinistral faults strike dominantly NNE-SSW at subvertical to steep dips and the normal faults strike N-S to NNW-SSE at steep to moderate dips. The associated striations reveal that the dextral faults are strike-slips to combined strike- and dip-slips, the sinistral faults are dominantly strike-slips and the normal faults are mostly dip-slips.

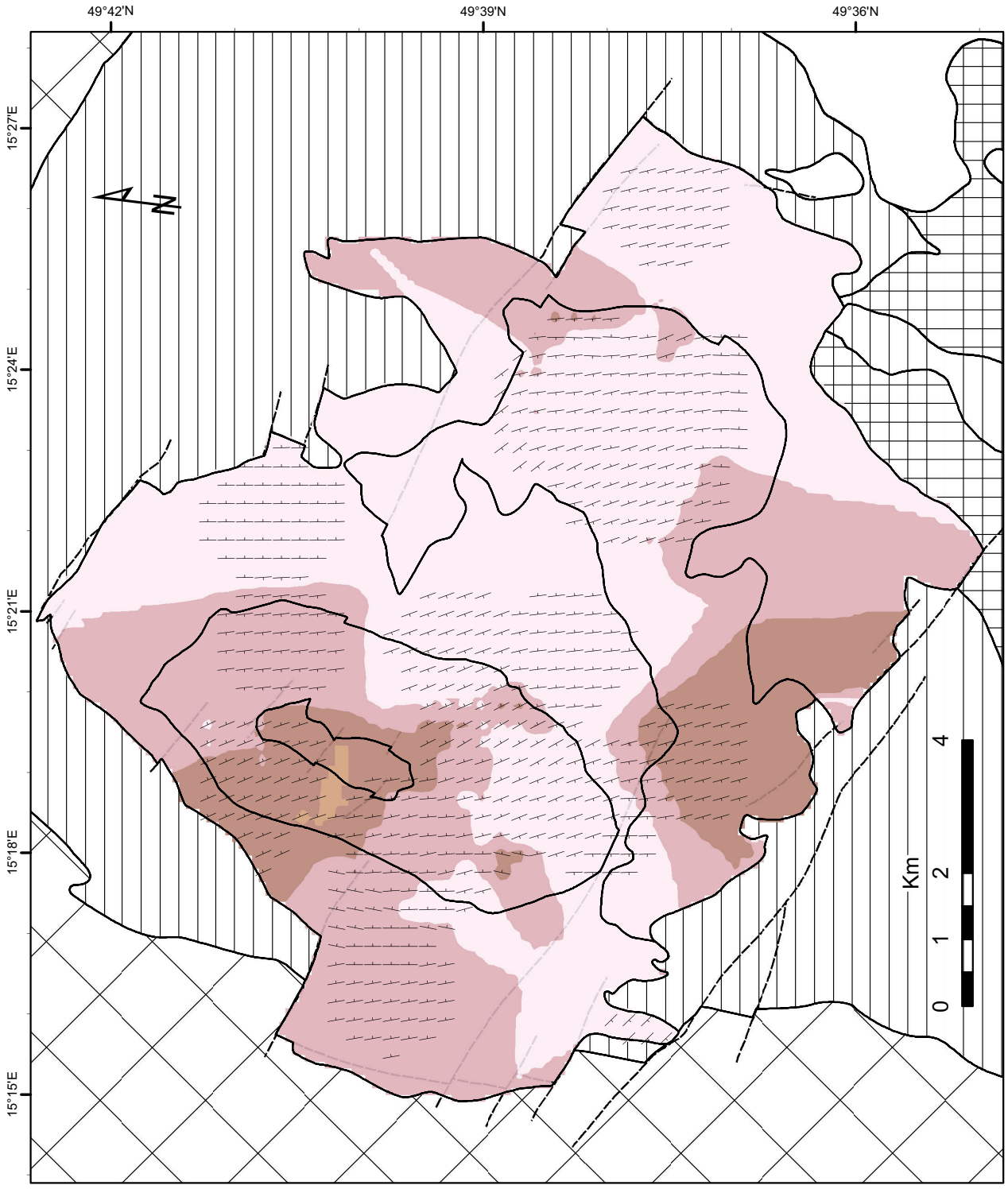

Figure 13. Map of set 3 joints trajectories. The structural symbols represent spatially averaged orientation values based on field measurements. The raster background shows interpolated dip values.

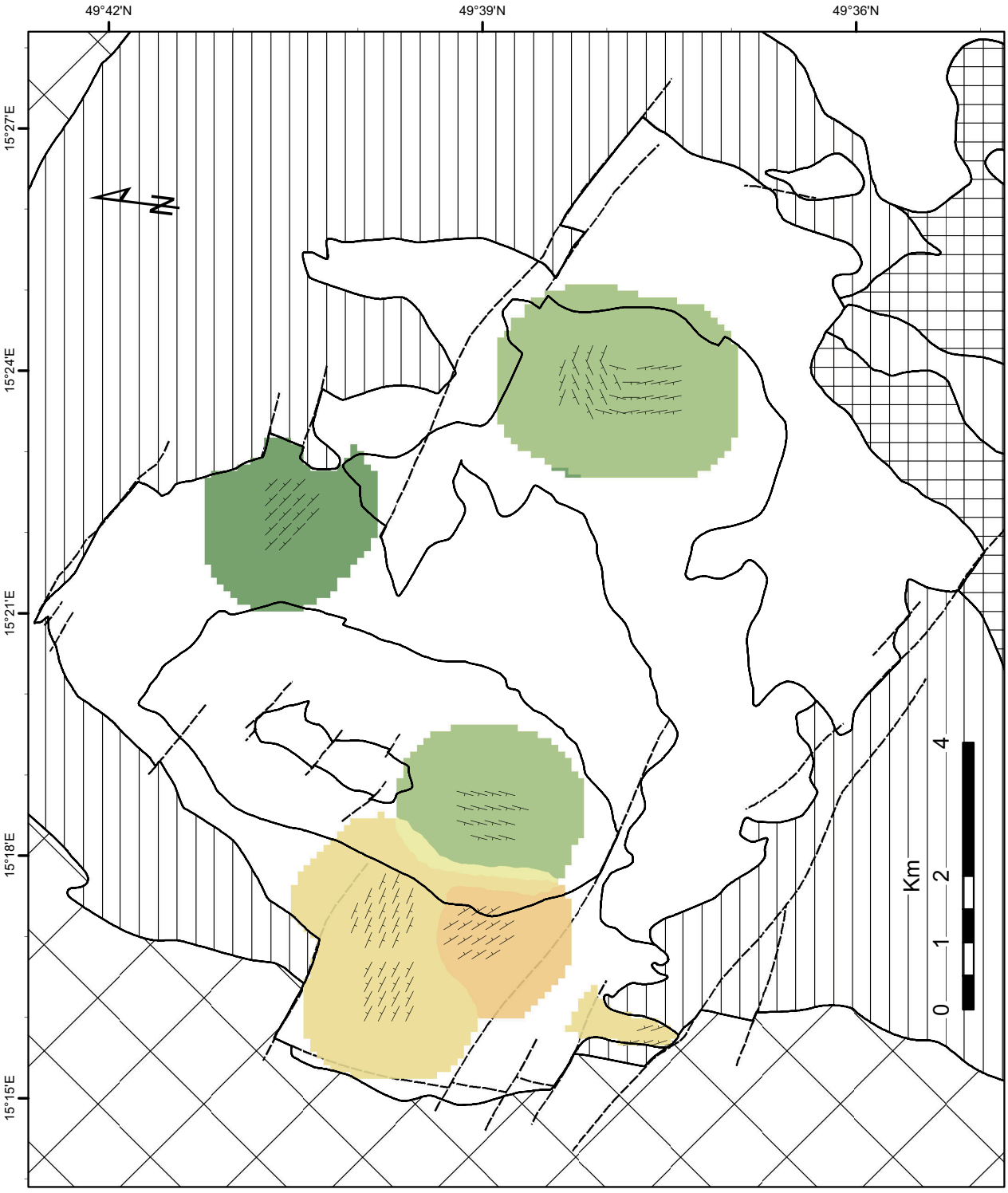

Figure 14. Map of set 4 joints trajectories. The structural symbols represent spatially averaged orientation values based on field measurements. The raster background shows interpolated dip values.

3.3 Summary

The following results of the structural analysis are of primordial importance for interpretation of the deformational history of the granitic massif.

In the massif host rock three structural domains characterized by different peak metamorphic conditions show distinct patterns of both ductile and brittle structures. The rocks of the lowest degree VG outcropping W of the massif show W-NW moderately dipping dominant foliation folded by W-NW-verging asymmetric folds with flat to foliation-subparallel axial planes and gently plunging axes. The dominant foliation in the low degree migmatitic paragneisses of the MG north and northeast of the massif dips moderately NNE and is folded by NNE-verging asymmetric folds with steep to foliation-subparallel axial planes and gently plunging axes. The dominant foliation within the highest-degree migmatites of the MG southeast of the massif strikes steeply NNE-SSW and is folded by ESE-verging mainly symmetric folds with moderately to gently dipping axial planes and gently plunging axes. The foliation and the fold axes tend to dip steeper towards the massif and their strikes or plunges are deviated from the general direction pattern mostly near the granite-host rock contacts. The deviation is represented by alignment to the direction of the large-scale discontinuities (major faults and lithotectonic boundaries) of either NNE-SSW or WNW-ESE strike.

The extension fractures of the host rock are represented by subhorizontal to gently southward dipping pegmatite and aplite veins, by steep eastward dipping quartz veins and by steep joints striking, in the order of abundance, WNW-ESE, NNW-SSE and NW-SE. The shear fractures are dominantly steep and strike NNE-SSW or NW-SE in the VG and NW-SE in the MG. The fault displacement indicators preserved in the VG point to dextral movements along the NW-SE striking faults and sinistral and normal movements along the NNE-SSW striking faults.

The magnetic susceptibility within the granitic massif is remarkably higher in the Lipnice granite and lower in the Melechov granite. The intensity of magnetic fabric is generally low and the relatively higher values are scattered within the Lipnice granite and the northern part of the Melechov granite. The related anisotropy shape is mostly oblate and tends to prolate shapes within the Melechov granite and along the E-W striking southern part of the Lipnice granite. Within the Lipnice granite the magnetic foliation is steep and oriented concentrically around the massif core with NNE-SSW strikes in the northeast turning into WNW-ESE strike in the southwest. Within the Melechov granite the foliation is moderately dipping to flat with dominant WNW-ESE strikes. The generally flat magnetic lineation trends mostly along the magnetic foliation strikes and orientation of

both the structures co-varies more or less remarkably with strike of the granite-granite and the granite-host rock boundaries.

The pegmatite veins show bi-verging distribution with dominantly ENE or WNW moderate dips, the aplite veins are steep and N-S striking and the quartz veins cluster into two steep sets of NE-SW and NNW-SSE strikes.

The system of joints comprises two principal and two supplementary sets of joints apart the exfoliations which are neglected here. The largest set 1 joints strike WNW-ESE at subvertical to locally moderate dips and the set 2 joints are subvertical and subperpendicular to the set 1 joints on which they terminate. Locally developed set 3 joints are subvertical and N-S striking and the joint set 4 is represented by rarely developed flat fractures. The joint trajectories revealed sigmoidal pattern for both the sets 1 and 2 developed at the massif scale. Joints of set 1 show stable WNW-ESE and W-E strikes in central parts of the Lipnice and the Melechov granite, respectively, and the joints of set 2 tend to perpendicularity to the set 1. The most important variations in strike of the three dominantly steep joint sets are associated with relatively lower dips and are localized near the massif limits.

The most abundant faults strike WNW-ESE at steep dips and are associated with dextral strike-slip movements. Less abundant sinistral faults strike NNE-SSW at steep dips and the least abundant normal faults dip moderately to steeply towards E or W.

4. Discussion

The presented data provide constrains on deformation processes resulting in the actual distribution of the concerned structures and indicate the stress field acting during their formation.

4.1 Development of the magmatic fabrics

The oldest structures within the granitic massif are related to its magmatic origin. There are several lines of evidence that the older granites (Lipnice and Kouty) are structurally and spatially closely related to the high-grade metasediments of the MG. On the other hand, the younger granites (Melechov and Stvořidla) show properties distinguishing them clearly from both the older granites and the metasediments.

Field observations in the older granites revealed frequently preserved schlieren and enclaves of migmatitized paragneisses and diffuse contact with the high-degree migmatites to the south and east of the massif. The contact is marked by incompletely granitised

blocks of host rock enveloped in granite and further towards the host rock by granitic dikes or large melt pockets within the steeply folded migmatite structure. The results of analysis of magnetic properties of the granitic massif presented in this study show clearly that the highest magnetic susceptibilities (100-260 x 10^{-6} SI) are related to the eastern part of the massif and particularly of the Lipnice granite (Fig. 10). The younger granites, on the other hand, show remarkably lower values of c. 20-60 x 10^{-6} SI. These results show the same trend as results of Ondra & Šrámek (1995) indicating 30-40 x 10^{-6} SI for the younger granites and 70 - 80 x 10^{-6} SI for the mean of Lipnice granite. In addition, the latter work characterized the metasediments by values of 270-315 x 10^{-6} SI comparable to the ones presented here for the eastern part of the Lipnice granite.

The prevailing oblate shape of the AMS ellipsoids within the Lipnice and Kouty granite (Fig. 10) suggests affinity to the planar metasedimentary fabric. In addition, the schlieren-rich eastern part of the Lipnice granite and the high-grade migmatites along the massif southeastern boundary show strikingly similar structural pattern. The magnetic foliation and lineation in the granite and the macroscopic foliation and fold axes in the migmatites are, respectively, subparallel (Figs. 4 and 5). The later observation is valid also for the least oblate (~ triaxial) AMS ellipsoid shapes on the easternmost sites within the Lipnice granite thus excluding the general insignificance of k_1 in purely oblate shapes ($k_1=k_2$). This means that also the linear structures in the compared rocks are subparallel. Following our study focused on the schlieren-bearing granite microfabrics and including AMS measurements (Chapter IV), the concerned triaxial to oblate shapes of the AMS ellipsoids may reflect a folded schlieren-rich fabric and the magnetic lineations may correspond to the schlieren fold axes. Consequently, it is likely that the compared granite and migmatite feature also similar folding pattern, which is in agreement with field measurements of orientation of the macroscopic schlieren (Chapter IV; Schulmann et al. 1997). On the other hand, the fabric orientation similarity does not imply structural continuity between the two rocks and based on our data it cannot be confirmed or excluded as the closest structural data points are ~ 3 km distant. In addition, even if there was the continuity it would not imply its origin in magmatic processes as these might be easily reset (Paterson 1998). However, the subparallel structures are very probably due to similar stress configuration and, taking into account that no solid-state reprint of the Lipnice granite microstructure has been reported, also due to similar, melt-related processes. Compared to the migmatites, the principal difference of the eastern part of the Lipnice granite thus consists in the higher melt fraction which, however, did not lead to obliteration of the migmatitic structure. The higher melt fraction may be due to higher degree of in-situ partial melting or due to higher experienced strain

leading to localization of the melt pathways (De Saint-Blanquat et al. 1998). Coherently, it might correspond to less or more internally disintegrated and assimilated stoped block or roof pendant of the host rock. Such a setting was proposed in terms of sank raft of Moldanubian by Procházka et al. (1998) based on geochemical analysis and particularly on high content of Th within the eastern part of the Lipnice granite.

The NNE-SSW strike characterizing both the schlieren-rich Lipnice granite and the high-degree migmatites corresponds to the strike of the major structures and discontinuities within the study area as well as in the regional geological context. These are notably the VG-MG boundary, the discontinuity between the MM and the CMP outcropping as the highest-grade migmatites, the CMP itself and finally contact of the Moldanubian unit and the easterly Brunia microplate (Dudek 1980; Štípská & Schulmann 1995; Štípská et al. 2004; Racek et al. 2006; Schulmann et al. 2009; Žák et al. 2011). We assume structures of this strike as primary structural pattern later modified by the granitisation processes. In contrast to the Lipnice (and Kouty) granite, the low Th content within the Melechov granite and analytical zero content in the Stvořidla granite result from magmatic segregation and progressive fractionation of a distinct deeper source (Procházka & Matějka 2006). Furthermore, their coarse-grained to porphyric textures point to lower cooling rates and suggest intrusion into still hot Kouty granite as supported also by magnetic foliations subparallel to the granite-granite contact in the very proximity of the contacts. The prevailing WNW-ESE strike of the magnetic fabric in the southern-central part of the Melechov granite represents the principal structural direction during the later magmatic stage.

The maps of magnetic fabric (Figs. 4 and 5) show a continuous transition from the primary NNE-SSW to the secondary WNW-ESE fabric from the east to the west in the Lipnice granite and less remarkably also in the central part of the Kouty granite. Taking into account the above considerations on the origin and timing of the poly-phase magmatic activity within the MM, it appears that the change of the fabric orientation was coupled with magmatic evolution. The center of the magmatic activity moved towards the east and during the magmatic evolution of the MM the protolithic NNE-SSW fabric progressively changed into possibly magmatic WNW-ESE fabric preserved until and after solidification of the late central intrusion of the Melechov granite.

Within the older granite (mainly Lipnice) this double structural pattern may be explained in terms of dextral shearing along the WNW-ESE striking discontinuities active (at least) between the initial and the late magmatic stage. Shear zones or brittle faults of this strike have played already in late Variscan ~ 330-320 Ma (Pitra et al. 1999) when the Moldanubian S-granites are supposed to form (Finger et al. 1997; Gerdes et al. 2003; Žák et

al. 2011) and were active from then on (Uličný et al. 2009 and references therein). Activity on such discontinuities may have deflected the southern part of the initially NNE-SSW striking fabric preserved in the massif core to the actual WNW-ESE strike preserved in the southwest. The magmatic fabric in the Melechov granite has been interpreted to be due to "circular movement of magma around the periphery of the intrusion" by Schulmann et al. (1997) based mainly on "clear concentric fabric of lineations". However, rather than concentric fabric, we see dominant WNW-ESE strike and trend of magnetic fabric mainly in the large southern core of the Melechov granite but also in its data-poorer northern part (Figs. 4 and 5). There are, however, NNE-SSW fabrics aligned to the inner and outer granite-granite contacts mainly in the constrained northern part, suggesting interaction with the pre-emplaced Kouty granite as well as with the post-emplaced Stvořidla granite. Hence, rather than circular flow (movement) the WNW-ESE strike may be due to emplacement along WNW-ESE discontinuities which would explain also the same strike and trend in the westerly Kouty granite where concentricity can be hardly seen.

4.2 Significance of the host rock ductile structures

The foliations and fold structures in the MG show anticlinal orientations with respect to the massif and dip steepening towards it suggesting a dome-like structural pattern (Figs. 4 and 5). The stress field leading to and coeval with the early stages of the doming is probably related to the primary structural pattern recorded within the study area in the SE structural domain. Here, the high-degree migmatites have been characterized by NNE-SSW striking steep foliation associated with moderately ESE-dipping folds with gently SSW plunging fold axes (Fig. 3). The related minimum principal stress was subhorizontal and subparallel to the NNE-SSW fold axes and the maximum principal stress was trending WNW-ESE subperpendicular to the fold axial planes. The dip of the axial planes is dominantly moderate, however both flat and steep dips have been recorded. This implies dominantly moderate WNW dip of the maximum stress axis and suggests little or variable difference between the principal maximum and intermediate stress, with both of them lying in the WNW-ESE striking vertical plane in general. The latter direction variability or instability of the stress field might be due to the high melt fraction within the concerned high-grade migmatites. The associated elevated pore fluid pressure probably led to reduction of the stress field anisotropy and to NNE-SSW minimum stress-dominated regime.

The structures reflecting the doming progression and host-rock unroofing are expressed the best in the NE structural domain. The related structural pattern is

characterized by WNW-ESE striking foliation and NNE-verging asymmetric folds with gently plunging fold axes and reflects the relative downward and NNE-ward movement of the roof of the protruding granitic dome along its northeastern WNW-ESE striking edge. The outcrops in MG near the southwestern massif limit, which is subparallel to the northeastern one, are rare and the structures are often obscured by the diffuse granite-host rock contact. Nevertheless, several measurements of orientation of macroscopic foliations and fold axes as well as of magnetic foliations and lineations (see Figs. 4 and 5) point to similar pattern as observed in the NE domain, though with the opposite, dominantly south vergence. The ductile structures in this part of the host rock were thus probably also due to the doming process. The structural pattern in the lowest grade and the structurally highest VG west of the massif probably reflects the relative displacement between the VG and MG along their boundary. The WNW vergence of the foliation and of the asymmetric folds with gently plunging axes suggest top-to-the-WNW displacement at ductile conditions with NNE oriented minimum principal stress and steep-moderate ESE orientation of maximum principal stress. The displacement probably continued at ductile-brittle conditions as demonstrated by E-dipping aplite veins cutting at high angle the folded structure and being sheared along the WNW-dipping foliation and fold axial planes (Schulmann et al. 1997) suggesting a coherent stress regime. Furthermore, the actually observable sharp and cold character of the granite-VG contact points to continuity of the initial regime also at brittle conditions. This is supported by the observation of Mitrenga et al. (1979) claiming major WSW-ward combined sinistral-normal movement along a NNW-striking segment of the Zahrádka fault near the southern VG-MG-granite triple point.

4.3 Extensional fractures in the massif

The granitic massif is fractured by two principal and two subordinate sets of joints, taking into account their size and spatial extent (Figs. 11-14). According to the concept of Cloos (1922) the orientation of the primary sets of joints is ruled by orientation of the magmatic foliation and lineation presumably aligned with the elongation of the granitic body. Our results demonstrate a similar pattern in the eastern part of the older granites showing NNE-SSW striking magnetic fabric in good correlation with the WNW-ESE striking set 1 and NNE-SSW striking set 2 (Figs. 4, 5, 11 and 12). The set 1 and 2 would thus correspond to the cross and the longitudinal joints, respectively. Within the eastern part including the younger granites the E-W striking set 1 joints are at low angle to subparallel to the dominant WNW-ESE magnetic fabric. On the other hand, the set 1 is perpendicular to the intrusion shape elongation along the NNE-SSW axis. This shows that here the

Cloos concept may be not entirely valid. Taking into account the subhorizontal NNE-SSW minimum principal stress orientation deduced from the orientation of the oldest MG host-rock ductile fabric, the formation of set 1 joints may reflect the regional stress field succeeding the cooling-related passage of the ductile-brittle transition. In relation to the dominant structural pattern of both the VG and MG these joints thus correspond to the ac-joints as they are subperpendicular to the fold axes (Sander 1930). The WNW-ESE striking steep slabs resulting from fracturing by the set 1 were then fractured by set 2 accommodating the continuing thermal contraction of the massif. This contraction induced minimum principal stress parallel to the planar slabs thus controlling their orientation perpendicular to the set 1. This is in agreement with the observation that joints of set 2 terminate on joints of set 1 and are generally smaller. In addition, well preserved fracture surface features including horizontal hackle plume axes observed on set 1 (Lexa & Schulmann 2006) indicate slow opening at deep confined conditions and tectonic stress at their origin (Engelder 1992; Bahat et al. 2003). Set 2 shows less developed fractographic features and variable propagation directions indicating later release-jointing in less confined and less tectonic-controlled regime (Engelder 1985). The shape of set 2 joints elongated along the bisector of sets 1 and 2 (Lexa & Schulmann 2006) further supports the proposed succession of the two sets. The orientation of the two cooling-related sets can be attributed to the same stress field that resulted in the oldest ductile fabric in the MG. Within this scope, the regional stress control of orientation is direct for the set 1 and indirect for the set 2 where it is intermediated by orientation of the set 1 pre-discontinuities. Consequently, the parallelism of the longitudinal joints to the magmatic fabrics according to Cloos may or may not be plausible depending on whether the first set formed or not perpendicular to the magmatic fabrics. Taking into account the concept assumption of parallelism between the plutonic body elongation and the magmatic lineation, the orientation of the longitudinal joints with respect to the intrusive boundaries may also be indirect. On the other hand, differential thermal expansion of the granite mineral phases and namely the high expansion of quartz may induce thermal cracks with orientation controlled by the alignment of the grains (Price & Cosgrove 1990; Fei 1995). This principle may represent the link between the Cloos structure-based concept and the purely thermally controlled cracking.

The set 3 joints terminate on joints of set 1 or 2 and are thus generally later. In the most common configuration of joint system on a given site, the set 3 joints may or may not be developed in addition to commonly developed set 1 and 2 joints. Given the angular difference ~ 30 ° in strike of sets 2 and 3 (Fig. 7) this implies that the set 3 developed under substantially different stress regime than the set 2. Otherwise the set 2 joints would be used

for the stress accommodation instead of formation of new fractures at low angle to them which was energetically more exigent. Taking into account the vertical dip and the N-S dominant strike of the set 3 joints, they formed under stress field characterized by E-W orientation of the minimum principal stress.

In contrast to the joint sets 1, 2 and 3, the rarely developed fractures of set 4 are mostly subhorizontal and the more inclined set members show bi-vergent dip direction at NW-SE strikes. The orientation suggests subvertical minimum principal stress and NW-SE maximum principal stress. However, the spatial distribution of the strikes is very variable (Fig. 14) suggesting the stress field dominated by the minimum principal stress. On the other hand, the set 4 joints have been observed mainly in the western massif part where, in addition, the bivergency at the dominant NW-SE (± 30 °) strike may be seen on a small area. The explication for their origin as the Cloos diagonal fractures is supported by their variable strike at low angle to the cross joints, obliquity to the cross and the longitudinal joints, bivergence and finally fault mirrors developed on some of them. In the original concept the diagonal joints should form to accommodate the relative displacement between the pluton roof or wall and the inner mobile core. The pronounced development of the set 4 in the western part may thus reflect the proximity of the cold contact with the VG rocks which might have formed the intrusion roof or (later) western wall. In addition to the given interpretation, another plausible setting not excluding the former may be linked to the set 4 fractures. As noted before, the western massif is specific by the cold, sharp and faulted character of granite-metasediments contact associated with (W)SW-dip normal movements (Mitrenga et al. 1979). It is thus likely that these joints represent conjugate fractures accommodating the normal movements on the master faults striking WNW-ESE and remarkably abundant in the western part of the study area (e.g. the map in Fig. 14; major faults according to CGS map 2013). The association with normal movements is further supported by the listric-like upward steepening of these fractures, their bivergent dip directions as well as their common development in closely spaced sets (Twiss & Moores 2007).

The maps of trajectories of the distinct joint sets in the massif have revealed a sigmoidal pattern of the set 1 and 2 and to a lesser measure also of the set 3 (Figs. 11-13). For the two first sets, the central parts of the Lipnice and Melechov granite represent two domains with stable orientation of the joints within the frame of the sigmoidal pattern (Figs. 11 and 12). On the other hand, the external parts as well as the part of the Kouty granite between the Lipnice and Melechov granites represent the kinks of the pattern. We suggest that the sigmoidal pattern may have resulted from conjugated relative horizontal

displacements of large domains of the massif. The considered kinematics corresponds to dextral and sinistral movement along WNW-ESE and NNE-SSW striking discontinuities, respectively. Taking into account the noted domains with stable and with kinked trajectories orientation, the central part of the granites acted more rigid whereas the strain was accommodated in the external and in the central transitional parts of the massif. The latter interpretation as well as the interpretation for development of the two different strikes of magnetic fabric was mechanically related to shear movements, i.e. fault activity, which we discuss in the subsection on shear fractures and reactivated extension fractures.

The pegmatites show bi-verging orientation distribution with dominant E or W gentle to moderate dips suggesting subvertical principal minimum stress and N-S subhorizontal principal maximum stress during the late magmatic activity. Comparison of orientation of veins and of joints (Figs. 6 and 7) indicates that the pegmatites may have partly emplaced along the set 4 joints. In general, pegmatites necessitate hot environment to produce large crystals and are understood as products of late stages of magmatic activity. Taking into account the interaction with the pluton roof considered for the set 4, the association with the pegmatites points to emplacement to the pluton-roof interface. The latter interpretation is supported by the bivergent distribution and by the broad range of dips of pegmatites which thus probably reflect all the shape of the assumed dome roof. Moreover, elongation of the dome in N(NE)-S(SW) direction and its gentle inclination towards the N(NE) may correspond to the asymmetric distribution of poles to pegmatites with respect to the vertical. The aplites show N(NW)-S(SE) strike at steep dips indicating similar stress configuration as for the set 3 joints or emplacement into these joints. The latest quartz veins probably emplaced to the set 1 and 2 joints based on the orientation similarity.

4.4 Extensional fractures in the country rock

The orientation of joints and veins in the country rock reveals a pattern distinct from the one in the massif (Figs. 6 and 7). The set 1 and 3 joints are clearly developed also in the country rock, whereas only rare set 2 orientations have been observed. The stress field related to the flat joints of set 4 may be reflected in the country rock by both the little populated moderately inclined joints and by the flat pegmatite and aplite veins. The quartz veins cluster around N-S or NNW-SSW strikes with steep dips and were thus emplaced into the country rock set 3 joints or formed as new fractures in a similar stress field.

4.5 Shear fractures and reactivated extension fractures

The orientations of the shear fractures and of the related fracture surface features recorded within the massif indicate that the set 1 and 2 joints were reactivated by dextral and sinistral strike-slip movements, respectively (Fig. 8). The WNW-ESE faults represent the largest brittle discontinuities in the massif, reaching hectometric or larger dimensions and often composed of linked overstepping segments (Schulmann & Lexa 2000). Coherently, the relative higher recorded abundance of dextral shear fractures may correspond to measurements of the numerous segments of such fault zones rather than to high abundance (dense spacing) of discrete discontinuities. The set 3 joints probably also accommodated sinistral displacement as indicated by the subordinate N-S strikes of sinistral faults. The dominant orientations of the two strike-slip fault sets is consistent with horizontal N-S (345 °) oriented maximum principal stress and horizontal E-W (255 °) oriented principal minimum stress. The reactivation of the set 3 joints may correspond either to general anti-clockwise rotation or to local variations of the principal stress field. Another explanation may be that the set 3 joints were reactivated as synthetic riedel fractures accompanying the principal two-set system. The latter possibility would also explain the formation of set 3 joints in a stress regime unrelated to the formation of joints of set 1 and 2. On the other hand, the term joint implies no important shear movement along the fracture plane, whereas the term riedel fracture does (e.g. Twiss & Moores 2007) and therefore all the set 3 fractures should show signs of faulting if formed as riedel fractures. However, the fractures of set 3 classified as joints might have experienced only little displacement (faulted joint, Wilkins et al 2001) the signs of which might have been imperceptible for the field worker or obliterated by later processes.

The orientation distribution of normal faults indicates activity on two systems of conjugate sets of fractures. The steep to subvertical NNW-SSE striking fractures probably correspond to reactivated set 3 joints given that normal faults hardly form at steep dips if no pre-discontinuity exists. The other system of conjugated sets of normal faults shows similar strike as the previous system but with moderate to gentle dips indicating rather newly formed fractures. On the other hand, the orientation of the latter system is partly coinciding with the set 4 joints, thus indicating possible reactivation of the latter. Despite the ambiguity concerning the primary or inherited character of the normal faults, the stress regime inducing the normal faulting was probably characterized by E-W to ENE-WSW minimum principal stress.

The orientations of striations indicate prevailing horizontal component for the dextral and sinistral faults, i.e. their strike-slip character, and similarly for the normal faults

the striations show their dip-slip character. Taking into account the common ~ E-W orientation of the minimum principal stress, the three fault types might have formed in a similar setting of N-S compression characteristic for the northerly Bohemian Cretaceous Basin (Uličný et al. 2009). On the other hand, more than one faulting episode per fracture has been rarely recognized and in general might be considered for frequent fractures with fault mirror showing no striations. According to studies focused on the shear fractures within the massif (Coubal 1997; Schulmann & Lexa 2000; Schulmann & Lexa 2001, Lexa & Schulmann 2006) three-stage reactivation affected the joint of sets 1, 2 and 3. The first was related to NW-SE maximum stress resulting in transcurrent strike-slip movements, the second related to NE-SW maximum stress resulting in transcurrent movements on set 4 and 2 and in formation of new, set 2-parallel joints, and the third related to ESE-WNW minimum stress reactivating set 3 joints. These observations thus point to stress field dominated by ~ N-S maximum stress or ~ E-W minimum stress, in agreement with the presented data.

The shear fractures within the country rock cluster to two sets of steep fractures with NW-SE and NNE-SSW strikes (Fig. 8). The faults with recognized sense of relative displacement show a similar kinematic pattern as the faults in the massif thus suggesting formation in similar stress field. However, the fault data for the country rock are scarce and the orientation of the shear fractures may be strongly affected by local variations of orientation of the strongly anisotropic metasedimentary fabrics and related strength anisotropy.

Chapter III:

The effect of Fracturing and Alteration on Petrophysical properties of Granite

1. Introduction

The evaluation of rock transfer properties is necessary when estimating the geological environment suitability for radioactive material stocking. The important properties of a repository host rock are the capacity of sealing and retention leading to inhibition of any moving contaminants, as well as the capacity to diffuse the heat generated by the nuclear decay of the stocked material. In terms of petrophysical properties these features can be studied by measurements of the rock permeability, pore space geometry and thermal conductivity. The rock permeability is controlled by the interconnectivity, aperture and geometry of the pore space. The porosity of crystalline rocks (e.g. granite) is mainly represented by low aspect voids (cracks, crystallographic cleavages, grain boundaries) which comply rapidly with depth if no pressurized fluid is in the porosity network. Hence, the porosity closure as a function of confining pressure is another important matter to be studied with the goal to constrain depths of porosity compliance. Accurate quantification of the petrophysical characteristics can only be achieved via direct measurements.

In this study, petrophysical characteristics acquired by five independent experimental techniques have been applied on samples representing a variety of fracturing and alteration facies of mainly the Lipnice granite (Melechov massif, Fig. 5). In the following text, the applied techniques with associated theoretical background are described, the sample collection is defined and the results of the applied techniques are presented and described. Based mainly on the petrophysical results we define the principal facies encountered within the sample collection and we discuss their significance for development of pore space with fracturing and alteration.

2. Experimental techniques

The used techniques and the resulting petrophysical characteristics are briefly described in Tab. 1 and their detailed description is given in the following sections.

2.1 Thermal conductivity measurements

Among the other commonly used methods for measuring the thermal conductivity (TC) such as line or point source or divided bar, the advantage of the one used here, the Optical Scanning method (OS, see Popov et al. 1999), is its contactless mode of measurement and the suitability for examination of specimens of various shapes and sizes including borehole cores.

Table1. Brief description of applied petrophysical techniques.

Experimental technique	Physical quantity	Quantity type	Sample	Experimental conditions
Optical scanning	Thermal conductivity	vector	Borehole core D = 4.5 cm, L ≥ 6 cm Sawed block min. 4 x 2 x 6 cm	ambient
Pulse transmission	*P*-wave velocity	vector	Plug D = L = 1.7 cm Sphere D = 5 cm	ambient p_{conf} ≤ 400 MPa
Nitrogen permeametry	Intrinsic permeability	vector	Plug D = L = 1.7 cm	p_{conf} = 1 MPa
Mercury porosimetry	Porosity Pore size Trapped / Free p. Skeletal density	scalar	polyhedron V ≈ 3 cm^3	

2.1.1 Theoretical background

Thermal conductivity (TC) is the ability of material to conduct thermal energy, i.e. the heat, without macroscopic displacement of the solid mass. At microscopic scale in crystalline materials (rocks, metals) the heat is transferred by exchange of kinetic energy by vibrations of the crystalline lattice. According to the second law of thermodynamics, differences in temperature in an isolated system tend to equilibrate over time with a preferred direction of progress opposite to the energetic potential, i.e. from hotter to colder region. In such a scheme the TC represents the material proportional constant of the heat transfer rate as defined by the Fourier's law:

$$Q = \frac{\lambda A t}{l}(T_1 - T_2)$$

Where Q is heat flux (W), λ is the thermal conductivity (W m^{-1} K^{-1}), A is cross-sectional area (m^2) and (T_1-T_2) is the temperature drop (K) over the distance *l* (m).

2.1.2 Experimental setup

The OS setup is shown on a photograph in Fig. 1. A laser heat source and two infrared radiometers for measurements of sample temperature are placed on a mobile platform that moves at a constant speed relative to samples and reference standards placed on the table. In this manner, temperatures of the sample(s) and of the reference standard(s) are measured before and after the heating by the laser heat source. Given that the heating power, the heat incidence area, the platform movement speed as well as the distances between the radiometers and the heat source are known and constant throughout the scanning, the TC at every examined point along the scanning line (typically each mm) is calculated from the difference of temperatures measured before and after the heat source passage and by comparison to the reference material of known TC.

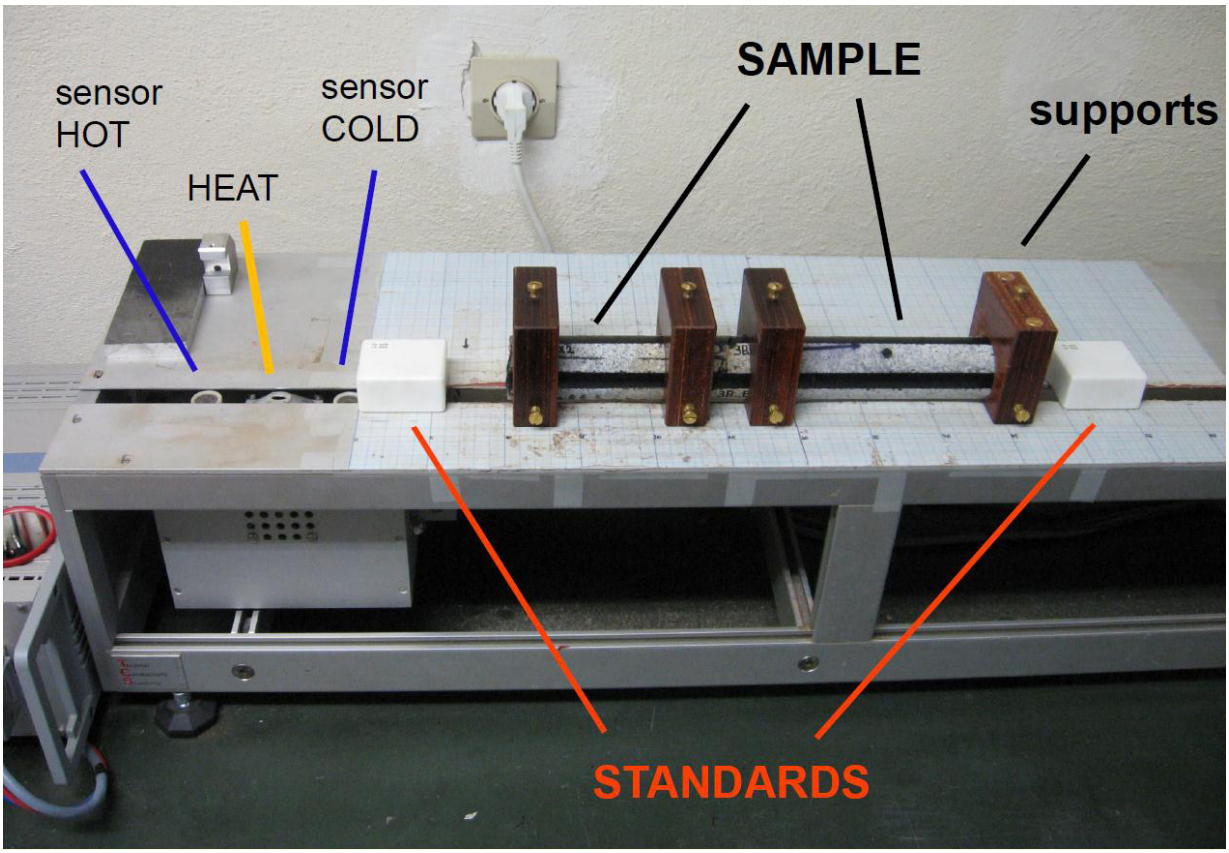

Figure 1. Photograph of the optical scanning apparatus for thermal conductivity measurement showing the working table with standards (marble) and an example of core specimens in supports prepared for analysis. During the anlysis the chariot with the two sensors and the heat source moves at constant speed beneath the specimens from left to right and the thermal conductivity is calculated from the difference in temperatures of the specimen before and after the heat source passage (see text for details).

2.1.3 Experimental procedure

The working surface of the sample has to be coated by a black matte layer prior to analysis in order to minimize the influence of varying optical reflection coefficients of the natural sample surface. Measurements are carried out on either plane or cylindrical surfaces of dry samples. In the case of plane-shaped samples, any direction in a plane can be scanned. In the case of cylindrical samples, scans are oriented along the core axis and executed on more than one face in order to integrate the inhomogeneities due to the mineral composition and/or grain size beneath the scanned surface of the sample. In addition, when working with cores of small diameter (e.g. 4.5 cm as in the actual case), supports for the core have to be used to prevent the core from entering the gap in the working table, which enables the heat transfer and radiometric measurement of temperature. In such a case, the estimated TC would be biased due to change of the working distance between the sample and the heat source.

2.1.4 Influence of sample shape and dimensions on measured TC

The TC estimated in any point along the scan line is representative for a layer of a certain thickness that depends on the adjusted heat source power, the platform movement speed and the material TC (Popov et al. 1999). For a given TC, the lower the heat source power or the higher the movement speed is set, the smaller is the examined thickness. If the goal is to examine the bulk TC of the sample rather than its superficial variations, a problem may arise in the case of small samples as the examined thickness may exceed the sample dimensions. In such a case, the estimated TC would be influenced by the TC of the medium surrounding the sample, i.e. the air in the laboratory. Because samples of different shapes and sizes were measured in this study (4.5 cm diameter borehole core vs. quarry blocks of decametric dimensions), two tests were performed to verify the validity of the estimated TCs. The tests were performed on samples with bulk TC comparable to TCs of all the other samples (2 - 3 W m^{-1} K^{-1}).

The goal of the first test was to verify whether the cylindrical shape of the borehole samples does bias the estimated TC. In a first step, the TC profile along a line on a flat surface of sample with decametric dimensions was measured. In a second step, the portion of the sample carrying the scanned line was extracted by drilling with a coring bit of 36 mm inner diameter. A core of smaller diameter than that of the actual samples was chosen intentionally in order to exaggerate the possible bias. Finally, the TC along the same profile as in the first step was measured. As can be seen on the chart comparing the two TC profiles (Fig. 2a), the change of the sample shape had no effect on the measurement.

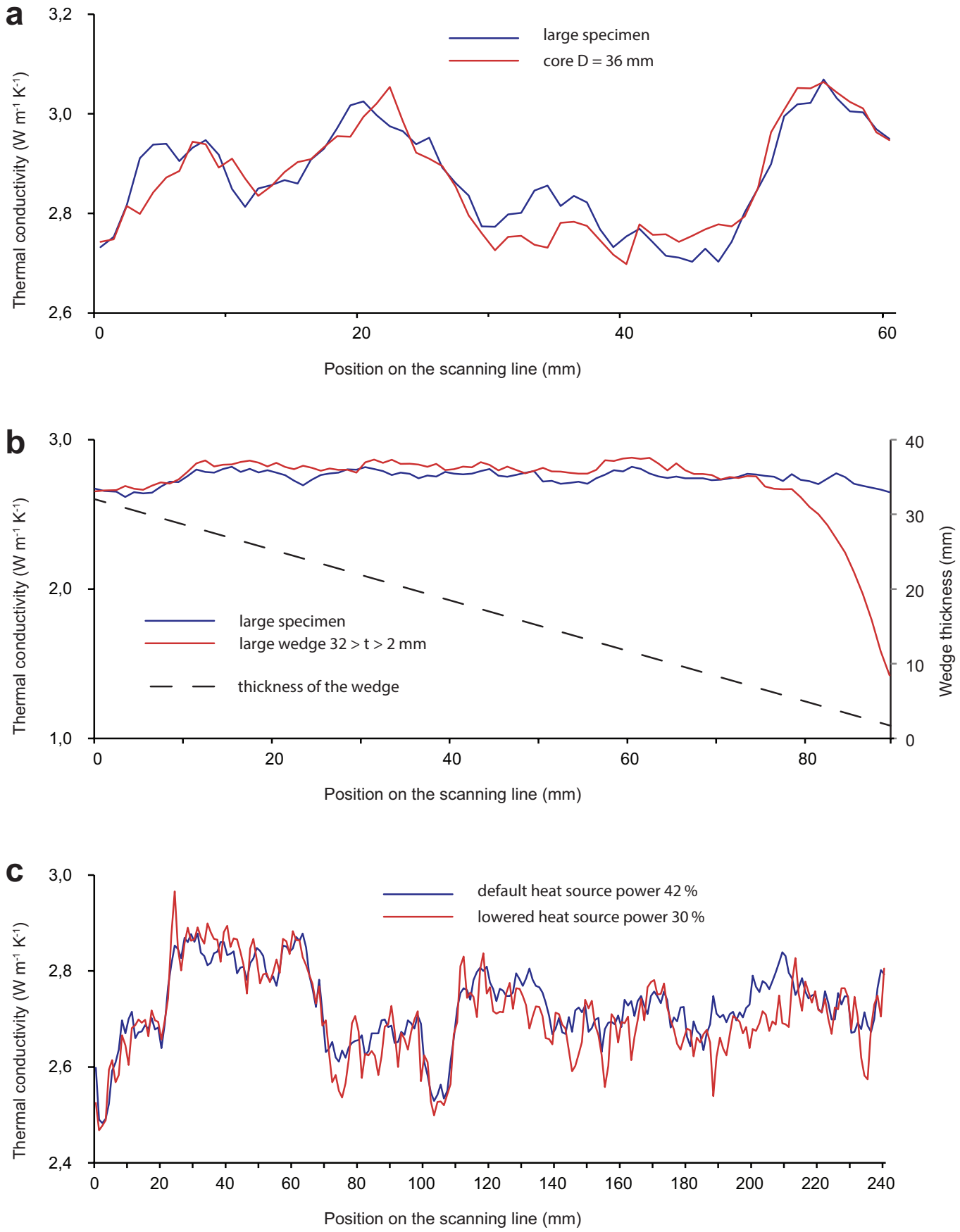

Figure 2. Effect of specimen shape and dimensions and of the heat source power on measured TC. Measured TC profiles along the same scanning lines on a large specimen and on a core with 36 mm diameter prepared from the large specimen (a), on a large specimen and on a wedge with decreasing thickness prepared from the large specimen (b) and on a large specimen using two different heat source powers (c).

The idea of the second test arose from the fact that many of the measured borehole core samples were limited by fracture planes oriented obliquely to the core axis, which resulted in progressively lower thickness of the samples towards their along-core limits (see Fig. A1). With the goal to extract as much information as possible even from such samples, the validity of the TC measurement on these thinned parts of samples had to be questioned. The goal of the second test was therefore to identify a critical thickness of sample below which the measured TC was biased. The first step of this test was the same as for the test mentioned above, i.e. measurement of TC along a line on a large sample. In the second step, the sample was sawed to form of a wedge preserving the initial length and width but having thickness from 32 to 2 mm on its limits corresponding to the beginning and the end of the scanning line. As can be seen on the chart in Fig. 2b, the bias for material of the actual TC is apparent for thickness lower than 7 mm.

2.1.5 Influence of heat source power on the measured TC

In order to quantify the effect of the heat source power setting on the measured TC, a scanning line on the sample 8 core was measured two times with different heat source power. The marble reference standards were used in both times and the heat source power was first set to the standards-recommended value (42% of the maximum power) and second to a significantly lower value (30% of the maximum power). The resulting TC profiles of this test can be seen in Fig. 2c. As can be expected, the lower power measurement resulted in a less smooth TC curve than the measurement at the standard-recommended power. Nevertheless, the mean of the differences of TC values in each of the measured point (each mm) between the two power settings is on the order of percents of W m^{-1} K^{-1}. Given the absolute values ranging between 2 and 3 W m^{-1} K^{-1} for all the samples, the effect of the heat source power setting is negligible for the inter-sample comparison.

2.2 V_p measurements

The P-wave propagation velocity in the studied granite was measured using two experimental setups with different properties. In one of the methods, simple ambient-pressure measurements along three orthogonal directions were applied either directly on sawed sample blocks or on plugs drilled from the samples. The main interest of this method was to test cored plug specimens prior to intended permeability measurements. The other method, executed at the Geophysical Institute ASCR in Prague, comprised multidirectional P-wave measurements at confining pressures up to 400 MPa using 5 cm spheres derived from the collected quarry samples. Here, the theoretical background of the P-wave propagation

measurement is given and the experimental setup and procedure for the basic methods is described. For a complete description of the advanced method see Chapter IV.

2.2.1 Theoretical background

Direct pulse transmission experiments are based on measurement of the mechanical pulse time-of-flight through a sample with known dimensions. The velocity V is then calculated as:

$$V = \frac{l}{t}$$

where l is the sample length in the measured direction and t is the measured time. The propagation of a mechanical pulse in a solid can be represented by elastic body waves. In isotropic homogeneous solids, the mode of propagation of a P-wave is always longitudinal and the direction of the relative movement of the solid particles is coaxial with the wave propagation direction. The P-wave propagation velocity (V_p) is related to the material properties as:

$$V_P = \sqrt{\frac{K + \frac{4}{3}\mu}{\rho}}$$

where K is the bulk modulus, μ is the shear modulus and ϱ is the density. The bulk rock elastic constants and density depend on the rock mineral composition and porosity as well as on geometrical arrangement of the rock microstructures. At ambient or low confining pressure open cracks represent the dominant agent reducing the pulse propagation velocity. This is mainly due to two facts. First, at ambient pressure the cracks are open which means filled by a fluid (e.g. air or brine) featuring V_p lower by an order of magnitude than most of common rocks. Second, cracks are high aspect voids (wide, long and thin) and therefore for a given void volume and wavelength are more likely to decelerate the propagating pulse as compared to an isometric pore. The results acquired at ambient pressure hence serve mainly for comparison with macroscopic degree of fracturing and alteration as well as with results of the other petrophysical measurements.

2.2.2 Experimental setup

A portable instrument PunditLink (Proceq SA) was used to measure V_p. It consists of a couple of piezo-transducers connected to an acquisition unit which can be connected to a PC via USB. The PunditLab software provided with the instrument was used to visualize the waveforms and to manually pick the first P-wave arrival. Two couples of piezo-transducers differing in resonant frequency and face plate size (54 kHz, 50 mm and 500 kHz, 5 mm) were used according to the pulse travel distance on the actual specimen (read below for details).

2.2.3 Experimental procedure

Prior to the first sample measurement and every time when the piezo-transducers or the connecting cables have been changed, the delay of the signal in the electrical circuit is corrected by measuring a reference standard with known, factory-calibrated time-of-flight. A couplant is applied on the transducers surfaces in order to minimise the signal attenuation on the transducer-sample interface. Then the transducers are attached to the opposite sides of a sample and the pulse transmission is started. Dependent on the received signal amplitude, the gain of the preamplifier integrated in the instrument can be increased so that the first arrival time can be clearly picked. The picked traverse time is recorded on a commercial spreadsheet program together with the measured length of the sample and the V_p is calculated.

For high travel distances (≥ 10 cm), only the larger transducers generated sufficiently strong pulse for clear first arrival time picking. In case of centimetric specimens, the use of the larger transducers resulted in clear first arrival even with no receiver signal preamplification. On the other hand, the small size of the specimens can lead to biased V_p values due to border effects and therefore the use of the large (low frequency) transducers on small specimens, though comfortable, has to be justified.

2.2.4 Limitations due to sample dimensions

According to various technological standards (ASTM, EN, IRSM), the pulse frequency, the sample dimensions and the grain size of the rock are interrelated factors that affect the pulse propagation velocity. Here, two kinds of specimens were examined. The majority of values comes from measurements on 17 mm plugs with length ranging from 15 to 30 mm. Some of these plugs were drilled from block samples of decametric dimensions, which themselves represent the other kind of examined specimens. Hence, the results acquired on the same material but on specimens with different size have been compared.

For reliable measurements, the ASTM D2845-05 (2005) norm states the following recommendations concerning the relation of the dominant wavelength of the pulse train λ, the mean grain size of the rock d, the plug diameter or the minimum lateral dimension of block sample D and the travel distance of the pulse l.

The travel distance of the pulse through the rock shall be at least 10 times the mean grain size so that an accurate average propagation velocity may be determined:

$$\frac{l}{d} \geq 10$$

The mean grain size of the Lipnice granite is 0.7 mm (see chapter IV), and therefore

even the shortest plug (l = 15 mm) satisfies the equation.

To reduce scattering and poorly defined first arrivals at the receiver, the transmitter shall be designed to generate wavelengths at least 3 times the mean grain size of the rock:

$$\frac{\lambda}{d} \geq 3$$

The pulse train wavelength depends on the frequency f of the transducer that generated the pulse and on V_P of the specimen:

$$\lambda = \frac{V_P}{f}$$

At 500 kHz frequency, specimens with V_P higher than 1.05 km/s satisfy the equation and at 54 kHz the critical V_P is roughly ten times lower. The minimum of the measured V_P values is 2.11 km/s and therefore all the specimens satisfy the equation.

It is recommended that the ratio of the pulse-travel distance to the minimum lateral dimension not exceed 5:

$$\frac{l}{D} \leq 5$$

As mentioned above, the measured plugs were 17 mm in diameter and 15 to 30 mm in length. Hence, their length-to-diameter ratios do not exceed 2 and therefore satisfy the equation.

The minimum lateral dimension of the test specimen shall be at least 5 times the wavelength of the compression wave so that the true dilatational wave velocity is measured:

$$\frac{D}{\lambda} \geq 5$$

At 500 kHz frequency, specimens with V_P lower than 1.7 km s^{-1} satisfy the equation, at 54 kHz the critical V_P is roughly ten times lower. The minimum of the measured V_P values is 2.11 km s^{-1} and therefore none of the specimens satisfies the equation.

2.2.5 Test of V_P bias due to pulse travel length

According to the last criterion mentioned in the previous section, the V_P values measured on the plugs are likely to be biased due to the small size of the specimens. Nevertheless, the lack of material for the majority of the samples from the 4.5 cm borehole core did not allow more voluminous specimens to be prepared. Furthermore, the manipulation of the 500 kHz transducers was uneasy due to the construction of their housing and also due to the small face plate. Consequently, it was difficult to press hard the two transducers against the opposite sides of the specimen and to simultaneously assure

the parallelism of the face plates. This resulted in unstable measurements with highly varying time-of-flight values in subsequent pulse transmissions. For this reason, it was preferred to use the large (54 kHz) transducers despite their inconvenience regarding the ASTM norm criteria. In order to quantify the possible bias, V_p measurements using the 54 kHz transducers have been conducted on the block samples and also on plugs drilled from these blocks. The comparison of the values is shown in Tab. 2. As can be seen on the set of 18 value couples, the difference between the values obtained on blocks and on plugs is on the order of percents. On the average it is 1% and only in one case exceeds 5% reaching 8%. In addition, the difference is not dependent on either the V_p values, either the length values or on the two lengths ratio. Similar results are reported by Fener (2011), who compared dependence of measured V_p on diameter of the plug used for the measurement and has shown that for granite plugs of 110 mm length and diameter ranging from 30 to 114 mm the variation of the values was approximately 5%. Thus, taking into account the possible error of 5%, the measurements acquired using the 54 kHz transducers will be presented in the results.

Table2. Effect of specimen dimensions on measured P-wave velocities (V_P)

Sample and direction	Block		Plug		Block / plug	
	V_P (km s^{-1})	Length (mm)	V_P (km s^{-1})	Length (mm)	V_P ratio ( )	Length ratio ( )
MS09_1X	3.39	101.38	3.42	18.48	0.99	5.5
MS09_1Y	3.14	178.20	3.10	16.72	1.01	10.7
MS09_1Z	2.74	84.10	2.62	18.10	1.04	4.6
MS09_2X	4.44	77.24	4.37	19.24	1.02	4.0
MS09_2Y	4.26	46.04	3.96	17.44	1.08	2.6
MS09_2Z	4.48	103.08	4.48	17.46	1.00	5.9
MS09_3X	4.17	155.52	4.25	18.70	0.98	8.3
MS09_3Y	3.96	80.88	4.03	18.12	0.98	4.5
MS09_3Z	4.29	101.70	4.36	17.00	0.98	6.0
MS09_4X	4.10	128.80	4.11	18.08	1.00	7.1
MS09_4Y	4.11	111.90	4.00	17.58	1.03	6.4
MS09_4Z	4.36	60.20	4.43	17.26	0.99	3.5
MS09_5X	4.61	111.60	4.41	17.20	1.05	6.5
MS09_5Y	4.11	110.20	4.01	17.66	1.02	6.2
MS09_5Z	4.44	132.82	4.62	18.00	0.96	7.4
MS09_6X	3.79	58.38	4.02	15.68	0.94	3.7
MS09_6Y	3.88	109.92	4.11	16.02	0.95	6.9
MS09_6Z	3.84	87.06	4.08	16.30	0.94	5.3

2.3 Permeability measurements

2.3.1 Theoretical background

The goal of the permeability measurements is to evaluate the intrinsic permeability of the examined rock specimen. Intrinsic permeability represents a mobility of fluid within porous medium and is solely related to pore geometry of the material (porosity, pore shape and pore size distribution), and is independent of fluid quality. It was first defined by Darcy (1856) as a proportional constant between the instantaneous discharge rate through a porous medium, the viscosity of the fluid and the pressure drop over a given distance:

$$Q = \frac{kA}{\mu L}(p_{up} - p_{down})$$

where Q is total discharge (m^3 s^{-1}), k is intrinsic permeability (m^2), A is cross-sectional area to flow, (pup-pdown) is pressure drop (Pa) over the distance L (m) and μ is the pore fluid viscosity (Pa.s).

The Darcy's law considers an ideal (uncompressible) fluid. In the actual experiment Nitrogen gas (compressible fluid, PV = constant) is used and the average gas permeability is expressed as (Scheidegger, 1974; Debschütz et al. 1989; Miguel & Serrenho 2007; Tanikawa & Shimamoto 2009):

$$Q = \frac{k_a A}{\mu L}\frac{\left(p_{up}\right)^2 - \left(p_{down}\right)^2}{2p_{down}}$$

where ka is apparent permeability as defined by Klinkenberg (1941).

Klinkenberg (1941) discovered that permeability to gas is relatively higher than that to water, and he interpreted this phenomenon as "slip flow" between gas molecules and solid walls. To quantify the intrinsic permeability, i.e. proper to the material and independent of the fluid, correction has to be made to account for the gas slippage effect. Gas molecules collide each other and to pore-walls during traveling through the porous medium. When the pore radius approaches to the mean free path of the gas molecules the frequency of collision between the gas molecules and the solid walls rises. Therefore this additional flux due to the gas flow at the wall surface becomes effective to enhance the flow rate. This phenomenon is called Klinkenberg effect, and its effect is expressed as follows:

$$k_a = k\left(1 + \frac{b}{p_m}\right)$$

where b is constant characteristic for the pore space geometry and pm is the mean pressure. In practice, the examined intrinsic permeability k (and also the geometric constant b) are defined from permeability tests at several mean pressures by extrapolating the ka to infinite mean pressure given that if $p_m \to \infty$ then $\left(1 + \frac{b}{p_m}\right) \to 1$, and therefore $k_a \to k$

In order to verify the plausibility of the Klinkenberg effect and/or the accurate adjustment of the experimental setup, the correlation (Pearson's correlation coefficient) of the pairs of values of ka and 1/Pm is calculated as:

$$Correl\left(k_a, \frac{1}{p_m}\right) = \frac{\Sigma\left(k_a - \overline{k_a}\right)\left(\frac{1}{p_m} - \overline{\left[\frac{1}{p_m}\right]}\right)}{\sqrt{\Sigma\left(k_a - \overline{k_a}\right)^2 \Sigma\left(\frac{1}{p_m} - \overline{\left[\frac{1}{p_m}\right]}\right)^2}}$$

The correlation coefficient ranges from -1 to +1, with values equal to +/- 1 corresponding to data with perfect linear correlation and 0 value corresponding to data with no linear correlation. Taking into account the principle of the Klinkenberg effect, i.e. the apparent gas permeability decreases linearly with increasing mean pressure, the data resulting from Klinkenberg effect should have correlation between ka and 1/pm close to +1. In practice, experimental results having correlation coefficient lower than 0.9 are considered as incorrect.

2.3.2 Experimental setup

The used experimental setup is schematically shown in Fig. 3. The essential parts of the setup are represented by a pressure vessel, 3 differential-pressure transducers, a thermal gas flow-meter, a source of pressurised gas (gas bottle in this case) and high pressure

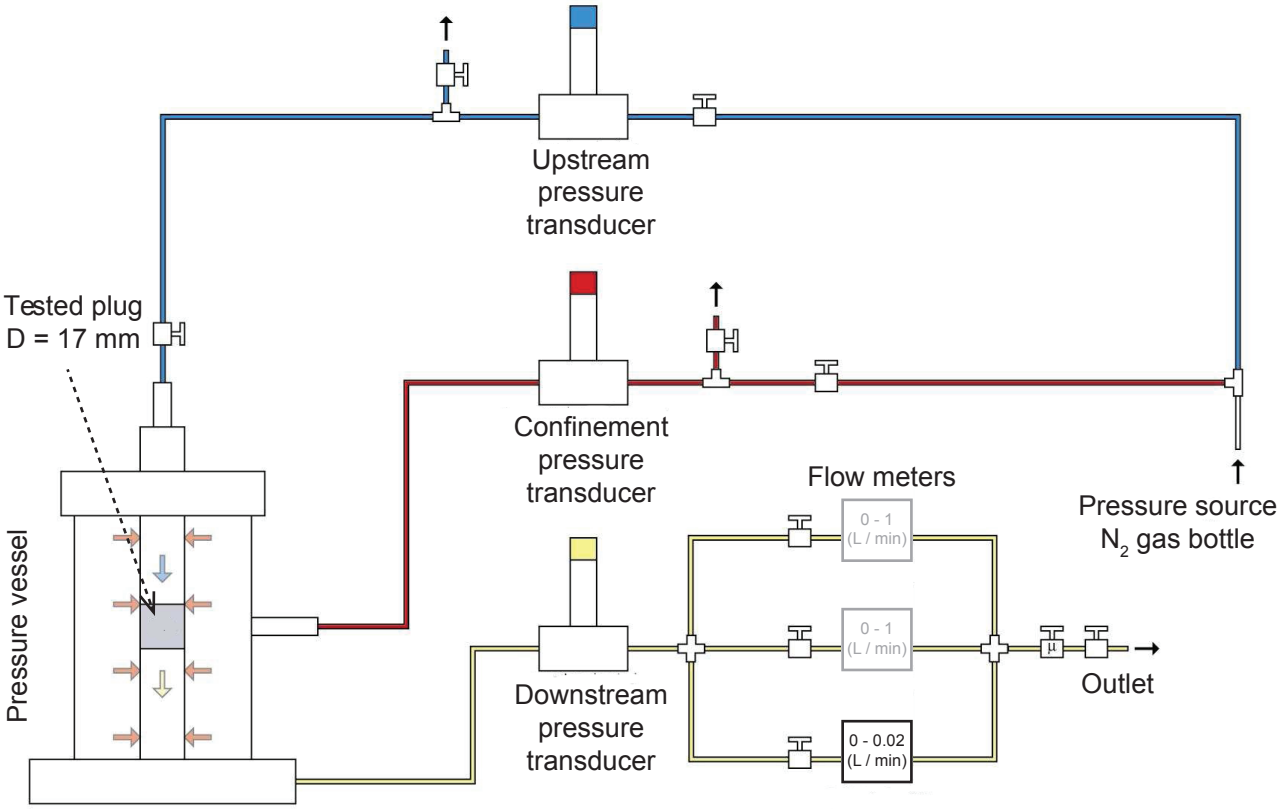

Figure 3. Setup for permeability measurements using nitrogen as flow medium (modified after Rosener 2007).

tubing, fitting and valves. Both the confining and the flow media is pure Nitrogen gas. Electrical outputs of all the 3 pressure transducers as well as those of the flow meter are connected to a data acquisition unit enabling continuous logging of the data throughout the experiment. The acquisition unit is connected to a PC allowing user-friendly displaying of the experimental data as well as their recording and treatment.

2.3.3 Experimental procedure

A cylindrical sample (D = L = 1.7 cm) is set into a perforated steel tube equipped by a rubber sleeve on its internal side. The sample assembly is then installed into a pressure vessel in a manner allowing application of confining pressure on the cylinder mantle and independent application of gas pressure on the cylinder bases. After installing the sample into the pressure vessel, confining pressure of 1 MPa (10 bar) is applied and the circuit of confining pressure is closed. Then, upstream pressure is increased and kept constant in order to create a constant pressure gradient across the sample. Gas flow across the sample is thus induced. When steady-state flow is reached (usually after a short period of time on the order of seconds or tens of seconds), the actual upstream and downstream pressures and the flow rate are recorded. In the next step the upstream pressure is increased and after reaching the steady state flow all the values are recorded again. One continues in this manner in order to record flow rates for at least 3 (usually 5 to 10) mean pressures, i.e. the average of upstream and downstream pressures. During such a procedure, the range of useful values of pressure is limited from one side by the sensitivity of the flow meter at low upstream pressures and from the other side by the necessity to keep difference of at least 0.5 MPa between the confining and the upstream pressure in order to avoid gas leakage along the sample-rubber interface at high upstream pressures.

2.3.4 Experimental setup limitations

For low-permeability materials a problem may arise due to low flow rates which are below sensitivity of the flow-meter. This problem can be overcome in some cases by increasing the diameter or decreasing the length of the cylinder. Another way is to work with higher upstream pressures and, therefore, also confining pressure. This way is nevertheless limited by the design of the pressure vessel and tubing which, in the actual case, could not support pressures higher than 1 MPa. With the available setup the lowest measurable permeability was on the order of 10^{-18} m^2.

2.4 Mercury porosimetry

2.4.1 Theoretical background

The method is based on calculation of mercury volume intruded into the sample pore network as a function of external pressure applied on the mercury. In contact with air or in vacuum, mercury is a not-wetting liquid (contact angle exceeding 90°) for most of common solid materials and therefore cannot be spontaneously absorbed by the pores of the solid itself, because of surface tension. However, this resistance to penetration can be won by applying an external pressure, which depends on the pore size. The relation between

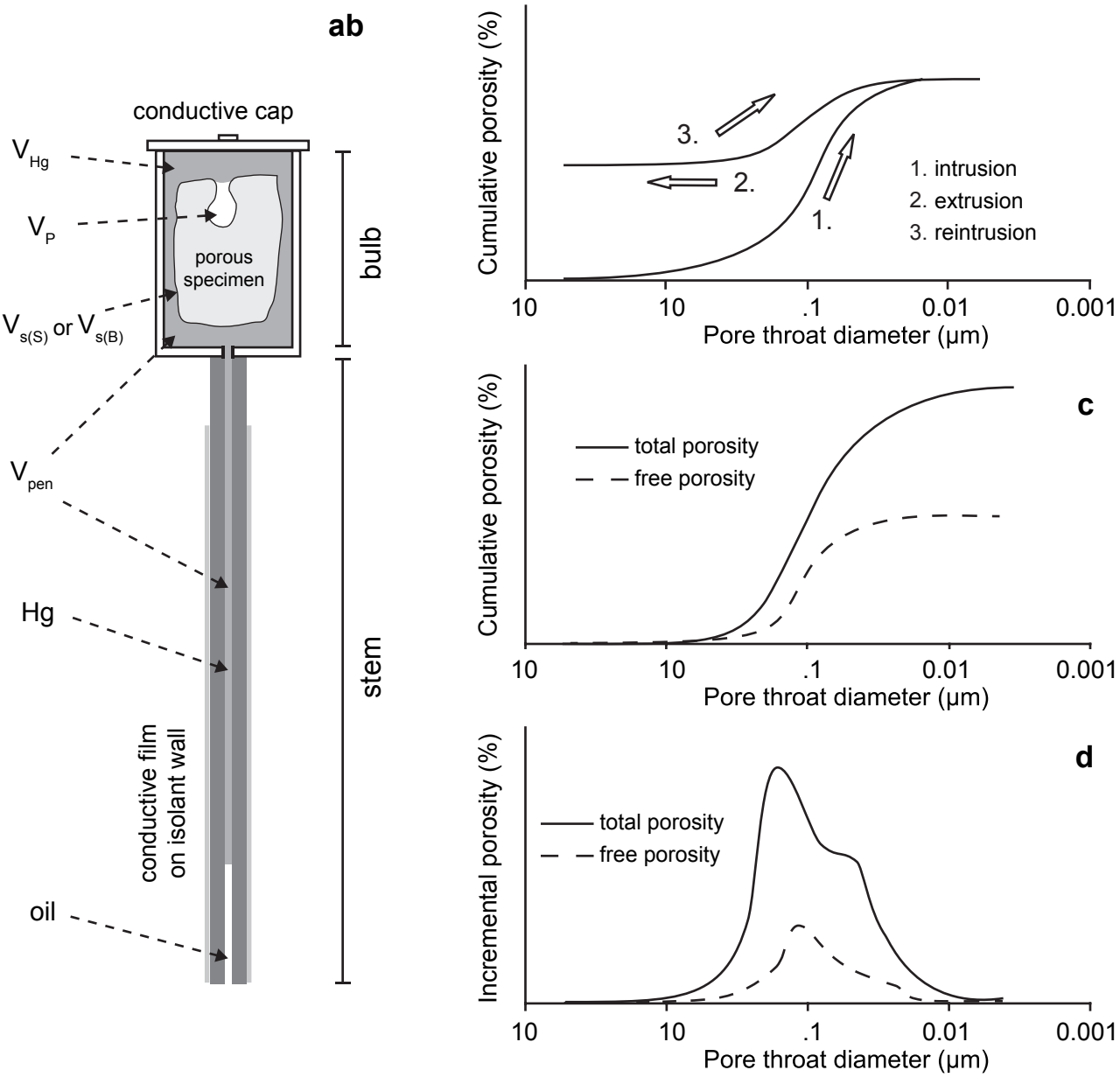

Figure 4. Mercury porosimetry technique basics. Schematic descripition of penetrometer showing the partial volumes used for calculation of sample density (a), charts of cumulative porosimetric curves showing the three basic phases of analysis (b) and the linked terms of total and free porosity (c) and chart of incremental porosimetric curve (d) calculated from the cumulative one (b, c and d modified after Rosener & Géraud 2007).

the pore size and the pressure applied on mercury, assuming the pore is cylindrical, is based on the Young-Laplace equation. For the purpose of experimental porosimetry this was first expressed by Washburn (1921), who stated that the pressure required to force mercury to enter an evacuated capillary pore is related to the capillary radius by the equation:

$$r = \frac{-2\sigma \cos\theta}{p}$$

where r is pore throat diameter, σ is the mercury surface tension, θ is contact angle between the liquid and the solid and p is pressure. Hence, the Washburn equation shows that the pore radius is inversely proportional to the applied pressure. Though in almost all natural porous substances no cylindrical pores exist, the Washburn equation is generally used to calculate the pore size distribution (PSD) starting from the data obtained by mercury porosimetry.

In addition, the method allows inferences about the geometry of the connected porosity. In a simplified scheme the pore space is made up of large spaces called pores, which are connected by smaller spaces or constrictions referred to as throats (Wardlaw et al. 1988). It has been demonstrated, that if large pores are accessible by small throats, the mercury forced to the pore remains in it after the mercury pressure is decreased to atmospheric (Wardlaw & McKellar 1981; Li & Wardlaw 1986a, b). To take advantage of this phenomenon called trapping, the mercury porosimetry analysis is usually executed in three phases (Fig. 4): (1) "intrusion" - the pressure increases from vacuum to the maximum; (2) "extrusion" – the pressure decreases down to atmospheric and (3) "reintrusion" - it increases again to the maximum pressure. Hence, the proportion of the pores and the throats on the total connected porosity can be evaluated. The volume of intruded mercury after the intrusion corresponds to the total connected porosity. The volume that remains in the sample after the pressure decrease at the end of the extrusion is considered to be contained in the pores and therefore corresponds to the trapped porosity. Finally, when the pressure is increased again, the mercury can only enter in pore space where trapping have not occurred and therefore the corresponding reintrusion curve relates to the so called "free" porosity only. In addition, also the PSD of the trapped porosity can be calculated by subtracting the curve of the free porosity from the curve of the total connected porosity.

2.4.2 Experimental setup

There are several commercial brands of mercury porosimeters. Here, the Micromeritics brand AutoPore IV 9500 v1.09 model was used. This model is able to apply

a maximum pressure of 220 MPa which corresponds to the smallest measurable pores of 6 nm. Mercury porosimeters are highly standardised and widespread analytical instruments and therefore only brief description is given. Apart of a pressure vessel, pressure transducer, vacuum and high pressure pumps and a pressure intensifier, the essential part of the setup is the penetrometer a sample-holder accommodating the specimen being intruded by mercury during the analysis. A schematic drawing of a penetrometer containing a porous sample can be seen in Fig. 4a. The penetrometer consists of two factory-joined parts: a glass bulb for the sample placement and a plastic stem coated by a thin metal layer. During analysis, the volume of mercury in the penetrometer stem changes due to progressively pressurized oil entering the stem and expulsing the mercury into the penetrometer bulb. Taking into account that the mercury and the stem coating are electrical conductors, whereas the oil and the plastic wall of the stem are dielectric, the replacement of the mercury by the oil induces change of capacitance of the stem. This change of the stem electric capacitance is measured by the apparatus during analysis and used as a proxy to calculate the volume of mercury that has moved into the bulb. After corrections for volumetric changes related to compressibility of the penetrometer and mercury, the volume of mercury present within the porous sample is estimated as a function of mercury pressure.

2.4.3 Experimental procedure

A dried sample is first weighted and then placed into the bulb of a chosen penetrometer. High-pressure grease is applied on the rim of the bulb to ensure sealing between the bulb and a metal cap placed atop as a cover in the next step. Such a preparation results in what is called the "penetrometer assembly", i.e. the penetrometer, the cap with the grease and the sample. The penetrometer assembly is weighted and then installed in horizontal position into the low-pressure port of the porosimeter. The low-pressure analysis begins by degassing of the sample by creating vacuum. In the next step, a valve connecting the penetrometer to a mercury reservoir is opened. Consequently, the mercury flows into the penetrometer, surrounds the sample and wets the sample surface irregularities. The rest of the low-pressure analysis consists of a step-wise measurement of the mercury volume intrusion at increasing mercury pressure up to 0.2 MPa, which is the strength limit for the unconfined penetrometer and also a higher pressure than the pressure exerted by the mercury column in vertically disposed penetrometer during the following high-pressure analysis. After the low-pressure analysis, the penetrometer assembly filled with mercury is removed from the low pressure port, weighted and installed in vertical position into the high-pressure vessel where oil serves as a confinement medium. Then the high-pressure

analysis follows and the step-wise measurement is executed in three stages. First, intrusion is characterised by increasing pressure up to the peak pressure of 220 MPa, second extrusion by decreasing pressure down to the atmospheric pressure and then reintrusion by increasing pressure up to the peak pressure again.

2.4.4 Physical constants and analysis parameters

We have first run a preliminary set of ~ 30 analyses at lower resolution setting to reveal the sample set general properties at rather time-saving rate (~ 3h per sample). Based on the preliminary results a second set of ~ 40 specimens with distinct characteristics was prepared and submitted to highly standardised, detailed and time-costly (~ 8h per sample) analyses. If not specified otherwise we will refer to the advanced set of analyses in the following text. The analyses were made using the same porosimeter, penetrometer, physical constant values and pressure increments. Special attention was also paid to prepare specimens of proximate volume and shape. The used penetrometer had 5 cm^3 bulb and 0.392 cm^3 stem capillary volume. Prior to analyses, calibration of the penetrometer bulb exact volume as well as penetrometer blank runs had been performed using the same analysis parameters as for the sample analyses themselves. The average of seven blank runs was used as a correction for all the sample analyses. The following values were used for the physical constants input to the Washburn equation: σ = 485 dynes cm^{-1} (48500 N m^{-1}), θ = 130°. The vacuum level for degassing of the sample was 13 Pa (≈ 0.1 mmHg), the evacuation time was 5 minutes and the mercury filling pressure was set to 4 kPa. For the low pressure analysis, 26 pressure levels were pre-set. For the high pressure analysis intrusion, extrusion and reintrusion, the same 40 pressure levels were preset. The equilibration time at each pressure increment was set to 20 seconds for the low pressure analysis and 180 seconds for the high pressure analysis.

2.4.5 Corrections of the raw intrusion data

For all the analyses, the volume due to compressibility of the mercury and the penetrometer has to be subtracted from the raw intrusion vs. pressure data recorded during the experiment. Here, the correction was done by the porosimeter factory software using the blank run average. In most cases (31/40) no other correction of my dataset was necessary before the data interpretation. In one case the intrusion values featured an abrupt rise at the data point corresponding to the transition from the low pressure to the high pressure analysis, which is associated with manual handling of the penetrometer and with use of another pressure transducer. Hence, error volume increments are likely to occur and in laboratory practice this error is frequent and hardly evitable when working with numerous

samples (Giesche, 2006). This error was corrected by subtracting the value of the error increment from all the following. Other common errors occurring also in my raw data are linked to the switch between intrusive and extrusive cycles, i.e. the intrusion to extrusion and extrusion to reintrusion transitions. These errors are probably linked to the difference of advancing and receding mercury contact angle and to the temperature hysteresis of the experimental setup. In general case, intrusion volume hysteresis was observed both during the extrusion and reintrusion. During the extrusion, the volume drop with decreasing pressure was shifted towards lower pressures or absent, whereas during the reintrusion, the first volume increment was typically an order of magnitude higher than all the others. For treatment of the reintrusion data, which further gives the information about the free and trapped porosity ratio, these error increments were subtracted from all the following cumulative intrusion values.

2.4.6 Calculation of pore size distribution

Corrected intrusion data were used to plot cumulative and incremental porosimetric curves and to calculate a set of values characteristic of the sample bulk pore space properties. The following data interpretation is based on the assumption that the pore space is composed of pores with the form of right spherical cylinder with open circular endings. To plot the PSD curves, intrusion volume at each pressure increment was attributed to pores with diameter given by the Washburn equation using the pressure value at the step-wise limit of the pressure increment. In order to display the pore volume on the vertical axis, the intrusion volume values (ml/g) were multiplied by a constant given by the measured bulk density (g/cm^3).

2.4.7 Calculation of total, trapped and free porosity

The intrusion and reintrusion data were used to calculate the respective contributions of the free and the trapped porosity to the total connected porosity. At the beginning of the reintrusion stage, the volume of mercury-filled free porosity is supposed to be zero and all the trapped porosity to be filled by mercury from the intrusion stage. Hence, the volume increments during the reintrusion stage are representative of the free porosity solely and its distribution as well as the total value was calculated by subtracting the volume at the end of the extrusion from the reintrusion data. The trapped porosity related values were then calculated by subtracting the free porosity volume from the connected porosity volume obtained during the intrusion stage.

2.4.8 Calculation of median pore throat diameter

For numerical comparison of sample-representative pore size values, the volumetric median pore throat diameter was estimated for each of the analysis. It corresponds to the pore throat diameter (PTD) at which the mercury has filled a half of the pore space volume during the step-wise intrusion. In case of quasi symmetric unimodal PSD the median PTD corresponds to the inflexion point on the cumulative intrusion curve, and, consequently, to the dominant peak on the incremental curve. The mercury porosimetry-estimated median PTD represents the percolation threshold of Katz & Thompson (1986) which, together with the total porosity value, controls the rock fluid permeability.

2.4.9 Calculation of sample density

The mercury porosimetry was also used to measure bulk and skeletal density of the specimens. Relative to mercury porosimetry, bulk density is defined as the unit weight per unit volume (usually $g.cm^{-3}$) of a material after the volume of the largest open pores (larger than a specific size) has been subtracted. The value for the largest pore included in the bulk density is an adjustable parameter of the analysis. In this study we used a value of 300 μm which corresponds to the mercury filling pressure of 4 kPa at the beginning of the low-pressure analysis. Skeletal density is computed after the volume of all pores accessible by throats larger than about 0.006 μm has been excluded from the volume presumed occupied by the sample. This value corresponds to the volume intruded at the highest applied pressure of 220 MPa.

Derivations of the formulas for bulk and skeletal densities can be found in manuals provided with porosimeters and relates to Fig. 4a. The internal volume of the penetrometer, including both the bulb and the stem, is known from the pre-analysis calibration procedure. In addition, the experimental procedure (see section 2.4.3) comprises weighing of the sample, of the sealed penetrometer with only the sample inside and of the sealed penetrometer with the sample inside and filled with mercury. Assume that now the sample has been inserted and the mercury has filled all the remaining volume except that occupied by the sample and its pores smaller than approximately 300 μm. We can now write:

$$V_{s(B)} = V_{pen} - V_{Hg}$$

where Vs(B) is bulk volume of the sample, Vpen is total internal volume of the penetrometer and V_{Hg} is volume of mercury occupying the remaining space. The volume of mercury occupying the remaining space around the sample can be written as:

$$V_{Hg} = \frac{W_{Hg}}{\rho_{Hg}}$$

where W_{Hg} is weight of the mercury occupying the remaining space in the penetrometer and ϱ_{Hg} is density of mercury. The mercury weight is:

$$W_{Hg} = W_{tot} - W_{pen} - W_{s(B)} = W_{tot} - \left(W_{pen+s(B)} - W_{s(B)}\right) - W_{s(B)} = W_{tot} - W_{pen+s(B)}$$

where Wtot is weight of the penetrometer assembly containing sample and filled by mercury (weighing after the low pressure analysis), Wpen is weight of the penetrometer assembly, Ws(B) is bulk weight of the sample (weighing at the beginning of the experimental procedure) and Wpen+s(B) is weight of the penetrometer assembly containing the sample (weighing just before the low-pressure analysis. The bulk volume of the sample can be calculated as:

$$V_{s(B)} = V_{pen} - \frac{W_{tot} - W_{pen+s(B)}}{\rho_{Hg}}$$

and the sample bulk density as:

$$\rho_{s(B)} = \frac{W_{s(B)}}{V_{pen} - \frac{W_{tot} - W_{pen+s(B)}}{\rho_{Hg}}}$$

where $\varrho_{s(B)}$ is bulk density of the sample ($g.cm^{-3}$).

The skeletal volume is found by subtracting the total volume of pores filled by mercury (after the end of the high-pressure analysis) from the bulk volume:

$$V_{s(S)} = V_{s(B)} - V_P$$

where $V_{s(S)}$ is the sample skeletal volume and VP is the total pore volume. The sample skeletal density is:

$$\rho_{s(S)} = \frac{W_{s(B)}}{V_{s(S)}}$$

2.5 Scanning electron microscopy

As a complementary method the scanning electron microscopy (SEM) has been used to characterise the fracture skins of the borehole samples. The apparatus JEOL scanning microscope JSM 840 at the Institut de Physique du Globe has been used. The technique is based on scanning of the studied material surface by beam of electrons emitted by the electron gun of the microscope (primary electrons) and on detection of either the primary electrons scattered from the sample surface (back-scattered electrons, BSE) or secondary electrons (SE) emitted by the sample surface as a result of the material excitation by the primary electrons. The SEM images from one or the other mode are reassembled from raster measurements using grayscale look-up table to convert between the detected electron count and the colour on the image. The scattering of the primary electrons is mainly affected by density of the material and the BSE mode is therefore useful

for displaying the distribution of materials on the fracture skin differing in composition such as silicates and oxides. Contrastingly, the SE mode provides high depth of field of the images and is thus useful for displaying the morphology of the fracture surface material and especially of phyllosilicate minerals (mica, chlorite, clay minerals).

3. Sample collection

Various granite facies differing in alteration and fracturing character were sampled and examined by the petrophysical methods. The collection comprises samples of two kinds: samples taken from exposures in active or abandoned quarries and samples of 4.5 cm core of a 140 m deep borehole MEL-5. The locations of the sampling sites and of the borehole are shown on a map of the Melechov massif (MM) in Fig. 5 and a parametric description of the samples is given in Tab. 3.

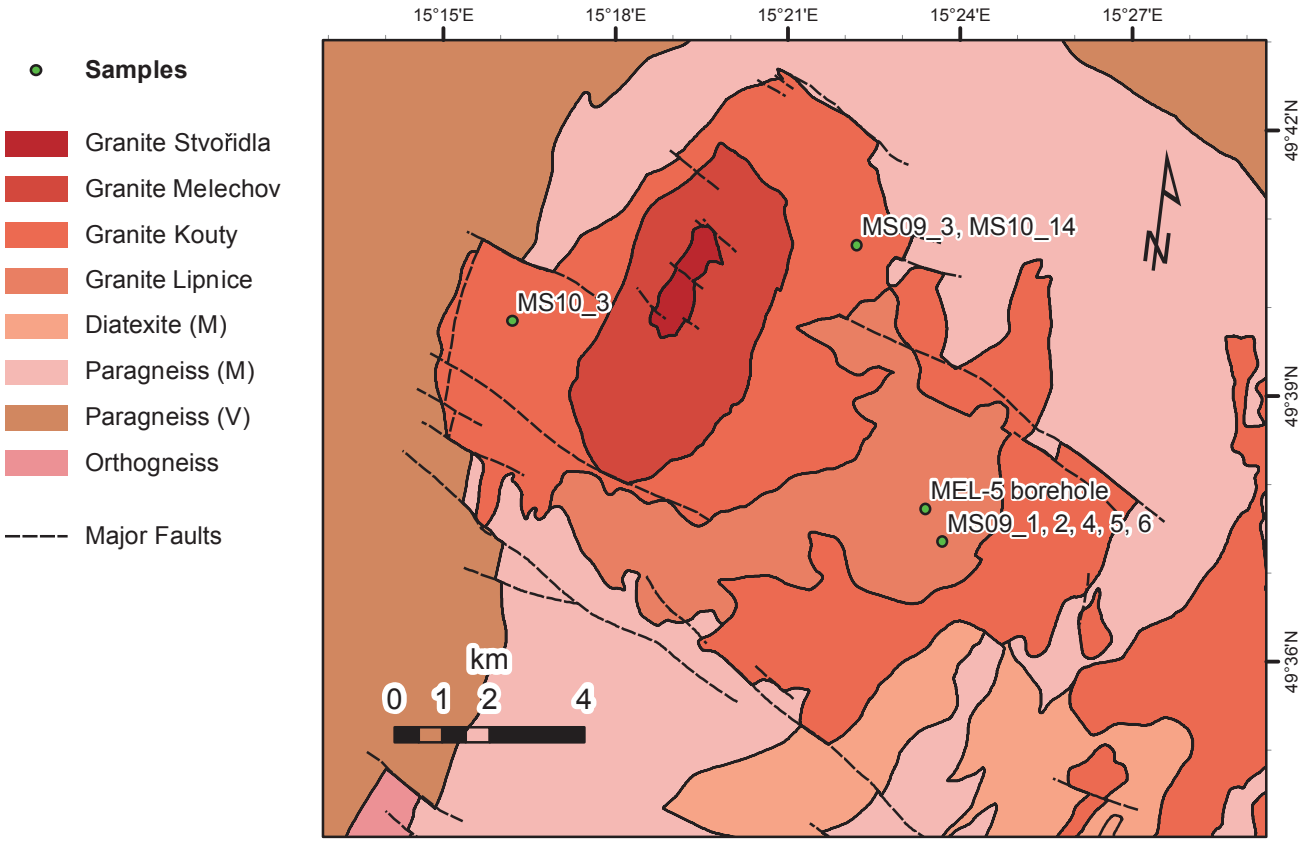

Figure 5. Geologic map of the study area showing position of the sampled borehole MEL-5 and of the quarry samples. The geologic map shows the extent of the four granite types within the Melechov massif and of the Kouty type-similar granite of the Central Moldanubian Pluton to the southeast, high grade migmatites and paragneisses of the Monotonous Group (M), paragneisses of the Varied Group (V), orthogneiss and major faults (simplified after CGS 1:50000 map 2013).

Table3. Brief description of samples. DD - dip direction, D - dip, ox. - oxide, chl. - chlorite, s. - steep, m. - moderate, g. - gentle; 0 - absent, 1 - weak, 2 - medium, 3 - strong; exf. - exfoliation joint.

Name	Type	Granite type	Provenance	Depth (m)	Fracture		Striae		Alteration		Characteristic features
					DD	D	DD	D	Fe-ox.	Chl. / clay	
1	borehole core 4.45 cm	Lipnice	MEL-5 borehole	0.5	-	s.	-	-	2	0	single fract., weathered
2				2.7	-	s., g.	-	-	3	1	two fract. sets, weathered
3				7.5	-	m.	-	-	2	0	single fract. Fe-ox. alt. halo 4 cm
4				15.7	-	s.	-	-	2	0	dense fract. + Fe-ox. alt.
5				20.3	-	m., s.	-	-	2	0	m. and s. fract. + Fe-ox. alt.
6				21.8	-	s., g.	-	-	2	3	gouge zone, chl. + Fe-ox. alt.
7				22.1	NNE, E	s., g.	-	-	2	2	fract. proximity of the gouge zone
8				33.3	SSW	s.	-	-	1	0	fract., weak Fe-ox. alt. halo 1 cm
9				50.1	E	s., g.	-	-	0	2	dense fract., clay alt., Fe-ox. on fract.
10				67.2	ESE	s.	-	-	0	1	single barren fracture
11				**73.9**	**-**	**-**	**-**	**-**	**0**	**0**	**pristine rock reference sample**
12				104.2	NNE, E	s., s.	-	-	0	1	two fract. sets, Fe-ox. on fract.
MS09_1	outcrop block	Lipnice	Lipnice n/S.	surface	265	20	-	-	1	0	schlieren 94/12 (DD/D), exf.
MS09_2			"Ucho" quarry	surface	284	62	-	-	1	0	joint set II
MS09_3		Kouty	"Horka" quarry	surface	263	85	-	-	0	1	joint set II
MS09_4		Lipnice	"Holý vrch" quarry	surface	135, 243	73, 89	-	-	0	0	fractures set II and III
MS09_5				surface	134	86	230	5	0	1	fault
MS09_6				surface	36	53	-	-	0	1	Fe-ox. alt. halo 5-8 cm
MS10_03ab	in-situ drilling core 2.54 cm	Kouty	"Kamenná Lhota" quarry	surface	22	26	-	-	1	0	joint
MS10_03cd				surface	24	48	108	5	1	0	faulted joint
MS10_14ab			"Horka" quarry	surface	209	67	113	9	1	0	fault

3.1 Borehole samples

Borehole core sampling was done mainly with the goal to sample variously altered facies of the Lipnice granite. The MEL-5 borehole core was chosen to be sampled given that from the six boreholes drilled by RAWRA in the massif in this one the optic and acoustic borehole image logging (OBI and ABI) had been executed (Geo-Log, 2006). This allowed the orientation of the cross-cut fractures to be determined, though only for subsurface depths greater than 22 meters given by the static water level. The characteristics of the borehole (fracture density and dip, alteration) based on the executed borehole methods are shown on logs in Fig. 6. The borehole samples are named 1 to 12 according to the relative depth they were extracted from, the sample 1 being the uppermost one (1st meter) and the sample 12 being the lowermost one (104th meter). At sampled borehole levels featuring distinct fracture, core samples were usually taken at each side of the fracture and indexed A and B after the sample number in order to indicate the lower and the upper block, respectively. The setting of the samples within the borehole is documented on photographs of the core boxes in Fig. A2 and detailed images of the samples are shown in Fig. A1.

3.1.1 Sampled alteration facies

Fresh rock

The least altered granitic material featured in the sample collection is characteristic by grey colour and usually observed far from fractures. Macroscopically visible weak alteration demonstrated by light green-yellow colour of feldspar crystals can be observed in most of the fresh rock. Microscopic observations revealed feldspar crystals sericitised particularly in their cores and a minority of biotite crystals partially replaced by chlorite (Fig. 7a). On the outcrop, the walls of fractures in fresh granite were in most cases macroscopically barren, though thin coatings (< 2 mm) were observed mainly in association with fault mirrors. Fresh granite sampled from the borehole core feature either dominantly barren fracture wall or Fe-oxide fracture skin as can be seen in Fig. 8a and c.

Oxidation alteration

It can be often seen in quarries as well as in the upper 50 meters of the borehole core that fractures are flanked by orange- to red-coloured alteration halo of cm-dm thickness, the limits of which are usually subparallel to the closest fracture plane. Microscopic observation revealed that the red colour is due to cracks and grain boundaries filled by orange to brown amorphous material, probably containing Fe-(hydro-)oxides. The macro- and microscopic appearance of oxidation-altered granite is exemplified by photos of the borehole sample 3 in Fig. 7b. Fractures in oxide-altered granite usually feature fracture skins of dark orange to

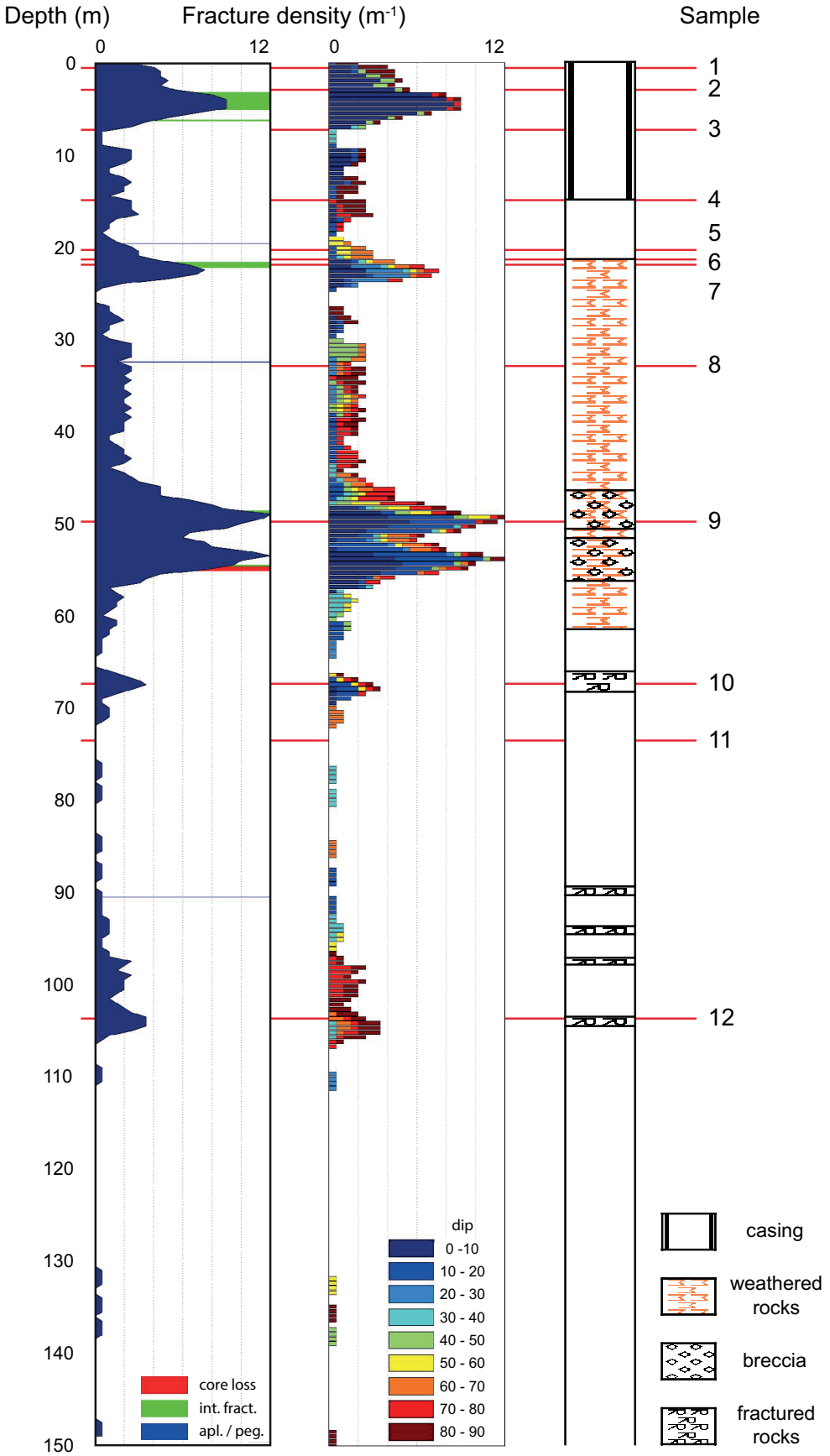

Figure 6. Fracturing and alteration logs of the borehole MEL-5 with position of the borehole core samples (logs modified after Lexa & Schulmann 2006). Left log - fracture density histogram (blue field) showing levels of core loss (red line), intensive fracturation (green line) and aplite or pegmatite veins (blue line). Central log - fracture density and fracture dip. Right log - position of casing and of levels of intensive alteration and fracturing. Int. fract. - level of intesnive fracturing, apl. - aplite, peg. - pegmatite.

brown coloured material as can be seen in Fig. 8b.

Chlorite and clay alteration

Though unseen in terrain, at two distinct levels of the borehole (22nd and 54th m) characteristic by high fracture density the rock features strong alteration giving the rock yellowish and greenish colour, respectively. Microscopic observation revealed that in both cases the alteration is associated with replacement of biotite by aggregates of fibrous phyllosilicates. Observed in polarised light the aggregates bear pale yellow to orange colour in the first case and are colourless in the second, as can be seen in Fig. 7c and d. In these two facies, the fracture skins are composed of both oxides and phyllosilicates which sometimes form alternating submillimetric layers that tend to detach along each other. The electron microscopy revealed that apart of mainly Fe- and Mn-oxides the fracture skin surfaces are covered dominantly by chlorite and clay minerals in the shallower and the deeper levels of the borehole, respectively (Fig. 8d, e).

3.1.2 Samples 1 and 2

These two samples were taken from the 1st and the 3rd meter, respectively, and represent the uppermost, highly weathered part of the granite. As indicated by their orange to red shade, both samples are altered by Fe-oxidation in their entire volume, with the highest degree of alteration being developed in the vicinity of fractures with Fe-oxide fracture skin. In sample 1 the highest degree of alteration can be seen in a diffused zone in the upper part of the sample, whereas a rather well delimited cm-thick alteration halo can be seen in its lower part. The alteration is pervasive in the sample 2, which, in addition, is macroscopically porous and features cracks of submillimetric thickness and length of up to 2 cm subparallel to the master fracture plane.

3.1.3 Samples 3, 5 and 8

These three samples were taken from the 8th, the 21st and the 34th meter, respectively, and represent rather massive, macroscopically non porous granite crosscut by distinct fractures with Fe-oxide fracture skins (Fig. 8b) and accompanied by Fe-oxidation alteration halo. In case of samples 3 and 8 the limits of the halo are at both sides sharp and subparallel to the fracture. In case of sample 5 the moderately dipping fracture is surrounded by a cm thick intensively altered zone with densely spaced cracks subparallel to the fracture. A steeply dipping cohesive fracture visible in both the parts of the sample 5 features a mm-thick halo of weak alteration in the upper (B) part and a several cm-thick halo of strong alteration in the lower (A) part.

3.1.4 Sample 4

The sample was taken from the 16th meter and represents a zone of subparallel densely spaced (cm^{-1}) steeply dipping fractures. Fe-oxide alteration is pervasive in the rock matrix and Fe-oxides are also featured by the fracture skins.

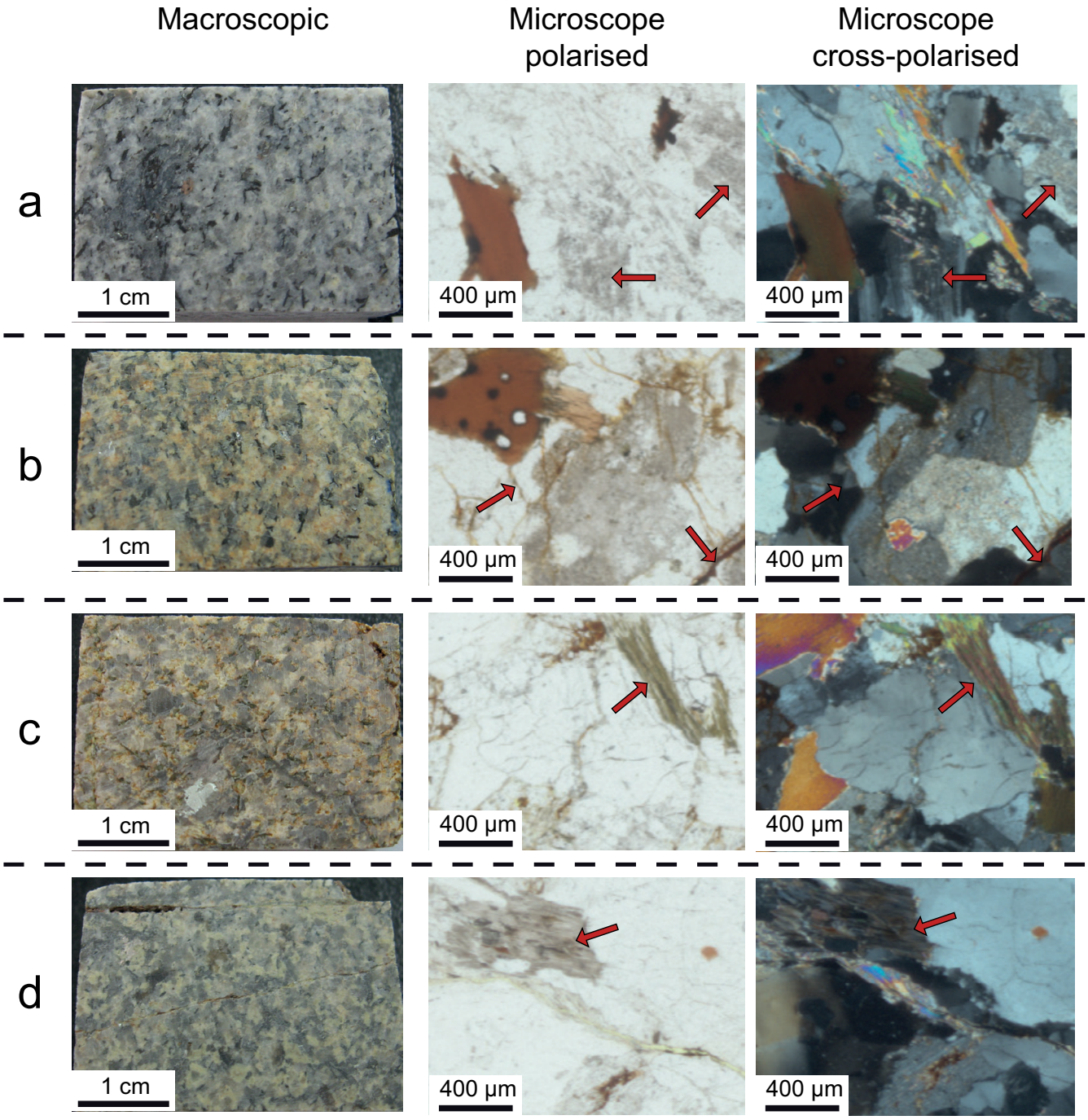

Figure 7. Comparison of sampled granite alteration facies: a - fresh rock: sericitisation of feldspars (sample 11), b - Fe-oxidation: fill of cracks and grain boundaries (sample 3), c - chlorite replacing biotite (sample 7), d - clay minerals replacing biotite (sample 9).

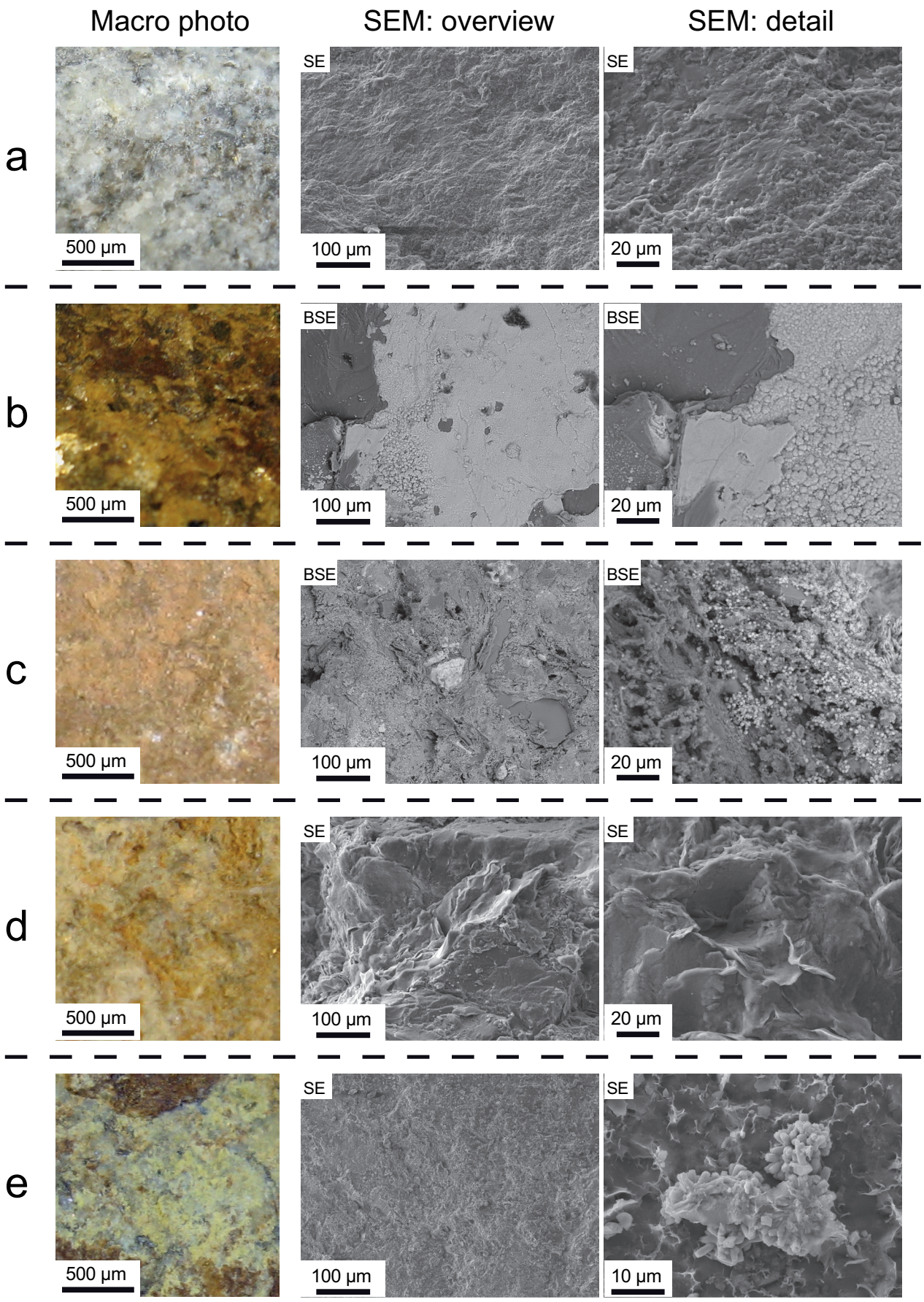

Figure 8. Fracture surfaces: a - barren fracture (sample 10), b - Fe-oxide (sample 5), c - Fe-oxide + heavy minerals (sample 12), d - chlorite + Fe-oxide (sample 7), e - smectite + chlorite + Fe-oxide + heavy meinrals (sample 9). The latter features an aggregate of monazite in the center (white) and veil-shaped smectite in the surrounding. SE - secondary electrons detector, BSE - back-scattered electrons detector.

3.1.5 Samples 6 and 7

These two samples represent highly deformed and altered rock at the level of the 22nd meter. According to the ABI, which begins several dm below the sample level, the very adjacent zone of the borehole is characterised by intersection of multiple fractures of various dip directions ranging from N to E and of various, gentle to steep dips. It is difficult to distinguish unique fractures on the core due to their coalescence and due to the samples friability, nevertheless several gently dipping fractures with spacing of two to ten cm can be seen to crosscut the sample 7 and limit the sample 6. In addition, a clearly visible, tortuous and steeply dipping fracture intersects the sample 7. Both oxidation and chlorite alteration affects this zone. Although the two kinds of alteration affect the majority of the samples volume, it can be seen on sample 7 that the gently dipping fractures feature predominantly Fe-oxide fracture skins, whereas the steeply dipping fracture features fracture skin formed dominantly by chlorite (Fig. 8d).

3.1.6 Sample 9

The sample was taken from the 51st meter and represents a zone of high fracture density with subparallel steeply dipping fractures spaced one to several cm and gently dipping fractures spaced two to ten cm. The rock matrix features strongly sericitised feldspars and bleached biotites and the facture skins feature Fe-oxides and clay minerals (Fig. 8e).

3.1.7 Sample 10, 11 and 12

These three samples represent rather fresh granite from the lower levels of the borehole (68th, 74th and 105th meter, respectively). Commonly for the three samples, only weak alteration affects the rock matrix as indicated by pale greenish-yellowish colour of feldspars. Except fractures not represented on the ABI and thus probably due to borehole drilling, the sample 10 features one steeply dipping barren fracture (Fig. 8a) with no alteration halo. Sample 11 was taken as a reference sample of non-fractured granite from a zone of low fracture density. According to the ABI, the closest fracture was in a distance of three meters at the 71st meter. Sample 12 represents a borehole level with densely spaced (10 to 20 m^{-1}) steep fractures with NNE and E dip directions and featuring Fe-oxide mm-thick and homogeneous fracture skins (Fig. 8c).

3.2 Quarry samples

The quarry samples were taken with the main goal to characterise the influence of large-scale (metric to decametric) fractures on the rock in their very proximity (< 10 cm).

Contrarily to the borehole core it was possible to sample rather voluminous blocks of massive rock and consequently to prepare a complete set of specimens for all the intended petrophysical methods. Six block samples of decimetric dimensions directly limited by a fracture plane were taken in oriented manner with respect to fractures belonging to different fracture sets and named MS09_1 to MS09_6. Supplementary quarry samples MS10_03 and MS10_14 represent 2.54 cm cores drilled in situ perpendicular to fracture planes by a portable drilling machine.

3.2.1 Sample MS09_1

This sample comes from the Lipnice granite outcropping in the town Lipnice nad Sázavou. The particularity of the outcrop consists in remarkably developed magmatic structure (schlieren) represented by alternation of several mm thick quartz- and mica-rich bands exfoliation fractures and. On the sample scale the schlieren are folded by asymmetric centimetric folds with the long limbs dipping gently to the E, N-S striking steep short limbs and N-S oriented subhorizontal fold axes. The sample was extracted from massive rock delimited by two exfoliation fractures spaced 12 cm and gently dipping to the W. In addition to the commonly executed methods, this sample has been subject to analysis of orientation of microstructures and of anisotropy of magnetic susceptibility. Based on the multidirectional V_p measurements and on the two additional techniques the detailed study gave rise to a peer-reviewed article presented in the chapter IV.

3.2.2 Samples MS09_2, _4, _5 and _6

These samples together with MS09_1 represent the Lipnice granite adjacent to the commonly developed fracture sets in the MM. Differently to the MS09_1 taken near post-uplift gently dipping exfoliation joint, these samples were taken with respect to steep fractures due to pre-uplift brittle deformation of the massif. The samples MS09_2 and MS09_5 are both related to fractures belonging to the fracture set II (orientations 284/62 and 134/86, respectively). In case of MS09_2 the fracture was a joint with no signs of displacement on the fracture plane whereas MS09_5 represents rock near a fault with clearly visible subhorizontal striations oriented 230/5. The sample MS09_4 was a block limited by two fractures with one of them belonging to the set III (243/89) and the other belonging to the set II (135/73). Finally, the sample MS09_6 was taken in proximity of a fracture of the set I (36/53), which, in addition, featured oxide alteration halo on both sides. The alteration zone was distinct from the fresh rock by orange to red colour and reached to a distance of several cm.

3.2.3 Sample MS09_3

This sample represents the Kouty granite exposed in an active quarry "Horka" near the town Dolní Březinka at the north extremity of the MM. The sample was extracted from between two subparallel fractures oriented 263/85 spaced ~ 10 cm and its main difference with respect to the other samples is its higher proportion of quartz.

3.2.4 Samples MS10_03 and MS10_14

These samples were obtained by a portable drilling machine via 2.54 cm coring perpendicular to fracture planes. Three fractures belonging to the set I were sampled in this manner. Samples MS10_03A+B and C+D represent respectively a fault and a joint in the "Kamenná Lhota" quarry in the east extremity of the MM, whereas MS10_14A+B represent a fault exposed in the "Horka" quarry.

3.3 Specimens for the experiments

Each of the applied petrophysical methods required a certain way of specimen preparation and therefore many specimens with different shape and volume were derived from each of the parent sample. This resulted in petrophysical characterisation of nearly 200 different parts of the sampled material. Consequently, the denomination of specimens is rather complex and will be precisely defined as a part of the sample description. On the other hand, two general rules are systematically taken into account for the final specimen denomination. First, the name of the parent sample is always kept as the root of the specimen name. Second, in case of measurement of a vector physical property (permeability, P-wave velocity, thermal conductivity), usually three oriented specimens were prepared with respect to the reference fracture plane and were noted by X, Y and Z letters. In case of the block samples the letters designate the geographic directions of the fracture plane strike and dip, and the direction perpendicular to the XY plane, respectively. In case of the borehole samples, X designates the direction of intersection of the fracture plane with the longitudinal section of the core, Y the direction of intersection of the fracture plane with the transversal section of the core and Z the direction perpendicular to the XY plane, respectively. The X, Y and Z letters are used exclusively for the purpose of direction indication. In case of MS09_4, the principal directions X, Y and Z were related to the fracture of the set III.

3.3.1 Optical scanning profiles

On borehole samples the TC has been measured usually (samples 1, 2, 3, 4, 5,

7, 8, 11, 12) along two or three profiles parallel to the core axis and differing in position on the core surface by 90°. Sample 6 was too small and irregular to provide reliable TC measurement by the used technique. On sample 9 only one profile was measured due to multiple fractures and consequent lack of continuous sample surface. Particular case is represented by sample 10 represented by 37 cm long part of the core which is crosscut by a geologic fracture oriented at low angle to the core axis and by several drilling-related fractures oriented at high angle to the core axis. This implied difficulties for placement of the sample on the working table and therefore the sample parts were reassembled together and fixed by a scotch tape leaving along-core spaces for continuous scanning profiles. The position of the profiles can be seen in Fig. A1.

On the quarry samples the TC was measured along the reference fracture-related X, Y and Z directions. On sample MS09_01 the TC was also measured along directions defined by the folded schlieren. The direction SX corresponding to the schlieren fold axis was subparallel to the fracture-related X direction due to the mutual orientation of the fracture and of the schlieren folds. Therefore the values representing the X and SX directions are considered to be equivalent. The SY direction was parallel to the schlieren fold long limb and perpendicular to the schlieren fold axis. Two scanning lines of SY direction were measured, with one of them showing macroscopic lack of biotite (SY1) and the other (SY2) showing abundance of biotite. Finally, the SZ direction was perpendicular to the schlieren fold long limb. Furthermore, a TC map of the sample Y-Z (SY-SZ) section was acquired by juxtaposition of scanning lines parallel to the Y direction executed each mm in the Z direction. In case of MS09_6 two sets of TC scanning lines were measured, with one of them on surface of the fresh part (MS09_6X, _6Y, _6Z) and the other on the surface of the altered part (MS09_6X_A, _6Y_A, _6Z_A). Samples MS10_03 and MS10_14 TC were measured along two scanning lines on the opposite sides of the cores.

3.3.2 Plugs for V_p and permeability measurements

For the majority of the borehole samples (1, 2, 4, 7, 8, 9, 10 and 12) three plugs per sample were drilled along the principal directions of the XYZ reference fracture-related system (Fig. A1). In case of sample 4 one of the plugs split along fracture during drilling and thus only two plugs were available for measurements (4_F_X, 4_F_Z). In case of sample 3, two plugs were drilled from the fracture-related alteration zone (3B_F_Y and 3B_F_Z) and one from the fresh rock (3B_A_Y). From sample 5, two sets of three mutually perpendicular plugs related to the sealed, steeply dipping fracture were drilled in both the fresh (upper, 5B) and the altered (lower, 5A) part of the sample. Due to splitting along fracture of one

of the plugs during drilling only five of them were available for measurements (5B_FI_Y, 5B_FI_Z, 5A_F_X, 5A_F_Y, 5A_F_Z). The sample 6 was too friable to prepare a plug. From sample 10 two additional plugs were drilled. In case of non-fractured sample 11 two plugs along mutually perpendicular directions were drilled.

The plugs from the quarry samples were drilled along three principal directions related to the reference fractures. From sample MS09_01 plugs were also drilled along directions defined by the folded schlieren (see the previous section on TC profiles) resulting in two more plugs (SY and SZ) for this sample. From sample MS09_06 two sets of three plugs were drilled, with one of them from the fresh rock (MS09_6X, _6Y, _6Z) and the other from the altered rock (MS09_6_AX, _6_AY, _6_AZ).

3.3.3 Spheres for multidirectional V_P measurements

One oriented sphere was prepared from each quarry sample except sample MS09_4 where two spheres were prepared with one of them representing the very proximity of the fracture of set II (MS09_4II) and the other of the fracture of set III (MS09_4III). In case of sample MS09_06 the sphere was prepared from the fresh part of the sample.

3.3.4 Mercury porosimetry specimens

During preparation of mercury porosimetry specimens from the borehole core special attention was paid to include as much of the rock variety as possible. Apart of the parent sample name representing a certain borehole level, three more criteria and sets of features were adopted to classify the differences between the specimens (specimens with unique names):

- matrix alteration type
  - fresh
  - Fe-oxide
  - chlorite
  - clay
- character of fracture skin
  - no skin (no fracture)
  - barren
  - Fe-oxide skin
  - chlorite skin
  - chlorite + Fe-oxide skin
  - clay + Fe-oxide skin

- presence of cracks visible by unaided eye
  - o no crack
  - o single crack
  - o many cracks

The number of specimens per sample is uneven and roughly proportional to the sample inhomogeneity, varying from one for the intact, fresh granite, to seven for the most fractured and/or altered samples. Photographs and the classification attributes of all the specimens are shown in Fig. A3. Due to its high friability and small size, only one specimen for mercury porosimetry was prepared from the sample 6.

One specimen was prepared from the fresh quarry samples (MS09_01 to MS09_05), whereas in case of sample MS09_06 one specimen was prepared from the fresh part and one from the ~ 5 cm thick Fe-oxide alteration halo developed around the reference fracture. These specimens have been subject to a preliminary set of porosimetry analyses aiming to quantify only the basic physical properties (porosity, density) of these rather homogeneous samples.

4. Results

4.1 Thermal conductivity measurements

The TC data were acquired on totality of ~ 60 scans which represent ~ 10 m of TC profiles with the TC value measured for each mm. From these data the mean values were calculated from all TC profiles on a given sample taking into account the necessary 1 cm cut-off of the extremities of the profiles due to border effect bias (see section 2.1 for details).

The mean TC of the measured samples ranges from 2.0 to 2.9 W m^{-1} K^{-1} (Tab. 4). The extremely low value of 2.0 W m^{-1} K^{-1} is featured by the strongly weathered and intensively fractured sample 2 showing also the highest inhomogeneity factor of 0.45. Low values from 2.3 to 2.5 W m^{-1} K^{-1} are featured by intermediately weathered or fractured samples (1, MS09_01, MS10_03, MS10_14). A similar mean value is featured by the densely fractured and pervasively Fe-oxide altered sample 4 showing also high TC variability along the profiles as documented by the high inhomogeneity factor of 0.38. Most of the measured values are in the range between 2.6 and 2.9 W m^{-1} K^{-1} with the fresh or little altered and fractured granite TC values (samples 10, 11, 12) clustering around 2.7 W m^{-1} K^{-1}. However, a similar value was yielded also by the strongly fractured and Fe-oxide-chlorite altered sample 7. The highest values are featured by quartz-rich or pervasively Fe-oxide altered quarry samples

Table 4. Thermal conductivity (W m^{-1} K^{-1}) of measured samples. Shown is the average (avg), minimal (min) and maximal (max) measured thermal conductivity and the inhomogeneity factor (IF) calculated as difference of the exteme values divided by the average value.

Sample	AVG	MIN	MAX	IF
1	2.53	2.40	2.75	0.14
2	1.97	1.37	2.25	0.45
3	2.62	2.39	2.97	0.22
3_A	2.68	2.51	2.84	0.13
4	2.51	1.86	2.81	0.38
5	2.64	2.31	2.88	0.22
5A_A	2.74	2.60	2.87	0.10
7	2.69	2.42	2.90	0.18
8	2.74	2.53	3.11	0.21
9	2.89	2.75	2.98	0.08
10	2.73	2.51	2.97	0.17
11	2.68	2.53	2.83	0.11
12	2.72	2.15	3.00	0.31
MS09_1	2.41	2.21	2.68	0.11
MS09_2	2.72	2.54	2.87	0.10
MS09_3	2.86	2.58	3.07	0.14
MS09_4	2.76	2.61	3.06	0.13
MS09_5	2.88	2.67	3.07	0.09
MS09_6	2.76	2.54	3.01	0.13
MS09_6_A	2.85	2.66	2.98	0.06
MS10_03AB	2.47	2.25	2.68	0.18
MS10_03CD	2.42	2.12	2.69	0.24
MS10_14AB	2.30	2.09	2.51	0.18

(MS09_03, MS09_6_A) and by the clay and oxide-altered and densely fractured borehole sample 9.

The comparison of TC of the fresh and Fe-oxide-altered parts (_A) of the samples 3, 5 and MS09_06 shows that the alteration is systematically related to TC higher by several per cent. The intra-sample variation of mean profile TC value was < 5 %. However, abrupt TC variations of 10 - 40 per cent per cm have been observed within scans traversing cohesive fractures or fresh-altered rock transitions. Similar TC increase progressively distributed along 10 to 20 cm from fracture plane towards the pristine rock was measured on the in-situ drilled cores. The mentioned TC variations and the related phenomena are documented

by TC profiles juxtaposed to photographs of the scans in Fig. 9. The measurement along profile featuring both fresh and Fe-oxide altered granite (Fig. 9a) shows clearly higher TC values for the altered part (2.9 W m^{-1} K^{-1}) as compared to the fresh segment (2.7 W m^{-1} K^{-1}). The measurement along profile on a core sample containing cohesive fracture oriented oblique to the core axis reveals fracture-related TC lower by about 20 % in the vicinity (cm) of the fracture than within the massive rock(Fig. 9b). Comparison of measurements along profiles perpendicular to different fracture types (joint, fault) shows that TC increases with distance from fracture for all the compared samples (Fig. 9c). The joint-related sample (MS10_03A+B) has higher TC near the fracture and lower TC increase with the distance from the fracture than its faulted joint-related analogue (MS10_03C+D) though both the samples show similar and rather constant TC at distance of 10 cm or higher from the fracture. The third compared sample MS10_14A+B drilled perpendicular to a fault of the same fracture set (I) as the two precedent, but on another locality, shows the lowest TC and similar TC increase with distance from the fracture as the faulted joint-related sample. However, in this case the TC continues to increase on the first 14 cm or possibly on the entire length of the TC profile (16 cm).

4.2 V_P measurements

4.2.1 V_P measurements on plugs at ambient pressure

The results of V_P measurements on total of 58 plugs are shown in Tab.5. The measured values range from 1.9 to 5.1 km s^{-1} with about a half of the values in the range from 4.0 to 4.6 km s^{-1}. The lowest values of 1.9 to 2.3 km s^{-1} have been measured on intensively altered and fractured borehole sample 2 with the minimum V_P perpendicular to the reference fracture plane. Low values from 2.6 to 3.4 km s^{-1} were measured on the schlieren-bearing quarry sample MS09_1 with the lowest V_P perpendicular to the fracture and to the schlieren and the highest values parallel to them. Low to intermediate values from 3.4 to 3.7 km s^{-1} were measured on weathered sample 1 and perpendicular to densely spaced fractures of Fe-oxide altered sample 4. The fractured and chlorite-altered sample 7 features values from 3.7 to 4.3 km s^{-1} with V_P perpendicular to the reference fracture higher than along it. Values from 4.0 to 4.7 km s^{-1} are featured by fresh fractured granite (quarry samples, borehole samples 3B_A and 5B), by the clay altered sample 9 and also by plugs of Fe-oxide-alteration halo either drilled perpendicular to the fracture plane in case of single fracture (3B_F_Z) or along the fracture plane in case of densely spaced fractures (4_F_X). The reference of pristine granite (sample 11) shows values from 4.4 to 4.6 km s^{-1} and

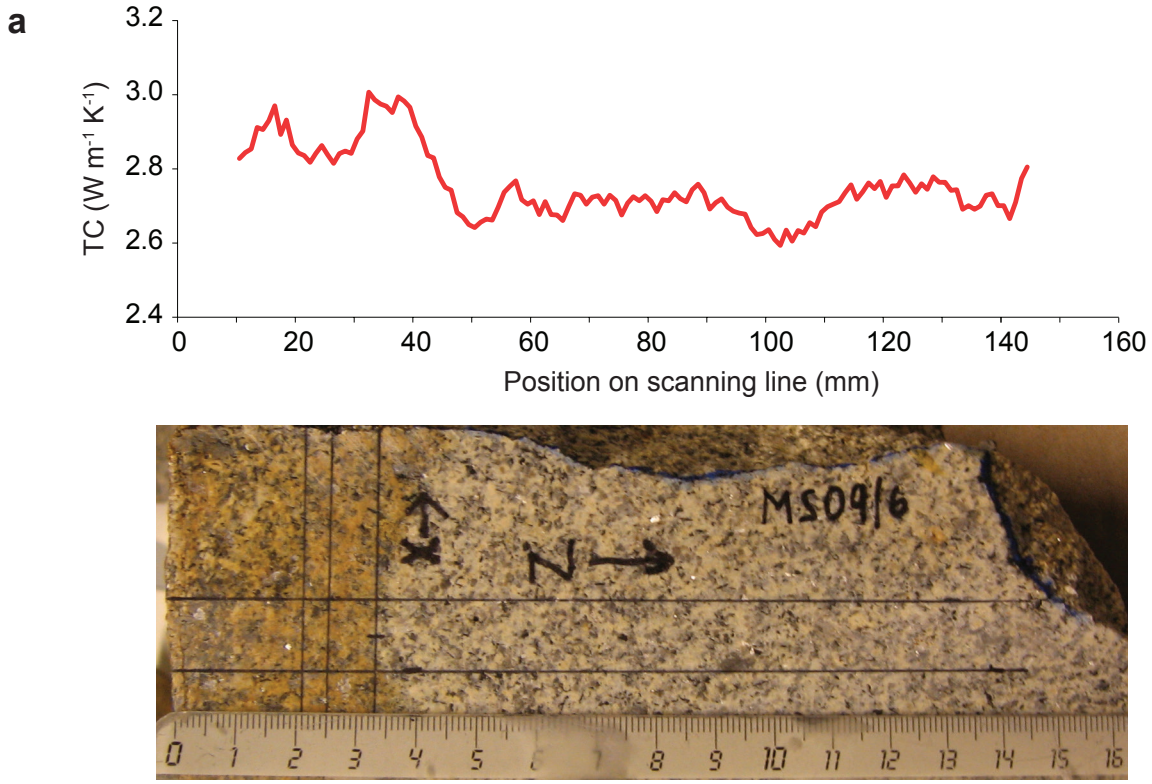

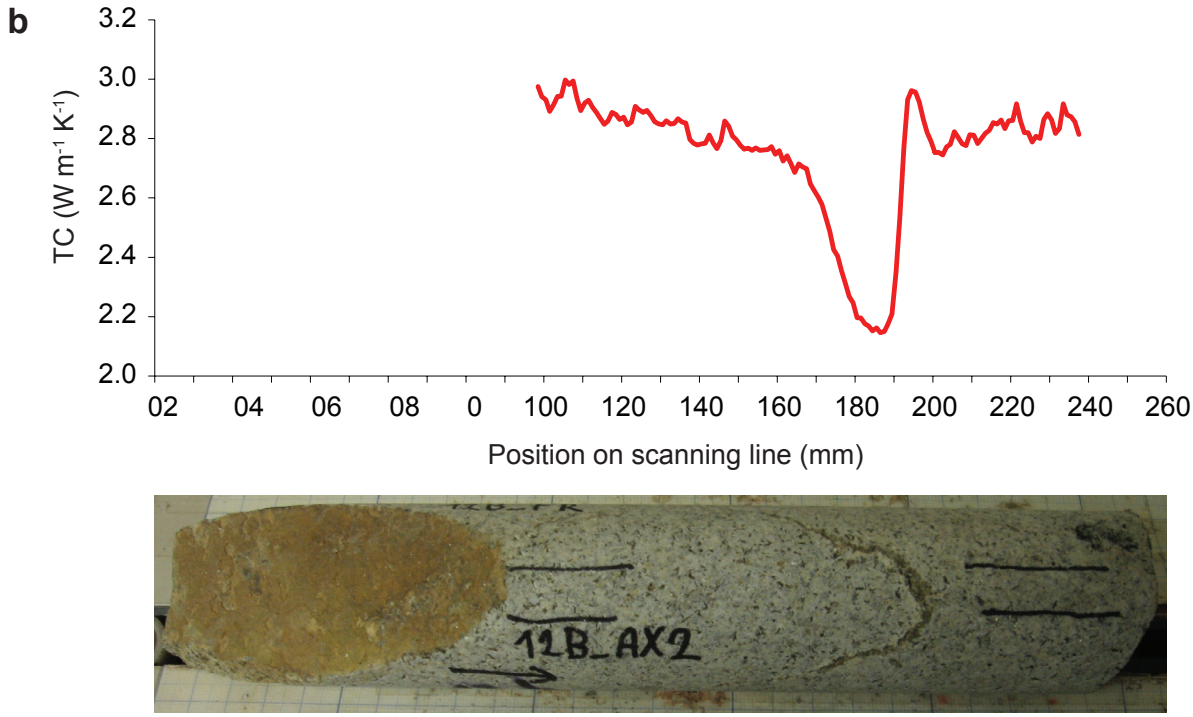

Figure 9 *(continued on the next page)*. Thermal conductivity (TC) variation due to (a) Fe-oxide alteration and due to (b) fracture. TC profiles juxtaposed to photographs of the scanned surface along (a) the Z direction of quarry sample MS09_06 and along (b) the AX2 profile on borehole sample 12B. The first and the last cm of the TC profiles are cut due to boundary effects.

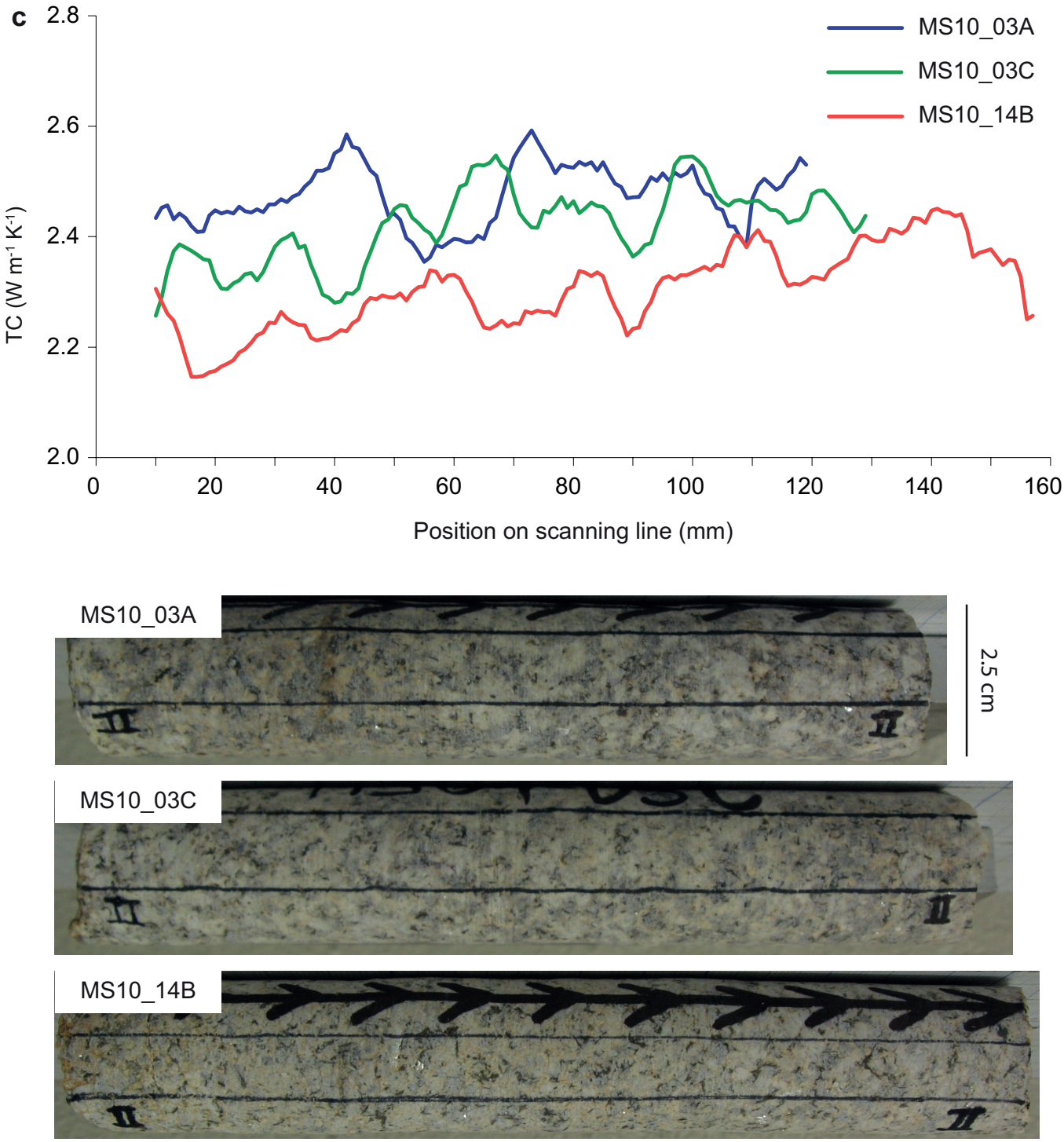

Figure 9 *(continued)*. (c) Thermal conductivity (TC) variation due to distance from fracture. Thermal conductivity profiles juxtaposed to photographs of scanned surfaces on quarry in-situ cored samples. Each of the TC profiles displayed in the chart is averaged from four TC profiles (2 profiles x 2 cores); one profile for each surface is documented by a photograph as an example. All the cores were drilled perpendicular to the fracture plane (left end) towards the massive rock (to the right). The first and the last cm of the scans are cut due to boundary effects.

similar values are also featured by the two other deep borehole samples 10 and 12. The highest values from 4.6 to 5.1 km s^{-1} are featured mostly by the Fe-oxide altered parts of the samples. The Fe-oxide altered parts show systematically higher values compared to its fresh analogues, the best example of which is presented by the sample MS09_6 where the mean V_p for the fresh and the altered part is 4.1 and 4.8 km s^{-1}, respectively.

4.2.2 V_p measurements on spheres at high confining pressure

The basic results of measurements on 7 spherical samples are presented by charts showing evolution of mean V_p and anisotropy degree k (Babuška 1968) with confining pressure during pressurization in Fig. 10. The V_p distributions at confining pressures from 0.1 to 400 MPa and calculated differences between the pressure steps are plotted on stereograms in Fig. A4 for samples MS09_2 to MS09_6, for the results of sample MS09_1 see chapter IV. Taking into account all the measurements, at ambient pressure the V_p ranges from 2.8 to 5.0 km s^{-1}, with the lowest values (2.8 to 3.6 km s^{-1}) featured by the schlieren-bearing sample MS09_1 and the highest ones (4.4 to 5.0 km s^{-1}) by joint-related samples MS09_2 and MS09_6. Low values (3.8 to 4.4 km s^{-1}) are featured by both the samples MS09_4 taken from block limited by fractures of two sets (II and III). Intermediate values from 4.0 to 4.8 km s^{-1} are featured by quartz-rich sample MS09_3 and by fault-related sample MS09_5. At the highest confining pressure (400 MPa) the V_p ranges from 6.0 to 6.4 km s^{-1}, with the lowest values featured by sample MS09_1 and the highest ones by samples MS09_3 and MS09_6a. The mean V_p of all the samples increases in the entire measured range of confinement (Fig. 10). Except sample MS09_1 featuring abnormally low values over the whole range, above 100 MPa the mean V_p of all the samples converges to a narrow interval of 0.3 km s^{-1}. At lower confinement the main difference between the samples is higher increase of mean V_p between 0.1 and 10 MPa featured by samples MS09_1 and MS09_3.

The degree of anisotropy for confinement 0.1 to 100 MPa correlates negatively with mean V_p and decreases from 24 % for sample MS09_1 and from between 11 and 18 % for the other samples at ambient pressure to less than 6 % for all the samples at pressures 100 MPa and higher. The observed shape of anisotropy is orthorhombic (MS09_5) or transversely isotropic (MS09_1, MS09_4 ii and iii, MS09_6) or transitional between the two (MS09_2, MS09_3). The anisotropy shape stays the same for all the samples during pressurisation over the entire pressure range. The subtractions between high (100, 200, 400 MPa) and ambient pressure show that the anisotropies of V_p increments with pressure match the V_p anisotropies at the ambient pressure. The directions of high increments

Table 5. Results of P-wave velocity and permeability measurements for the borehole samples (left) and for the quarry samples (right). Plug - name of the specimen derived from the sample, V_P - P-wave velocity, k - intrinsic permeability, CC - correlation coefficient of the permeability measurement.

Plug	V_P (km s^{-1})	k (m^2)	CC ( )	Plug	V_P (km s^{-1})	k (m^2)	CC ( )
1A_F_X	3.4	8.40E-18	0.97	MS09_1X	3.4	6.37E-17	0.99
1A_F_Y	3.6	3.09E-18	0.96	MS09_1Y	3.1	6.17E-17	0.98
1A_F_Z	3.7	1.47E-17	0.96	MS09_1Z	2.6	2.27E-17	0.99
2_F_X	2.3	9.41E-16	0.98	MS09_1SY	3.4	5.55E-17	0.99
2_F_Y	2.6	9.43E-16	0.97	MS09_1SZ	2.8	2.64E-17	0.99
2_F_Z	1.9	3.09E-16	0.98	MS09_2X	4.4	1.49E-17	0.98
3B_A_Y	4.8	8.46E-18	0.95	MS09_2Y	4.0	7.59E-18	1.00
3B_F_Y	5.1	< E-18	x	MS09_2Z	4.5	1.80E-17	0.96
3B_F_Z	4.5	< E-18	x	MS09_3X	4.3	7.11E-18	1.00
4_F_X	4.2	5.65E-18	0.94	MS09_3Y	4.0	< E-18	x
4_F_Z	3.7	5.24E-18	0.95	MS09_3Z	4.4	6.88E-18	0.99
5A_F_X	4.8	< E-18	x	MS09_4X	4.1	7.99E-18	0.94
5A_F_Y	4.9	< E-18	x	MS09_4Y	4.0	7.48E-18	0.97
5A_F_Z	4.5	< E-18	x	MS09_4Z	4.4	9.52E-18	0.99
5B_FI_Y	4.4	2.16E-16	0.99	MS09_5X	4.4	7.41E-18	1.00
5B_FI_Z	4.2	1.14E-17	1.00	MS09_5Y	4.0	5.12E-18	0.98
7_F_X	3.9	2.13E-17	0.99	MS09_5Z	4.6	6.87E-18	0.95
7_F_Y	3.7	2.13E-17	1.00	MS09_6X	4.0	2.06E-17	0.99
7_F_Z	4.3	2.19E-17	0.97	MS09_6Y	4.1	1.70E-17	0.96
8A_F_Y	4.6	< E-18	x	MS09_6Z	4.1	1.04E-17	0.96
8A_F_Z	4.4	< E-18	x	MS09_6_AX	4.8	2.88E-18	0.95
8B_F_X	4.9	< E-18	x	MS09_6_AY	4.9	3.16E-18	0.94
9A_F_X	4.3	< E-18	x	MS09_6_AZ	4.6	2.42E-18	0.97
9A_F_Y	4.4	7.06E-18	0.96				
9A_F_Z	4.7	3.52E-18	0.98				
10A_F_X	5.0	< E-18	x				
10A_F_Y	4.6	< E-18	x				
10A_F_Z	4.5	< E-18	x				
10B_F_Z	4.6	< E-18	x				
10C_F_Y	4.7	< E-18	x				
11_A_X	4.4	< E-18	x				
11_A_Y	4.6	< E-18	x				
12B_F_X	4.9	2.70E-18	0.95				
12B_F_Y	4.5	1.92E-17	0.96				
12B_F_Z	4.6	< E-18	x				

correspond to directions of low V_P and vice versa for low increments and high V_P. Except sample MS09_1, the orientations of the maximum and minimum V_P show no systematic relation to orientations of the reference fractures. Directions of maximum V_P oriented subperpendicular to the fracture plane and of minima at low angles to it are featured by samples MS09_2, MS09_3 and MS09_4 (ii and iii), whereas directions of both the extreme V_P are oriented at low angles to the fracture plane for samples MS09_5 and MS09_6.

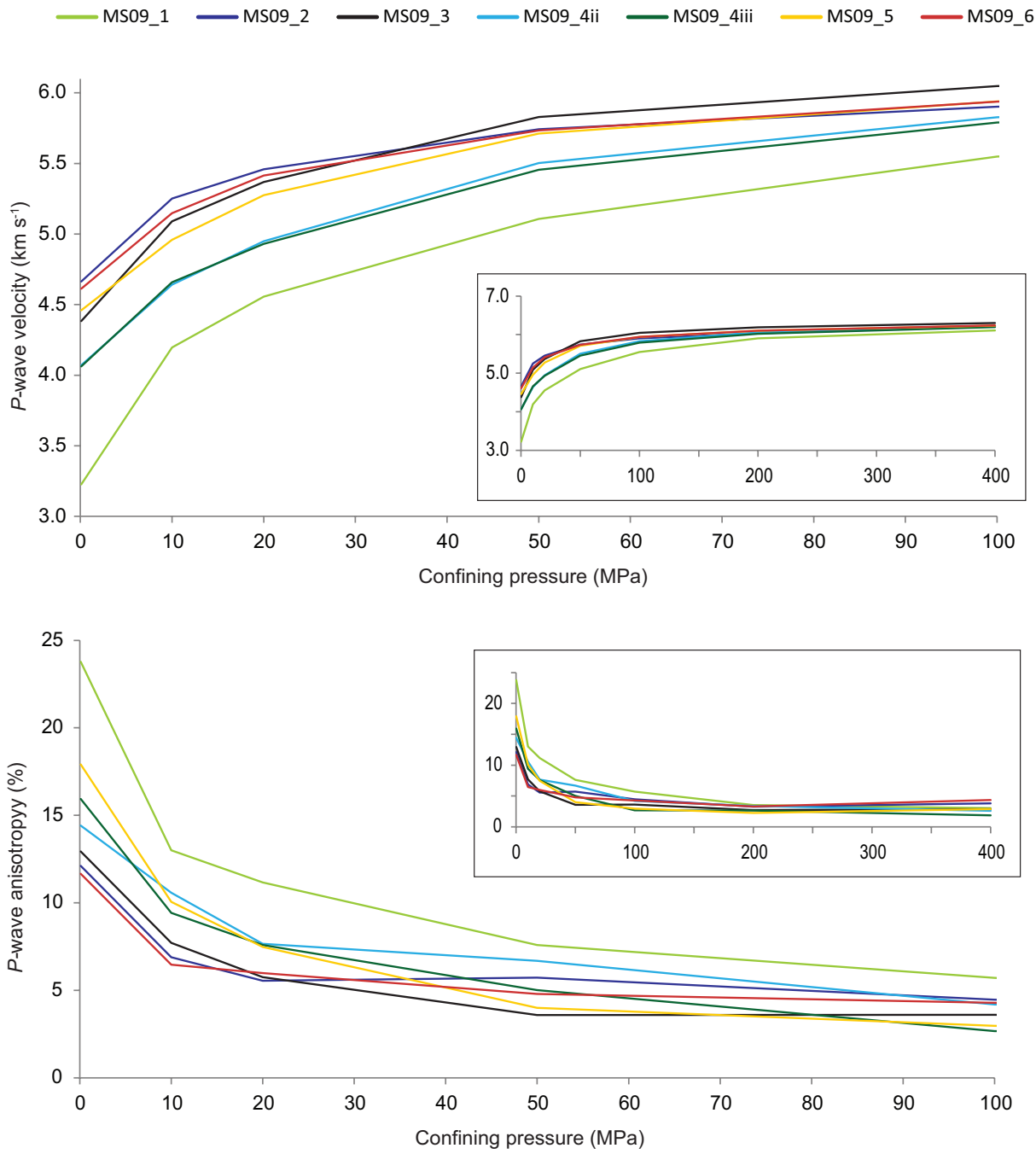

Figure 10. P-wave velocity average (top) and P-wave velocity anisotropy (bottom) during pressurisation as a function of confining pressure. The principal charts show results for confining pressure range 0.1 to 100 MPa for better resolution and the insets show results for the entire range 0.1 to 400 MPa. The legend (top of the figure) is common for all the charts.

4.3 Permeability measurements

The results of permeability measurements executed on the plugs used for the V_P measurements are shown in Tab. 5. The measured permeability ranges from 3 x 10^{-18} to 9 x 10^{-16} m^2. Lower permeabilities were not quantifiable by the used setup and the results of such measurements are denoted by value < 10^{-18} m^2.

The lowest values (< 10^{-18} m^2) are featured by the reference sample of pristine granite (sample 11), by fresh or weakly altered fractured samples 10 and 12, by massive Fe-oxide-altered parts of the samples 3 and 5 and by one of the plugs of sample 9, which represents zone of densely spaced fractures associated with clay-alteration facies. The values on the order of 10^{-18} m^2 were measured on the weakly weathered sample 1, on sample 4 representing zone of densely spaced fractures associated with pervasive Fe-oxide alteration, on the two other plugs of sample 9 and on one of the plugs of sample 12. Values on the order of 10^{-18} to 10^{-17} m^2 are common for the quarry samples. The highest values are featured by the schlieren-bearing sample MS09_1 (4 x 10^{-17} m^2) and the fresh part of the sample MS09_6 (2 x 10^{-17} m^2). The lowest value is featured by the Fe-oxide altered part of the latter sample (3 x 10^{-18} m^2). The highest values within the borehole samples are featured by the intensively fractured and altered samples 7 (2 x 10^{-17} m^2) and 2 (7 x 10^{-16} m^2), the latter being the most permeable sample of the collection. In case the plug drilled from otherwise massive fresh rock contained a macroscopic fissure subparallel to the plug axis (1A_F_Z, 3B_A_Y, 5B_FI_Y, 9A_F_Y, 12B_F_Y), the yielded permeability was by one order of magnitude or more higher than for its analogue without fissure.

Excluding the plugs containing fissure and samples with too low permeabilities, the permeability anisotropy of the samples can be considered. Low or no anisotropy is featured by borehole samples 4 and 7 and by the quarry samples except MS09_1. The borehole samples 2, 9 and 12 show two to three times higher values along directions parallel to the reference fracture (X, Y) than perpendicular to it (Z). Similar anisotropy is featured by the schlieren-bearing quarry sample MS09_1 with the highest values along directions parallel to the schlieren and/or to the fracture and the lowest values along directions perpendicular to them.

4.4 Mercury porosimetry

The basic results of porosimetric measurements are summarized in Tab. 6. In the following, the specimens are characterized by pore size distribution and four scalars: total connected porosity, median pore throat diameter, trapped to total porosity ratio and skeletal density (see section 2.4 for details). The sample 6 analysis was performed in a preliminary set

Table 6 *(continued on the next page)*. Results of mercury porosimetry analyses calculated for microporosity only (pore throat diameters 5 nm to 6 µm, this page) and for the whole measured range (pore throat diameters 5 nm to 300 µm, next page). Φ_{total} - total connected porosity, MPTD - median pore throat diameter calculated from volume. TTR - trapped to total porosity ratio, BD - bulk density, SD - skeletal density, Φ_{trap} - trapped porosity, Φ_{free} - free porosity, ox. - oxide, chl. - chlorite, 1 - present, 0 - absent.

Subsample	Φ_{total} (%)	MPTD (µm)	TTR (%)	BD (g cm^{-3})	SD (g cm^{-3})	Φ_{trap} (%)	Φ_{free} (%)	Matrix alteration			Fracture skin		
								Fe-ox.	Chl.	Clay	Fe-ox.	Chl.	Clay
1_1	1.64	0.36	74	2.580	2.623	1.21	0.43	1	0	0	1	0	0
1_2	1.47	0.52	78	2.593	2.632	1.15	0.33	1	0	0	0	0	0
1_3	1.40	0.44	72	2.593	2.630	1.01	0.39	0	0	0	0	0	0
2_2	2.94	0.72	65	2.524	2.601	1.92	1.02	1	0	0	0	0	0
3A_1	0.88	0.39	74	2.617	2.640	0.65	0.23	0	0	0	0	0	0
3A_2	0.66	0.20	79	2.631	2.648	0.52	0.14	1	0	0	0	0	0
3B_1	0.79	0.32	75	2.619	2.640	0.59	0.20	0	0	0	0	0	0
3B_2	0.52	0.17	89	2.622	2.636	0.47	0.06	1	0	0	0	0	0
4_1	0.99	0.18	81	2.589	2.615	0.80	0.19	1	0	0	1	0	0
4_2	1.08	0.27	79	2.599	2.627	0.85	0.23	1	0	0	0	0	0
5A_1	1.00	0.27	69	2.606	2.632	0.69	0.30	0	0	0	0	0	0
5A_7	0.64	0.17	81	2.612	2.628	0.52	0.12	1	0	0	0	0	0
7_1	3.80	0.62	77	2.529	2.629	2.91	0.89	1	1	0	0	1	0
7_3	2.52	0.36	87	2.535	2.600	2.21	0.32	1	1	0	0	0	0
7_5	2.50	0.30	76	2.542	2.607	1.90	0.60	1	1	0	1	0	0
7_7	3.13	0.38	76	2.541	2.623	2.36	0.77	1	1	0	1	1	0
8B_1	0.52	0.20	78	2.642	2.656	0.41	0.12	1	0	0	1	0	0
8B_3	0.49	0.31	82	2.636	2.649	0.40	0.09	0	0	0	0	0	0
9_3	1.98	0.18	80	2.609	2.661	1.59	0.39	0	0	1	1	0	1
9_4	1.60	0.15	80	2.583	2.625	1.28	0.32	0	0	1	1	0	1
9_5	1.32	0.11	80	2.575	2.609	1.06	0.26	0	0	1	1	0	1
9_6	2.02	0.11	79	2.582	2.635	1.58	0.43	0	0	1	1	0	1
10_1	0.85	0.28	81	2.616	2.638	0.69	0.16	0	0	0	0	0	0
10_2	0.82	0.21	82	2.614	2.635	0.68	0.15	0	0	0	0	0	0
11	0.32	0.26	77	2.645	2.653	0.25	0.07	0	0	0	0	0	0
12_4	0.53	0.17	89	2.630	2.644	0.47	0.06	0	0	0	0	0	0

Table 6 *(continued).*

Subsample	Φ_{total} (%)	MPTD (µm)	TTR (%)	BD (g cm^{-3})	SD (g cm^{-3})	Φ_{trap} (%)	Φ_{free} (%)	Fe-ox.	Chl.	Clay	Fe-ox.	Chl.	Clay	single	mutliple
1_1	2.21	0.60	80	2.580	2.638	1.78	0.43	1	0	0	1	0	0	0	0
1_2	1.79	0.65	82	2.593	2.640	1.46	0.33	1	0	0	0	0	0	0	0
1_3	1.72	0.50	77	2.593	2.638	1.33	0.39	0	0	0	0	0	0	0	0
2_1	4.72	0.86	79	2.500	2.623	3.72	1.00	1	0	0	1	0	0	1	0
2_2	3.83	1.08	73	2.524	2.625	2.81	1.02	1	0	0	0	0	0	0	0
2_3	6.53	2.87	79	2.453	2.624	5.14	1.39	1	0	0	0	0	0	0	1
3A_1	1.35	0.50	83	2.617	2.653	1.12	0.23	0	0	0	0	0	0	0	0
3A_2	0.89	0.19	84	2.631	2.654	0.75	0.14	1	0	0	0	0	0	1	0
3B_1	0.99	0.34	80	2.619	2.645	0.78	0.20	0	0	0	0	0	0	0	0
3B_2	0.86	0.13	92	2.622	2.645	0.80	0.07	1	0	0	0	0	0	0	0
4_1	1.49	0.28	87	2.589	2.628	1.30	0.19	1	0	0	1	0	0	0	0
4_2	1.38	0.29	83	2.599	2.635	1.15	0.23	1	0	0	0	0	0	0	0
5A_1	1.28	0.27	76	2.606	2.640	0.97	0.30	0	0	0	0	0	0	0	0
5A_2	0.55	0.20	87	2.635	2.649	0.48	0.07	1	0	0	0	0	0	0	0
5A_3	3.51	3.41	88	2.575	2.669	3.10	0.41	1	0	0	1	0	0	0	1
5A_4	3.24	6.35	88	2.575	2.661	2.87	0.38	1	0	0	1	0	0	1	1
5A_5	1.10	0.46	88	2.619	2.648	0.96	0.13	1	0	0	0	0	0	1	0
5A_7	0.92	0.18	87	2.612	2.636	0.80	0.12	1	0	0	0	0	0	0	0
5B_5	1.32	0.45	83	2.599	2.634	1.10	0.22	0	0	0	0	0	0	0	0
7_1	4.29	0.61	79	2.529	2.643	3.40	0.89	1	1	0	0	1	0	0	0
7_10	4.26	0.36	89	2.517	2.629	3.81	0.46	1	1	0	0	0	0	1	0
7_3	2.95	0.26	80	2.535	2.611	2.37	0.58	1	1	0	0	0	0	0	0
7_5	3.06	0.24	78	2.542	2.622	2.37	0.69	1	1	0	1	0	0	0	0
7_7	3.41	0.48	83	2.541	2.630	2.83	0.58	1	1	0	1	1	0	0	0
8B_1	0.72	0.21	84	2.642	2.662	0.61	0.12	1	0	0	1	0	0	0	0
8B_3	0.66	0.25	87	2.636	2.654	0.57	0.09	0	0	0	0	0	0	0	0
9_1	2.82	0.26	86	2.585	2.660	2.44	0.39	0	0	1	0	0	1	1	0
9_2	2.32	0.20	85	2.606	2.667	1.98	0.34	0	0	1	0	0	1	0	1
9_3	2.31	0.19	83	2.609	2.670	1.92	0.39	0	0	1	1	0	1	0	0
9_4	2.01	0.19	84	2.583	2.636	1.69	0.32	0	0	1	1	0	1	0	0
9_5	1.70	0.14	85	2.575	2.619	1.44	0.26	0	0	1	1	0	1	0	0
9_6	2.38	0.12	82	2.582	2.645	1.95	0.43	0	0	1	1	0	1	0	0
9_7	1.66	0.13	83	2.608	2.652	1.38	0.28	0	0	1	0	0	0	1	0
10_1	0.99	0.20	84	2.616	2.642	0.83	0.16	0	0	0	0	0	0	0	0
10_2	1.11	0.27	87	2.614	2.643	0.97	0.15	0	0	0	0	0	0	0	0
11	0.50	0.43	85	2.645	2.658	0.43	0.07	0	0	0	0	0	0	0	0
12_1	1.53	0.14	87	2.595	2.635	1.33	0.20	0	0	0	1	0	0	1	0
12_2	1.41	0.20	89	2.603	2.641	1.26	0.15	0	0	0	0	0	0	1	0
12_3	1.55	13.76	94	2.603	2.644	1.46	0.09	0	0	0	0	0	0	1	0
12_4	0.76	0.17	92	2.630	2.650	0.70	0.06	0	0	0	0	0	0	0	0

of analyses with differently pre-adjusted pressure intervals and using different penetrometer and compressibility correction. As a consequence the corresponding incremental volume values are not to scale with those of the other specimens and its bulk properties may also feature a systematic and hardly estimable bias. On the other hand, the PSD (i.e. regardless the amplitude) is highly reproducible by the method despite the different setting of the experiment. Therefore the sample PSD is presented and accompanied by notice about the scale difference, whereas the sample data are not featured in other plots where the absolute values play key roles.

4.4.1 Value range of measured quantities

Including all specimens, the value of total connected porosity ranges from 0.3 to 6.5 %, median pore throat diameter from 0.1 to 13 μm, skeletal density from 2.60 to 2.66 g cm^{-3} and trapped to total porosity ratio from 73 to 94 %.

Excluding samples with macroscopic cracks and recalculating the parameters for the microporosity (< 6 μm) only leads to a modified range of exclusively microstructure-relative values: total connected porosity 0.3 to 3.8 %, median pore throat diameter from 0.1 to 0.7 μm, skeletal density from 2.60 to 2.66 g cm^{-3} and trapped to total porosity ratio from 65 to 89 %.

4.4.2 PSD variation within samples

All the incremental curves grouped according to the parent sample are plotted in Fig. 11.

Sample 1

The dominant PTDs of all the specimens are in the range 0.1 to 1 μm. The specimen 1_1 bearing Fe-oxide fracture skin features elevated porosity in PTD range 0.01 to 0.04 μm.

Sample 2

In the submicron range the porosity peak is at 0.3 to 0.4 μm for the least altered specimens (2_1 and 2_2) and at 0.1 to 0.2 μm for the most altered 2_3. All the specimens feature substantial porosity in the range 1 to 10 μm and the two specimens containing cracks (2_1 and 2_3) also in the range 10 to 100 μm.

Sample 3

All the specimens feature porosity only in the submicron range. A single peak at 0.4 μm is featured by the fresh specimens (3A_1 and 3B_1) and at 0.15 μm by the Fe-oxide altered ones (3A_2 and 3B_2).

Sample 4

The submicron porosity has a bimodal distribution for both the specimens with

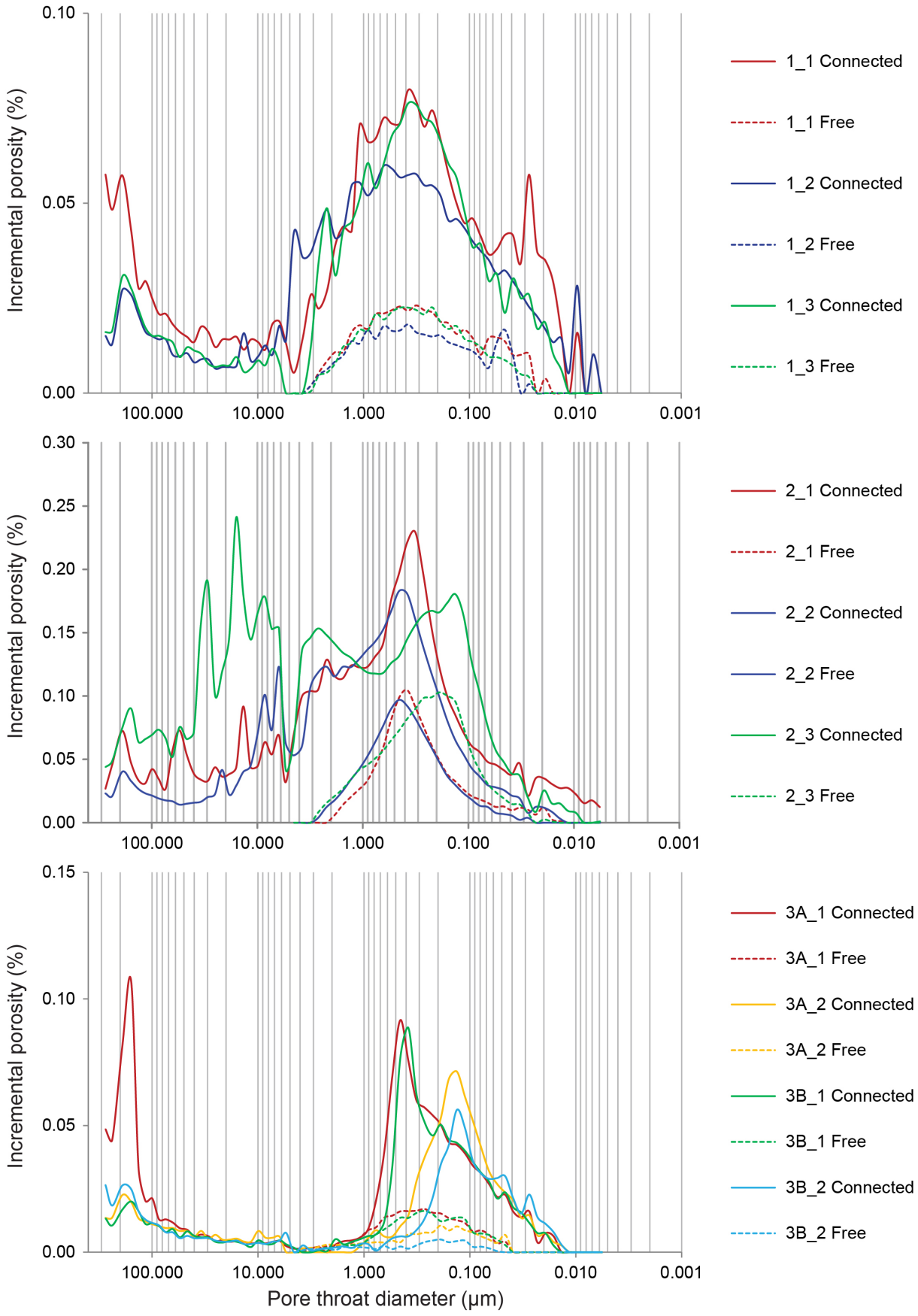

Figure 11. *(continued on the following three pages)*. Connected (full line) and free (dashed line) incremental porosity of subsamples grouped according to the parent sample. Pore throat diameter (µm) on the horizontal axis.

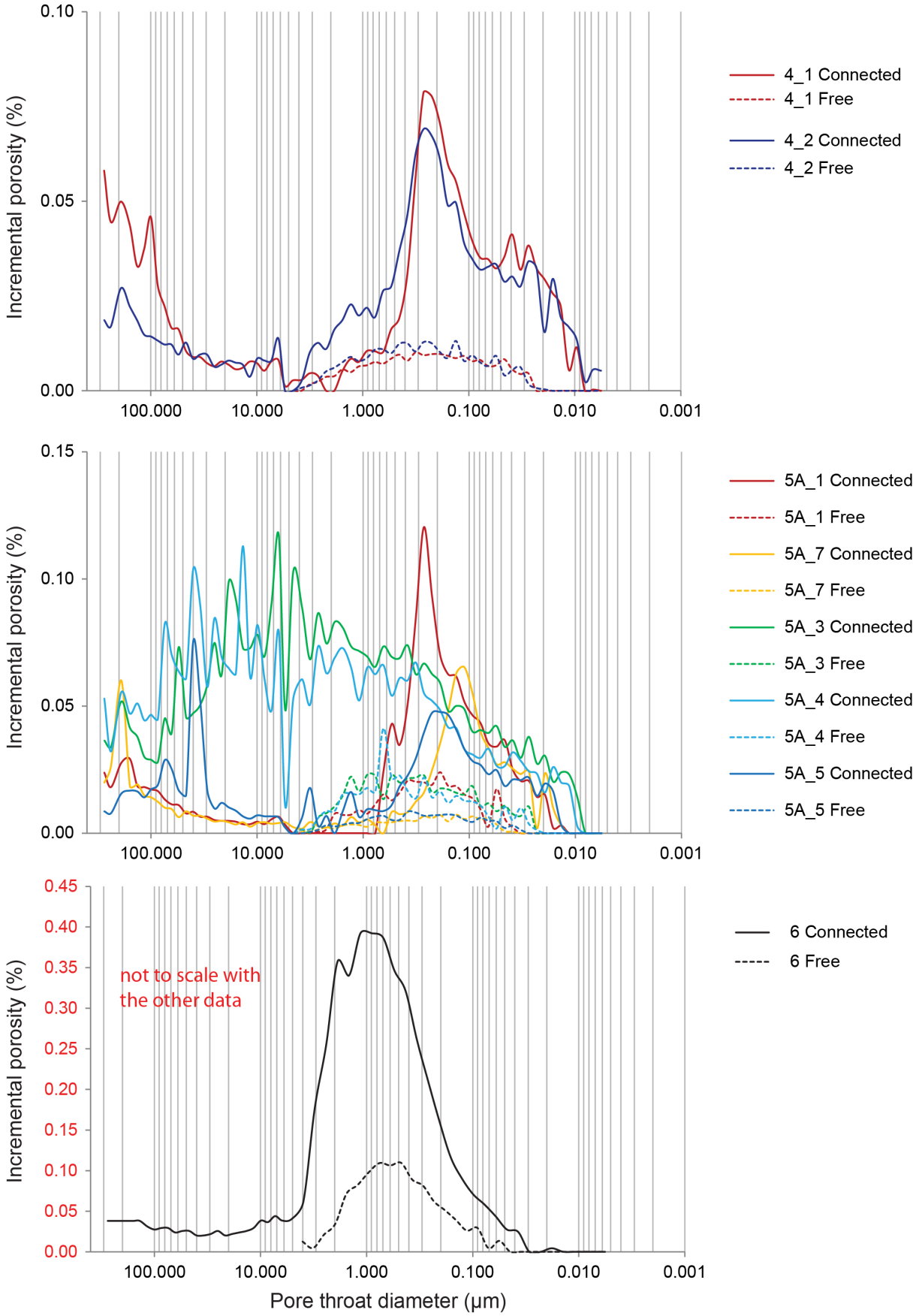

Figure 11. *(continued)*. Connected (full line) and free (dashed line) incremental porosity of subsamples grouped according to the parent sample. Pore throat diameter (µm) on the horizontal axis.

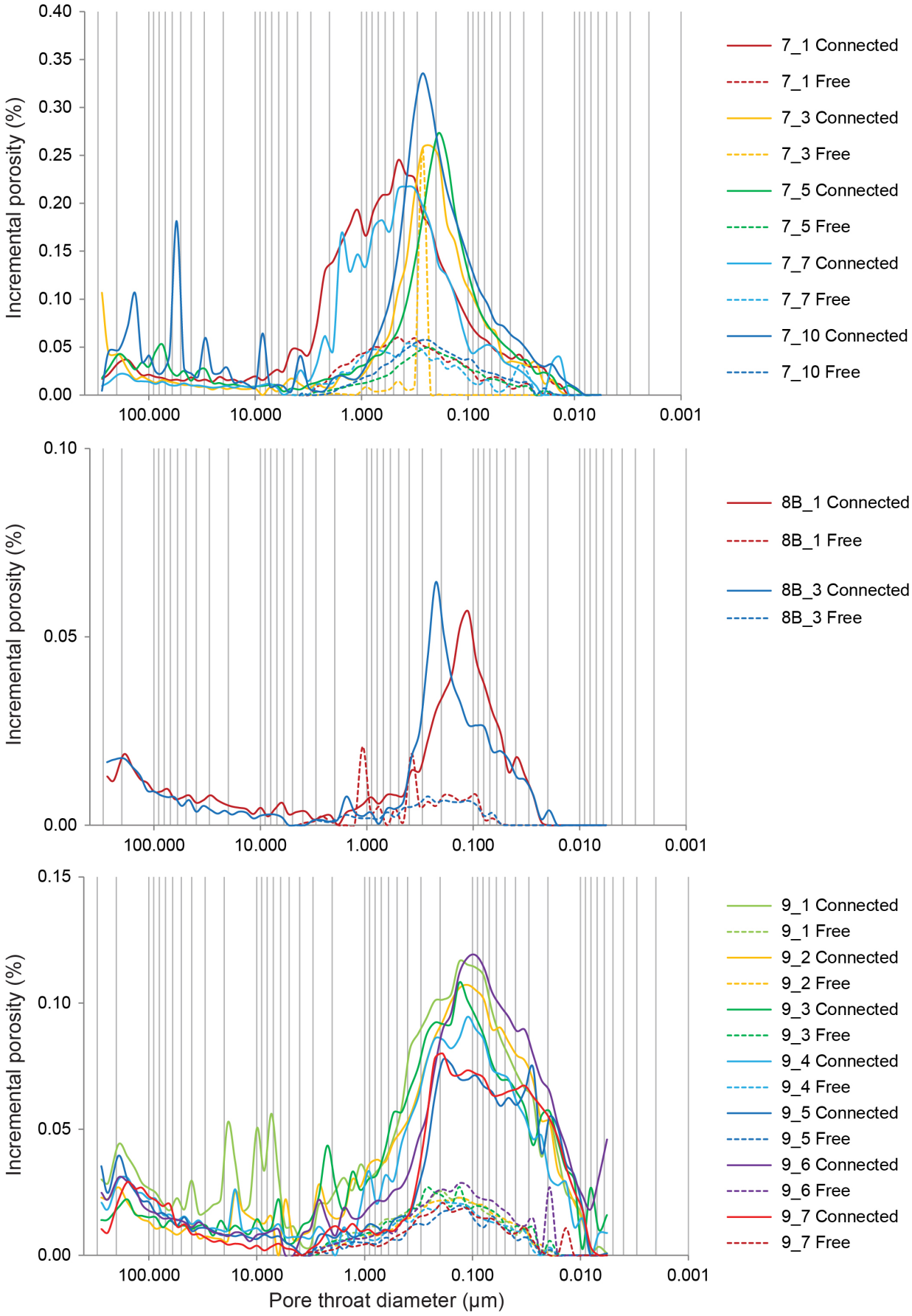

Figure 11. *(continued)*. Connected (full line) and free (dashed line) incremental porosity of subsamples grouped according to the parent sample. Pore throat diameter (µm) on the horizontal axis.

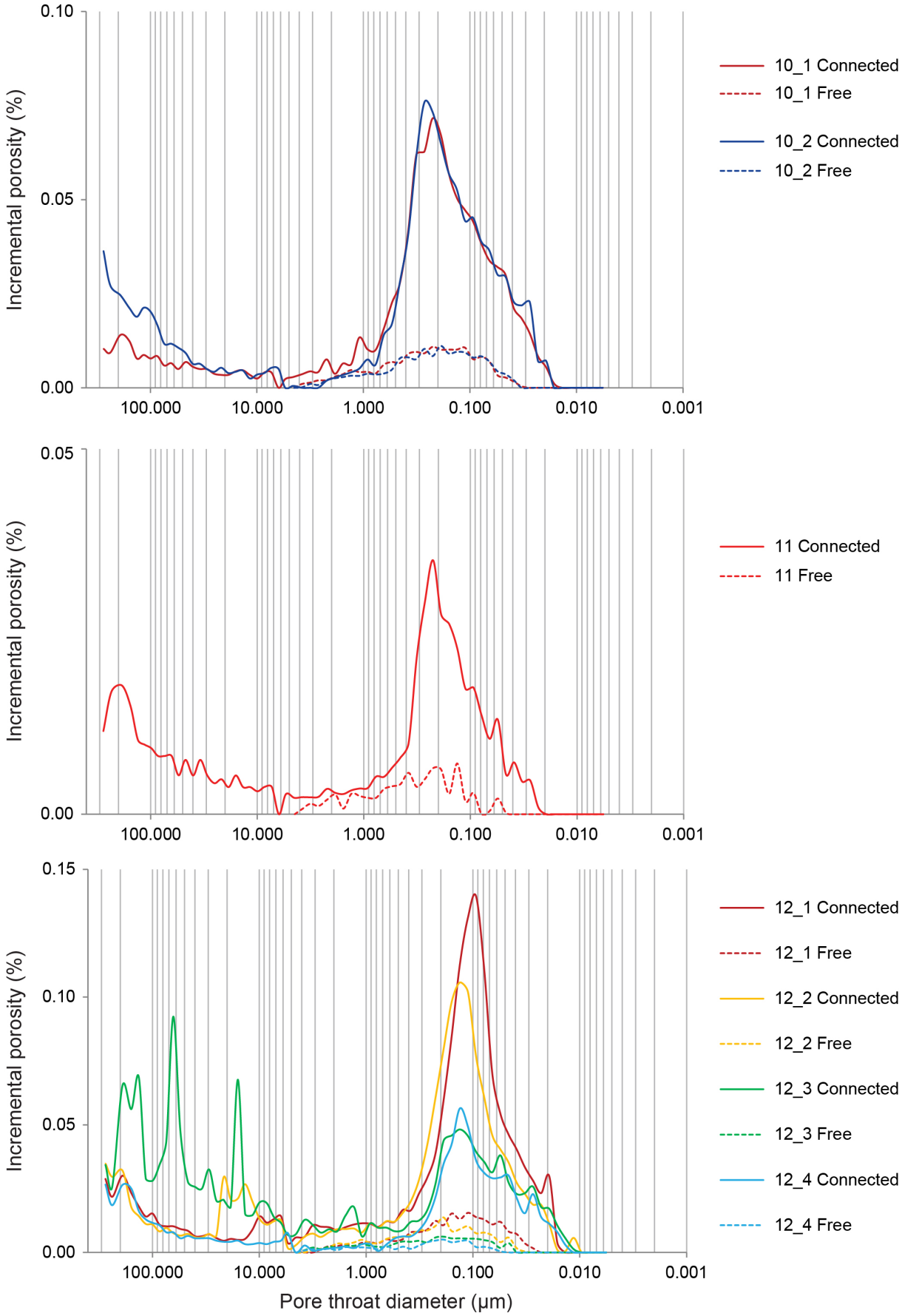

Figure 11. *(continued)*. Connected (full line) and free (dashed line) incremental porosity of subsamples grouped according to the parent sample. Pore throat diameter (µm) on the horizontal axis.

a dominant peak at 0.25 μm and a subdominant peak at 0.015 to 0.04 μm, the latter being more remarkable on the specimen with Fe-oxide fracture skin (4_1).

Sample 5

The specimens without fracture skin feature unimodal distribution in the submicron range with peak at 0.3 μm for the fresh (5A_1) and at 0.1 to 0.2 μm for the Fe-oxide altered specimens (5A_5 and 5A_7). The specimens comprising cracks and fracture skins (5A_3 and 5A_4) show important porosity accessible by PTD from 0.5 to 100 μm, whereas only an isolated macroporosity peak at 40 μm can be seen in the case of the specimen 5A_5 comprising only a crack.

Sample 6

The sample is characteristic by a single wide peak with limits at 0.1 and 5 μm and culminating at 1 μm. The free porosity peak is slightly shifted towards smaller PTDs and culminates at 0.5 to 0.8 μm.

Sample 7

The specimens without fracture skin (7_3 and 7_10) feature unimodal distribution in the submicron range with peak at 0.3 μm. The specimen bearing the Fe-oxide fracture skin (7_5) shows a shift of the dominant peak to 0.2 μm, whereas the chlorite fracture skin-bearing specimens (7_1 and 7_7) show the peak shifted towards larger PTDs between 0.4 and 2 μm. The only specimen comprising a crack (7_10) shows several peaks in the range 1 to 100 μm with the dominant one at 55 μm.

Sample 8

Both the specimens feature unimodal distribution in the submicron range with the peak at 0.2 μm for the fresh (8B_3) and at 0.1 μm for the Fe-oxide altered specimen (8B_1).

Sample 9

The specimens commonly feature porosity in the range 0.01 to 0.5 μm within which subdominant peaks of variable mutual proportions can be distinguished at 0.02, 0.1 and 0.2 μm. Cracked specimens (9_1 and 9_2) show also peaks in the range from 5 to 50 μm.

Sample 10

Both the specimens show the same unimodal distribution with peak at 0.2 to 0.3 μm. No striking difference can be seen linked to the presence (10_1) or absence (10_2) of the barren fracture wall surface.

Sample 11

The sample shows unimodal distribution with peak at 0.2 to 0.3 μm. On the example of this massive and fresh sample having the lowest porosity within the collection (0.3 %) the

possible error due to the low pressure part of the analysis can be well demonstrated. Taking into account the observation that the prepared specimen featured no macroscopic pores on its surface, the intrusion volume measured in the macroscopic PTD range (> 10 µm) is probably due to wetting of the specimen surface irregularities. Note that for material of that low total porosity, the absolute error porosity measured for the macroscopic PTDs of ~ 0.2 % is comparable to that of the actually present porosity of ~ 0.3 % accessible by micropores.

Sample 12

In the submicron range all the specimens show unimodal distribution with a peak between 0.1 and 0.15 µm for those without fracture skin and at 0.09 µm for the one with Fe-oxide fracture skin (12_1). The two samples comprising a crack (12_2 and 12_3) show extra peaks at 15, 60 and 150 µm.

4.4.3 PSD variation within the borehole

The incremental curves representing the sample means and the sample means diminished by values of the sample 11 (reference sample of fresh and non-fractured granite)

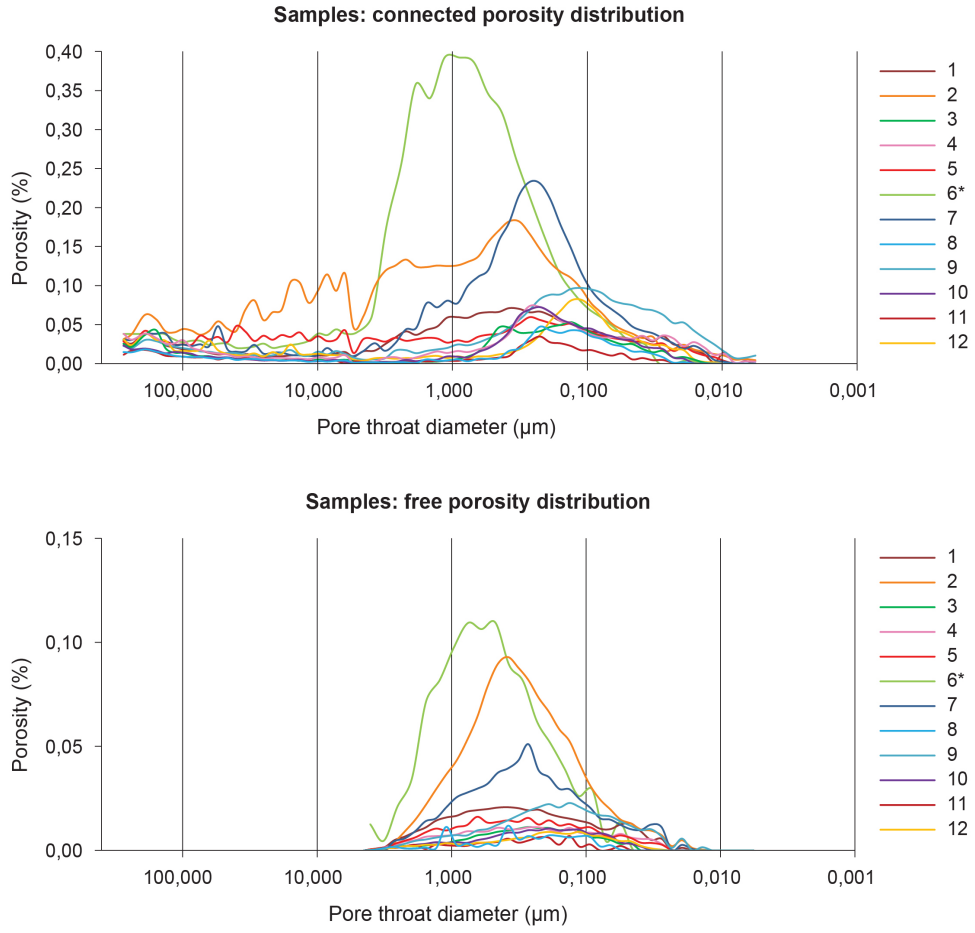

Figure 12 *(continued on the next page)*. Connected (top) and free (bottom) incremental porosity of sample averages). Porosity values of sample 6 are not to scale due to different analysis setting.

are plotted in Fig. 12. As can be seen on the plots, sample 11 features the lowest incremental porosity values in the entire range. Sample 11-similar PSDs featuring low-porosity (< 1%) with dominant peak in the range 0.1 to 0.5 μm are associated with rather massive and weakly altered samples (3, 8, 10). Porosity accessible by PTDs bigger than 0.5 μm is developed in altered and fractured samples from the shallow (< 25 m) part of the borehole (samples 2, 6, 7; to a lesser measure also 1 and 5) and the porosity accessible by PTDs smaller than 0.1 μm is populated the most in the sample 9 (51st meter).

4.4.4 PSD trends related to alteration and fracturing

To simplify the image of the PSD at the scale of the borehole, nine subfacies differing in alteration and fracturing character were chosen to represent the principal PSD trends. In order to depict the rock matrix-relative PSD, only specimens featuring neither crack nor fracture skin were selected. Exception was made in case of the sample 9, where such a specimen was not available, and thus the least heterogeneous crack-containing specimen without external fracture skins was selected. The chosen subfacies and the corresponding

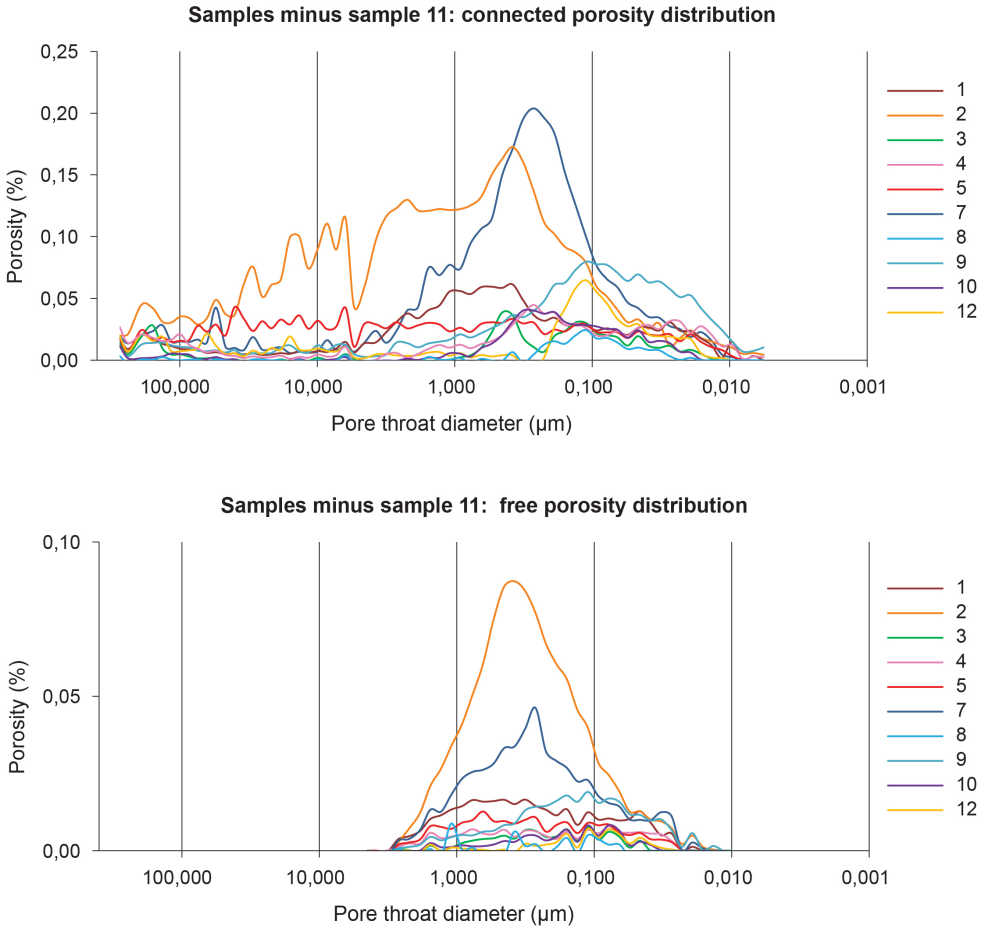

Figure 12 *(continued)*. Connected (top) and free (bottom) incremental porosity of sample averages diminished by values of the sample 11, which is a reference sample of fresh and non fractured granite.

specimens are:

- Pristine
  - 11
- Fresh in vicinity of a fracture
  - 3A_1, 3B_1, 5A_1, 8B_3, 10_2, 12_4
- Fe-oxide altered in vicinity of single fracture
  - 3A_2, 3B_2, 5A_7, 8B_1
- Fe-oxide altered in zone of densely spaced fractures
  - 4_2
- Chlorite and Fe-oxide altered fractured
  - 7_3
- Chlorite and Fe-oxide altered intensively fractured
  - 6
- Clay altered fractured
  - 9_7
- Weathered fractured
  - 1_1, 1_2, 1_3
- Weathered intensively fractured
  - 2_2

The incremental curves of the corresponding specimens were averaged and plotted in Fig. 13. Compared to the fresh intact rock, the fresh rock sampled near fractures (but beyond alteration halo, if developed) differs by higher porosity values of otherwise similarly shaped and positioned PSD with the dominant peak between 0.2 and 0.3 μm. With respect to its unaltered analogue the rock sampled within fracture-related Fe-oxide alteration halo features PSD shifted towards smaller pores with the dominant peak at 0.1 to 0.2 μm, slightly lower connected porosity values and remarkably lower free porosity values. In case the Fe-oxide alteration is associated with zone of densely spaced fractures (~ cm^{-1}) the rock features slightly higher porosity values as compared to the two precedent fracture-related subfacies and the same dominant PTD as the fresh subfacies. Compared with the three previous subfacies, only this one features non-negligible incremental values of connected porosity accessible by PTDs larger than 0.5 μm. The weathered subfacies differs from the previous ones mainly by higher porosity values for PTD in the range 0.5 to 5 μm. The porosity in this range is even more populated in case of intensively fractured weathered subfacies, which features also porosity with PTDs up to 10 μm in diameter. Compared to all the other subfacies the rock featuring both chlorite and Fe-oxide alteration features the

highest porosity values in the range from 0.05 to 0.4 μm. In case such alteration character is accompanied by intensive fracturing, the rock features globally the highest porosity values in the range from 0.4 to 4 μm with the dominant peak at 1 μm. The subfacies associated with clay alteration features rather evenly distributed porosity in the PTD range from 0.02 to 0.3 μm and features globally predominating porosity values for PTDs below 0.05.

4.4.5 Bulk properties related to alteration and fracturing

The values of median pore throat diameter (MPTD), skeletal density (SD) and trapped to total porosity ratio (TTR) versus total porosity are plotted in Fig. 14. Similarly as in the previous subsection, only non-cracked specimens were selected in order to characterise the rock microstructure only. However, in this case the specimens featuring fracture skins were included in the selection in order to show their effect on the bulk properties. To eliminate any error intrusion volume related to filling of the sample surface irregularities or to the misfit of the blank correction in the low pressure analysis, the bulk properties values were recalculated from the initial data taking into account the high pressure part, i.e. PTDs smaller than 6 μm, only. The same classification into subfacies as in the previous subsection is applied, except that the sample 6 values are not used here regarding its different analysis setting and the possibly related bias. The selected subfacies and the corresponding specimens are:

- Pristine
  - 11
- Fresh in vicinity of a single fracture
  - 3A_1, 3B_1, 5A_1, 8B_3, 10_1, 10_2, 12_4
- Fe-oxide altered in vicinity of a single fracture
  - 3A_2, 3B_2, 5A_7, 8B_1
- Fe-oxide altered in zone of densely spaced fractures
  - 4_1, 4_2
- Chlorite and Fe-oxide altered
  - 7_1, 7_3, 7_5, 7_7
- Clay altered
  - 9_3, 9_4, 9_5, 9_6,
- Weathered
  - 1_1, 1_2, 1_3
- Weathered intensively fractured
  - 2_2

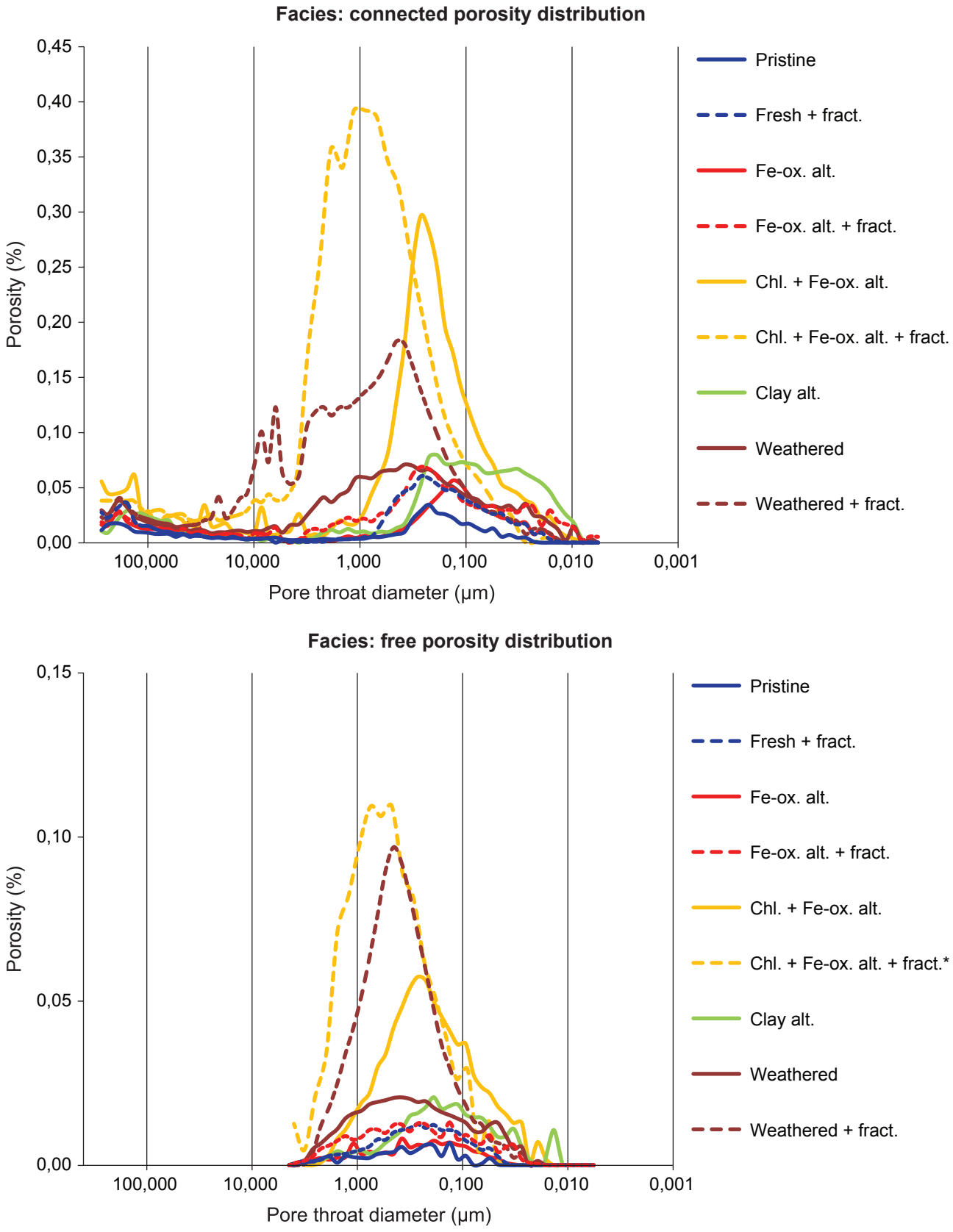

Figure 13 *(continued on the next page)*. Connected (top) and free (bottom) porosity pore size distribution characteristic for facies sampled in the MEL-5 borehole core. Fract. - fractured, ox. - oxide, alt. - alteration, chl. - chlorite. *) Porosity values of "Chl. + Fe-ox alt. + fract." are represented by the sample 6 not to scale with the other data.

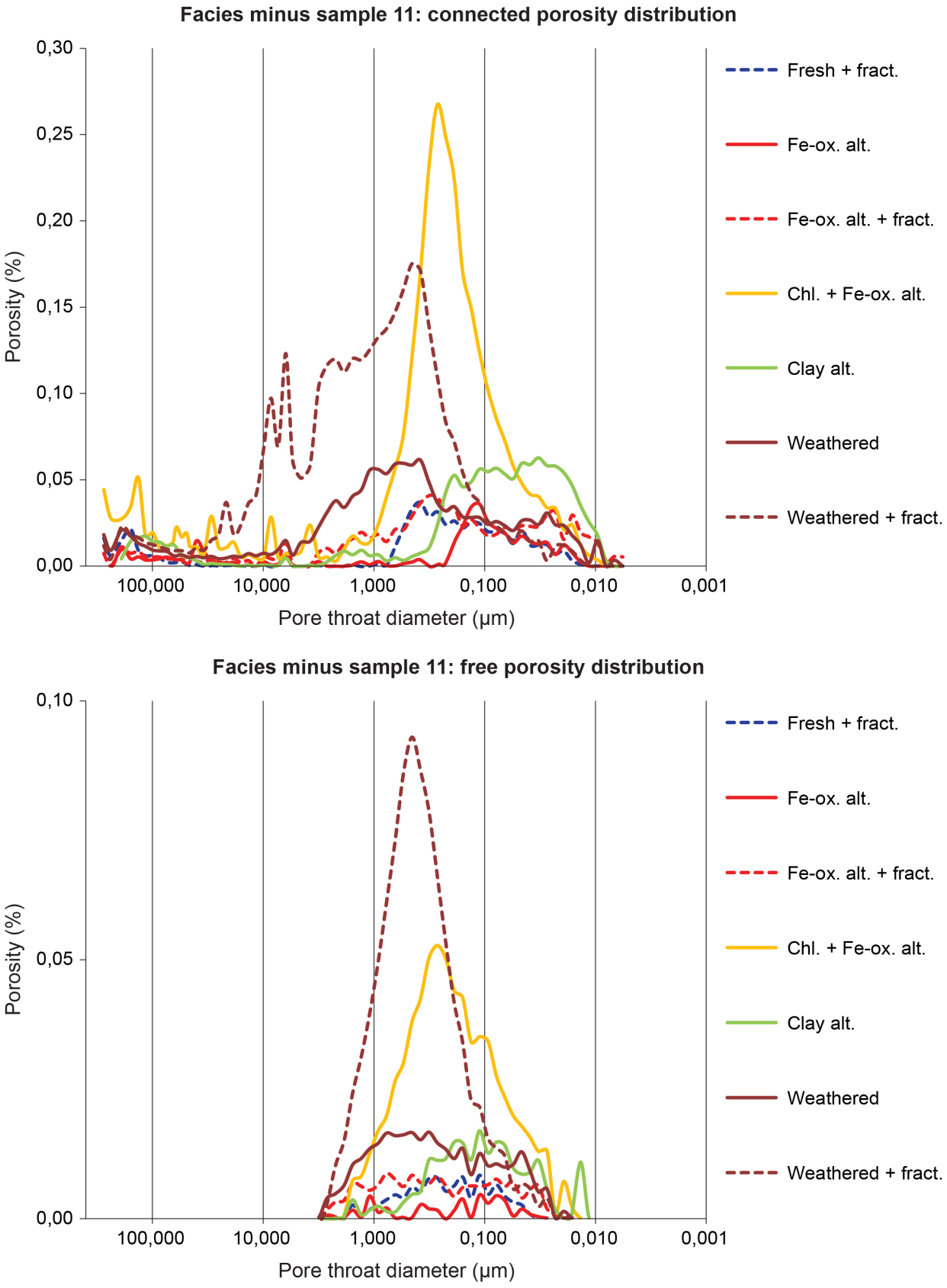

Figure 13 *(continued).* Connected (top) and free (bottom) porosity pore size distribution of the sampled facies after subtraction of the pore size distribution of the sample 11, which is the reference sample of fresh and non-fractured granite. Fract. - fractured, ox. - oxide, alt. - alteration, chl. - chlorite.

Compared to the other specimens the fresh intact rock features the lowest porosity (0.3 %), intermediate MPTD of 0.3 μm, intermediate TTR of 77 % and high SD of 2.65 g cm^{-3}. The fractured fresh rock features higher porosity values from 0.5 to 1 %, higher MPTD between 0.3 and 0.4 μm, highly variable TTR from 70 to 90 % and SD in the range 2.63 to 2.65 g cm^{-3}. The Fe-oxide altered analogues of the precedent subfacies feature lower and less scattered values of porosity ranging from 0.5 to 0.7 %, MPTD of 0.2 μm and TTR above mean varying from 78 to 90 %. The SD varies between 2.63 and 2.66 g cm^{-3}. The two intensively fractured Fe-oxide altered specimens show commonly higher porosity of 1 % and differ relative to each other in the other quantities. The specimen containing the Fe-oxide fracture skin (4_1) shows lower SD and MPTD and higher TTR as compared to the one without the fracture skin (4_2). The subfacies with mixed chlorite and Fe-oxide alteration features porosity from 2.5 to 3.8 %, MPTD between 0.3 and 0.7 μm, TTR from 75 to 87 % and SD from 2.60 to 2.63 g cm^{-3}. Regarding the fracture skin character, increase in porosity, MPTD and SD is associated with the change from the Fe-oxide-dominated to the chlorite-dominated material. The TTR of the three fracture skin-containing specimens is similar (~ 76 %) and remarkably lower compared to the specimen with no fracture skin, which shows also the lowest SD. The clay altered subfacies is characteristic by porosity between 1.3 and 2 %, similar TTR of 80% and MPTD between 0.1 (global minimum) and 0.2 μm. The SD varies from 2.61 to the global maximum of 2.66 g cm^{-3}. The high SD value is featured by the specimen 9_3 containing fracture skin with the most of the Fe-oxide material within the subfacies. The weathered subfacies is characteristic by porosity from 1.4 to 1.7 %, MPTD from 0.3 to 0.6 μm, TTR below 80% and SD from 2.62 to 2.63 g cm^{-3}. The fractured weathered subfacies shows porosity of 3 %, MPTD of 0.7 μm, SD of 2.60 g cm^{-3} and the lowest TTR of 65 %.

In addition to the subfacies-related characteristics, the plots reveal some general relations between the measured quantities. It can be seen in the plot of median PTD vs. porosity that the PTD generally increases with porosity. In addition, two specimen groups differing in proportionality of the latter trend can be discerned: specimens featuring chlorite- or clay-alteration and the other specimens. For a given porosity the former group is characterized by smaller PTD than the latter. The TTR tends to decrease with porosity, however this dependence is little net especially for the low porosity facies. Comparing the relation of SD and porosity, it can be seen that the higher is the subfacies overall porosity the lower is its SD. Within subfacies the latter trend is apparent for the fresh, the Fe-oxide altered and the weathered subfacies. An inverse trend can be seen within subfacies featuring chlorite- or clay-alteration which are in addition both associated with high variability of the SD values.

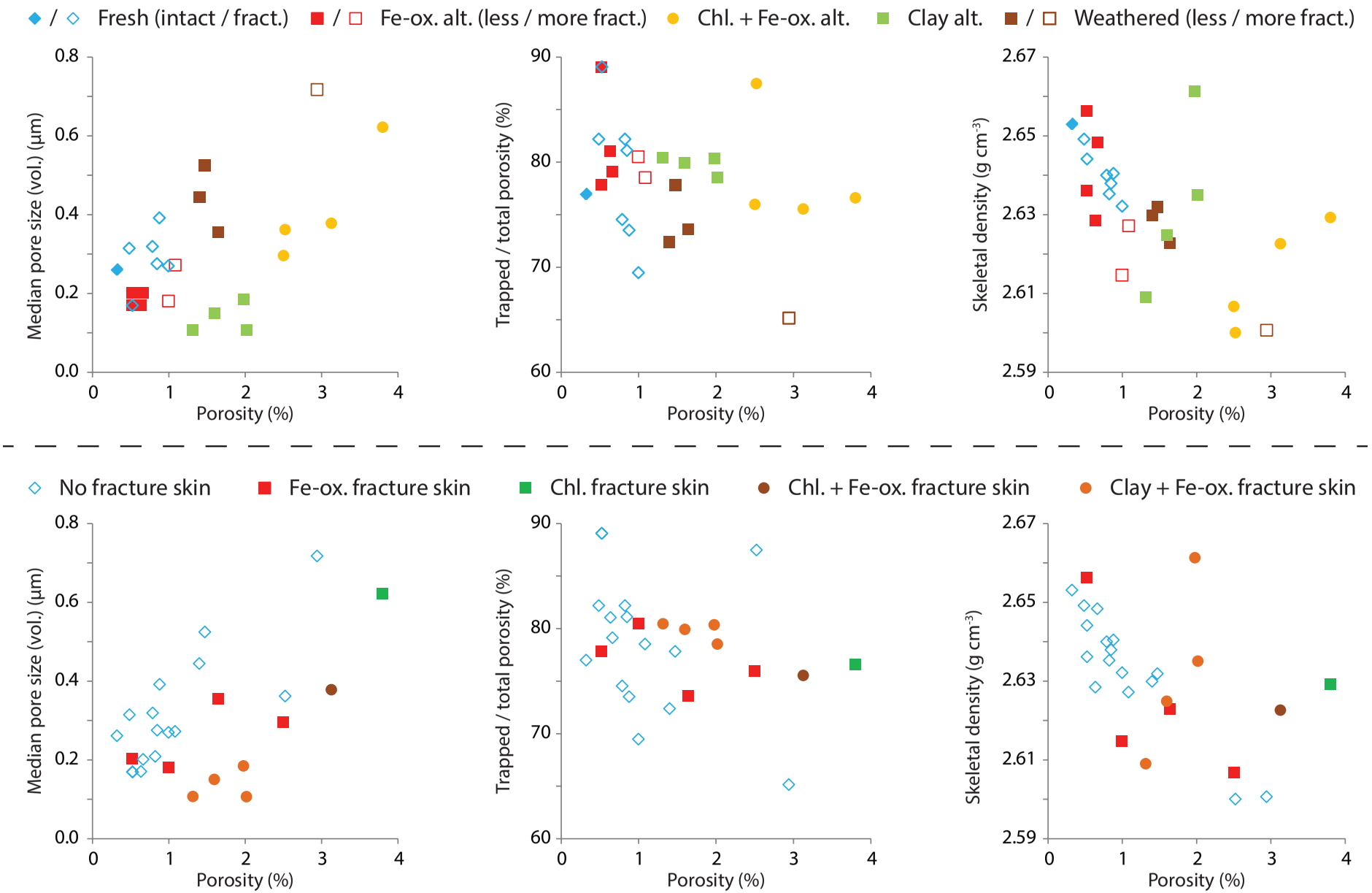

Figure 14. Bulk properties of subsamples grouped according to the alteration and fracturing facies (top row) and according to the fracture skin character (bottom row). Fract. - fractured, ox. - oxide, alt. - altered, chl. - chlorite, vol. - volume.

4.4.6 Pore space volume associated to the macrocracks

In order to evaluate the pore volume within the macroscopically visible cracks, the cumulative porosities in PTD range 6 - 300 µm of the cracked specimens have been calculated and plotted on bar chart in Fig. 15. For comparison, the respective microporosity values are also shown. As can be seen in the plot, the macroporosity of the cracked specimens ranges from 0.30 to 2.79 %. These values are all higher than the error-related value of the specimen 11 (0.18 %) although the lowest ones are comparable with it (0.2 to 0.5 %). The lowest values are represented by specimens (3A_2, 5A_5, 9_2, 9_7, 12_1, 12_2) where external fracture skins were absent or sawed off and where the internal cracks were thin (<< 1 mm) and with straight and parallel walls (compare with photographs of the specimens in fig. FA3). Intermediate values from 0.8 to 1.0 % are represented by specimens with still no external fracture skins but featuring rather open (~ 1 mm) and tortuous internal cracks (7_10, 9_1, 12_3). Values higher than 1 % are featured by specimens of samples 2 and 5 that contained intensively cracked fracture walls or fracture skins, the highest value

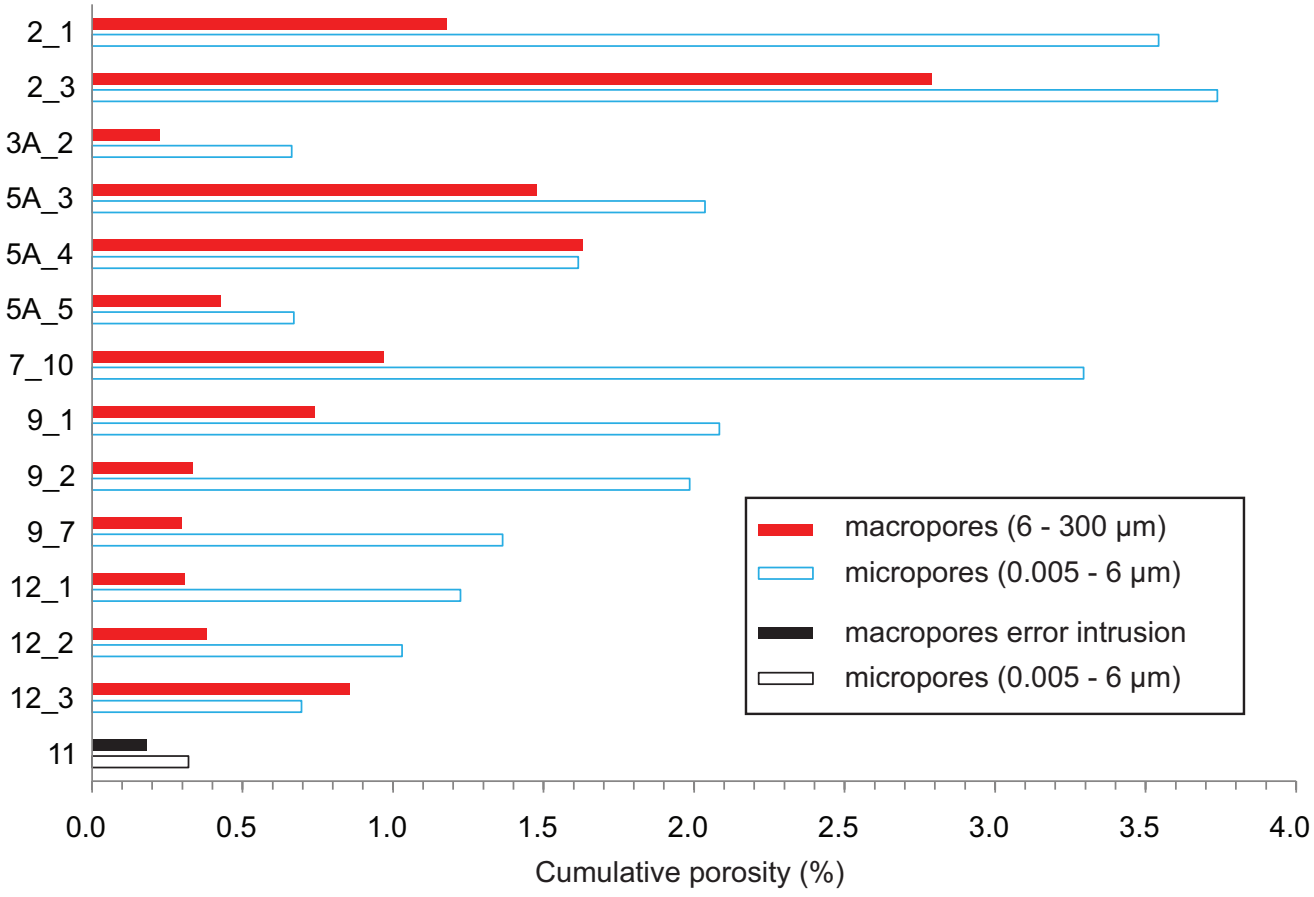

Figure 15. Bar chart showing cumulative porosity values for macroporosity (6 - 300 µm, red filled bars) and microporosity (0.005 - 6 µm, blue empty bars) of subsamples featuring macroscopically visible crack(s). For comparison, values of sample 11 (reference of non-cracked granite) are shown, with the macroporosity (black filled bar) corresponding to error intrusion volume due to the surface irregularities and/or misfit of the compressibility correction and the microporosity (black empty bar) representing the actual sample porosity.

2.8 % being featured by highly friable material of the specimen 2_3. The proportion of macro- and microporosity volume of the specimens varies from 1/6 to 5/4 with the lowest ratio featured by specimens of the sample 9 and with the highest values featured both by specimens containing the intensively cracked fracture walls and fracture skins of sample 5 and by the specimen 12_3 containing an open crack.

4.4.7 Summary

The following section summarizes the acquired petrophysical data and highlights the trends of values of the measured petrophysical properties in association with the observed intensity and character of fracturing and alteration.

Thermal conductivity measurements

The pristine Lipnice granite has been characterized by TC value of 2.68 W m^{-1} K^{-1}. The lowest TC values of 2.0 - 2.5 W m^{-1} K^{-1} have been reported for strongly to intermediately weathered and fractured granite from quarries and borehole depth < 3 m. Excluding the latter, the lowest mean TC of 2.5 W m^{-1} K^{-1} has been measured in association with pervasive Fe-oxide alteration zone of densely spaced (1-2 cm^{-1}) subparallel fractures. Mean TC values 2.6 - 2.8 W m^{-1} K^{-1} have been measured on weakly fractured and weakly altered granite from walls of localized fractures and also for intensively fractured and chlorite-Fe-oxide altered granite. Within the borehole, the highest TC of 2.9 W m^{-1} K^{-1} has been measured in association with clay alteration zone of densely spaced (1-2 cm^{-1}) subparallel fractures. Comparably high values have also been measured on the quarry samples of the strongly Fe-oxide altered Lipnice granite and of quartz-rich and weakly altered Kouty granite.

In addition to the trends observed on the scale of the sample collection, the TC profiles demonstrated the increase of TC related to Fe-oxide alteration fracture halo as well as the decrease of TC towards fractures in weakly altered granite. Finally, the TC has been shown to substantially differ for distinct alteration facies associated with otherwise similar macroscopic intensity of fracturing.

V_p measurements

At ambient pressure the pristine Lipnice granite has been characterized by V_p values 4.4-4.6 km s^{-1}. V_p Values 4.0-4.8 km s^{-1} have been measured on weakly fractured and unaltered or on weakly fractured and weakly altered samples and also on densely fractured and clay altered sample. Schlieren and intermediate cracking associated with exfoliation joints has been characterized by V_p 2.6-3.4 km s^{-1} with low values perpendicular to both the structures. V_p values 1.9-2.3 km s^{-1} and 3.4-3.7 km s^{-1} have been measured on strongly and on intermediately fractured and weathered granite, respectively. Chlorite-Fe-oxide altered

sample has been characterized by V_P values 3.7-4.3 km s^{-1}. The highest V_P values 4.6-5.1 km s^{-1} have been measured on Fe-oxide altered granite and were ~ 10% higher as compared to the fresh granite in the corresponding samples. Remarkably lower V_P perpendicular to the reference fracture than parallel to it has been measured on strongly weathered and fractured sample and on Fe-oxide altered samples. For chlorite-Fe-oxide and clay altered samples the highest V_P has been measured perpendicular to the reference fracture.

Multidirectional measurements have characterized the quarry samples by V_P anisotropy of 11-24% at ambient pressure and < 6% at confinement 100 MPa or higher. The degree of V_P anisotropy has been shown to negatively correlate with mean V_P in the given low pressure range and both the V_P and V_P anisotropy inter-sample difference is remarkably reduced at higher confinements. Both orthorhombic and transversely V_P anisotropy shapes have been measured and observed to persist up to confinement of 400 MPa. No systematic relation of V_P anisotropy to orientation of the reference fractures has been observed except for the fractured schlieren granite with high values along the fracture and schlieren and low values perpendicular to these structures.

Permeability measurements

The lowest permeability values (< 10^{-18} m^2) have been measured for pristine granite, for fresh granite near single fracture and for granite within Fe-oxide alteration halo of single or two intersecting fractures. Permeability on the order of 10^{-18} m^2 has been measured mainly on Fe-oxide or clay altered and densely fractured granite. Higher values of the latter order and lower values on the order of 10^{-17} m^2 have been measured for intermediately weathered and fractured granite, for strongly chlorite-Fe-oxide altered and fractured granite, for rather fresh and fractured quarry samples as well as for the several plugs containing along-axis open fissure. Permeability values distributed on the order of 10^{-17} m^2 have been measured for the fractured schlieren granite and the highest values on the order of 10^{-16} - 10^{-15} m^2 have been measured for the strongly weathered and fractured granite.

Permeability anisotropy of the fractured schlieren granite has been measured with high values along the fracture and schlieren and low values perpendicular to these structures. Permeability anisotropy with high values in directions parallel to the reference fracture has been observed for the strongly weathered and fractured granite.

Porosimetric measurements

For microporosity (6 μm > PTD > 5 nm) the lowest total connected porosity (porosity) value 0.3 % has been measured for the pristine granite further characterized by median pore throat diameter (MPTD) 0.3 μm, skeletal density (SD) 2.65 g cm^{-3} and trapped-to-total porosity ratio (TTR) 77%. For weakly fractured and weakly altered rock, higher

porosities of 0.5-1.0 % and MPTD of 0.2-0.4 μm have been measured in association with variable TTR 70-90 %. Compared with the latter, lower porosity 0.5-0.7 %, lower MPTD 0.2 μm and higher TTR of 78-90% have been measured for strong Fe-oxide alteration halo associated with weak fracturing. Compared with the latter, higher porosity ~ 1.0 %, higher MPTD 0.2-0.3 μm and higher TTR ~ 80 % have been measured for Fe-oxide alteration halo associated with dense fracturing. SD of 2.62-2.66 g cm^{-3} has been measured for the Fe-oxide altered granites. For fractured and chlorite-Fe-oxide altered granite, high porosity 2.5-3.8 %, high MPTD 0.3-0.7 μm, low TTR 75-87 % and low SD 2.60-2.63 g cm^{-3} have been measured. For fractured and clay-altered granite, intermediate porosity 1.3-2.0 %, the lowest MPT 0.1-0.2 μm and TTR ~ 80% have been measured. Variable SD 2.61-2.66 g cm^{-3} has been measured for different fracture skins. For intermediately weathered and fractured granite, intermediate porosity 1.4-1.7 %, high MPTD 0.3-0.6 μm and low TTR < 80% and low SD 2.62-2.63 g cm^{-3} have been measured. Compared to the latter, higher porosity ~ 3.0 %, higher MPTD 0.7 μm, the lowest TTR 65% and the lowest SD 2.62-2.63 g cm^{-3} have been measured.

The lowest values 0.2-0.5 % of macroporosity (300 μm > PTD > 6 μm) have been measured for specimens containing thin internal cracks with straight subparallel walls. Intermediate values 0.8-1.0 % have been measured for specimens with open internal cracks with tortuous walls. High values 1.0-1.6 % have been measured for specimens containing intensively cracked fracture skins and fracture walls and the highest value 2.8 % has been measured for strongly weathered and cracked granite.

5. Discussion

The results of the five applied petrophysical techniques provide us with a vast series of descriptive parameters of the examined facies of granite. It appears from our results that all the applied techniques are sensitive to the degree of both fracturing and alteration. In specific cases where the two phenomena are weak, the permeability and thermal conductivity measurements did not reveal striking differences in the presumably low porous and little anisotropic primary rock microstructure. Consequently, the mercury porosimetry has a privileged significance among the applied techniques for several reasons. Given the small specimen size for porosimetric analyses, materials with well specified combinations of macroscopic intensities of fracturing and alteration have been delimited and analyzed. Moreover, the porosimetric analyses seem to reflect the studied rock nature the most sensitively and with high resolution in the whole range of the encountered facies. In addition, despite the low porosities of measured samples implying low signal-to-noise ratio (Giesche 2006), the elaborated routine allowed precise calculations of connected porosity and its pore throat size and shape distribution. These porosimetric parameters play a key role in porosity-permeability models of porous media (Scheidegger 1974; Walsh & Brace 1984; Katz & Thompson 1986; Guéguen & Dienes 1989; Kachanov 1993; Guéguen & Palciauskas 1992; Matthews et al. 1995; Mavko & Nur 1997; Bernabé et al. 2003; Guéguen & Boutéca 2004; Sarout 2012) and their importance for fractured granite studies has also been demonstrated experimentally (Brace et al. 1968; Zoback & Byerlee 1975; Brace 1977; Bernabe 1986; Sausse et al. 2001). Finally, in combination with the other petrophysical measurements, these parameters have been used to describe the effect of fracturing and alteration on the rock physical properties including the hereby treated permeability, thermal conductivity and P-wave velocity (Géraud 1994; David et al. 1999; Boness & Zoback 2004; Benson et al. 2006; Chaki et al. 2008; Géraud et al. 2010; Yasuhara et al. 2011).

The most continuous and detailed series of specimens within our collection has been derived from the Lipnice borehole samples. Their common provenance is a positive indicator for reliability of detailed inter-sample comparison we engage. Hence, the principal facies defined on the basis of porosimetric analyses of the Lipnice granite borehole samples are used as a reference frame for interpretation of the petrophysical dataset in terms of origin and development of rock microstructures affecting transfer properties of the studied rocks.

Table 7. Petrophysical properties of studied granite alteration and fracturing facies. Φ - total connected porosity, MPTD - median pore throat diameter (volume), TTR - trapped to total porosity ratio, SD - skeletal density, k - intrinsic permeability, VP - P-wave velocity, TC - thermal conductivity, TC IF - TC inhomogeneity factor, ox. - oxide, chl. - chlorite, weat. - weathered, + - macroscopic fracturing intensity of the alteration facies.

Facies	Φ (%)	MPTD (μm)	TTR (%)	SD (g cm^{-3})	k (m^2)	V_P (km s^{-1})	TC (W m^{-1} K^{-1})	TC IF ( )	Fracturing	Fe-ox.	Chlorite	Clay
Pristine	0.32	0.26	77	2.653	< 10^{-18}	4.4 - 4.6	2.68	0.11	0	0	0	0
Fractured	0.53 - 1.00	0.17 - 0.39	69 - 89	2.635 - 2.644	< 1 x 10^{-17}	4.0 - 4.8	2.66	0.24	1	0	0	0
Fe-ox. +	0.49 - 0.66	0.17 - 0.31	78 - 89	2.648 - 2.656	< 10^{-18}	4.4 - 5.1	2.72	0.12	1	1	0	0
Fe-ox. ++	0.99 - 1.08	0.18 - 0.27	79 - 81	2.615 - 2.627	5 x 10^{-18}	3.7 - 4.2	2.51	0.38	2	2	0	0
Chl. +++	2.52 - 3.80	0.30 - 0.62	76 - 87	2.600 - 2.629	2 x 10^{-17}	3.7 - 4.3	2.69	0.18	3	2	3	0
Clay ++	1.32 - 2.02	0.11 - 0.18	79 - 80	2.609 - 2.661	< 7 x 10^{-18}	4.3 - 4.7	2.89	0.08	2	1	0	3
Weat. ++	1.40 - 1.64	0.36 - 0.52	72 - 78	2.623 - 2.632	10^{-18} - 10^{-17}	3.4 - 3.7	2.53	0.14	2	2	2	0
Weat. +++	2.94	0.72	65	2.601	6 x 10^{-16}	1.9 - 2.6	1.97	0.45	3	3	3	0

5.1 Petrophysical properties of studied granite facies

The fracturing and alteration facies defined on the Lipnice borehole samples and their characteristic petrophysical properties are displayed in Tab 7. The presented porosimetric and density values are based on the microporosity range calculations thus allowing comparison of rather homogeneous and facies-representative volumes controlled by the rock matrix fabric and the microcrack network. For phenomena related to the macroporosity which are rather heterogeneous within and between facies we will refer to specific specimens and results displayed in Tabs. 4, 5 and 6 and in Fig. 15.

5.1.1 Pristine granite

The pristine granite facies defined on sample 11 is characteristic by absence of strong alteration of the primary magmatic microstructure showing sericitized feldspars and minority of weakly chloritized biotites (Fig. 7). Within the sample collection, the pristine granite is the least porous with 0.32 % which is c. twelve times lower than the highest measured microporosity (PTD 5 nm to 6 μm) value 3.80 % (specimen 7_1) and c. twenty-two times lower than the highest measured bulk porosity (PTD 5 nm to 300 μm) value 6.53 % (specimen 2_3). Previous works involving mercury porosimetry of fresh granite facies have reported porosities 0.13 - 0.82 % for Soultz-sous-Forêts granite (SSF, Jacquemont 2002; Surma 2003; Surma & Géraud 2003; Rosener 2007; Rosener & Géraud 2007; Géraud et al. 2010), 0.4 % with the porosity network made up dominantly by cracks for La Borne granite (Géraud 1994) and 0.5 % associated with intragranular cracks for Toki granite (Onishi & Shimizu 2005). Porosity 0.2 % has been measured and attributed to combined pore (0.1 %) and crack (0.1 %) porosity by Brace et al. (1965) on Troy granite featuring, however, substantially larger grain size (4.0 mm) than the hereby studied Lipnice granite (0.7 mm, c.f. chapter IV). The latter author has also characterized Westerley and Casco granite respectively with grain sizes 0.75 and 5.0 mm and with porosity values 0.9 and 0.7 % from which the crack porosity was 0.2 and 0.5 %. Relative to the set of the mentioned values from the latter work, it is worth noting the V_p measurements of the same specimens by Nur & Simmons (1969). At ambient pressure the authors have measured V_p of 4.5, 3.8 and 3.2 km s^{-1} for the Troy, Westerly and Casco granites, respectively. As can be seen (compare with Tabs. 5 - 7), our pristine granite sample matches the best the coarse-grained Troy granite in terms of V_p (4.4 - 4.6 km s^{-1}) and total porosity, whereas it differs substantially in both the quantities from the similarly-grained Westerly granite. Within these reference-granite types the pristine Lipnice granite porosity of 0.32 % thus seems to be well estimated as higher porosity would probably be associated with lower V_p values especially at its low grain size due to higher grain boundary density per volumetric unit.

We have characterized the pristine granite by permeability lower than 10^{-18} m^2, which is also the case for some plugs extracted from the borehole fracture wall-samples showing no macroscopic cracks and having fresh appearance (Tabs. 5 and 7, Figs. A1, A3). All these specimens thus have permeability by at least three orders of magnitude lower than the most permeable ones in our collection with 9.4 x 10^{-16} m^2. The estimated low values of the pristine granite correspond in the literature mainly to fresh and also to weakly pervasively altered granite facies. Westerly granite has been characterized by permeability values between 10^{-17} m^2 and 10^{-19} m^2 at respectively 10 and 400 MPa confining pressure (Brace et al. 1968) and by permeability values on the order of 10^{-21} m^2 at confinements 10 - 23 MPa and effective pressures 4 - 16 MPa (Larive 2002). Permeabilities as low as 10^{-20} m^2 have been reported for fresh SSF granite (Rosener & Géraud 2007; Géraud et al. 2010) using a N_2 permeametry setup similar to the one used here but adapted for higher head pressures of up to 3.5 MPa at confining pressures of 4 MPa. Measurements of the Lipnice granite using dry air permeametry setup with 10 MPa confinement and 7 MPa maximal head pressure yielded the lowest permeabilities of 4 x 10^{-19} m^2 (Hanák & Ondra 1996). The latter work bears very important implications for our samples regarding mainly the thereby used setup allowing very low permeabilities to be accurately measured. The authors were able to reliably measure low permeabilities on the order of 10^{-20} m^2 as indicated within the work by results of measurements on paragneisses surrounding the Melechov Massif. Hence, in contrast to the lower limit of reliable measurements on the order of 10^{-18} m^2 (here) and of 10^{-19} m^2 (Rosener & Géraud 2007; Géraud et al. 2010), the lowest granite permeability values of Hanák & Ondra (1996) can be considered to represent the actual permeability and not the lower limit of the setup resolution. Therefore, the lowest permeabilities of fresh Lipnice granite we have characterized by interval < 10^{-18} m^2 are likely to be on the order of 10^{-19} m^2.

The pristine Lipnice granite TC value 2.68 W m^{-1} K^{-1} is lower than 2.84 - 3.45 W m^{-1} K^{-1} reported for three of four measured samples of fresh SSF granite in Surma & Géraud (2003), the last one featuring a lower value 2.55 W m^{-1} K^{-1}. The latter work characterized these fresh samples by porosities 0.33 - 0.82 % and two of them having porosities 0.56% also by density 2.64 - 2.65 g cm^{-3}. Hence, compared to the SSF granite, the Lipnice granite shows rather low TC given its porosity 0.32 % and bulk density 2.645 g cm^{-3} (Tab. 6). With respect to the mean composition, the Lipnice granite is likely to have higher TC with quartz content of 33-35 % (Chapter IV, Procházka & Matějka 2006) as compared to 28 % of the mean SSF granite (Genter 1990). The high variability of the cited values may be due to the coarse grain of SSF granite or to therein reported frequent quartz veins (TC of quartz is 6.5 - 7.7 W m^{-1} K^{-1}; Clauser & Huenges 1995; Guéguen et Palciauskas 1992).

5.1.2 Fractured fresh granite

According to our results the fractured fresh Lipnice granite facies is associated with porosity of at least ~ 0.5 % and not exceeding ~ 1 % accessible by throats slightly larger than characteristic for the pristine granite. Although the PTD increase is not striking as described by the MPTD of the pristine and the fractured facies (Tab. 7), a shift of the incremental porosity curve principal peak towards larger PTD can be seen on the example of samples 11 and 10 (Fig. 11) and also by comparison of the mean facies curves in Fig. 13. Furthermore, apart the peak shift it can be clearly seen on the same curves that the fractured facies is associated with higher incremental values for diameters larger than the MPTD, approximately in the range 0.5 - 0.8 μm. Despite the rather broad range of trapped-to-total porosity ratio and V_p for the fractured facies, it can be seen that the latter two quantities feature also substantially lower values than for the pristine granite. We term the facies "fractured" and attribute its values to the effect of microcracks for several reasons. First, the corresponding measurements were executed on specimens from walls of macroscopic fractures, typically extracted including the fracture surface or at several centimeters towards the wall rock beyond the alteration halo if developed. The presumed microcracks thus have formed due to the macroscopic fractures which are commonly accepted to be associated with microcracks formation in the fracture tip propagation process zone or ultimately during evolution of a fault damage zone (Scholz 1968; Tapponnier & Brace 1976; Kranz 1983; Scholz et al.1993; Anders & Wiltschko 1994; Caine et al. 1996; Evans et al. 1997; Vermilye & Scholz 1999; Zang et al. 2003; Wilson et al. 2003; Mitchell & Faulkner 2009; Faulkner et al. 2010; Faulkner et al. 2011).

Furthermore, rare permeability values above the setup sensitivity lower limit have been measured, which means increase in permeability with respect to the pristine samples where no such values have been measured. In addition, several fresh granite plugs containing a small fissure with straight walls intersecting longitudinally the plug yielded permeabilities ~ 10^{-18} - 10^{-16} m^2 (Tab. 5). The amplitude of the latter values within the hereby usual range of the fractured facies permeabilities is convincing on its own, however, the effect of the fissure is even more striking when the permeability values are compared relatively within a sample, i.e. presumably within the most proximate material. Hence, we have measured a difference of up to two orders of magnitude for sample 12 (12B_F_Y contained fissure) and of one order of magnitude for the fresh part of sample 5 (5B_FI_Y contained fissure). Even though different specimens were used for the porosimetry and for the permeametry measurements thus precluding direct derivation of the porosity-permeability relation, we can compare them approximately. Hence, the permeable fissure

porosity might have been ~ 0.3 - 0.4 % for sample 12 and ~ 0.4 % for sample 5 (specimens 12_1, 12_2, 5A_5, Fig. 15, see also photographs in Fig. A3). Simple comparison of the mentioned variations in permeability and porosity yields one or two order of magnitudes higher permeability per 0.2 % of fissure porosity. This estimation is in agreement with the values for granite specimens of group 1 of Rosener & Géraud (2007) characterized by no important alteration, by porosity made up dominantly of cracks and by abrupt increase of permeability with porosity at generally low total porosity values < 1 %. This may explain the similarly high values frequently reported for fresh SSF granite (Géraud et al. 2010) as well as the permeabilities of 6 x 10^{-18} - 1 x 10^{-17} m^2 reported by Machek (2011) for Kouty granite sampled near fractures. The effect of microcracks is also plausible to explain the higher range of permeability values (10^{-18} - 10^{-17} m^2) we have measured for the fresh, macroscopically non fractured specimens from quarry samples.

Based on our macroporosity measurements of specimens containing visible crack(s), pore volume of 0.22 % has been associated to a single and very thin (limit of visibility by unaided eye, ~ 10 μm) crack with straight walls (specimen 3A_2). For low as well as for high total porosities, the prevailing trend in the data is that the volume of macroporosity is lower than volume of microporosity (Fig. 15). Furthermore, high proportion of macroporosity characterizes the most cracked and pervasively altered specimens. However, a single, open and blunt crack may be related to macroporosity volume of ~ 0.85 % even in case of macroscopically otherwise massive and weakly altered granite with low microporosity volume ~ 0.70 % (specimen 12_3, Fig. A3). These observations highlight both the very low porosity of the studied pristine granite 0.32 % as well as the effect of cracks on the rock total porosity.

Regarding previous porosimetric measurements of the Melechov Massif granites, water-saturation triple weighing technique applied on Lipnice granite yielded 1.5 - 3.5 % (Hanák & Ondra 1996) and the same technique applied on the other, medium to coarse grained granite types yielded 1.7 - 3.8 % (Machek 2011). Based on the description in the cited works we are unable to judge the state of alteration of the examined specimens. However, the apparent discordance with respect to our values and in particular to the lowest ones arises probably from the different applied techniques. It has been shown that the mercury and water porosimetry applied on specimens with common source granite type may roughly correlate on the scale of 10 % of total porosity (Surma & Géraud 2003). However, the associated error is sufficient to cause the observed discordance particularly for total porosities below 1 %.

Our final remark regarding the fractures in fresh granite relates to the porosimetric

measurements of the two specimens prepared from sample 10. Before describing the related phenomena, in this case it is worth detailing the way of preparation of such specimens. To prepare them, we have first extracted a parallelepiped of the fracture wall including the fracture surface. The size of this small orthogonal pre-specimen was ~ 3 x 3 x 2 cm with the longer dimensions representing on one side the area of the fracture surface. In a second step, we have sawed the pre-specimen in two equal parts and from one of the parts we have carefully removed the outermost (< 1 mm) layer of the fracture surface. Doing so resulted in two specimens with no macroscopic difference except the presence or absence of the fracture surface (Fig. A3). Within the analytical error, the porosimetric curves (Fig. 11) as well as the bulk porosimetric properties (Tab. 6) measured on these two specimens are identical and lead us to claim two important implications. First, there is no porosimetric effect linked to the presence (or absence) of the fracture surface in case of barren fractures in fresh granite. This is in agreement with macroscopic observation of the fracture surface showing no convincing signs of mineral precipitation as confirmed by the SEM observation (Fig. 8a). Second, the degree of similarity of the porosimetric results implies high resolution of the hereby applied experimental setting and routine even for very low total porosity (0.82 - 0.85 % in this case) of the material under test.

5.1.3 Fractured Fe-oxide-altered granite

The characteristic treat of the Fe-oxide altered facies is a macroscopic reddish colour and distribution of amorphous orange-red-brown, Fe-rich material along grain boundaries and cracks in the corresponding granite samples (Fig. 7). Within this facies we distinguish two subfacies according to the macroscopic degree of fracturing and of the related petrophysical properties.

The values for the less fractured of the two distinguished Fe-oxide alteration facies have been measured on specimens from the Fe-oxide alteration halos of samples 3, 5 and 8 intersected by localized single fractures. In addition, sample 5 featured two mutually intersecting fractures associated with variable macroscopic intensity of the alteration (see Figs. A1, A2 and section 3 for details). According to our measurements, the Fe-oxide alteration is associated with porosities 0.49 - 0.66 % and with permeabilities < 10^{-18} m^2. Hence, this weakly fractured Fe-oxide altered facies has lower porosities and permeabilities than the fractured fresh facies (Tab. 7). Intra-sample comparison of porosimetric curves measured on specimens from the fractured fresh and the fractured altered sample parts documents two important phenomena in addition to the mentioned decrease in total porosity. The alteration is associated with shift of the PSD principal peaks towards lower sizes from

~ 0.4 - 0.5 to ~ 0.1 - 0.2 μm and with decrease of free porosity volume dominantly in the characteristic PTD range of the fresh fractured specimen (the most evident for sample 3, see also samples 8 and 5, Figs. 11 and A3 and Tab. 6). The absolute positions of the two peaks (the fractured fresh and the fractured altered) differs from sample to sample, however the shift is in all the cases clearly discernible. The decrease of free porosity volume means lower accessibility to low aspect pores, i.e. most probably cracks, the thickness of which is consistent with the submicron PTD range of the free porosity decrease (Tapponnier & Brace 1976).

The permeability decrease linked to the Fe-oxide alteration can be documented the best on the example of quarry sample MS09_6 where a 5 - 8 cm halo of strong alteration was developed in the fracture wall. We have prepared one set of three plugs in mutually orthogonal directions from the halo and one from the fresh wall rock and measured permeability on the order of 10^{-18} m^2 for the altered part and of 10^{-17} m^2 for the fresh part. In addition, both the sets show very consistent values differing not more than the sensitivity of the applied setup suggesting low anisotropy of porosity interconnection. For the fresh part this might mean either primary microstructure isotropy or crack orientation isotropy or both of them. Furthermore, in the altered part the effect of the alteration has to be considered as a possible agent decreasing former anisotropy.

The related V_p data bring some more light onto these complex relations. The measurements on the set of fresh MS09_6 plugs yielded low V_p anisotropy with maximum difference of 0.1 km s^{-1} between the three directions. The altered set, on the other hand, yielded V_p higher by 0.2-0.3 km s^{-1} along both fracture-parallel directions than in the direction perpendicular to the fracture. These measurements can be interpreted in two compatible ways. First, there is a high-V_p material discontinuously distributed along planar structures with the anisotropy shape longer axes parallel to the fracture plane. Hence, the P-waves travelling parallel to the fracture plane have traversed the material earlier than those travelling perpendicular to it due to deceleration by the intercalated low-V_p material. Second, there are low-V_p planar structures preferentially oriented parallel to the fracture. Hence, again, the P-waves travelling perpendicular to the fracture plane are decelerated more than the P-waves travelling parallel to the fracture thus bypassing the low-V_p structures. We suggest that both the principles can be result of fracture-parallel preferentially oriented planar fabric made up by cracks filled by the Fe-oxide material. Given the elevated V_p of Fe-oxides (hematite and magnetite respectively 6.5 and 7.4 km s^{-1}, Birch 1961), the low V_p of air (~ 0.3 km s^{-1}, e.g. Wyllie et al. 1956) and finally the decelerating effect of any mechanical discontinuity, the high-V_p material is represented by the Fe-oxides observed along cracks,

the walls of which represent the low-V_p structures.

Finally, the Fe-oxide altered specimens have yielded slightly (~ 5 %) yet regularly higher mean TC values than either the fractured fresh or the pristine facies specimens (Tabs. 7 and 4) in good agreement with the hematite and magnetite TC respectively 12.5 and 4.5 W m^{-1} K^{-1} (Clauser & Huenges 1995). Increase in TC of ~ 0.2 W m^{-1} K^{-1} has also been demonstrated by TC measurement along a profile traversing the rather sharp transition from the fresh to the altered fracture wall rock of sample MS09_06 (Fig. 9a).

Hence, results of all the methods point to crack filling by Fe-oxide material sealing the crack permeability network and increasing the thermal conductivity. Sealing by hematite at low total porosities has also been observed in SSF granite by Sausse (2002). Given that the alteration is related to higher specimen SD than for both the unaltered facies, import of external Fe-rich material can be assumed related to this alteration facies.

The values measured on the densely fractured sample 4 show distinct properties as compared to the less fractured sample 3, 5 and 8 and has lead us to distinguish a facies of Fe-oxide alteration associated with intense fracturing (Tab. 7). Compared to the less fractured Fe-oxide facies, the total porosity is higher and close to the upper limit of the fresh fractured facies, i.e. ~ 1%, the permeability is by one order of magnitude higher and the V_p substantially lower with 3.7 - 4.2 km s^{-1}. The MPTD shows no striking difference, however, population of porosity with larger PTD can be clearly seen by comparing the porosimetric curves of sample 4 with e.g. sample 3 (Fig. 11). In addition, the same comparison also shows increase of free porosity as compared to the less fractured Fe-oxide facies (3A_2, 3B_2) with the shape of the free-porosity incremental curve similar to the one in the fractured fresh specimens (3A_1, 3B_1). Furthermore, the PTD range of the free porosity increase coincides with the one observed in fractured fresh specimens (see the corresponding subsections above). This similarity indicates probably the same phenomena in both the fresh (pristine) and the Fe-oxide facies, i.e. formation of cracks. Hence, the intensive fracturing reopens the cracks sealed by the Fe-oxide alteration or leads to formation of new ones. Furthermore, the assumed sealing effect of the Fe-oxide material can be demonstrated in another way also on the facies-representative sample 4. The porosimetric curves of the two tested specimens show very similar shape in the PTD range below ~ 0.3 μm with, however, the Fe-oxide coating-bearing specimen 4_1 showing slightly higher amplitudes. Inversely, in the PTD range 0.4-3 μm it is the coating-free (removed) specimen 4_2 showing clearly higher porosity values. Hence, we suggest that the Fe-oxide coating prevented the mercury intrusion to the large-throat cracks providing in the uncoated specimen the access to the principal porosity of the sample. In turn, this porosity was only intruded by the mercury at

higher pressure, i.e. via smaller throats thus resulting in apparent increase in porosity with PTD below 0.3 μm. For this interpretation we have assumed that the internal structure of the specimens is similar, and a consequence of the interpretation is that no change in crack fabric (sealing or formation) should be observed between the specimens. Both the assumption and the consequence are in good agreement with the proximate values of total porosity and of TTR and finally also with the shape and amplitude of the free porosity curves of both the specimens.

5.1.4 Fractured chlorite-altered granite

The fractured chlorite altered facies was based on sample 7 featuring strongly chloritized majority of biotite grains and accompanied by the Fe-oxide alteration characteristics, i.e. Fe-rich material along grain boundaries and cracks (Fig. 7). Observations on SEM revealed chlorite on the fracture walls (Fig. 8). Apparent macroscopic porosity is dominated by one steep and two flat fractures marked by dominantly chlorite and Fe-oxide precipitates, respectively. We have sampled walls of these fractures including the chlorite- and the Fe-oxide-dominated parts as well as the mixed parts appearing near intersection of the two fracture sets (Figs. A1 and A3). Porosimetric analyses on these specimens yielded microporosity values ~ 2.5-3.8 % associated with high values of MPTD ~ 0.3 - 0.6 μm, variable TTR and low skeletal density (Tab. 7). Taking into account all the measured PTD range (5 nm - 300 μm), the chlorite facies is associated with total porosity values up to ~ 4.3 %, which is, apart the weathered facies, the highest value (Tab. 6). Furthermore, apart the weathered facies, the chlorite facies features the highest permeability ~ 2 x 10^{-17} m^2 with no significant anisotropy (Tab. 5). In SSF granite, the alteration facies involving hematite and chlorite has been characterized by total porosity values 5.6 - 6.7 %, permeability ~1 x 10^{-19} m^2 and thermal conductivity 2.81 - 2.96 W m^{-1} K^{-1} (Géraud et al. 2010). The chlorite facies of Lipnice granite thus shows lower porosities, higher permeabilities and lower TC (2.69 W m^{-1} K^{-1}) indicating important interconnection of porosity as also supported by the permeability anisotropy. Within this scope, the Lipnice chlorite facies corresponds to the least porous specimens of group 3 of Rosener & Géraud (2007) characterized by increasing permeability with porosity of up to ~ 4 % and decreasing permeability for higher porosity values. The latter work has explained this behavior in terms of increase of the porosity connectivity turning into increase of the porosity tortuosity at higher porosities. This interpretation was supported by lower ratio of pore area over pore volume for this facies than for the less altered ones. Hence, the rather high permeabilities coupled with intermediate porosities of the Lipnice chlorite facies correspond to the stage of fracturing-

alteration process where the porosity is made up dominantly by cracks as also supported by high TTR and low VP for most of the specimens (Tab. 6).

5.1.5 Fractured clay-altered granite

This facies was based on porosimetric measurements of sample 9 characteristic by densely spaced fractures (Fig. A1), by prevailing bleached biotite grains and Fe-rich material along major cracks (Fig. 7) and by veil-shaped smectite associated with grape aggregates of monazite on fracture walls (Fig. 8). The facies features respectively micro- and bulk porosities of 1.3 - 2.0 and 1.7 - 2.8 %, the lowest measured MPTD values ~ 0.1 - 0.2 μm, low permeability on or below the order of 10-18 m2, highly variable SD 2.609 - 2.661 g cm^{-3} including one of the lowest as well as the highest measured value, variable V_p and the highest mean TC value 2.89 W m^{-1} K^{-1} (Tab. 7). According to the shape of the incremental porosimetric curve characteristic by a dominant peak at PTD ~ 0.1 μm and a subdominant peak at ~ 0.02 - 0.04 μm (Fig. 11), this facies correspond well to the SSF granite group 3 of Rosener & Géraud (2007). The clay facies thus probably corresponds to the low porous members of the mentioned group as indicated by the lower porosity by ~ 1 - 2 % and the permeability lower by one or two orders of magnitude relatively to the chlorite facies. The low permeability is also in good agreement with the associated generally low pore throat diameters (Katz & Thompson 1986). The high variability of the skeletal density corresponds to the variability in composition of the prepared specimens with the highest one having been measured on specimen containing the most of the Fe-rich material on the fracture wall (Tab. 6, Figs. 14 and A3). Similarly, the high TC might be due to the Fe-rich precipitates but most probably also to the abundant monazite featuring at room temperature higher TC than granite ~ 3 - 12 W m^{-1} K^{-1} (Winter & Clarke 2007).

5.1.6 Fractured weathered granite

The weathered facies was defined based on the two uppermost samples from the borehole (1st and 3rd m) being macroscopically the most porous and in case of sample 2 also the most altered giving it the appearance similar to that of the chlorite facies sample 7 (Figs. A1, A3). Within the sample collection, the measured weathered facies values are extreme in terms of many of the measured quantities with the sample 1 being exceeded by the sample 2. The microporosity varies from ~ 1.4 - 1.6 % for the less fractured to ~ 2.9 % for the more fractured sample 2 and in terms of the bulk porosity the ranges are respectively ~ 1.8 - 2.2 % and ~ 3.8 - 6.5 % pointing to the importance of macroporosity in the weathered facies (Tab. 6 and Fig. 15). Both the facies are associated with high MPTD 0.36 - 0.72 μm and

low TTR 65 - 78 % in agreement with the macroscopic high intensity of fracturing. Both V_p and TC of the facies are low, 3.4 - 3.7 km s^{-1} and 2.53 W m^{-1} K^{-1} for the less fractured and 1.9 - 2.6 km s^{-1} and 1.97 W m^{-1} K^{-1} for the more fractured. All the parameters indicate increasing effect of fractures causing probably also the highest measured permeability value 6 x 10^{-16} m^2 for the most fractured and altered sample 2. A network of fracture-subparallel cracks could also explain the sample 2 V_p and permeability anisotropy with the lowest V_p and permeability perpendicular to the fracture and high values along directions subparallel to it (Tab. 5).

5.2 Relation between measured petrophysical properties

The scheme of facies is based mainly on the detailed porosimetric analyses which yielded distinct parameters in function of both the degree of fracturing and the alteration mineralogy (Figs. 13 and 14). The other methods also reflect these and the macroscopic properties of the samples, however, with more variability. This is partly due to lower number of specimens and also to the apparently complex interplay between the intensity and style of fracturing on one hand and the intensity and mineralogy of alteration on the other hand. In order to examine the relation of permeability, P-wave velocity and thermal conductivity on the pore space properties, we have plotted a system of XY charts showing the relations between the two sets of values (Fig. 16). The porosimetric values measured on the specimens used to define the facies were averaged, whereas all the sample-related values measured by the other petrophysical techniques were plotted to show their variability range. In addition to this exclusively MEL-5 borehole-related data, the values of permeability, P-wave velocity and thermal conductivity for all the dataset including also the quarry samples were plotted against each other in Fig. 17.

The permeability increases proportionally to the pore throat diameter and the pore volume seems to be important mainly for the strongly altered high porosity facies. On the other hand, for fresh and Fe-oxide facies the permeability features high variability in a small porosity range < 1% suggesting primordial dependence on the interconnectivity of the pore space dominantly provided by cracks. The decrease of permeability with higher proportion of trapped porosity may signify increase in the pore network tortuosity.

The V_p is variable for the least porous Fe-oxide and fresh facies and decreases markedly with fracturing and associated higher pore volume and lower trapped porosity proportion. The V_p decrease is more sensible for the weathered facies than for the clay and chlorite facies in good agreement with their respective MPTD suggesting dependence of the V_p also on the pore throat diameter. The change in mineralogy related to the strongly

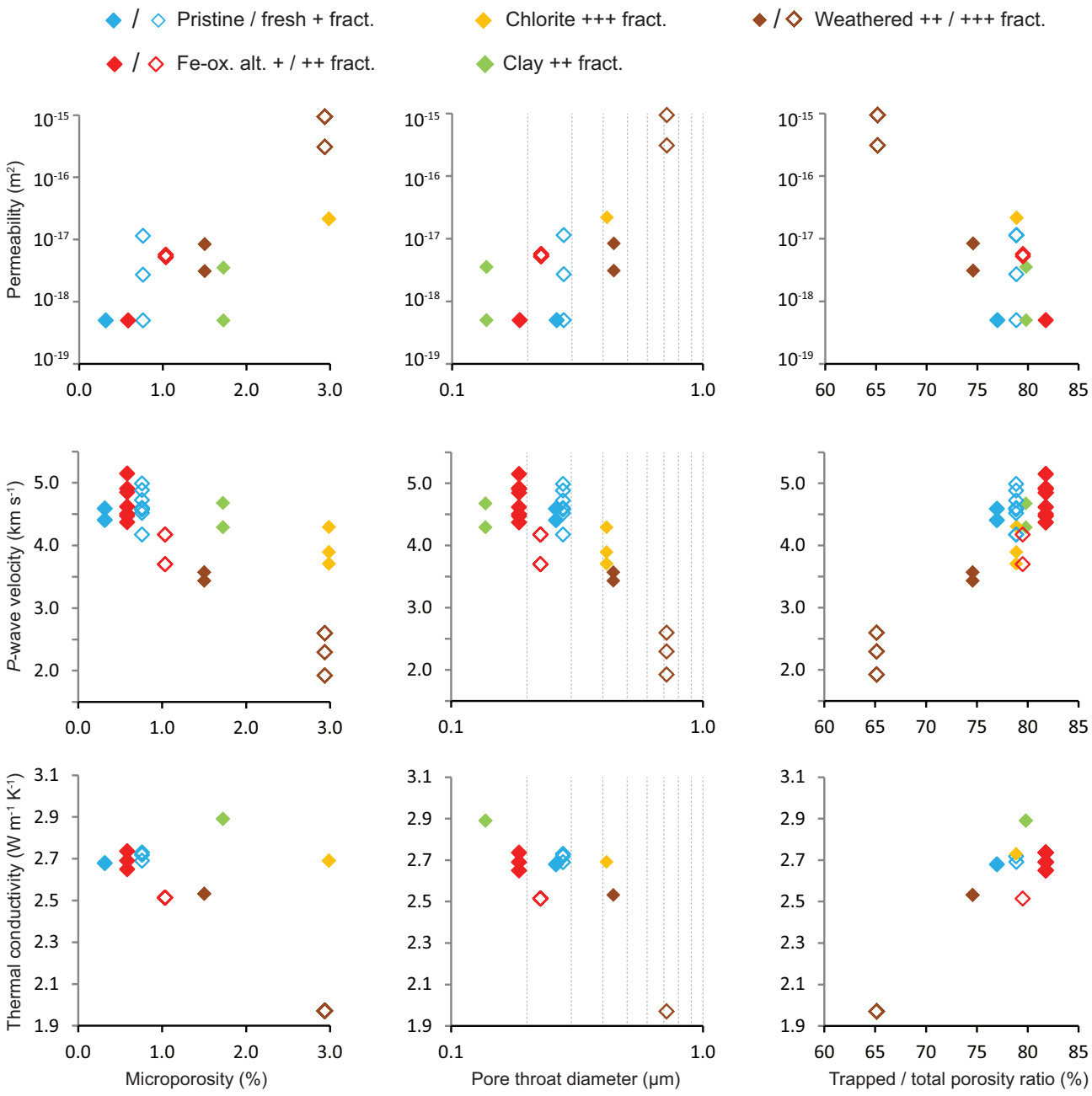

Figure 16 *(continued on the next page)***.** Relations between measured petrophysical properties. X-Y charts showing relation between permeability, P-wave velocity, and thermal conductivity on vertical axes (from top to bottom, also on the next page) and microporosity (5 nm - 6 µm), median pore throat diameter (volumetric), trapped-to-total porosity ratio, bulk density and skeletal density on horizontal axes (from left to right continued to the next page). Symbols represent different fracturing and alteration facies of the granite (see legend above the charts; full / empty symbols for less / more fractured variety within alteration facies; "+" symbols correspond to macroscopic degree of fracturing (fract.); ox. - oxide.

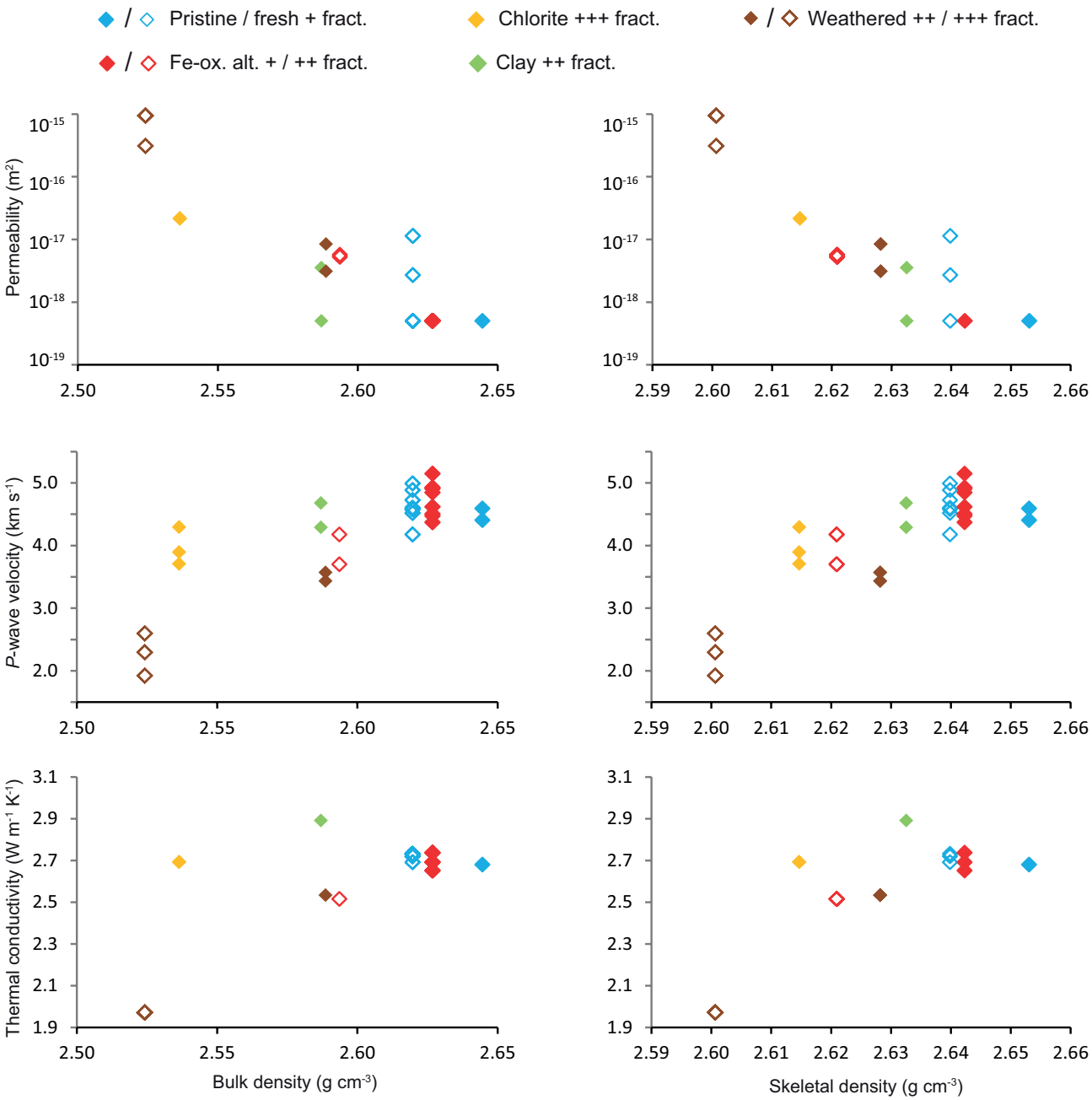

Figure 16 *(continued)*. Relations between measured petrophysical properties.

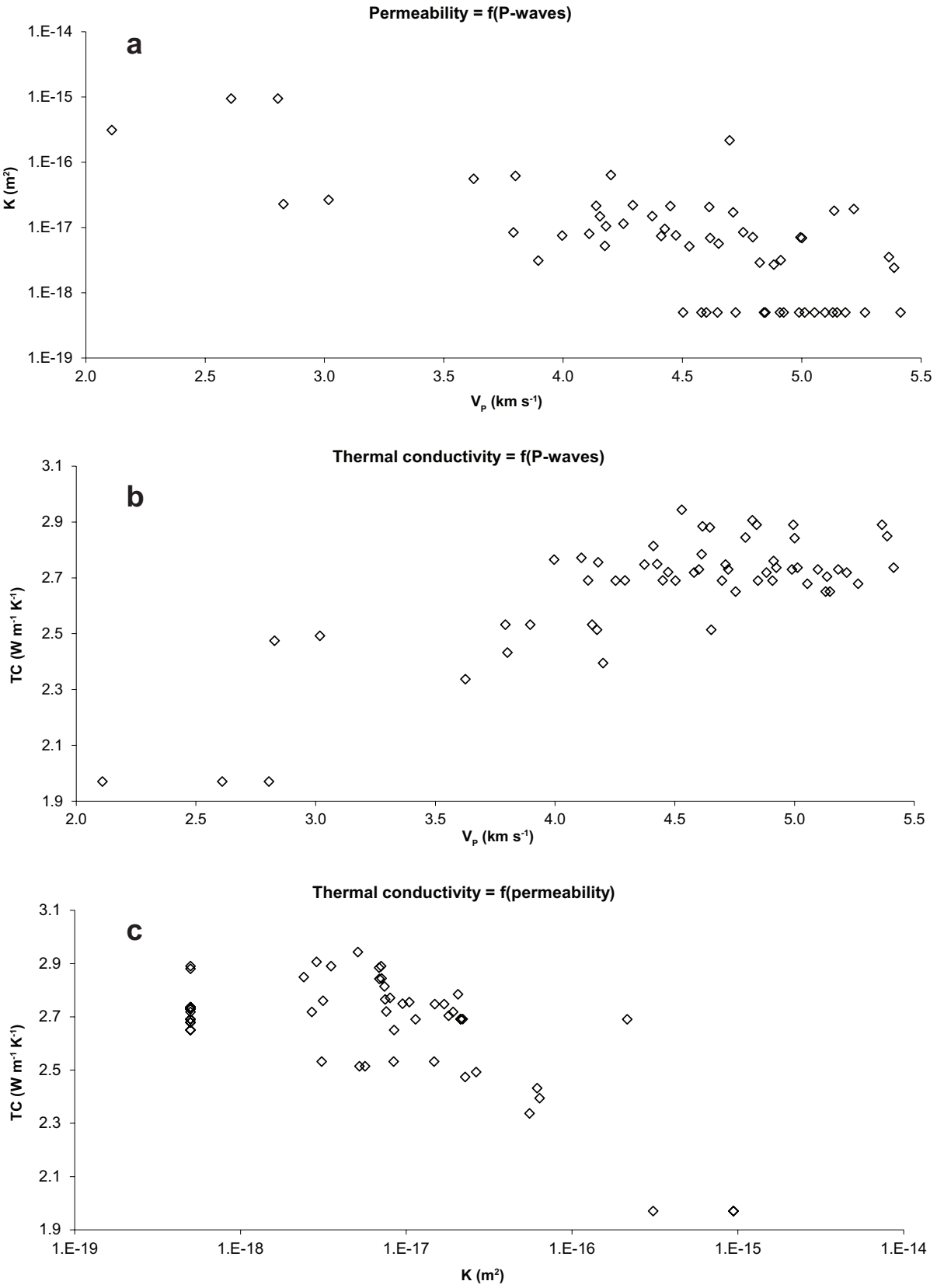

Figure 17. Correlations of measured petrophysical quantities. (a) permeability vs. P-wave velocity, (b) thermal conductivity vs. P-wave velocity and (c) thermal conductivity vs. permeability. Values of permeability and P-wave velocity measured on identic plugs. Permabilities lower than the used setup sensitivity are attributed a constant value of $5x10^{-19}$ m^2. For thermal conductivity the mean value per sample is attributed to all values of permeability and P-wave velocity measured on plugs from the corresponding samples

altered facies may also decrease the V_p via intragranular porosity associated with the phyllosilicate alteration phases.

The thermal conductivity correlates the most remarkably with the pore throat diameter whereas it shows rather scattered or clustered pattern in relation to the pore space volume and the trapped porosity proportion. This suggests the TC to be dependent on the aperture of voids rather than on their volume or on the pore network geometry. This observation is coherent with the correlation of the TC and the permeability (Fig. 17c) as the latter is also dependent mainly on the MPTD, i.e. on the aperture of voids.

The decrease of permeability with bulk density (Fig. 16) is probably linked to the change in mineralogy associated with the character and intensity of alteration which consequently modify the pore space connectivity and tortuosity conditioning the permeability. With decreasing bulk and skeletal density the V_p and TC decrease suggesting influence both of fracturing intensity and of alteration-related change of mineralogical composition and this particularly for the V_p.

5.3 Relation of the massif fracture system and alteration

The most fractured and altered samples were taken from the borehole levels of intense fracturing characterized by multiple intersecting fractures, by multiple densely spaced subparallel fractures, by combination of the two previous or by pervasive fracturing. The orientation of the sample-related fractures (Tab. 3) reveals that the most altered chlorite facies sample 7 and the clay facies sample 9 are linked to WNW-ESE or N-S striking steep fractures intersected by a set of gently dipping fractures. For the shallow parts of the borehole the most fractured and altered samples are linked to multiple intersecting gently and moderately dipping fractures. Furthermore, the fresh sample 10 featuring barren fracture is the only related to steep NNW-SSE striking joint. The Fe-oxide facies are associated dominantly with the shallow (< 35 m) borehole levels and related to fractures of various dips suggesting interplay of several sets of fractures including exfoliation joints. The latter together with steep N-S striking fractures may be involved in alteration of the clay facies, whereas only steep fractures including WNW-ESE and N-S strikes probably allowed precipitation of Fe-oxides on fracture walls of the deep sample 12 showing otherwise weak alteration. In terms of the massif fracture system (see chapter II), apart exfoliations mainly fractures of set 1 and 3 are associated with wall rock alteration or precipitations whereas the barren fracture in fresh granite is related to a set 2 joint.

The fact that we do not observe higher porosities than 1 % linked to fractured fresh granite but we do in the intensively fractured and altered facies is striking and leads

us to consider several explanations. First, we may have unintentionally not sampled such material possibly present within the borehole core. Though we cannot exclude such possibility, it seems unlikely as our focus during sampling was on various appearance of granite in vicinity of fractured rock and except the pristine granite sample 11 all of our samples contained or were limited by fractures. Second, it has to be considered that higher porosities within the granitic massif are exclusively associated with strong alteration which itself is conditioned by high intensity of fracturing. In field as well as in the borehole core the Fe-oxide alteration is clearly limited to distance of several centimeters from localized fractures. On the other hand, the chlorite and clay alteration facies encountered only in the borehole core were associated with fracture zones rather than with single fractures (see Figs. A1 and A2). These observations indicate that the alteration is highly localized and thus not due to any process which may affect significantly larger volumes of the non-fractured rock within the fractured massif. Hence, it is possible that only fractures being part of an interconnected fracture network allowed fluid circulation and enabled the rock alteration. In turn, this implies that the fractures in the sampled fresh granite have not been part of such interconnected network. In other words, for the fresh facies the fracturing intensity either in terms of fracture density or size was not important enough to connect it to the network. In consequences this explains the limited range of porosities associated with fractures in fresh granite. Either the fracturing was not intense enough to interconnect the network and thus we now measure low total porosities of fresh granite or the fracturing was more intense and enabled alteration, the facies of which we may now measure as both high or low porosity samples that are, however, strongly altered in association with the necessary fracturing. Finally, a third way to explain the low porosities of fractured fresh granite is that the porosity we have measured did not comprise some part of the total pore volume of the rock under test. This effect is inherent to mercury porosimetry technique due to the measurement principle of fluid intrusion from outside into the specimen by voids accessible via its external interface to which the mercury is forced during the experiment. Such a case can only hardly be excluded for natural material and therefore should be a priori considered as true in the present study. A comparison of granite porosity measurements by mercury porosimetry and by X-ray tomography supported by SEM analysis has been demonstrated by Géraud et al. (1993). In this work, porosity 0.4% of fresh La Borne granite was observed to increase with alteration to 5.1 % as measured by the mercury injection or to 8.2 % as observed by the X-ray technique. The absolute difference in porosity of 3.1 % means that the mercury porosimetry underestimated the X-ray tomography value by 38 % and such discrepancy has to be taken into account when considering the porosimetric data. The

phenomena of not connected porosity may also explain the above mentioned discordance between the total porosity values measured by mercury porosimetry (here) and by the triple weighing method (Hanák & Ondra 1996).

Chapter IV:

Article in Geophysical Journal International:

Elastic anisotropy and pore space geometry of schlieren granite: direct 3-D measurements at high confining pressure combined with microfabric analysis

Geophysical Journal International

Geophys. J. Int. (2013) doi: 10.1093/gji/ggt053

Geophysical Journal International Advance Access published April 19, 2013

Elastic anisotropy and pore space geometry of schlieren granite: direct 3-D measurements at high confining pressure combined with microfabric analysis

Martin Staněk,[1,2,3] Yves Géraud,[2] Ondrej Lexa,[3] Petr Špaček,[4] Stanislav Ulrich[5] and Marc Diraison[2]

[1] *Institute of Geophysics, Czech Academy of Sciences, Boční II* 1401, 14131, *Praha* 4, *Czech Republic. E-mail: stanekm@ig.cas.cz*
[2] *University of Lorraine, Nancy, France*
[3] *Charles University, Praha, Czech Republic*
[4] *Masaryk University, Brno, Czech Republic*
[5] *Centre for Exploration Targeting, University of Western Australia,* 35 *Stirling Highway, Crawley, WA* 6009, *Australia*

Accepted 2013 February 5. Received 2013 January 24; in original form 2012 August 27

SUMMARY

Pore space geometry of granitic rocks and its evolution with depth are key factors in large-scale seismics or in projects of enhanced geothermal systems or of deep hazardous waste repositories. In this study, we studied macroscopically anisotropic schlieren-bearing granite by experimental *P*-wave velocity (V_P) measurements on spherical sample in 132 directions at seven different confining pressures in the range 0.1–400 MPa. In order to discriminate the phenomena affecting the rock elastic properties we analysed the orientation of microcracks and of grain boundaries and we measured the anisotropy of magnetic susceptibility of the rock. Three sets of microcracks were defined, with two of them linked to the massif exfoliation process and one to cooling contraction of the massif. During pressurization the measured mean V_P and V_P anisotropy degree at ambient pressure and at highest confinement (400 MPa) yielded 3.3 km s^{-1} and 24 per cent, and 6.2 km s^{-1} and 3 per cent, respectively. The associated V_P anisotropy pattern was transversely isotropic and governed by the schlieren, with a minimum V_P direction perpendicular to them and a girdle of high V_P directions parallel to them. The highest change in V_P was observed between 0.1 and 10 MPa, suggesting a significant closure of porosity below depths of 500 m. Change of the V_P anisotropy pattern to orthorhombic together with increase of mean V_P and V_P anisotropy degree during depressurization was attributed to inelastic response of one of the sets of microcracks to the loading-unloading cycle.

Key words: Magnetic fabrics and anisotropy; Microstructures; Seismic anisotropy; Fractures and faults.

INTRODUCTION

Over the last three decades, granitic rocks have been prospected as possible host rock massifs for deep (<1 km) radioactive waste repositories (Rempe 2007) and for even deeper (<5 km) enhanced geothermal systems (Tester *et al.* 2006). In addition, large scale models on continental crust seismicity (Goleby *et al.* 2006) and strength (DeNosaquo *et al.* 2009) take granite to be the rock representative of the continental upper crust. In all these applications, understanding of petrophysical properties of granitic rocks, such as permeability, thermal conductivity (TC), elastic wave velocity and mechanical strength, among others, appears to be critical. The anisotropic attributes of the above mentioned physical properties are controlled by the anisotropy of both the rock pore space and the rock solid matrix.

The microporosity in crystalline rocks is represented mainly by microcracks (microfractures, cracks), which can be differentiated according to their position with respect to the rock matrix (inter- or intragranular cracks, grain boundary cracks and cleavages cracks; Kranz 1983). The key microstructural characteristics of the rock matrix affecting the rock elastic properties are grain size, grain shape and shape preferred orientation (SPO) as well as the rock modal composition and crystallographic preferred orientation (CPO) of the constituent phases.

The contribution of each of the above mentioned features to the bulk elastic anisotropy is thoroughly discussed in the literature (see Ullemeyer *et al.* 2006; Machek *et al.* 2007 and references therein). The crack-induced porosity is important only at shallow levels of the crust as it is assumed that cracks close progressivelywith increasing lithostatic pressure and become completely closed at depths of

3–6 km, that is, at effective pressures of 100–200 MPa. CPO becomes the main parameter controlling rock elastic anisotropy at depths where the crack porosity is closed (Kern & Wenk 1990; Kern 1993), and plays an important role in low porosity (<10 per cent), crystalline rocks. In granitic rocks, even small fractions (<10 per cent) of micas and amphiboles contribute significantly to elastic anisotropy due to their cleavage cracks, which have been shown to stay open even at confining pressures of up to 300 MPa (Babuška & Pros 1984). Especially biotite can contribute to the bulk rock elastic anisotropy significantly (Kern & Wenk 1990), as shows its single crystal elastic anisotropy of 44 per cent (Simmons & Wang 1971). In addition to CPO, biotite and muscovite SPO has been found to contribute significantly to the bulk rock elastic anisotropy (Kern *et al.* 2009).

In granites containing biotite and muscovite, but no amphibole or ferromagnetic minerals, the orientation of biotite can be easily evaluated by analysis of anisotropy of magnetic susceptibility (AMS; Hrouda 1982; Borradaile & Henry 1997), as the paramagnetic biotite is the principal carrier of the magnetic fabric with single crystal magnetic susceptibility one order of magnitude higher than that of muscovite and two to three orders of magnitude higher than those of diamagnetic quartz or feldspars (Tarling & Hrouda 1993). In the case of dia- and paramagnetic minerals, the AMS is controlled by orientation of the crystallographic axes of minerals (Khan 1962). Isometric crystals of biotite have an AMS ellipsoid that is nearly rotationally symmetric, with its short axis subparallel to the crystallographic *c*-axis, that is, perpendicular to the cleavage plane (Zapletal 1990; Martín-Hernández & Hirt 2003). For granite containing elongated biotite crystals, strong agreement has been observed between the orientations of the long axis of the biotite crystals and the direction of the highest magnetic susceptibility (Archanjo *et al.* 1995).

In order to understand the evolution of elastic anisotropy with depth and its relation to rock matrix and microporosity in mesoscopically anisotropic granite, we measured *P*-wave velocities (V_P) of spherical sample of Lipnice granite, Melechov massif, Czech Republic, for confining pressures up to 400 MPa. Furthermore, we analysed the AMS and performed qualitative and quantitative microstructural analysis of microporosity. As such, our experiments provide us with a method to study the pressure compliance with increasing depth of genetically distinct kinds of microporosity encountered in such rocks. Consequently the results can form a basis to predict the evolution of rock porosity and permeability at depth, though this was outside the scope of the present work. The applied pressure conditions simulate *in situ* depths of up to 10 km, thereby including the typical depths where engineering applications such as radioactive waste repositories or enhanced geothermal systems are commonly envisaged.

GEOLOGICAL SETTING

The Melechov massif

The sample material was obtained from the Lipnice granite outcropping near the town of Lipnice nad Sázavou, Czech Republic (49.61484°N; 15.41360°E), situated within the Melechov massif (MM) that has been chosen by the Czech radioactive repository authority (RAWRA) as a research training site. The MM represents the northernmost part of the Central Moldanubian Pluton, which belongs to the Moldanubian zone of the Bohemian Massif (Fig. 1a). The MM covers an area of about 120 km^2 and reaches down to a depth of 2–17 km (Šrámek *et al.* 1996; Mlčoch *et al.* 2000). The columnar batholith of the MM consists of four types of peraluminous two-mica granite disposed in a concentric manner. From the centre outwards these are the Stvořidla, Melechov, Kouty and Lipnice granites (Fig. 1b). Based on the discordance between the magmatic and the host rocks (Chlupáč *et al.* 2002), the intrusion of the MM granites is considered to be post-orogenic relative to the Variscan events, and formed in a time span of 315 ± 0 Ma, based on radiometric dating of monazites crystals (Breiter & Sulovský 2005). Post-intrusion deformation of the massif is represented by two principal sets of cooling-related and sometimes reactivated subvertical joints (Lexa & Schulmann 2004). Set 1 is characterized by WNW–ESE trending and fractures of several tens of meters in length and by fracture spacing of 1–5 m. Set 2 is NNE–SSW trending and is characterized by fractures of several meters in length and fracture spacing of 0.5–5 m. Another third set is recognized, which is represented by shallowly dipping (<20°) sheeted fractures (exfoliations) related to the exhumation of the massif.

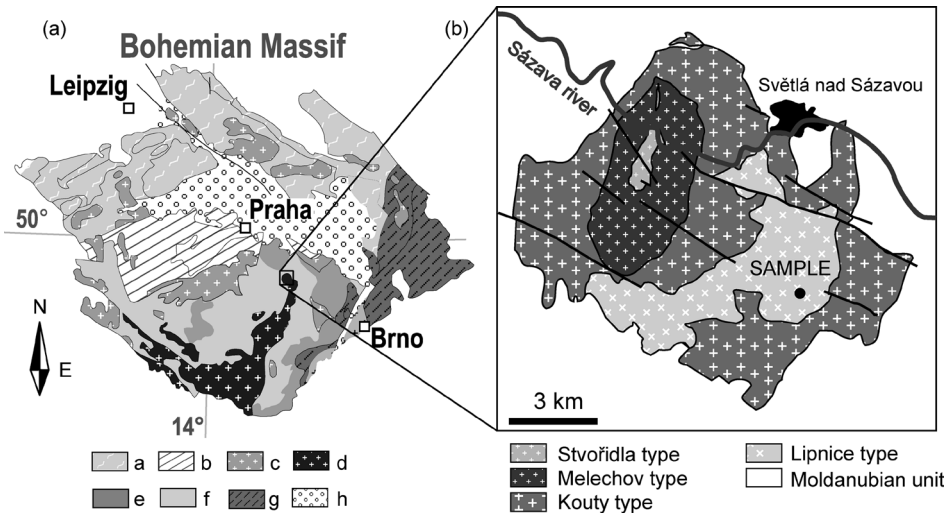

Figure 1. (a) Map showing the location of the study area, simplified geological map of the Bohemian Massif (modified after Franke 2000) (a – Saxothuringian and Lugian, b – Teplá-Barrandian, c – Variscan granitoids, d – Moldanubian Batholith, e – Gföhl unit, Varied and Monotonous unit, g – Brunovistulian, h – Cretaceous sedimentary cover), (b) Geological map of the Melechov massif with the location of the sampled outcrop (modified after Machek 2011).

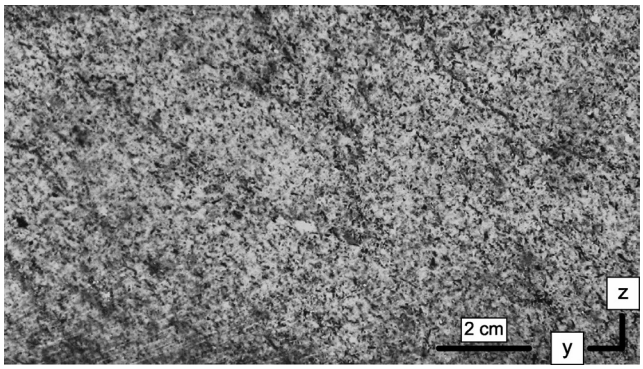

Figure 2. Photograph of the *YZ* face of the sampled block showing the folded schlieren visible in the upper part of the image. The reference fractures orientation (*XY*) is perpendicular to the section and parallel to its longer side.

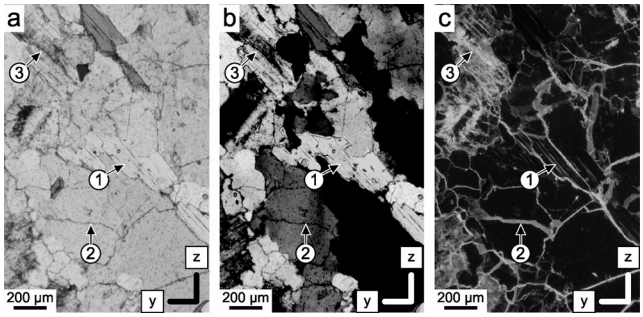

Figure 3. Photomicrograph of Lipnice granite obtained in polarized (a), cross-polarized (b) and UV (c) light. The thin section (*YZ*) is perpendicular both to the reference fractures and to the schlieren. Arrows point to representative examples of intragranular cracks in mica (1), in quartz (2) and in feldspar (3).

The sampled outcrop of the Lipnice granite

The Lipnice granite at L.n.S. displays a clear foliation visible at the mesoscale and defined by quartz- or biotite-rich bands (Fig. 2). The foliation is asymmetrically folded at both the outcrop scale and at the scale of the hand specimen. The long limbs of the folds dip at very moderate E (ESE) angles, while the short limbs are steep and strike N–S, with the fold axis lying subhorizontally in the N–S direction. Fractures observed at the outcrop follow the general characteristics given above except that set 2 is characterized by fracture clusters spaced by one to several tens of metres, with each cluster containing fractures with cm–dm spacing. A block of Lipnice granite 30 cm × 20 cm × 12 cm in size was taken in oriented manner from between two subparallel exfoliation fractures dipping 20°W. These fractures will be referred to as reference fractures in the following text. With respect to the sample block, the closest fractures of set 1 and set 2 were at distances of 1 and 10 m, respectively.

Characteristics of the samples

From this block, an oriented spherical sample of 50 mm in diameter was prepared for V_P measurements and six cylindrical cores measuring 25.4 mm in diameter and 21 mm in length were prepared for AMS measurements. After preparation to final shape, the spherical sample was oven-dried during 24 hr at 50 °C and then covered by three thin layers of epoxy resin to protect the material from the confining oil, present in the setup.

Three mutually perpendicular thin sections were also prepared from the block, with one of them perpendicular both to the reference fractures and to the schlieren and another one perpendicular to the reference fractures. As can be seen in thin section photomicrographs (Fig. 3), the sample material features elongated crystals preferentially aligned with the schlieren and ubiquitous microcracks. The quartz shows mostly intra- or transgranular, curved cracks, whereas in micas and feldspars rather straight cracks often follow the mineral cleavages and are interconnected into intergranular cracks.

Microstructural analysis of the three sections was performed to determine the sample mineral composition, grain size and grain aspect ratio. A total of 779 grains was analysed using ESRI ArcGIS software for manual tracing of digital photographs and MATLAB™ PolyLX toolbox (Lexa *et al.* 2005) for geometric evaluation of the traced objects. The results of our thin section analysis are summarized in Table 1.

Mercury porosimetry yielded a sample density of 2.626 g cm^{-3} and a total porosity of 1.4 per cent, taking into account pores with access diameter between 0.3 and 5 nm. TC was measured by optical scanning method (Popov *et al.* 1999) along the principal directions of two orthogonal systems defined by the reference fractures and by the schlieren long limb. Independently on the chosen direction, the analysis yielded TC in a narrow range of 2.3–2.5 W m^{-1} K^{-1}.

EXPERIMENTAL METHODS AND TECHNIQUES

Experimental *P*-wave velocity measurement

We performed laboratory V_P measurements on a spherical sample of Lipnice granite described by Pros & Babuška (1968) (see also Pros *et al.* 1998a, 2003; Machek *et al.* 2007). The main advantage of using a spherical sample, as opposed to using an orthogonal or multiple cylindrical samples is the possibility to continuously evaluate the spatial distribution of V_P within the studied material. The method inherently eliminates any errors introduced by assumptions

Table 1. Modal proportion, grain size and grain shape aspect ratio of the Lipnice granite. Shown are means of values of the three traced thin sections. ALL, all grains; Qtz, quartz; Pl, plagioclase; Kf, K-feldspar; Bt, biotite; Ms, muscovite; a_1, a_3, long and short axis of grain shape; Q_1, Q_3, first and third quartile of the population of traced grains.

Phase	Area (per cent)	Equal area diameter (mm)				Axial ratio a_1/a_3			
		Min	Mean	Max	Q1–Q3	Min	Mean	Max	Q1–Q3
ALL		0.17	0.70	2.22	0.45–0.87	1.0	1.8	4.1	1.4–2.1
Qtz	35	0.15	0.70	1.92	0.49–0.87	1.0	1.6	3.4	1.3–1.9
Pl	33	0.17	0.71	2.78	0.42–0.89	1.0	1.7	3.4	1.3–1.9
Kf	17	0.18	0.70	2.44	0.46–0.82	1.0	1.9	4.8	1.4–2.3
Bt	5	0.19	0.52	1.11	0.36–0.64	1.0	2.8	7.7	1.8–3.4
Ms	9	0.22	0.98	2.42	0.47–1.37	1.0	2.0	3.7	1.4–2.4

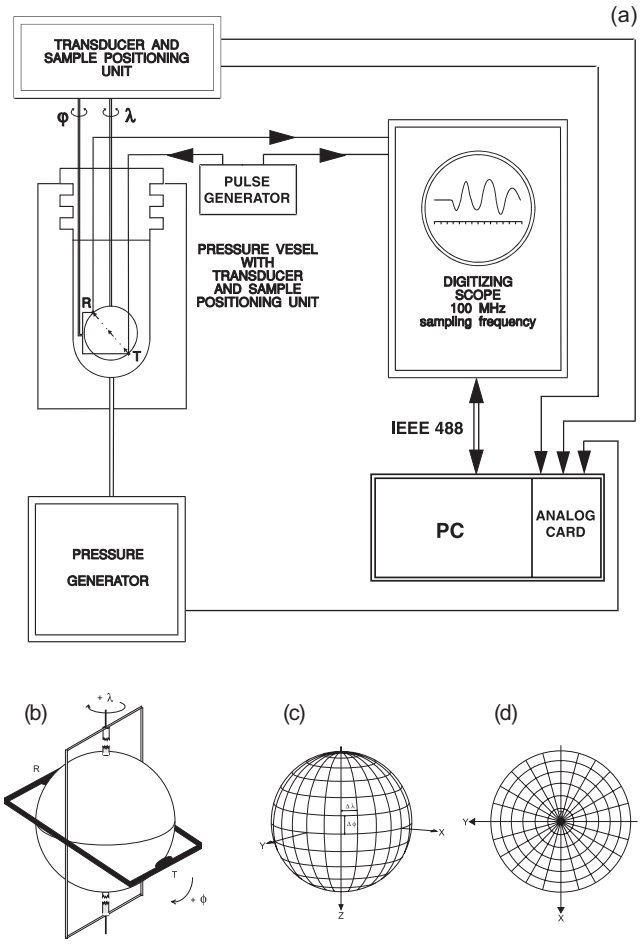

Figure 4. (a) Equipment for the laboratory study of *P*-wave anisotropy on spherical samples under hydrostatic pressure of up to 400 MPa, (b) Sample set up (T – transmitter, R – receiver) and (c, d) Grid of measurement directions with a step of 15°.

regarding the rock texture, modal composition, density and elastic constants. In this light the multidirectional measurements on spherical sample are irreplaceable, even though a recent study using 21 directions of three orthogonally cored subsamples reaches a good fit relative to the measurements on spherical sample (Louis *et al.* 2012).

For our V_P experiments we used the apparatus set up by Z. Pros (see Pros *et al.* 1998a) at the Institute of Geophysics in Prague, which consists of a pressure vessel containing the sample, which is placed in a special positioning unit, a pulse generator, a pulse acquisition unit and an oscilloscope (Fig. 4a). For placement into the positioning unit, two pinions were glued to the poles of the spherical sample. After mounting the sample into the pressure vessel, this enabled rotation of the sample around its vertical axis. Furthermore, a rectangular frame containing two spring-hold piezoelectric transducers, with eigenfrequency of 1 MHz, allows symmetrical rotation of the transducers around a horizontal axis (Fig. 4b). This setup of the sample enables measurement of *P*-wave traveltime in any direction, with exception of an area of 15° as a result of interference with the pinions. We measured V_P in 132 directions with a step size of 15° (Figs 4c and d), at confining pressure (P_c) of 0.1, 10, 20, 50, 100, 200 and 400 MPa). V_P measurements were performed both during stepwise pressurization and depressurization of the sample.

During our experiments *P*-wave traveltimes were continuously logged using a PC. The measured traveltimes were corrected for any time delay caused by the epoxy layers and by the acquisition elements of the apparatus. The thickness of the epoxy is calculated by subtraction of diameter of the sample before and after epoxy application, typically being 0.05 mm. The delay of the acquisition elements was calibrated by measuring a standard metal sample with known traverse time. The compressional wave velocity was then calculated using the distance given by the sphere diameter.

Anisotropy of magnetic susceptibility

We measured the AMS on AGICO MFK-1A kappabridge by means of rotating specimen method (Jelínek 1997). Measurements were made at an operating frequency of 976 Hz and peak field intensity of 200 A m^{-1}. A statistical analysis of the AMS data was carried out using the ANISOFT 4.2 MS Windows application. In order to characterize the intensity and shape of the magnetic fabric ellipsoid two parameters (Nagata 1961; Jelínek 1978) were calculated: degree of anisotropy $P = k_1/k_3$, and the shape factor $T = 2\ln(k_1/k_2)\ln(k_2/k_3) - 1$, where $0 < T < 1$ indicates oblate and $-1 < T < 0$ prolate shapes of magnetic susceptibility ellipsoids. The $k_1 \geq k_2 \geq k_3$ are principal susceptibilities, respectively. The mean magnetic susceptibility $k_m[k_m = (k_1 + k_2 + k_3)/3]$ reflects the qualitative and quantitative content of magnetic minerals in the rock. In relation to the magnetic fabric the maximum principal susceptibility (k_1) represents the magnetic lineation and the minimum principal susceptibility (k_3) is considered as a pole to magnetic foliation.

Tracing of grain boundaries and microcracks

We used microphotographs of three mutually perpendicular, epoxy-saturated thin sections to manually trace grain boundaries, intergranular cracks and intragranular cracks in quartz, feldspars and in micas using ESRI ArcMap 9.3 GIS software. Grain boundaries were traced on microphotographs obtained under cross-polarized light, whereas microphotographs obtained under UV-excited fluorescence light were used for tracing of the cracks. The sample material was epoxy-saturated prior to preparation of the thin-section and so any cracks due to the preparation do not appear in the UV image and are consequently not accounted for during the tracing. The traced networks were processed in MATLAB^{TM} FracnetLX toolbox (Lexa 2010), in order to visualize the orientation distribution functions on rose diagrams and to calculate the bulk anisotropy of preferred orientation [SURFOR '$A(\alpha)$' function after Panozzo (1984)] for each of the traced features. The presented normalized value of the SURFOR function ranges from 0 for perfect unimodal orientation to 1 for pluri-modal or non-preferred orientation.

RESULTS

Note that we use the term 'schlieren' to refer to the planar structure represented by the long limb of the schlieren fold, as it is the predominant mesoscopic structure in the sample compared to the short limb. Also we will use the terms UP and DOWN to refer to the pressurization and the depressurization stages of the *P*-wave experiment, respectively.

Ultrasonic *P*-wave velocity data

We plotted the results of our V_P measurements on the lower hemisphere of equal area projection using grey scale look up table unique

for each of the plot in order to accentuate the anisotropy evolution throughout the experiment. For easier visual comprehension the plot data are contoured by isolines. In total, we constructed three types of stereo plots that we use for interpretation:

(1) V_P plots for each of the 13 confinement levels (seven during pressurization, six during depressurization). These plots show the V_P range and directional dependence of V_P with confining pressure (depth).

(2) $\Delta V_P(\Delta p)$ plots showing changes of V_P pattern between successive levels of confining pressure, for both pressurization and depressurization. Changes in V_P are correlated to the closing or opening of microporosity as a function of confining pressure (depth).

(3) Hysteresis ΔV_P plots showing differences in V_P pattern at the same constant confinement level between pressurization and depressurization. Hysteresis is a measure for any irreversible deformation induced by pressure loading and unloading.

In addition to the V_P scale, all plots also show the degree of V_P anisotropy k, defined as (Babuška 1968)

$$k = (V_{P\max} - V_{P\min})/[(V_{P\max} + V_{P\min})/2], \quad (1)$$

where $V_{P\max}$ and $V_{P\min}$ are, respectively, the maximum and the minimum V_P values.

We constructed stereo plots visualizing the anisotropy of V_P, at different confining pressures (Fig. 5). At ambient pressure (0.1 MPa) the anisotropy is nearly transversely isotropic, with high V_P directions parallel to the schlieren and the lowest V_P direction perpendicular to them. This pattern persists over the entire pressurization, though a rapid decrease of anisotropy is observed between 0.1 and 50 MPa from 24 to 8 per cent, which further decreases to 3 per cent towards peak confinement. Note that for the depressurization a progressive transition from transversely isotropic to orthorhombic pattern can be seen, with the minimum V_P direction perpendicular to the schlieren and the higher values arranged in an elliptical pattern with the long axis lying in the plane of the schlieren. The orthorhombic pattern persists for the remainder of the DOWN part. An increase of the degree of anisotropy is observed reaching a value of 36 per cent at ambient pressure, that is, a value 1.5 times the value at the onset of the experiment (0.1 MPa UP). The evolution of the minimal, mean and maximal V_P values ($V_{P\min}$, $V_{P\mathrm{mean}}$, $V_{P\max}$) as a function of confining pressure is plotted in Fig. 6(a), for both UP and DOWN sequence and the pressures of 0.1–100 MPa. Note that the slope $\Delta V_P/\Delta p$ becomes successively gentler going from the ambient to the highest pressure. Whilst the values of $V_{P\min}$ UP and $V_{P\min}$ DOWN at ambient pressure are similar, they differ strikingly for the $V_{P\max}$ UP and $V_{P\max}$ DOWN. Comparison of the six V_P curves on the entire displayed pressure interval reveals a strongly deviatory $V_{P\max}$ DOWN function, which, contrarily to the others, features only slight breaks at the levels of 20, 50 and even 100 MPa.

Stereo plots displaying the changes in V_P with pressure, $\Delta V_P(\Delta p)$, for each of the pressure steps, are shown in Fig. 7. As can be seen, the pressure step between 10 and 0.1 MPa shows similar values of mean $\Delta V_P(\Delta p)$ for both the UP (94 m s^{-1} MPa^{-1}) and the DOWN (99 m s^{-1} MPa^{-1}) sequences. Furthermore, these mean values of $\Delta V_P(\Delta p)$ are the highest of all the pressure steps. For the low pressure steps (0.1–100 MPa), the steps 20–10 MPa display the least anisotropy, whereas the steps 50–20 MPa [mean $\Delta V_P(\Delta p)$ of 18 and 14 m s^{-1} MPa^{-1} for the UP and DOWN sequence, respectively] show a marked difference in anisotropy of $\Delta V_P(\Delta p)$. A clear transition from transversely isotropic to an orthorhombic anisotropy pattern is observed in the DOWN step, whereas this change in anisotropy is not observed in the UP step. The orthorhombic anisotropy can be also seen in the DOWN steps of 100–50 MPa and 200–100 MPa. Striking information on the evolution of the V_P anisotropy degree k is visible through the curve of its hysteresis plotted in Fig. 6b. One can see that there is hardly any hysteresis of V_P anisotropy for pressure 100 MPa (and higher), whereas there is a gradual increase of V_P anisotropy hysteresis towards the ambient pressure defining three intervals 100–50, 50–10 and 10–0.1 MPa as progressively more hysteretic ones.

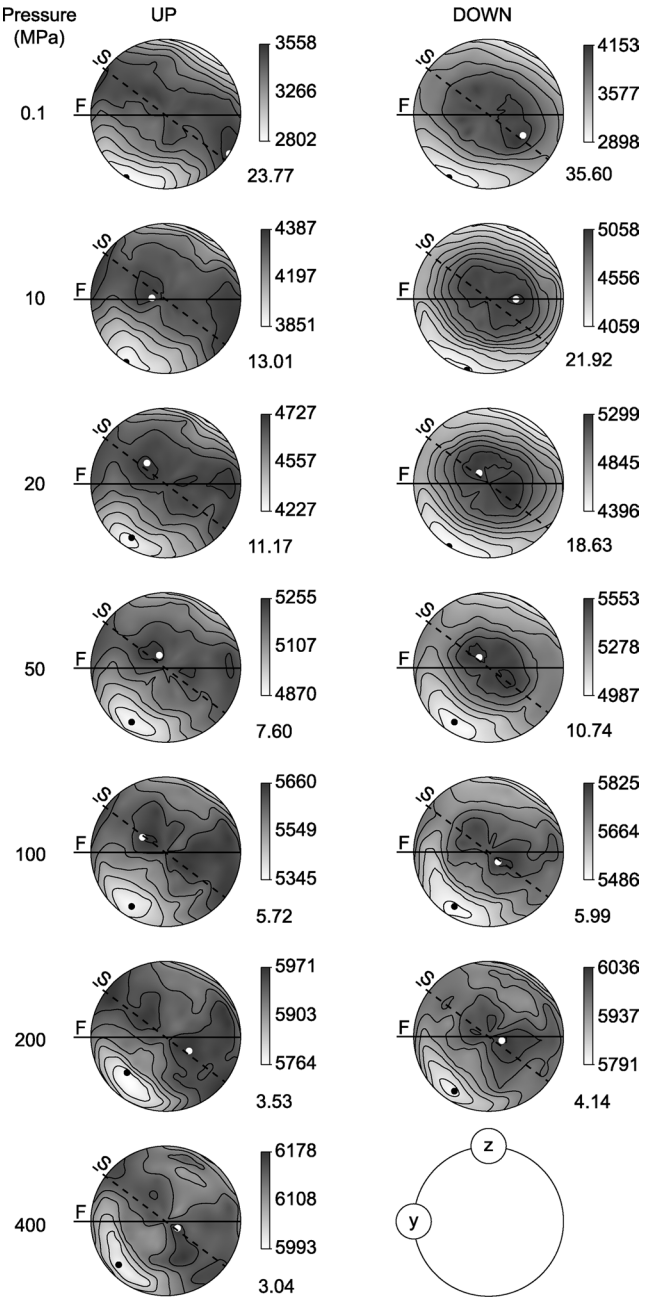

Figure 5. Results of measurements of *P*-wave velocity spatial distribution at confining pressures 0.1–400 MPa for pressurization (UP) and depressurization (DOWN) plotted on lower hemisphere of equal area projection. For each step, minimum, mean and maximum V_P (m s^{-1}) are shown near the grey scale and V_P anisotropy degree k (per cent) is shown below the grey scale. The directions of maximum and minimum V_P are represented by white and black dot, respectively. Orientations of the schlieren (S) and of the reference fractures (F) are represented by dashed and full line, respectively.

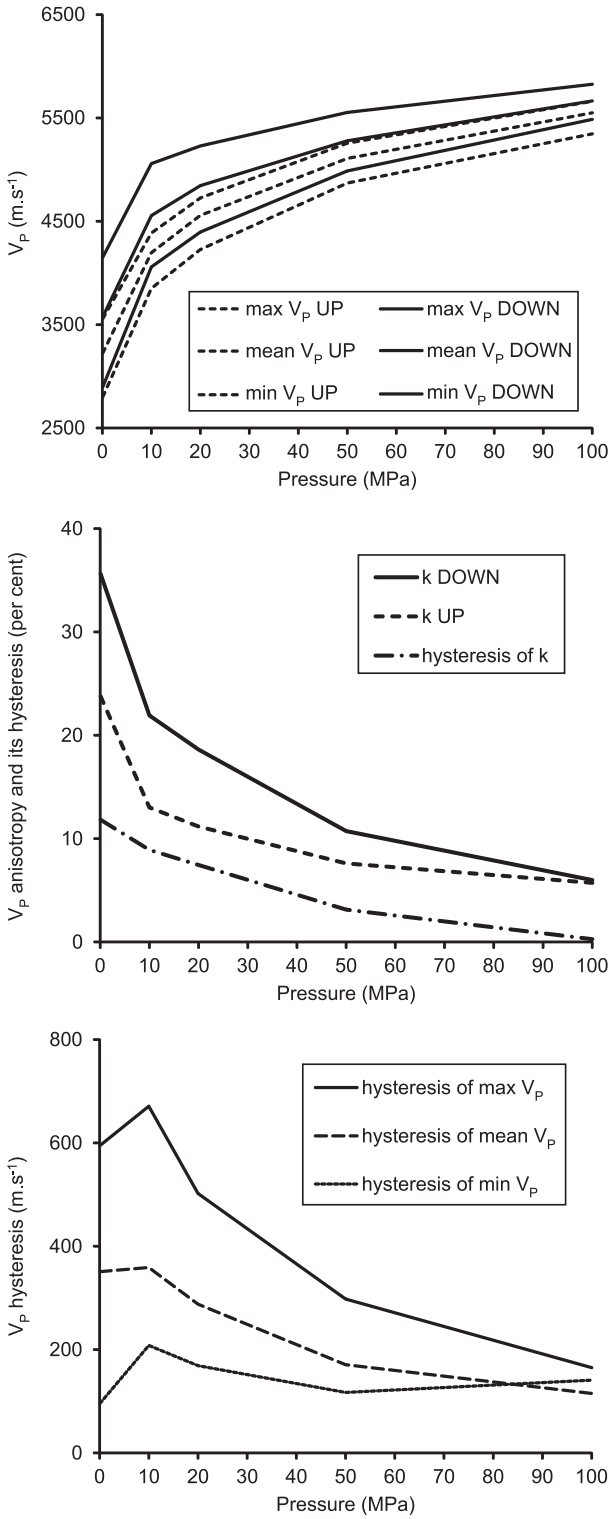

Figure 6. Evolution of minimum, mean and maximum V_P (a), V_P anisotropy (b) and hysteresis of minimum, mean and maximum V_P (c) with hydrostatic pressure for pressurization (UP) and depressurization (DOWN).

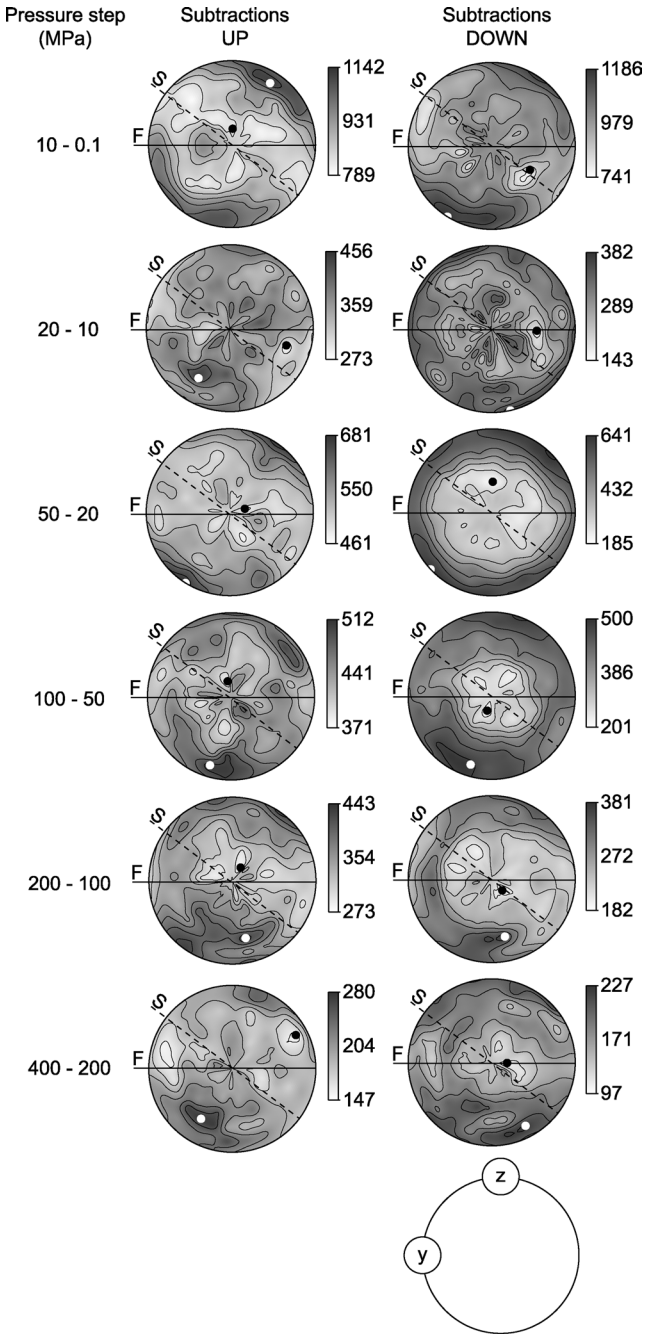

Figure 7. Spatial distributions of calculated differences $\Delta V_P(\Delta p)$ for pressurization (UP) and depressurization (DOWN) plotted on lower hemisphere of equal area projection. For each step, minimum, mean and maximum $\Delta V_P(\Delta p)$ (m s^{-1}) are shown near the grey scale. The directions of maximum and minimum $\Delta V_P(\Delta p)$ are represented by white and black dot, respectively. Orientations of the schlieren (S) and of the reference fractures (F) are represented by dashed and full line, respectively.

Stereo plots showing V_P hysteresis, ΔV_P, that is, the difference V_P UP minus V_P DOWN at a given confining pressure, are shown in Fig. 8, for P_c of 0.1, 50, 100 and 200 MPa. As can be seen, hysteresis anisotropy is negligible at high pressures (100 and 200 MPa), whereas it is striking for the low pressures (0.1 and 50 MPa), showing a clear transversely isotropic pattern. This is confirmed by the larger interval $V_{Pmax} - V_{Pmin}$ at lower pressures, compared to higher pressures. The hysteresis stereo plots show that there is an irreversible change within the sample material, as a result of pressurization. During depressurization, down to P_c of 100 MPa, the rock responds in an elastic fashion, while further depressurization suggests non-elastic response, resulting from irreversible deformation. The hystereses of V_{Pmin}, V_{Pmean} and V_{Pmax} are plotted in Fig. 6c as a

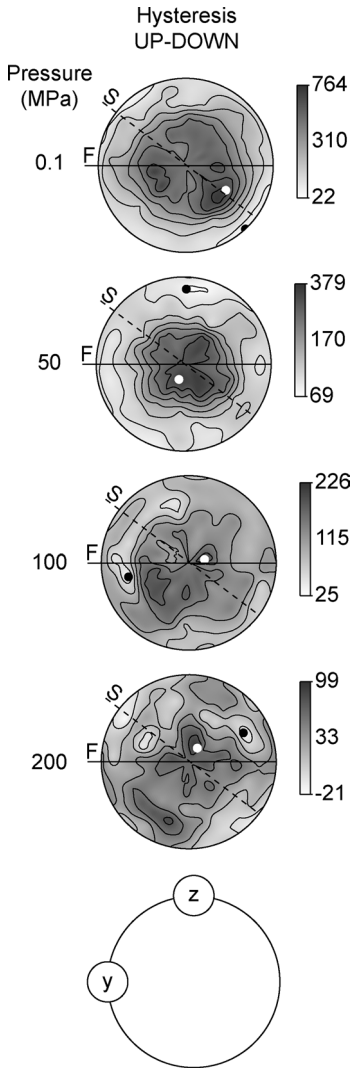

Figure 8. Spatial distributions of calculated hystereses (ΔV_P) plotted on lower hemisphere of equal area projection. For each step, minimum, mean and maximum ΔV_P (m s^{-1}) are shown near the grey scale. The directions of maximum and minimum ΔV_P are represented by white and black dot, respectively. Orientations of the schlieren (S) and of the reference fractures (F) are represented by dashed and full line, respectively.

function of confining pressure for P_c of 0.1–100 MPa. Note that the hysteresis of V_{Pmax} is higher than that of V_{Pmin} for all the pressure levels and that all the three functions culminate at the pressure level of 10 MPa.

Anisotropy of magnetic susceptibility

The mean magnetic susceptibility (k_m) in the analysed samples ranges from 70.2 to 97.8 $\times$ 10^{-6} SI. Such mean magnetic susceptibility is at the lower limit of susceptibilities typical of the Variscan biotite granites of the Bohemian Massif. As can be seen on *P–T* diagram in Fig. 9(a), the magnetic anisotropy degree parameter *P* ranges from 1.093 to 1.109 and the shape parameter *T* varies between 0 and 0.7, suggesting oblate susceptibility ellipsoid. Stereo plot relating the principal susceptibility directions to the orientation of the sample mesostructures (Fig. 9b) shows that the maximum susceptibility (k_1) direction is parallel with the schlieren and the minimum susceptibility (k_3) direction is perpendicular to them.

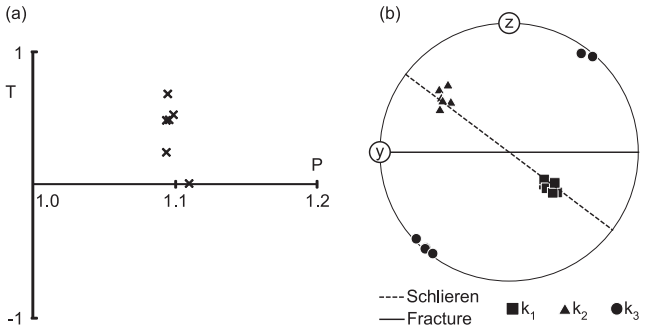

Figure 9. Results of AMS analysis. (a) *P–T* plot, (b) Orientation of principal axes of the AMS ellipsoid (k_1, k_2, k_3) plotted on lower hemisphere of equal area projection. Orientations of the schlieren and of the reference fractures are represented by dashed and full line, respectively.

Tracing of grain boundaries and microcracks

The results of the tracing for each of the defined microstructural feature are shown in Figs 10(b)–(f), in the form of rose diagrams and values of normalized SURFOR '$A(\alpha)$' value for each of the three sections.

It is clear that the section (*YZ*) perpendicular to both mesoscopic structures, that is, the schlieren and the fractures, bears the most anisotropy. A clear pattern was obtained for all features with exception of the feldspar cracks, for which a dominant orientation is accompanied by two subdominant ones. Overall, *XY* section shows less anisotropy, though one dominant orientation can still be seen for all the features, with the exception of the feldspar cracks. In case of the least anisotropic section *XZ*, a clear dominant orientation for grain boundaries and mica and feldspar cracks is observed, whereas several directions of similar strength can be discerned in the cases of intergranular and quartz cracks.

SUMMARY AND DISCUSSION

The schlieren represent a dominant structure for both of the petrophysical methods and are reflected by the preferred orientation of grain boundaries. The effect of microcracks on elastic properties is expressed by the rapid increase in bulk V_P during the low-pressure stages of pressurization and by the anisotropy of some of the V_P measurements and calculations. We will now discuss the orientation of the traced features and of the magnetic fabric and we will examine their relation to the V_P data. We will also discuss the relation of the microcracks to the massif fracture system and compare the bulk elastic properties of our sample with those of other granitic rocks reported in the literature. Finally, we will consider implications of the presented data for the evolution of the rock porosity, permeability and TC with confining pressure.

Orientation of grain boundaries, cracks and magnetic fabric

Based on the preferred orientation of the 2-D traces acquired by tracing of the thin sections shown above (Fig. 10), we derived the orientation of planes representing each of the traced features (Fig. 11). The *YZ* section, which is perpendicular to both the schlieren and the fractures, displays the highest preferred orientation for all the traced features and was therefore attributed the main importance. The 3-D orientation of grain boundaries and of intragranular feldspar cracks

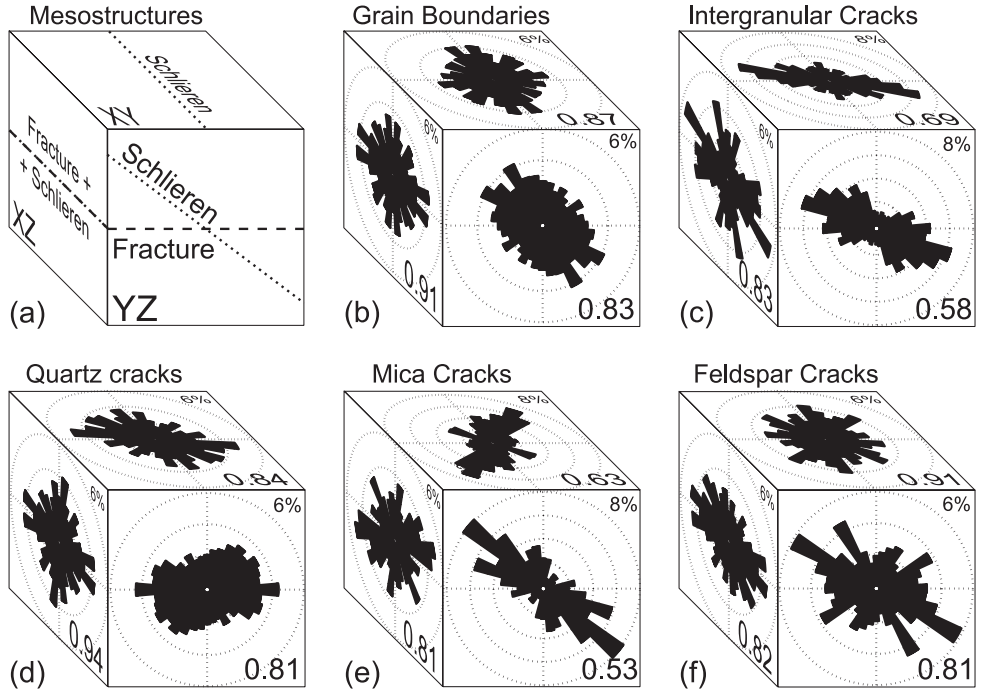

Figure 10. Results of photomicrograph tracing. (a) Orientation of thin sections with respect to the sample mesostructures, (b–f) orientation rose diagrams for grain boundaries, intergranular cracks, and intragranular cracks in quartz, mica and feldspar featuring the normalized value of SURFOR '$A(\alpha)$' function [after Panozzo (1984)] on the bottom right.

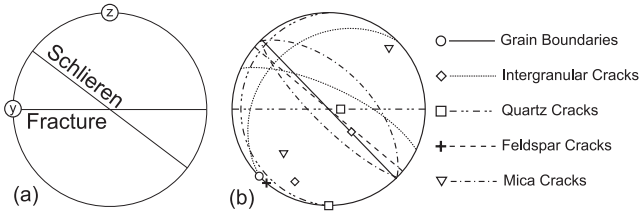

Figure 11. Interpretation of the traced features 3-D orientation. Lower hemisphere equal area projections showing orientation of the sample mesostructures (a) and of the traced features (b). For easier comparison with the V_P data both great circles (lines) and poles to the planes (symbols) are plotted to represent the orientation of the traced features.

are each represented by one plane, whereas for intergranular cracks and intragranular cracks in quartz and micas, the 2-D patterns could not be reasonably combined into one plane and they are therefore represented by two differently oriented planes. Although other interpretations of the 2-D patterns are possible, for the sake of clarity we present only the simplest solution reflecting the sample mesostructures and the results of the two petrophysical methods.

Comparison of the stereo plots displaying the orientation of the sample mesostructures and of the traced features in Figs 11(a) and (b) shows that the grain boundaries, mica and feldspar cracks and one of two populations of intergranular cracks are subparallel to the schlieren. The other population of intergranular cracks and one population of quartz cracks are subperpendicular both to the schlieren and to the reference fractures. Finally, the other population of intraquartz cracks is subparallel to the reference fractures.

The AMS analysis results indicate that the rock magnetic fabric is controlled by biotite and that the magnetic susceptibility ellipsoid is rather oblate, with the symmetry axis (k_3) oriented perpendicular to the schlieren, that is, that the biotite basal planes are coplanar with them (Fig. 9b). This observation is coherent with the evaluated preferred orientation of mica cracks (Fig. 11b), taking into account that the mica cracks predominantly follow the mica cleavage planes.

Pore fabric effect on elastic properties

The ultrasonic experiment characterizes the sample at ambient pressure before pressurization by a transversely isotropic pattern with minimum V_P direction perpendicular to the schlieren. In terms of the traced features, the minimum V_P direction is sub-parallel to the poles to grain boundaries, feldspar cracks and one population of intergranular cracks. Also poles to both of the mica crack populations are close (<20°) to the minimum V_P directions. Detailed look on the corresponding V_P stereo plot (Fig. 5, 0.1 MPa UP) reveals that the distribution of the low V_P directions surrounding the absolute minimum is slightly deviated towards the direction of pole to the population of quartz cracks that are subparallel to the reference fractures. The interference of the quartz cracks at low pressures is accentuated by the first step 10–0.1 MPa of the pressurization part, where two separate directions of high $\Delta V_P(\Delta p)$ partly coincide with the 0.1 MPa level low V_P directions (compare Figs 5 and 7). The high mean $\Delta V_P/\Delta p$ value (93 m s^{-1} MPa^{-1}) during this first pressurization step suggests major closing of porosity below pressure of 10 MPa. It is likely that the porosity reduction is linked to the closing of the quartz cracks and the schlieren-related cracks given that the two high $\Delta V_P(\Delta p)$ directions coincide with poles to these two cracks populations.

At higher confinement levels the elastic anisotropy pattern stays transversely isotropic and schlieren-controlled, the most important phenomenon being a strongly anisotropic V_P change during the 50–20 MPa step with mean $\Delta V_P/\Delta p$ value of 18 m s^{-1} MPa^{-1}. Differently to the major V_P change during the 10–0.1 step, in this case the directions of high $\Delta V_P(\Delta p)$ are concentrated in proximity of the poles to the schlieren-oriented cracks only, suggesting that the quartz cracks do not comply significantly. The step 100–50 MPa

exhibiting low $\Delta V_P/\Delta p$ value of 9 m s^{-1} MPa^{-1}, indicates compliance of quartz and intergranular cracks as the $\Delta V_P(\Delta p)$ maximum direction is close to the poles to both of them.

The populations of quartz and intergranular cracks that are subperpendicular to both the schlieren and the reference fracture seem to respond to the loading only very subtly as hardly any particular direction of V_P increase can be linked to their orientation. On the other hand, their presence is manifested during the depressurization sequence of the ultrasonic experiment by the high V_P hysteresis directions clearly oriented about poles to these two crack populations. The hysteresis is thus linked to irreversible closing of the cracks in reaction to the pressure loading, probably due to collapse of the cracks or due to crushing of the crack wall asperities. As a consequence, during sample unloading the V_P anisotropy degree k at each pressure level is greater than at its pressurization equivalent and reaches 36 per cent after complete unloading with hand-in-hand change of anisotropy pattern from transversely isotropic to orthorhombic.

Taking into account that the hysteresis can be clearly seen only at pressures of 100 MPa or lower, there is only elastic response (in all directions) at pressures higher than 100 MPa. Furthermore, the fact that the UP and DOWN steps of 10–0.1 MPa agree quite precisely in values of minimum and maximum $\Delta V_P(\Delta p)$ as well as in the anisotropy pattern implies that the rock reacted in elastic manner also at confining pressures below 10 MPa, which can be seen from a different point of view via the plot of $V_P(p)$ curves (Fig. 6). The values of V_{Pmax} DOWN, which correspond to the directions of the highest V_P hysteresis, decreased over the pressure interval 100–10 MPa during depressurization at clearly lower rate than the corresponding V_P means and minima, whereas for the last step (10–0.1 MPa) the three values decreased at similar rate. Synthesizing the above observations, the pressure interval where irreversible change dominantly takes place can be constrained to 10–100 MPa.

It should be noted that the V_P measurements were carried out on a dry rock sample, that is, with the air as pore fluid. However, in *in situ* conditions, the rock pore space can be filled by another fluid (e.g. water solution) as a consequence of high pore fluid pressure. In such a setting, one can expect increase of bulk rock V_P and decrease of V_P anisotropy with respect to the presented values. Both the effects would then be proportional to the *in situ* total porosity and to the V_P ratio of the air and of the *in situ* pore-filling fluid.

Comparison of the V_P data to previous studies

In Table 2, we have displayed the mean V_P and V_P anisotropy at different confining pressures for granitic rocks of similar density as the Lipnice granite (2.627 ± 0.05 g cm^{-3}). As can be seen, at ambient pressure the Lipnice granite shows very low minimum V_P and strong anisotropy. Although studies report samples with similar V_P and k values, these samples feature two or three times higher bulk porosity. Furthermore, in comparison with the slowest reported granites, the mean V_P of the Lipnice granite at high confining pressures (≥100 MPa) yields only slightly lower (~0.1 km s^{-1}) values. The low mean V_P at ambient pressure coupled with the low porosity, as well as the regain of 'normal' V_P at high confining pressures of Lipnice granite indicates that its porosity is mainly composed of low aspect ratio pores, that is, cracks, which are more susceptible to decelerate a propagating elastic wave and to comply at lower confining pressure as compared to equant pores. This hypothesis is supported by the observation that the minimum V_P in our sample was measured in direction perpendicular to intergranular cracks

Table 2. Comparison of mean V_P (V_{Pmean}) and anisotropy degree (k) of the Lipnice granite and of previously studied granitic rocks as a function of confining pressure (P_c). Sample superscript numbers refer to: 1 – this study, 2 – Machek (2011), 3 – Pros *et al.* (1998b), 4 – Nur & Simmons (1969).

				P_c (MPa)															
				0.1		10		20		50		100		200		400			
Sample	Grain size (mm)	Density (g cm^{-3})	Porosity (per cent)	V_P (km s^{-1})	k (per cent)	V_P (km s^{-1})	k (per cent)	V_P (km s^{-1})	k (per cent)	V_P (km s^{-1})	k (per cent)	V_P (km s^{-1})	k (per cent)	V_P (km s^{-1})	k (per cent)	V_P (km s^{-1})	k (per cent)	V_P (km s^{-1})	k (per cent)
Lipnice[1]	0.7	2.626	1.4	3.3	23.8	4.1	13.0	4.5	11.2	5.1	7.6	5.5	5.7	5.9	3.5	6.1	3.0		
Kouty-f[2]	0.7	–	1.7	4.4	12.4	5.0	10.4	5.3	8.5	5.6	5.7	5.8	4.8	6.0	3.9	6.2	3.2		
Kouty-m[2]	0.9	–	2.2	–	–	4.6	7.3	4.9	6.2	5.4	4.9	5.7	3.9	6.0	2.8	6.1	2.8		
Melechov[2]	1.5	–	3.3	–	–	4.2	24.0	4.7	16.7	5.3	10.8	5.7	8.2	6.0	5.8	6.1	5.2		
KVP G5[3]	0.4	2.651	–	5.5	6.0	–	–	5.8	4.0	6.0	–	6.1	3.6	6.1	3.3	6.3	–		
SP G6[3]	0.3	2.627	2.9	3.7	23.8	–	–	4.7	14.6	5.3	–	5.8	4.7	6.1	2.8	6.3	–		
SP G8[3]	0.9	2.621	3.0	3.2	24.6	–	–	–	–	5.3	–	5.7	5.8	6.0	6.0	6.2	–		
KVP G9[3]	0.6	2.608	4.1	3.3	38.6	–	–	4.8	8.1	5.3	–	5.6	5.2	5.9	3.4	6.0	–		
KVP ZC19[3]	–	2.578	–	5.1	14.7	–	–	5.6	15.8	6.0	–	6.2	5.5	6.2	5.8	6.3	–		
Casco[4]	5.0	2.626	0.7	3.3	–	5.1	–	5.7	–	–	–	6.5	–	6.6	–	–	–		
Westerly[4]	0.8	2.646	0.9	3.8	–	5.0	–	5.3	–	–	–	5.9	–	6.1	–	–	–		
Troy[4]	4.0	2.670	0.2	4.4	–	5.9	–	6.2	–	-	–	6.5	–	–	–	–	–		

and mica cracks. In this regard, the schlieren-bearing Lipnice granite is similar to the orthogneiss sample RP3 studied by Přikryl *et al.* (2005), which was characterized by similar modal proportions (including a similar mica content of 15 per cent) and by high preferred orientation of mica and which yielded a V_{Pmin} value of 2.7 km s^{-1} in a direction perpendicular to mica basal planes. Compared to granite samples from the Melechov massif studied by Machek (2011), the Lipnice granite corresponds the best to the fine-grained variety of Kouty granite (Table 2). Compared to West Bohemian granites (Pros *et al.* 1998b) in terms of mean V_P and grain size it is similar to the muscovite granite from the Smrčiny massif (sample G8) and the two-mica granite from the Karlovy Vary massif (sample G9).

Microcracks origin and its relation to the fracture system of the granitic massif

Microcracks in rock form generally in response to differential stress which can be provoked by larger-scale fractures propagation (Lespinasse & Pêcher 1986; Scholz *et al.* 1993; Faulkner *et al.* 2010), thermally induced volumetric changes (Géraud 1994; Chaki *et al.* 2008) or volumetric changes due to phase transition (Angerer *et al* 2011; Lachassagne *et al.* 2011). If no former discontinuity exists, their orientation is normal to the local minimum principal stress acting during their formation. The orientations of the remote and of the local stress may or may not be the same, which distinguishes shear fractures (faults), where remote stress is oblique to the local one, and tensile fractures (joints), where the two correspond in orientation.

The sampled outcrop of Lipnice granite shows an orthogonal fracture system formed by two sets of steep and one set of flat joints. At the scale of the granitic massif, the steep and the flat joints were related to the post-magmatic cooling of the granitic massif and to the exhumation-induced exfoliation, respectively (Lexa & Schulmann 2004). The proposed tectonic setting of the joints formation is valid also for our sample outcrop, given that the observed joints do not display any sign of faulting and that no important mineral alteration was observed in the sample material.

Taking into account the above facts, we refer to the mutual orientation of the microcracks and the outcrop fractures to decipher their genetic relation. Hence, the steep E–W trending intergranular and quartz cracks are linked to the subvertical E–W trending cooling-related joints of set 1 and the flat-lying quartz cracks to the shallowly W dipping exfoliation joints. The intergranular cracks oriented at low angle to the reference exfoliation fractures were induced by the exfoliation process as well. The formation of two differently oriented populations of microcracks by the exfoliation process can be attributed to the absence of cleavage in quartz, and, on the other hand, to the strong cleavage in anisometric crystals of micas oriented subparallel to the schlieren. Hence, in the cleavage-free crystals of quartz the exfoliation-related stress field induced cracks oriented perpendicular to the minimum compressive stress, whereas in micas the cleavage planes represented favourably oriented zones of weakness and were therefore privileged sites for the intergranular cracks propagation.

The presence of microcracks subparallel to one of the sets of vertical joints (set 1) and, on the other hand, the absence of microcracks parallel to the other one (set 2), reflects the difference in the fracture sets characteristics and the distances of the closest fractures of the respective sets from the sample block. We remind that the set 1 is represented by decametric factures and the closest fracture of this set was 1 m distant from the sample block, whereas the set 2 is characterized by metric fractures with the closest one 10 m distant from the sample block. Assuming that the width of the facture process zone scales with fracture length this means that only the fracture of the set 1 was large and/or close enough to induce cracking in the sampled material.

Implications on the rock physical properties

The presented data and observations enable us to formulate several implications on physical properties of the studied rock and their evolution with depth. However, we propose rather qualitative constraints as exact quantification is beyond the scope of this paper.

We have shown that the rock crack-related porosity decreased markedly in the pressure interval 0.1–100 MPa, in which the effect of cracks was clearly discernible by important, anisotropic change in V_P. For approximate evaluation of the porosity reduction we follow the approach of Pros *et al.* (1998a) to estimate the state of openness of cracks as a function of confining pressure. The author proposes an equation, which combines linear and exponential terms to account for increase of V_P with increasing confinement due to elastic parameters and due to closing of cracks, respectively. This approach allows calculating the relative crack-induced deceleration of V_P as the difference between a hypothetic V_P of an ideal non-cracked medium and the experimentally measured values. The hypothetic V_P of the non-cracked medium is a linear function of hydrostatic pressure defined by the measured V_P values at the two high-pressure levels (200 and 400 MPa), where all the cracks are supposed to be closed. Assuming that there is a linear proportionality between the change in V_P due to cracks closing and the change in the crack porosity volume, the two pressure steps 0.1–10 MPa and 20–50 MPa indicating important closing of cracks are related to relative decrease in crack porosity to 61 and 26 per cent of its initial value at ambient pressure. The strong assumption on the cracks closure at the two highest pressure levels is surely questionable if no direct porosity measurement is available. On the other hand, in our results we see two strong arguments for its plausibility. Firstly, the pressure step 200–400 MPa features very low mean $\Delta V_P(\Delta p)$ (1 m s^{-1} MPa^{-1}) and low anisotropy (see Fig. 7). Such characteristics are hardly associable with crack closure. Secondly, the V_P anisotropy at the two highest pressure levels is very low (3–4 per cent) and the V_P minima are oriented subperpendicular to the grain boundaries. Therefore this V_P anisotropy reflects rather the material SPO than any open cracks.

Many studies have shown that microcracks closure induces important reduction of fluid permeability (Benson *et al.* 2006, and references therein). Given that cracks represent an important part of the porosity of our sample material, it is likely that its permeability would decrease with confining pressure progressively with the crack porosity reduction. Simultaneous measurements of porosity and permeability of a cracked granite by Benson *et al.* (2006) show that a relative decrease in porosity of 10 per cent may reduce the bulk permeability by one order of magnitude and that the permeability along the cracks is several times higher than perpendicular to them. We have observed three differently oriented sets of microcracks, with majority of the crack populations subparallel to the schlieren. We therefore suppose that the permeability anisotropy is controlled by the schlieren, with high permeability directions parallel to them. Particularly the intersections of the schlieren-related cracks with the cracks of the two other sets are likely to represent the most permeable conduits. Taking into account the irreversible closing of cracks perpendicular to the

schlieren and to the reference fractures, the principal permeability direction after a possible loading-unloading cycle would be defined by the intersection of the other two crack sets that reopen during depressurization.

Both the schlieren and the microcracks can be expected to affect markedly the thermal properties of the studied granite. For TC of granite, the quartz content and distribution are crucial as quartz features two to three times higher TC than the other rock constituent phases (Clauser & Huenges 1995). In this light the schlieren-related quartz bands represent principal heat conductors and their orientation defines the principal TC anisotropy. Concerning *in situ* rock thermal properties, higher confinement leads also to higher TC of minerals. Although for rocks the rate of pressure change of the TC is generally very small (0.03–0.9 W m^{-1} K^{-1} GPa^{-1}; Abdulagatov *et al*. 2006, and references therein), it is worth noting that the highest TC dependence is featured by quartz (3.3 W m^{-1} K^{-1} GPa^{-1}, Horai & Susaki 1989) highlighting the impact of the schlieren.

Géraud (1994) has shown that granitic rock submitted repeatedly to heating-cooling cycle with maximum temperatures of 100 °C became less porous, whereas at higher maximum temperatures it became progressively more cracked. From this point of view it is the quartz that features the highest thermal expansion (Fei 1995). Consequently, the schlieren-related quartz bands would expand the most and cracking would preferentially take place along their boundaries.

It has been shown experimentally that the V_P of granite and other quartz-rich rocks tested at 200 and 600 MPa confining pressure decreases significantly in the temperature range of 500–700 °C and that this V_P decrease is less important at higher confinement (Kern 1979, 1982). This phenomenon caused by thermal cracking and by the α–β quartz transition should be taken into account when considering the *in situ* elastic properties of the studied rock.

The role of cracks on the rock TC is twofold. On one hand, at dry conditions, open cracks represent a barrier for the heat conduction in granite (Géraud *et al.* 2010) and therefore the inferred reduction of crack porosity with confining pressure in our sample would be associated with higher bulk TC and lower TC anisotropy. On the other hand, open cracks filled by another fluid than air, for example, water solution, may enhance the bulk TC of the rock and reduce the TC anisotropy proportionally to the TC of the pore fluid. In addition, well-interconnected system of open cracks enables heat transfer by convection.

CONCLUSIONS

We have characterized a schlieren-bearing sample of the Lipnice granite using three independent methods: multi-directional measurements of *P*-wave velocity at confining pressure up to 400 MPa, AMS analysis and manual tracing of grain boundaries and microcracks. The schlieren have been demonstrated to control the anisotropy pattern of the sample elastic properties and of its magnetic fabric. Three sets of microcracks differing in orientation have been genetically related to the fracture system of the granitic massif. High pressure loading-unloading cycle has been shown to induce irreversible closure of microcracks associated with joints related to post-magmatic thermal cooling, whereas microcracks associated with sheeted fractures have been shown to react to the pressure cycle in elastic manner. Major crack closing characterized by rapid V_P increase of 93 m s^{-1} MPa^{-1} has been observed in the pressure range 0.1–10 MPa, corresponding to depths less than 500 m. Implications on the evolution with depth of the rock porosity, permeability and TC have been discussed and the importance of the schlieren structure has been accentuated.

REFERENCES

Abdulagatov, I.M., Emirov, S.N., Abdulagatova, Z.Z. & Askerov, S.Y., 2006. Effect of pressure and temperature on the thermal conductivity of rocks, *J. Chem. Eng. Data,* **51,** 22–33.

Angerer, T., Greiling, R.O. & Avigad, D., 2011. Fabric development in a weathering profile at a basement-cover interface, the sub-Cambrian peneplain, Israel: implications for decollement tectonics, *J. Struct. Geol.,* **33,** 819–832.

Archanjo, C.J., Launeau, P. & Bouchez, J.L., 1995. Magnetic fabric vs. magnetite and biotite shape fabrics of the magnetite-bearing granite pluton of Gameleiras (Northeast Brazil), *Phys. Earth planet. Inter.,* **89,** 63–75.

Babuška, V., 1968. Elastic anisotropy of igneous and metamorphic rocks, *Stud. geophys. Geod.,* **12,** 291–303.

Babuška, V. & Pros, Z., 1984. Velocity anisotropy in granodiorite and quartzite due to the distribution of microcracks, *Geophys. J. R. astr. Soc.,* **76,** 121–127.

Benson, P.M., Meredith, P.G. & Schubnel, A., 2006. Role of void space geometry in permeability evolution in crustal rocks at elevated pressure, *J. geophys. Res.,* **111,** B12203, doi:10.1029/2006JB004309.

Borradaile, G.J. & Henry, B., 1997. Tectonic applications of the magnetic susceptibility and its anisotropy, *Earth Sci. Rev.,* **42,** 49–93.

Breiter, K. & Sulovský, P., 2005. Geochronology of the Melechov granite massif, *Geological Research Reports for the Year 2004,* Czech Geological Survey, Prague, pp. 16–19.

Clauser, C. & Huenges, E., 1995. Thermal conductivity of rocks and minerals, in *A Handbook of Physical Constants,* pp. 105–126, ed. Ahrens, T.J., American Geophysical Union, Washington, DC.

Chaki, S., Takarli, M. & Agbodjan, W.P., 2008. Influence of thermal damage on physical properties of a granite rock: porosity, permeability and ultrasonic wave evolutions, *Constr. Build. Mater.,* **22,** 1456–1461.

Chlupáč, I., Brzobohatý, R., Kovanda, J. & Stráník, Z., 2002. *Geologická minulost České republiky,* Academia, Praha.

DeNosaquo, K.R., Smith, R.B. & Lowry, A.R., 2009. Density and lithospheric strength models of the Yellowstone–Snake River Plain volcanic system from gravity and heat flow data, *J. Volc. Geotherm. Res.,* **188,** 108–127.

Faulkner, D.R., Jackson, C.A.L., Lunn, R.L., Schlische, R.W., Shipton, Z.K., Wibberley, C.A.J. & Withjack, M.O., 2010. A review of recent developments concerning the structure, mechanics and fluid flow properties of fault zones, *J. Struct. Geol.,* **32,** 1557–1575.

Fei, Y., 1995. Thermal expansion, in *A Handbook of Physical Constants,* pp. 29–44, ed. Ahrens, T.J., American Geophysical Union, Washington, DC.

Franke, W., 2000. The mid-European segment of the Variscides: tectonostratigraphic units, terrane boundaries and plate tectonic evolution, in *Orogenic Processes: Quantification and Modelling in the Variscan Belt,* pp. 35–61, eds Franke, W., Haak, V., Oncken, O. & Tanner, D., Geological Society, Special Publication 179, London.

Géraud, Y., 1994. Variations of connected porosity and inferred permeability in a thermally cracked granite, *Geophys. Res. Lett.,* **21,** 979–982.

Géraud, Y., Rosener, M., Surma, F., Place, J., Le Garzic, E. & Diraison, M., 2010. Physical properties of fault zones within a granite body: example of the Soultz-sous-Forêts geothermal site, *C. R. Geosci.,* **342,** 566–574.

Goleby, B.R. *et al.*, 2006. An integrated multi-scale 3D seismic model of the Archaean Yilgarn Craton, Australia, *Tectonophysics,* **420,** 75–90.

Hrouda, F., 1982. Magnetic anisotropy of rocks and its application in geology and geophysics, *Surv. Geophys.,* **5,** 37–82.

Horai, K. & Susaki, J., 1989. The effect of pressure on the thermal conductivity of silicate rocks up to 12 kilobars, *Phys. Earth planet. Inter.,* **55,** 292–305.

Jelínek, V., 1978. Statistical processing of anisotropy of magnetic susceptibility measured on groups of specimens, *Stud. geophys. Geod.,* **22,** 50–62.

Jelínek, V., 1997. Measuring anisotropy of magnetic susceptibility on a slowly spinning specimen—basic theory, Agico Print No. 10, Brno.

Kern, H., 1979. Effect of high-low quartz transition on compressional and shear wave velocities in rocks under high pressure, *Phys. Chem. Min.,* **4,** 161–171.

Kern, H., 1982. Elastic-wave velocity in crustal and mantle rocks at high pressure and temperature: the role of the high-low quartz transition and of dehydration reactions, *Phys. Earth planet. Inter.,* **29,** 12–23.

Kern, H. & Wenk, H.R., 1990. Fabric-related velocity anisotropy and shear wave splitting in rocks from the Santa Rosa mylonite zone, California, *J. geophys. Res.,* **95,** 11 213–11 223.

Kern, H., 1993. P- and S-wave anisotropy and shear-wave splitting at pressure and temperature in possible mantle rocks and their relation to the rock fabric, *Phys. Earth planet. Inter.,* **78,** 245–256.

Kern, H., Mengel, K., Strauss, K.W., Ivankina, T.I., Nikitin, A.N. & Kukkonen, I.T., 2009. Elastic wave velocities, chemistry and modal mineralogy of crustal rocks sampled by the Outokumpu Scientific Drill Hole: evidence from lab measurements and modelling, *Phys. Earth planet. Inter.,* **175,** 151–166.

Khan, M.A., 1962. Anisotropy of magnetic susceptibility of some igneous and metamorphic rocks, *J. geophys. Res.,* **55,** 2873–2885.

Kranz, R., 1983. Microcracks in rocks — a review, *Tectonophysics,* **100,** 449–480.

Lachassagne, P., Dewandel, B. & Wyns, R., 2011. The fracture permeability of Hard Rock Aquifers is due neither to tectonics, nor to unloading, but to weathering processes, *Terra Nova,* **23,** 145–161.

Lespinasse, M. & Pêcher, A., 1986. Microfracturing and regional stress field: a study of the preferred orientations of fluid-inclusion planes in a granite from the Massif Central, France, *J. Struct. Geol.,* **8,** 169–175, 177–180.

Lexa, O., 2010. FracNetLX—fracture network analysis toolbox for MATLAB. Available at http://petrol.natur.cuni.cz/∼ondro/fracnetlx:home, last accesed 2013 March 19.

Lexa, O. & Schulmann, K., 2004. *Zprávy k projektu "Provedení geologických a dalších prací na testovací lokalitě Melechovský masív 2. etapa",* Česká geologická služba, Správa úložiště radioaktivních odpadů, Praha.

Lexa, O., Štípská, P., Schulmann, K., Baratoux, L. & Kroner, A., 2005. Contrasting textural record of two distinct metamorphic events of similar P-T conditions and diferent durations, *J. Metamorph. Geol.,* **23,** 649–666.

Louis, L., David, C., Špaček, P., Wong, T.-F., Fortin, J. & Song, S.R., 2012. Elastic anisotropy of core samples from the Taiwan Chelungpu Fault Drilling Project: direct 3-D measurements and weak anisotropy approximations, *Geophys. J. Int.,* **188,** 239–252.

Machek, M., Špaček, P., Ulrich, S. & Heidelbach, F., 2007. Origin and orientation of microporosity in eclogites of different microstructure studied by ultrasound and microfabric analysis, *Eng. Geol.,* **89,** 266–277.

Machek, M., 2011. Relation of pore space geometry, permeability and microstructure in low-porosity rocks, *PhD thesis,* Charles University, Prague.

Martín-Hernández, F. & Hirt, A.M., 2003. The anisotropy of magnetic susceptibility in biotite, muscovite and chlorite single crystals, *Tectonophysics,* **367,** 13–28.

Mlčoch, B., Breiter, K. & Schulmannová, B., 2000. Výzkum melechovského granitového masívu, in *Zpráva o geologickém výzkumu 1999,* Český geologický ústav, Praha, pp. 91–93.

Nagata, T., 1961. *Rock Magnetism,* Maruzen, Tokyo.

Nur, A. & Simmons, G., 1969. Stress-induced velocity anisotropy in rock: an experimental study, *J. geophys. Res.,* **74,** 6667–6674.

Panozzo, R., 1984. Two-dimensional strain from the orientation of lines in a plane, *J. Struct. Geol.,* **6,** 215–221.

Popov, Y.A., Pribnow, D., Sass, J.H., Williams, C.F. & Burkhardt, H, 1999. Characterization of rock thermal conductivity by high resolution optical scanning, *Geothermics,* **28,** 253–276.

Přikryl, R., Klíma, K., Lokajíček, T. & Pros, Z., 2005. Non-linearity in multidirectional P-wave velocity: confining pressure behaviour based on real 3D laboratory measurements, and its mathematical approximation, *Geol. Soc. Spec. Pub.,* **240,** 323–334.

Pros, Z. & Babuška, V., 1968. An apparatus for investigating the elastic anisotropy on spherical rock samples, *Stud. geophys. Geod.,* **12,** 192–198.

Pros, Z., Lokajíček, T. & Klíma, K., 1998a. Laboratory study of elastic anisotropy on rock samples, *Pure appl. Geophys.,* **151,** 619–629.

Pros, Z., Lokajíček, T., Přikryl, R., Špičák, A., Vajdová, V. & Klíma, K., 1998b. Elastic Parameters of West Bohemian Granites under Hydrostatic Pressure, *Pure appl. Geophys.,* **151,** 631–646.

Pros, Z., Lokajíček, T., Přikryl, R. & Klíma, K., 2003. Direct measurement of 3D elastic anisotropy on rocks from the Ivrea zone (Southern Alps, NW Italy), *Tectonophysics,* **370,** 31–47.

Rempe, N.T., 2007. Permanent underground repositories for radioactive waste, *Prog. Nucl. Energ.,* **49,** 365–374.

Šrámek, J., Sedlák, J. & Obr, J., 1996. *Melechovský masív, vizualizace tíhových dat a kvantitativní tíhový řez,* Geofyzika a.s., Brno, pp. 1–34.

Scholz, C.H., Dawers, N.H., Yu, J.-Z., Anders, M.H. & Cowie, P.A., 1993. Fault growth and fault scaling laws: preliminary results, *J. geophys. Res.,* **98,** 21 951–21 961.

Simmons, G. & Wang, H., 1971. *Single Crystal Elastic Constants and Calculated Aggregate Properties: A Handbook,* Massachusetts Institute of Technology Press, Cambridge.

Tarling, D.H. & Hrouda, F., 1993. *The Magnetic Anisotropy of Rocks,* Chapman & Hall, London.

Tester, J.W. *et al.*, 2006. *The future of geothermal energy: Impact of enhanced geothermal systems (EGS) on the United States in the 21st century, DOE Contract DE-AC07–05ID14517 Final Report,* Massachusetts Institute of Technology Press, Cambridge.

Ullemeyer, K., Siegesmund, S., Rasolofosaon, P.N.J. & Behrmann, J.H., 2006. Experimental and texture-derived P-wave anisotropy of principal rocks from the TRANSALP traverse: an aid for the interpretation of seismic field data, *Tectonophysics,* **414,** 97–116.

Zapletal, K., 1990. Low-field susceptibility anisotropy of some biotite crystals, *Phys. Earth planet. Inter.,* **63,** 85–97.

Chapter V:

Conclusions

A granitic massif has been studied by field structural and laboratory petrophysical methods with the goal to estimate the distribution and the effect of structures controlling transfer properties of the granite.

A complex structural image of the study area has been provided based on an extensive dataset including field structural measurements of ductile and brittle structures as well as AMS data. Uneven distribution of mean magnetic susceptibility within the massif showing high values for the easterly Lipnice granite and low values for the westerly younger intrusions has been interpreted to reflect a progressive differentiation from high-susceptibility migmatite protolith to low susceptibility granite with less biotite. The estimated spatial distributions of AMS parameters have revealed rather oblate anisotropy shapes in the older granites and triaxial or rarely prolate shapes in the younger intrusions and along the SW granite-host rock contact. The similar folding pattern of schlieren in the core of the Lipnice granite and of the high-grade migmatites to the SE has been interpreted to represent the S-granitic origin of the massif characteristic by diffuse transition between source rock, granite and host rock. A change in magmatic evolution coupled with change in stress field has been suggested to explain the different structural pattern within the western part of the massif marked by later discordant granite intrusion and discordant granite-host rock contacts. Rotation of the initial migmatite NNE-SSW fabrics to late-magmatic WNW-ESE striking fabrics has been argued to be associated with distributed deformation related to relative horizontal displacements along conjugated sets of shear zones. These shear zones have been interpreted to be subparallel to the regional WNW-ESE and NNE-SSW striking discontinuities and associated with dextral and sinistral kinematics, respectively. The concentric distribution of foliations and fold axes in the host rock and particularly NE and SW of the massif has been related to migmatite-paragneiss dome structure around the studied massif. The massif-outward vergence of asymmetric folds in the host rock has been suggested to reflect the unroofing of the dome. The fracture system of the massif has been described by two principal and two supplementary sets of joints and by faults formed mainly by joint reactivation or less frequently as shear fractures. The recognized fracture sets have been related to the regional stress field in context of the fracture system evolution. The largest fractures in the massif have been identified as the incipient cooling-related set of joints formed perpendicular to the NNE-SSW direction of minimum regional stress and of the granitic body elongation. Structural predisposition and thermal contraction aspects have been discussed to explain the perpendicularity of orientation of the second cooling-related set of joints formed at shallower conditions during further cooling. The reactivation of the two cooling-related sets of joints accompanied or followed by formation of discordant

shear fractures has been proposed to accommodate horizontal strike-slip movements and dip-slip movements in a coherent regime of N-S oriented maximum principal stress.

Samples related to different fracture setting and alteration character have been collected and prepared for analyses by a set of laboratory petrophysical experiments. The measured petrophysical data have been used to characterize the effect of fracturing and alteration on pore space geometry and in turn on permeability, thermal conductivity and elastic properties of the studied samples. Distinct petrophysical properties have been identified for pristine granite, for fractured fresh granite as well as for fractured granite altered by Fe-oxide, chlorite and clay minerals. The lowest porosity and one of the lowest permeabilities have been measured on the pristine granite and its fracturing has been shown to increase the porosity several times and to be associated with variable permeability including values relatively higher by up to two orders of magnitude. Measurements of porosity and permeability of specimens containing localized macroscopic fissures have been used to estimate increase of permeability by one to two orders of magnitude for ~ 0.2 % of fissure-related pore volume. These observations have been attributed to increasing interconnectivity of pore space by cracking at relatively low total porosities below ~ 1 %. Measured decrease in permeability of at least one order of magnitude has been attributed to the sealing effect of pervasive Fe-oxide alteration associated with weak fracturing. Based on decrease of pore volume and pore throat size of free porosity measured on specimens of the corresponding samples, the sealing effect has been suggested to be due to filling of cracks by the Fe-oxide material. The sealing effect of the Fe-oxide alteration has been shown to be counteracted by intensive fracturing which has been associated with increased free porosity volumes, larger pore throat diameters and higher permeabilities in a similar manner as observed for the fracturing effect on the pristine granite. Elevated values of thermal conductivity have been measured both on weakly fractured Fe-oxide-altered granite and on densely fractured clay-altered granite and the effect has been attributed to reduction of pore throat size and to higher thermal conductivity of associated alteration phases in good agreement with measured low permeabilities. The multidirectional V_p measurements on specimens of little fractured walls of steep fractures have shown that the orientation of V_p anisotropy may be generally unrelated to the orientation of the fractures thus suggesting dominant role of the magmatic structure anisotropy. At low confining pressures the mean V_p has been shown to increase with confining pressure at different rates for different samples which may however show mutually proximate mean V_p values at high confining pressures.

A detailed microstructural study combined with multidirectional P-wave velocity measurements at high confining pressure and with analysis of anisotropy of magnetic

susceptibility has been conducted on a specimen of the schlieren-bearing Lipnice granite prepared from a block limited by subparallel exfoliation fractures. The study has shown that the granite V_p anisotropy at low confining pressure was controlled by intergranular cracks interconnecting schlieren-subparallel cleavages and cleavage cracks in micas and feldspars and by discordant exfoliation fracture-subparallel intra- or trans-granular cracks in cleavage-free quartz. Low confinement permeability measurements of the schlieren granite have revealed remarkable anisotropy with the lowest values measured along directions perpendicular to the schlieren and to the fractures and with the highest values measured along the direction of intersection of the two structures. Major closing of both the sets of cracks below depth of 500 m has been interpreted in terms of crack compliance reflected by rapid anisotropic increase in V_p with confining pressure featuring high V_p increase directions perpendicular to each of the set of cracks. The role of the magmatic structure as a prediscontinuity for crack formation as well as its control of the anisotropy at higher confining pressures has thus been demonstrated.

The suitability of the applied techniques for measurement of transfer properties of granite has been demonstrated with each of them showing different sensitivity on the studied phenomena. The highest resolution at the scale of the sample collection has been attained by the mercury porosimetry and routines for acquisition of high precision porosimetric data on very low porosity granites have been developed and used. The effect of experimental setup setting as well as of specimen shape and dimensions on the measured petrophysical properties has been examined. The acquired information and experience imply further research challenges related both to the revealed effects of structures on petrophysical properties as well as to the limitations imposed by the available experimental setups. Use of different permeametry setup should be envisaged for reliable measurements of the lowest permeabilities in pristine granite as well as in the alteration-sealed granite facies. Further development of the mercury porosimetry techniques should be attempted to attain better resolution for distribution between the free and the trapped porosity for different pore throat size ranges possibly including also the macropores as such information is not available for actually standard setups and at the same time is particularly important for the crack-related porosity. Including the mentioned technological tests, limitations and suggestions, the present study has demonstrated the application of complementary structural and petrophysical techniques in the field of transport properties of granitic rocks. The insight this study brings may thus be appreciated within geoingeneering projects based on the knowledge of transport properties of granite thus including the underground waste stocking and geothermal and hydrocarbon exploitation of basement rocks.

References

Anders, M. H., and D. V. Wiltschko (1994), Microfracturing, paleostress and the growth of faults, Journal of Structural Geology, 16(6), 795-815.

Angerer, T., R. O. Greiling, and D. Avigad (2011), Fabric development in a weathering profile at a basement–cover interface, the sub-Cambrian peneplain, Israel: Implications for decollement tectonics, Journal of Structural Geology, 33(5), 819-832.

Arzi, A. A. (1978), Critical phenomena in the rheology of partially melted rocks, Tectonophysics, 44(1–4), 173-184.

ASTM D2845-05 (2005), Standard Test Method for Laboratory Determination of Pulse Velocities and Ultrasonic Elastic Constants of Rock, ASTM International, West Conshohocken.

Babuška, V. (1968), Uprugaya anizotropiya izvyerzhyennykh i myetamorfichyeskikh gornykh porod, Studia Geophysica Et Geodaetica, 12(3), 291-303.

Bagdassarov, N., and A. Dorfman (1998), Viscoelastic behavior of partially molten granites, Tectonophysics, 290(1-2), 27-45.

Bahat, D., and A. Rabinovitch (1988), Paleostress determination in a rock by a fractographic method, Journal of Structural Geology, 10(2), 193-199.

Bahat, D., K. Grossenbacher, and K. Karasaki (1999), Mechanism of exfoliation joint formation in granitic rocks, Yosemite National Park, Journal of Structural Geology, 21(1), 85-96.

Bahat, D., P. Bankwitz, and E. Bankwitz (2003), Pre-uplift joints in granites: Evidence for subcritical and postcritical fracture growth, Geological Society of America Bulletin, 115, 148-165.

Balk, R. (1937), Structural behavior of igneous rocks, Geological Society of America Memoire 5, 1–177.

Bankwitz, P., and E. Bankwitz (1994), Event related jointing in rocks on Bornholm (Denmark), Zeitschrift für geologische wissenschaften, 22, 97-97.

Bankwitz, P., and E. Bankwitz (1997), Fractographic features on joints in KTB drill cores as indicators of the contemporary stress orientation, Geologische Rundschau, 86(S1), S34-S44.

Benson, P. M., P. G. Meredith, and A. Schubnel (2006), Role of void space geometry in permeability evolution in crustal rocks at elevated pressure, Journal of Geophysical Research, 111(B12).

Berger, A. R., and W. S. Pitcher (1970), Structures in granitic rocks; a commentary and a critique on granite tectonics, Proceedings of the Geologists' Association 81(Part 3), 441-461.

Bernabe, Y. (1986), The effective pressure law for permeability in Chelmsford granite and Barre granite, International Journal of Rock Mechanics and Mining Sciences & Geomechanics Abstracts, 23(3), 267-275.

Bernabé, Y., U. Mok, and B. Evans (2003), Permeability-porosity relationships in rocks subjected to various evolution processes, Pure and Applied Geophysics, 160(5-6), 937-960.

Birch, F. (1961), Role of fluid pressure in mechanics of overthrust faulting: Discussion, Bulletin of the Geological Society of America, 72(9), 1441-1444.

Boness, N. L., and M. D. Zoback (2004), Stress-induced seismic velocity anisotropy and physical properties in the SAFOD Pilot Hole in Parkfield, CA, Geophysical Research Letters, 31(15), L15S17 11-14.

Bonin, B. (2007), A-type granites and related rocks: Evolution of a concept, problems and prospects, Lithos, 97(1-2), 1-29.

Bouchez, J.-L., D. Hutton, and W. E. Stephens (1997), Granite: from segregation of melt to emplacement fabrics, 358 pp., Kluwer, Dordrecht ; Boston.

Brace, W. F. (1977), Permeability from resistivity and pore shape, Journal of Geophysical Research, 82(23), 3343-3349.

Brace, W. F., A. S. Orange, and T. R. Madden (1965), The effect of pressure on the electrical resistivity of water-saturated crystalline rocks, Journal of Geophysical Research, 70(22), 5669-5678.

Brace, W. F., J. B. Walsh, and W. T. Frangos (1968), Permeability of granite under high pressure, Journal of Geophysical Research, 73(6), 2225-2236.

Breiter, K. (2006), Geologicka dokumentace a vyhodnoceni vrtnych praci. Dilči zprava ukolu Provedeni geologickych a dalších praci na testovaci lokalitě Melechovsky masiv – 2. etapa. Rep., MS SURAO, Praha.

Breiter, K., and P. Sulovský (2005), Stáří granitů melechovského masivu. Geochronology of the Melechov massif. Rep., 16–19 pp, Praha.

Brown, M. (1973), The definition of metatexis, diatexis and migmatite, Proceedings of the Geologists' Association, 84, 371-IN372.

Brown, M. (2001), Orogeny, migmatites and leucogranites: A review, Journal of Earth System Science, 110(4), 313-336.

Brown, M. (2007), Crustal melting and melt extraction, ascent and emplacement in orogens: mechanisms and consequences, Journal of the Geological Society, 164(4), 709-730.

Brown, M. (2013), Granite: From genesis to emplacement, Geological Society of America Bulletin, 125(7-8), 1079-1113.

Caine, J. S., J. P. Evans, and C. B. Forster (1996), Fault zone architecture and permeability structure, Geology, 24(11), 1025-1028.

Cháb, J., Z. Stráník, and M. Eliáš (2013), Geologická mapa ČR 1 : 500000, edited, CGS, http://ags1.geology.cz/ArcGIS/services.

Chaki, S., M. Takarli, and W. P. Agbodjan (2008), Influence of thermal damage on physical properties of a granite rock: Porosity, permeability and ultrasonic wave evolutions, Construction and Building Materials, 22(7), 1456-1461.

Chappell, B. W., and A. J. R. White (2001), Two contrasting granite types: 25 years later, Australian Journal of Earth Sciences, 48, 489-499.

Chappell, B. W., A. J. R. White, and D. Wyborn (1987), The importance of residual source material (restite) in granite petrogenesis. , Journal of Petrology 28, 1111-1138.

Chappell, B. W., White A.J.R. (1974), Two contrasting granite types, Pacific Geology, 8, 173-174.

Clarke, D. B. (1992), Granitoid rocks, 1st ed., 283 pp., Chapman & Hall, London

Clarke, D. B., and S. Erdmann (2008), Is stoping a volumetrically significant pluton emplacement process?: Comment, Geological Society of America Bulletin, 120(7-8), 1072-1074.

Clauser, C., and E. Huenges (1995), Thermal conductivity of rock and minerals, Rock physics and phase relations - a Handbook of physical constants, T.J. Ahrens Ed. AGU reference shelf, 3, 105-126.

Clemens, J. (2003), S-type granitic magmas—petrogenetic issues, models and evidence, Earth-Science Reviews, 61(1-2), 1-18.

Clemens, J. D. (1998), Observations on the origins and ascent mechanisms of granitic magmas, Journal of the Geological Society, 155(5), 843-851.

Clemens, J. D., and C. K. Mawer (1992), Granitic magma transport by fracture propagation, Tectonophysics, 204(3-4), 339-360.

Clemens, J. D., and G. Stevens (2012), What controls chemical variation in granitic magmas?, Lithos, 134-135, 317-329.

Clemens, J. D., J. R. Holloway, and A. J. R. White (1986), Origin of an A-type granite; experimental constraints, American Mineralogist, 71(3-4), 317-324.

Clemens, J. D., G. T. R. Droop, and G. Stevens (1997), High-grade metamorphism, dehydration and crustal melting: a reinvestigation based on new experiments in the silica-saturated portion of the sytem $KAlO_2$ -MgO-SiO_2 -H_2O-CO_2 at $P \leq 1.5$ GPa, Contributions to Mineralogy and Petrology, 129(4), 308-325.

Clemens, J. D., G. Stevens, and F. Farina (2011), The enigmatic sources of I-type granites: The peritectic connexion, Lithos, 126(3-4), 174-181.

Cloos, H. (1922), Tektonik und Magma, Bd. 1 Abh. d. Preuss. Geolo. Land, 89.

Cloos, H. (1925), Einfurhrung in die tectonische Behandlung magmatischer Erscheinungen. Das Riesengebirge in Schlesien., Borntraeger Berlin.

Coleman, D. S., W. Gray, and A. F. Glazner (2004), Rethinking the emplacement and evolution of zoned plutons: Geochronologic evidence for incremental assembly of the Tuolumne Intrusive Suite, California, Geology, 32(5), 433-436.

Collins, W. J. (1996), Lachlan Fold Belt granitoids: Products of three-component mixing, pp. 171-181.

Connolly, J., and Y. Podladchikov (1998), Compaction-driven fluid flow in viscoelastic rock, Geodinamica Acta, 11(2-3), 55-84.

Coubal, M. (1994), Report on structural geologic research on locality Melechov massif, In: Procházka et al., 1998 (in Czech), Praha.

Coubal, M. (1997), Křehké porušení melechovského masivu, in Geologický výzkum testovací lokality «Melechovský masiv» Souborná zpráva za období 1992-1997 edited by J. Procházka, pp. 54-63, Český geologický ústav, Praha.

Cruden, A. R. (1990), Flow and fabric development during the diapiric rise of magma, Journal of Geology, 98(5), 681-698.

Darcy, H. (1856), Les Fontaines Publiques de la Ville de Dijon, Dalmont, Paris,.

David, C., B. Menéndez, and M. Darot (1999), Influence of stress-induced and thermal cracking on physical properties and microstructure of La Peyratte granite, International Journal of Rock Mechanics and Mining Sciences, 36(4), 433-448.

De Saint Blanquat, M., B. Tikoff, C. Teyssier, and J. L. Vigneresse (1998), Transpressional kinematics and magmatic arcs, pp. 327-340.

Debschütz, W., U. Kruckel, and J. R. Schopper (1989), Effects of geostatic stress and pore pressure on the Klikenberg permeability factor and other fluid parameters, in Proceeding the Symposium «Rock at great depth», pp. 179-185, Balkema.

Dell`Angelo, L. N., J. Tullis, and R. A. Yund (1987), Transition from dislocation creep to melt-enhanced diffusion creep in fine-grained granitic aggregates, Tectonophysics, 139(3-4), 325-332.

Dudek, A. (1980), The crystalline basement block of the Outer Carpathians in Moravia: Bruno-Vistulicum, Rozpr. Čs. Akad. Věd, Ř. Mat. Přír. Věd, 90(8), 1-85.

Engelder, T. (1985), Loading paths to joint propagation during a tectonic cycle: an example from the Appalachian Plateau, U.S.A, Journal of Structural Geology, 7(3-4), 459-476.

Engelder, T. (1992), Stress regimes in the lithosphere, pp. 492.

Engelder, T., K. Schulmann, and O. Lexa (2004), Indentation pits: A product of incipient slip on joints with a mesotopography, pp. 315-324.

Engvik, A. K., A. Bertram, J. F. Kalthoff, B. Stöckhert, H. Austrheim, and S. Elvevold (2005), Magma-driven hydraulic fracturing and infiltration of fluids into the damaged host rock, an example from Dronning Maud Land, Antarctica, Journal of Structural Geology, 27(5), 839-854.

Evans, J. P., C. B. Forster, and J. V. Goddard (1997), Permeability of fault-related rocks, and implications for hydraulic structure of fault zones, Journal of Structural Geology, 19(11), 1393-1404.

Faulkner, D. R., T. M. Mitchell, E. Jensen, and J. Cembrano (2011), Scaling of fault damage zones with displacement and the implications for fault growth processes, Journal of Geophysical Research B: Solid Earth, 116(5).

Faulkner, D. R., C. A. L. Jackson, R. J. Lunn, R. W. Schlische, Z. K. Shipton, C. A. J. Wibberley, and M. O. Withjack (2010), A review of recent developments concerning the structure, mechanics and fluid flow properties of fault zones, Journal of Structural Geology, 32(11), 1557-1575.

Fei, Y. (1995), Thermal expansion, in AGU Reference Shelf, edited by T. J. Ahrens, pp. 29-44, American Geophysical Union, Washington, D. C.

Fener, M. (2011), The effect of rock sample dimension on the P-wave velocity, Journal of Nondestructive Evaluation, 30(2), 99-105.

Finger, F., M. P. Roberts, B. Haunschmid, A. Schermaier, and H. P. Steyrer (1997), Variscan granitoids of central Europe: their typology, potential sources and tectonothermal relations, Mineral. Petrol., 61(1-4), 67-96.

Frost, B. R. (2001), A Geochemical Classification for Granitic Rocks, Journal of Petrology, 42(11), 2033-2048.

Geraud, Y. (1994), Variations of connected porosity and inferred permeability in a thermally cracked granite, Geophysical Research Letters, 21(11), 979-982.

Geraud, Y., F. Mazerolle, and S. Raynaud (1993), Porosity measurements of weathered granitic material: the computerized tomography used, Essai de quantification de la porosite d'un granite altere: utilisation du scanner medical (tomodensitometre X), 164(2), 243-253.

Géraud, Y., M. Rosener, F. Surma, J. Place, E. Le Garzic, and M. Diraison (2010), Physical properties of fault zones within a granite body: Example of the Soultz-sous-Forêts geothermal site, Comptes Rendus - Geoscience, 342(7-8), 566-574.

Gerdes, A., G. Friedl, R. R. Parrish, and F. Finger (2003), High-resolution geochronology of Variscan granite emplacement - the South Bohemian Batholith, Journal of the Czech Geological Society, 48(1-2), 53-54.

Ghani, A. A., M. Searle, L. Robb, and S.-L. Chung (2013), Transitional I to S type characteristic in the Main Range Granite, Peninsular Malaysia, Journal of Asian Earth Sciences.

Giesche, H. (2006), Mercury Porosimetry: A General (Practical) Overview, Particle & Particle Systems Characterization, 23(1), 9-19.

Glazner, A. F., and J. M. Bartley (2008), Reply to comments on «Is stoping a volumetrically significant pluton emplacement process?», Geological Society of America Bulletin, 120(7-8), 1082-1087.

Glazner, A. F., J. M. Bartley, D. S. Coleman, W. Gray, and R. Z. Taylor (2004), Are plutons assembled over millions of years by amalgamation from small magma chambers?, GSA Today, 14(4).

Guéguen, Y., and J. Dienes (1989), Transport properties of rocks from statistics and percolation, Mathematical Geology, 21(1), 1-13.

Guéguen, Y., and V. Palciauskas (1992), Introduction à la physique des roches, Hermann, Paris.

Guéguen, Y., and B. M. (2004), Mechanics of fluid saturated rocks, 450 pp., Elsevier Academic Press, Amsterdam.

Guy, A., J.-B. Edel, K. Schulmann, Č. Tomek, and O. Lexa (2011), A geophysical model of the Variscan orogenic root (Bohemian Massif): Implications for modern collisional orogens, Lithos, 124(1-2), 144-157.

Hanák, J., and P. Ondra (1996), Physical properties of rocks: action Melechov, In: Schulmann et al. 1997.

Holzhausen, G. R. (1989), Origin of sheet structure, 1. Morphology and boundary conditions, Engineering Geology, 27(1-4), 225-278.

Hutton, D. H. W. (1992), Granite sheeted complexes: evidence for the dyking ascent mechanism, in Geological Society of America Special Papers, pp. 377-382.

IAEA (2009), Geological disposal of radioactive waste: technological implications for retrievability, International Atomic Energy Agency, Vienna.

Jacquemont, B. (2002), Etude des interactions eau-roche dans le granite de Soultz-sous-Forêts. Quantification et modélisation des transferts de matière par les fluides, 189 pp, Strasbourg, France

Kachanov, M., J. E. Hutchinson, T. Y. Wu, and T. University (1993), Elastic Solids with Many Cracks and Related Problems, Academic Press/Elsevier.

Katz, A. J., and A. H. Thompson (1986), Quantitative prediction of permeability in porous rock, Physical Review B, 34(11), 8179-8181.

Keay, S., W. J. Collins, and M. T. McCulloch (1997), A three-component Sr-Nd isotopic mixing model for granitoid genesis, Lachlan fold belt, eastern Australia, Geology, 25(4), 307-310.

Kilpatrick, J. A., and D. J. Ellis (1992), C-type magmas: igneous charnockites and their extrusive equivalents, Transactions - Royal Society of Edinburgh: Earth Sciences, 83(1-2), 155-164.

Klinkenberg, L. J. (1941), The permeability of porous media to liquids and gases, Drilling and Production Practice, American Petroleum Inst., 200–213.

Kranz, R. L. (1983), Microcracks in rocks: A review, Tectonophysics, 100(1-3), 449-480.

Lachassagne, P., R. Wyns, and B. Dewandel (2011), The fracture permeability of Hard Rock Aquifers is due neither to tectonics, nor to unloading, but to weathering processes, Terra Nova, 23(3), 145-161.

Larive, E. (2002), Etude expérimentale des roches à très faible perméabilité par la mise en oeuvre d'un perméamètre de précision, 191 pp, Université Montpellier II, Montpellier.

Lejeune, A. M., and P. Richet (1995), Rheology of crystal-bearing silicate melts: an experimental study at high viscosities, Journal of Geophysical Research, 100(B3), 4215-4229.

Lespinasse, M., and A. Pêcher (1986), Microfracturing and regional stress field: a study of the preferred orientations of fluid-inclusion planes in a granite from the Massif Central, France, Journal of Structural Geology, 8(2), 169-180.

Lexa, O., and K. Schulmann (2004), Strukturní dokumentace a vyhodnocení vrtných prací MEL-3 a MEL-4 a detailní strukturní výzkum na lokalitě Holý vrchRep., Czech Geological Survey, Praha.

Lexa, O., and K. Schulmann (2005), Strukturní dokumentace a vyhodnocení vrtných prací MEL-3 a MEL-4 a detailní strukturní výzkum na lokalitě Holý vrchRep., Czech Geological Survey, Praha.

Lexa, O., and K. Schulmann (2006), Vyhodnocení povrchových křehkých struktur a puklinové sítě na testovací lokalitě Melechovský masivRep., Czech Geological Survey, Praha.

Lexa, O., K. Schulmann, V. Janoušek, P. Štípská, A. Guy, and M. Racek (2011), Heat sources and trigger mechanisms of exhumation of HP granulites in Variscan orogenic root, Journal of Metamorphic Geology, 29(1), 79-102.

Li, Y., and N. C. Wardlaw (1986a), The influence of wettability and critical pore-throat size ratio on snap-off, Journal of Colloid And Interface Science, 109(2), 461-472.

Li, Y., and N. C. Wardlaw (1986b), Mechanisms of nonwetting phase trapping during imbibition at slow rates, Journal of Colloid And Interface Science, 109(2), 473-486.

Machek, M. (2011), Relation of pore space geometry, permeability and microstructure in low-porosity rocks, 132 pp, Charles University, Praha.

Maierova, P., O. Cadek, O. Lexa, and K. Schulmann (2012), A numerical model of exhumation of the orogenic lower crust in the Bohemian Massif during the Variscan orogeny, Studia Geophysica Et Geodaetica, 56(2), 595-619.

Matthews, G. P., A. K. Moss, and C. J. Ridgway (1995), The effects of correlated networks on mercury intrusion simulations and permeabilities of sandstone and other porous media, Powder Technology, 83(1), 61-77.

Mavko, G., and A. Nur (1997), The effect of a percolation threshold in the Kozeny-Carman relation, Geophysics, 62(5), 1480-1482.

Mecklenburgh, J., and E. H. Rutter (2003), On the rheology of partially molten synthetic granite, Journal of Structural Geology, 25(10), 1575-1585.

Mehnert, K. R. (1971), Migmatites and the origin of granitic rocks, Elsevier Publishing Company, Amsterdam.

Miguel, A. F., and A. Serrenho (2007), On the experimental evaluation of permeability in porous media using a gas flow method, Journal of Physics D: Applied Physics, 40(21), 6824-6828.

Miller, R. B., and S. R. Paterson (1999), In defense of magmatic diapirs, Journal of Structural Geology, 21(8-9), 1161-1173.

Milord, I., E. W. Sawyer, and M. Brown (2001), Formation of diatexite migmatite and granite magma during anatexis of semi-pelitic metasedimentary rocks: An example from St. Malo, France, Journal of Petrology, 42(3), 487-505.

Mitchell, T. M., and D. R. Faulkner (2009), The nature and origin of off-fault damage surrounding strike-slip fault zones with a wide range of displacements: A field study from the Atacama fault system, northern Chile, Journal of Structural Geology, 31(8), 802-816.

Mitrenga P., Rejl L., and W. J. (1979), Geology of the wider surroundings of Humpolec (in Czech). Proceedings "Příspěvky ke geologickému výzkumu jihozápadní části Českomoravské vrchoviny". Jihočeské muzeum, České Budějovice.

Nur, A., and G. Simmons (1969), Stress-induced velocity anisotropy in rock: an experimental study, Journal of Geophysical Research, 74, 6667–6674.

Ondra, P., and J. Šrámek (1995), Petrofyzikální a detailní tíhový průzkum na lokalitě Dolni Město v roce 1995, Praha.

Onishi, C. T., and I. Shimizu (2005), Microcrack networks in granite affected by a fault zone: Visualization by confocal laser scanning microscopy, Journal of Structural Geology, 27(12), 2268-2280.

Paterson, S. R. (1998), Late-stage sinking of plutons: Comment, Geology, 26(9), 863-864.

Paterson, S. R., and T. K. Fowler Jr (1993), Re-examining pluton emplacement processes, Journal of Structural Geology, 15(2), 191-206.

Paterson, S. R., and R. H. Vernon (1995), Bursting the bubble of ballooning plutons: A return to nested diapirs emplaced by multiple processes, Geological Society of America Bulletin, 107(11), 1356-1380.

Paterson, S. R., and R. B. Miller (1998), Stoped blocks in plutons: paleo-plumb bobs, viscometers, or chronometers?, Journal of Structural Geology, 20(9–10), 1261-1272.

Paterson, S. R., T. K. Fowler, K. L. Schmidt, A. S. Yoshinobu, E. S. Yuan, and R. B. Miller (1998), Interpreting magmatic fabric patterns in plutons, Lithos, 44(1-2), 53-82.

Paterson, S. R., G. S. Pignotta, D. Farris, V. Memeti, R. B. Miller, R. H. Vernon, and J. Zak (2008), Is stoping a volumetrically significant pluton emplacement process?: Discussion, Geological Society of America Bulletin, 120(7-8), 1075-1079.

Petford, N. (1996), Dykes or diapirs?, Transactions of the Royal Society of Edinburgh, Earth Sciences, 87(1-2), 105-114.

Petford, N. (2003), Rheology of granitic magmas during ascent and emplacement, Annual Review of Earth and Planetary Sciences, 31, 399-427.

Petford, N., R. C. Kerr, and J. R. Lister (1993), Dike transport of granitoid magmas, Geology, 21(9).

Petford, N., A. R. Cruden, K. J. W. McCaffrey, J. L. Vigneresse, and others (2000), Granite magma formation, transport and emplacement in the Earth's crust, Nature, 408(6813), 669-673.

Pignotta, G. S., and S. R. Paterson (2007), Voluminous stoping in the Mitchell peak granodiorite, Sierra Nevada batholith, California, USA, The Canadian Mineralogist, 45(1), 87-106.

Pinkerton, H., and R. J. Stevenson (1992), Methods of determining the rheological properties of magmas at sub-liquidus temperatures, Journal of Volcanology and Geothermal Research, 53(1-4), 47-66.

Pitcher, W. S. (1979), The nature, ascent and emplacement of granitic magmas, Journal of the Geological Society, 136(6), 627-662.

Pitra, P., J. P. Burg, and M. Guiraud (1999), Late Variscan strike-slip tectonics between the Tepla-Barrandian and Moldanubian terranes (Czech Bohemian Massif): Petrostructural evidence, Journal of the Geological Society, 156(5), 1003-1020.

Pollard, D. D. (1973), Derivation and evaluation of a mechanical model for sheet intrusions, Tectonophysics, 19(3), 233-269.

Popov, Y. A., Pribnow D., J. H. Sass, C. F. Williams, and H. Burkhardt (1999), Characterization of rock thermal conductivity by high resolution optical scanning, Geothermics, 28, 253-276.

Price, N. J. (1975), Rates of deformation, Journal of the Geological Society, 131(6), 553-575.

Price, N. J., and J. W. Cosgrove (1990), Analysis of geological structures, Cambridge University Press.

Procházka J., et al. (1998), Geological investigation of the test- locality „Melechovský masiv" (in Czech), Czech Geological Survey.

Procházka, V., and D. Matějka (2006), Rock-forming Accessory Minerals in the Granites of the Melechov Massif (Moldanubian Batholith, Bohemian Massif), Acta Univ. Carol.

Procházka V. (2005), Interpretation of chemistry of the so-called Kouty type granite (in Czech), Zprávy o geologických Výzkumech za Rok 2004(111-112).

Racek, M., P. Štípská, P. Pitra, K. Schulmann, and O. Lexa (2006), Metamorphic record of burial and exhumation of orogenic lower and middle crust: A new tectonothermal model for the Drosendorf window (Bohemian Massif, Austria), Mineral. Petrol., 86(3-4), 221-251.

Rajlich, P. (2001), Structural-geological mapping for localization of test polygons in the Melechov massif area (in Czech), MS Czech Geological Survey, Praha.

Ramberg, H. (1980), Diapirism and gravity collapse in the Scandinavian Caledonides, Journal of the Geological Society, 137(3), 261-270.

Ramsay, J. G. (1989), Emplacement kinematics of a granite diapir: the Chindamora batholith, Zimbabwe, Journal of Structural Geology, 11(1-2), 191-209.

Rempe, N. T. (2007), Permanent underground repositories for radioactive waste, Progress in Nuclear Energy, 49(5), 365-374.

René M. (2001), Xenoliths of paragneisses of the Moldanubian Zone in two-mica granites of the Moldanubian batholith (in Czech), Bull. Mineral.-petrolog. Odd. Nár. Muz., 9, 257-261.

Roscoe, R. (1952), The viscosity of suspensions of rigid spheres, British Journal of Applied Physics, 3(8), 267-269.

Rosenberg, C. (2001), Deformation of partially molten granite: a review and comparison of experimental and natural case studies, International Journal of Earth Sciences, 90(1), 60-76.

Rosenberg, C. L., and M. R. Handy (2005), Experimental deformation of partially melted granite revisited: Implications for the continental crust, Journal of Metamorphic Geology, 23(1), 19-28.

Rosener, M. (2007), Petrophysical study and numerical modelling of heat transfer effects between rock and fluid in the Soultz-sous-Forêts geothermal project., University of Strasbourg, Strasbourg.

Rosener, M., and Y. Géraud (2007), Using physical properties to understand the porosity network geometry evolution in gradually altered granites in damage zones, edited by David and M. Le Ravalec-Dufin, pp. 175-184.

Rutter, E. H., and D. H. K. Neumann (1995), Experimental deformation of partially molten westerly granite under fluid-absent conditions, with implications for the extraction of granitic magmas, Journal of Geophysical Research-Solid Earth, 100(B8), 15697-15715.

Sander, B. (1930), Gefugekunde der Gesteine, 352 pp., Vienna.

Sarout, J. (2012), Impact of pore space topology on permeability, cut-off frequencies and validity of wave propagation theories, Geophysical Journal International, 189(1), 481-492.

Sausse, J. (2002), Hydromechanical properties and alteration of natural fracture surfaces in the Soultz granite (Bas-Rhin, France), Tectonophysics, 348(1-3), 169-185.

Sausse, J., E. Jacquot, B. Fritz, J. Leroy, and M. Lespinasse (2001), Evolution of crack permeability during fluid–rock interaction. Example of the Brézouard granite (Vosges, France), Tectonophysics, 336(1-4), 199-214.

Sawyer, E. W. (1996), Melt segregation and magma flow in migmatites: implications for the generation of granite magmas, in Special Paper 315: The Third Hutton Symposium on the Origin of Granites and Related Rocks, edited, pp. 85-94, Geological Society of America.

Sawyer, E. W. (1998), Formation and Evolution of Granite Magmas During Crustal Reworking: the Significance of Diatexites, Journal of Petrology, 39(6), 1147-1167.

Sawyer, E. W. (1999), Criteria for the recognition of partial melting, Physics and Chemistry of the Earth, Part A: Solid Earth and Geodesy, 24(3), 269-279.

Sawyer, E. W., B. Cesare, and M. Brown (2011), When the Continental Crust Melts, Elements, 7(4), 229-234.

Scheidegger, A. E. (1974), The physics of flow through porous media, University of Toronto Press.

Scholz, C. H. (1968), Microfracturing and the inelastic deformation of rock in compression, Journal of Geophysical Research, 73(4), 1417-1432.

Scholz, C. H., N. H. Dawers, J. Z. Yu, M. H. Anders, and P. A. Cowie (1993), Fault growth and fault scaling laws: Preliminary results, Journal of Geophysical Research, 98(B12).

Schulmann, K., and O. Lexa (2000), Výzkumné práce na projektu Strukturně geologického výzkumu na lokalitě MELECHOV za rok 2000, Ústav petrologie a strukturní geologie

Schulmann, K., J. Konopásek, P. Štípská, Š. Táborská, S. Ulrich, and Z. Venera (1997), Studie Strukturních poměrů Melechovského masivu a fysikálních vlastností jeho horninRep., Ústav petrologie a strukturní geologie Přírodovědecká fakulta University Karlovy, Praha-Brno.

Schulmann, K., A. Kröner, E. Hegner, I. Wendt, J. Konopásek, O. Lexa, and P. Štípská (2005), Chronological constraints on the pre-orogenic history, burial and exhumation of deep-seated rocks along the eastern margin of the Variscan orogen, Bohemian Massif, Czech Republic, American Journal of Science, 305(5), 407-448.

Schulmann, K., J. Konopásek, V. Janoušek, O. Lexa, J.-M. Lardeaux, J.-B. Edel, P. Štípská, and S. Ulrich (2009), An Andean type Palaeozoic convergence in the Bohemian Massif, Comptes Rendus Geoscience, 341(2-3), 266-286.

Schulmann K., Z. Venera, J. Konopásek, and O. Lexa (1998), Structural and geological investigation of the Melechov massif (in Czech), MS Faculty of Science of the Charles University, Geofond P93389.

Solar, G. S., R. A. Pressley, M. Brown, and R. D. Tucker (1998), Granite ascent in convergent orogenic belts: Testing a model, Geology, 26(8).

Spera, F. J. (2000), Physical properties of magma, Encyclopedia of volcanoes, 171-190.

Šrámek, J., J. Sedlák, and J. Obr (1996), Melechovský masív, vizualizace tíhových dat a kvantitativní tíhový řezRep., pp. 1–34, Brno.

Stipska, P., and K. Schulmann (1995), Inverted metamorphic zonation in a basement-derived nappe sequence, eastern margin of the Bohemian Massif, Geological Journal, 30(3-4), 385-413.

Štípská, P., K. Schulmann, and A. Kröner (2004), Vertical extrusion and middle crustal spreading of omphacite granulite: A model of syn-convergent exhumation (Bohemian Massif, Czech Republic), Journal of Metamorphic Geology, 22(3), 179-198.

SUJB (2011), Národní zpráva pro účely Společné úmluvy o bezpečnosti při nakládání s vyhořelým palivem a o bezpečnosti při nakládání s radioaktivními odpady.

Surma, F. (2003), Détermination de la porosité des zones endommagées autour des failles et rôle de l'état du matériau sur les propriétés d'échange fluides-roches : minéralogie, structures de porosité, caractéristiques mécaniques, 297 pp, University of Strasbourg, Strasbourg.

Surma, F., and Y. Geraud (2003), Porosity and thermal conductivity of the Soultz-sous-forêts granite, Pure and Applied Geophysics, 160(5-6), 1125-1136.

Tanikawa, W., and T. Shimamoto (2009), Comparison of Klinkenberg-corrected gas permeability and water permeability in sedimentary rocks, International Journal of Rock Mechanics and Mining Sciences, 46(2), 229-238.

Tapponnier, P., and W. F. Brace (1976), Development of stress-induced microcracks in Westerly Granite, International Journal of Rock Mechanics and Mining Sciences and, 13(4), 103-112.

Townend, J., and M. D. Zoback (2004), Regional tectonic stress near the San Andreas fault in central and southern California, Geophysical Research Letters, 31(15), L15S11 11-15.

Twiss, R. J., and E. M. Moores (2007), Structural Geology, 532 pp., New York.

UJV, A. Vokál, R. Trtílek, J. Tarasová, E. Popelová, J. Podlaha, J. Krmela, H. Vojtěchová, and J. Uhlíř (2013), Podkladová studie pro koncepci nakládání s VJP a RAO v ČR.

Ulicny, D., J. Laurin, and S. Cech (2009), Controls on clastic sequence geometries in a shallow-marine, transtensional basin: the Bohemian Cretaceous Basin, Czech Republic, Sedimentology, 56(4), 1077-1141.

van der Molen, I., and M. S. Paterson (1979), Experimental deformation of partially-melted granite, Contributions to Mineralogy and Petrology, 70(3), 299-318.

Vermilye, J. M., and C. H. Scholz (1999), Fault propagation and segmentation: insight from the microstructural examination of a small fault, Journal of Structural Geology, 21(11), 1623-1636.

Vrana, O. (1988), Effect of the Concrete Mixture Components on the Concrete Pore Structure and Shrinkage, 36(3), 235-254.

Vrána, S., P. Blümel, and K. Petrakakis (1995), Metamorphic evolution of the Moldanubian Zone, in Pre-Permian Geology of Central and Eastern Europe, edited by R. D. Dallmeyer, Franke, W., Weber, K. (Eds.), pp. 453-466, Springer, Berlin.

Wall, V. J., J. D. Clemens, and D. B. Clarke (1987), Models for Granitoid Evolution and Source Compositions, The Journal of Geology, 95(6), 731-749.

Walsh, J. B., and W. F. Brace (1984), The effect of pressure on porosity and the transport properties of rock, Journal of Geophysical Research, 89(B11).

Wardlaw, N. C., and M. McKellar (1981), Mercury porosimetry and the interpretation of pore geometry in sedimentary rocks and artificial models, Powder Technology, 29(1), 127-143.

Wardlaw, N. C., M. McKellar, and L. Yu (1988), Pore and throat size distributions determined by mercury porosimetry and by direct observation, Carbonates and Evaporites, 3(1), 1-16.

Washburn, E. W. (1921), The Dynamics of Capillary Flow, Physical Review, 17(3), 273-283.

Weinberg, R. F. (1996), Ascent mechanism of felsic magmas: news and views, Earth and Environmental Science Transactions of the Royal Society of Edinburgh, 87(1-2), 95-103.

Weinberg, R. F., and Y. Y. Podladchikov (1995), The rise of solid-state diapirs, Journal of Structural Geology, 17(8), 1183-1195.

Weinberg, R. F., and K. Regenauer-Lieb (2010), Ductile fractures and magma migration from source, Geology, 38(4), 363-366.

White, A. J. R., B. W. Chappell, and D. Wyborn (1999), Application of the Restite Model to the Deddick Granodiorite and its Enclaves --a Reinterpretation of the Observations and Data of Maas et al. (1997), Journal of Petrology, 40(3), 413-421.

Wilkins, S. J., M. R. Gross, M. Wacker, Y. Eyal, and T. Engelder (2001), Faulted joints: Kinematics, displacement-length scaling relations and criteria for their identification, Journal of Structural Geology, 23(2-3), 315-327.

Wilson, C. J. L., and T. M. Will (1990), Slickenside lineations due to ductile processes, Deformation mechanisms, rheology and tectonics, 455-460.

Wilson, J. E., J. S. Chester, and F. M. Chester (2003), Microfracture analysis of fault growth and wear processes, Punchbowl Fault, San Andreas system, California, Journal of Structural Geology, 25(11), 1855-1873.

Winter, M. R., and D. R. Clarke (2007), Oxide materials with low thermal conductivity, Journal of the American Ceramic Society, 90(2), 533-540.

Wyllie, M., A. Gregory, and G. Gardner (1956), Elastic wave velocities in heterogeneous and porous media, Geophysics, 21, 41-70.

Yasuhara, H., N. Kinoshita, H. Ohfuji, D. S. Lee, S. Nakashima, and K. Kishida (2011), Temporal alteration of fracture permeability in granite under hydrothermal conditions and its interpretation by coupled chemo-mechanical model, Applied Geochemistry, 26(12), 2074-2088.

Žák, J., B. Vyhnálek, and P. Kabele (2006), Is there a relationship between magmatic fabrics and brittle fractures in plutons?, Physics of the Earth and Planetary Interiors, 157(3-4), 286-310.

Žák, J., S. R. Paterson, and V. Memeti (2007), Four magmatic fabrics in the Tuolumne batholith, central Sierra Nevada, California (USA): Implications for interpreting fabric patterns in plutons and evolution of magma chambers in the upper crust, Geological Society of America Bulletin, 119(1-2), 184-201.

Žák, J., K. Verner, J. Klomínský, and M. Chlupáčová (2009), "Granite tectonics" revisited: insights from comparison of K-feldspar shape-fabric, anisotropy of magnetic susceptibility (AMS), and brittle fractures in the Jizera granite, Bohemian Massif, International Journal of Earth Sciences, 98(5), 949-967.

Žák, J., K. Verner, K. Johnson, and J. J. Schwartz (2012), Magma emplacement process zone preserved in the roof of a large Cordilleran batholith, Wallowa Mountains, northeastern Oregon, Journal of Volcanology and Geothermal Research, 227-228, 61-75.

Žák, J., K. Verner, F. Finger, S. W. Faryad, M. Chlupácová, and F. Veselovskỳ (2011), The generation of voluminous S-type granites in the Moldanubian unit, Bohemian Massif, by rapid isothermal exhumation of the metapelitic middle crust, Lithos, 121(1-4), 25-40.

Zang, D., and A. Li (2003), Rock mechanics properties under the stress field of true uniaxial compression, Yanshilixue Yu Gongcheng Xuebao/Chinese Journal of Rock Mechanics and Engineering, 22(7), 1099-1103.

Závada, P., K. Schulmann, J. Konopásek, S. Ulrich, and O. Lexa (2007), Extreme ductility of feldspar aggregates—Melt-enhanced grain boundary sliding and creep failure: Rheological implications for felsic lower crust, Journal of Geophysical Research, 112(B10).

Zoback, M. D., and J. D. Byerlee (1975), The effect of microcrack dilatancy on the permeability of westerly granite, Journal of Geophysical Research, 80(5), 752-755.

Appendix

Figure A1 *(continued on the following four pages).* Borehole core samples shown on photographs taken prior to extraction from the core boxes (left) and after marking of position of the TC scanning profiles and of the plugs for permeability and V_p measurements (right). The core diameter 4.45 cm represents the scale. Where present, the bold black marker indicates the sample name (number) and direction towards the top of the borehole (arrow). The TC scanning profiles are represented by black painting stripes parallel to the core axis. The positions of the plugs for permeability and V_p measurements are indicated by red marker.

Figure A1 *(continued)*. Borehole core samples shown on photographs taken prior to extraction from the core boxes (left) and after marking of position of the TC scanning profiles and of the plugs for permeability and V_P measurements (right).

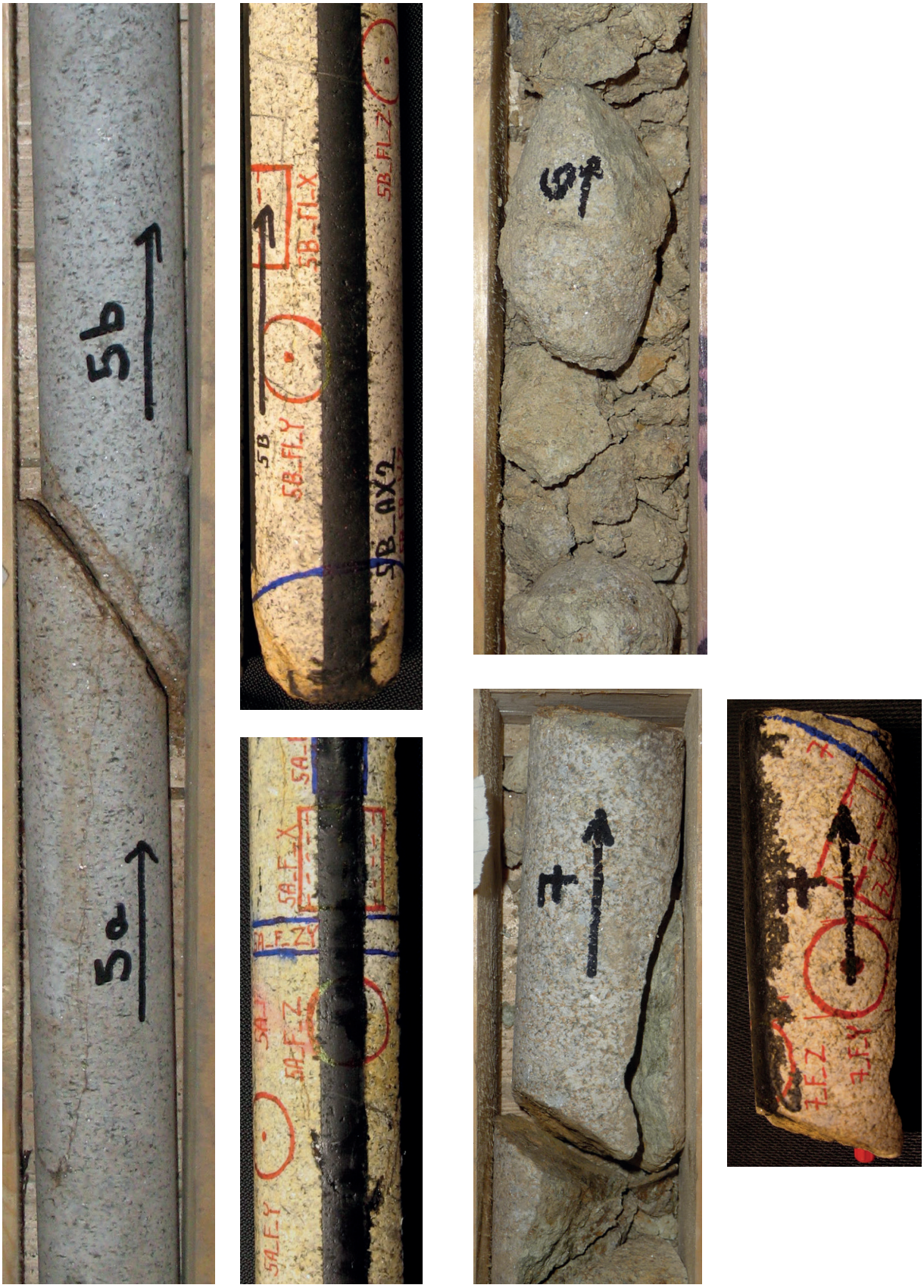

Figure A1 *(continued)*. Borehole core samples shown on photographs taken prior to extraction from the core boxes (left) and after marking of position of the TC scanning profiles and of the plugs for permeability and V_P measurements (right).

Figure A1 *(continued)*. Borehole core samples shown on photographs taken prior to extraction from the core boxes (left) and after marking of position of the TC scanning profiles and of the plugs for permeability and V_P measurements (right).

Figure A1 *(continued)*. Borehole core samples shown on photographs taken prior to extraction from the core boxes (left) and after marking of position of the TC scanning profiles and of the plugs for permeability and V_P measurements (right).

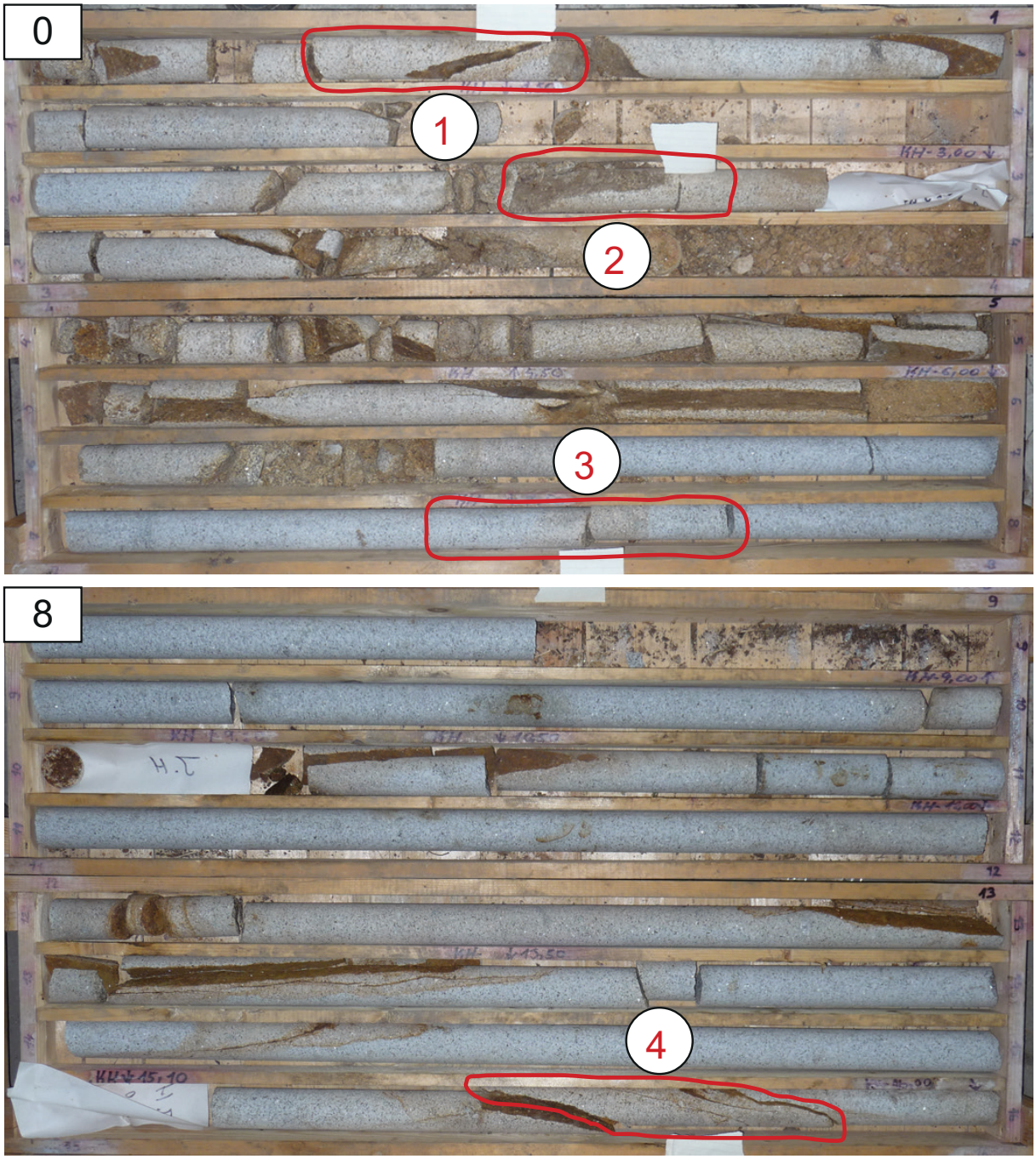

Figure A2 *(continued on the following four pages).* Position of the borehole core samples within the borehole core. The core with diameter 4.45 cm is stocked by meters. The numbers in top left corner of the photgraphs indicate the upper borehole level (m) of the sequence.

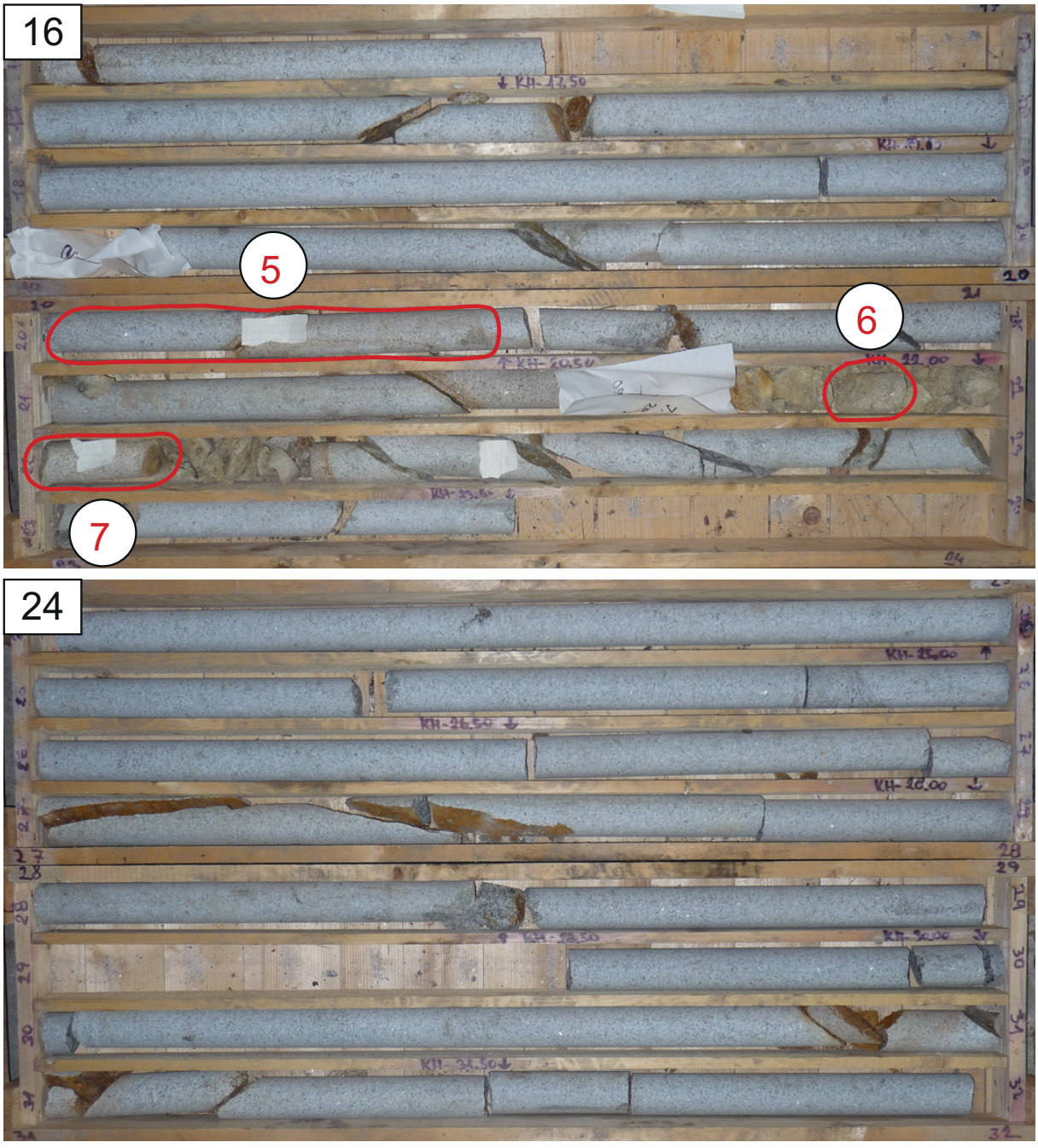

Figure A2 *(continued).* Position of the borehole core samples within the borehole core. The core with diameter 4.45 cm is stocked by meters. The numbers in top left corner of the photgraphs indicate the upper borehole level (m) of the sequence.

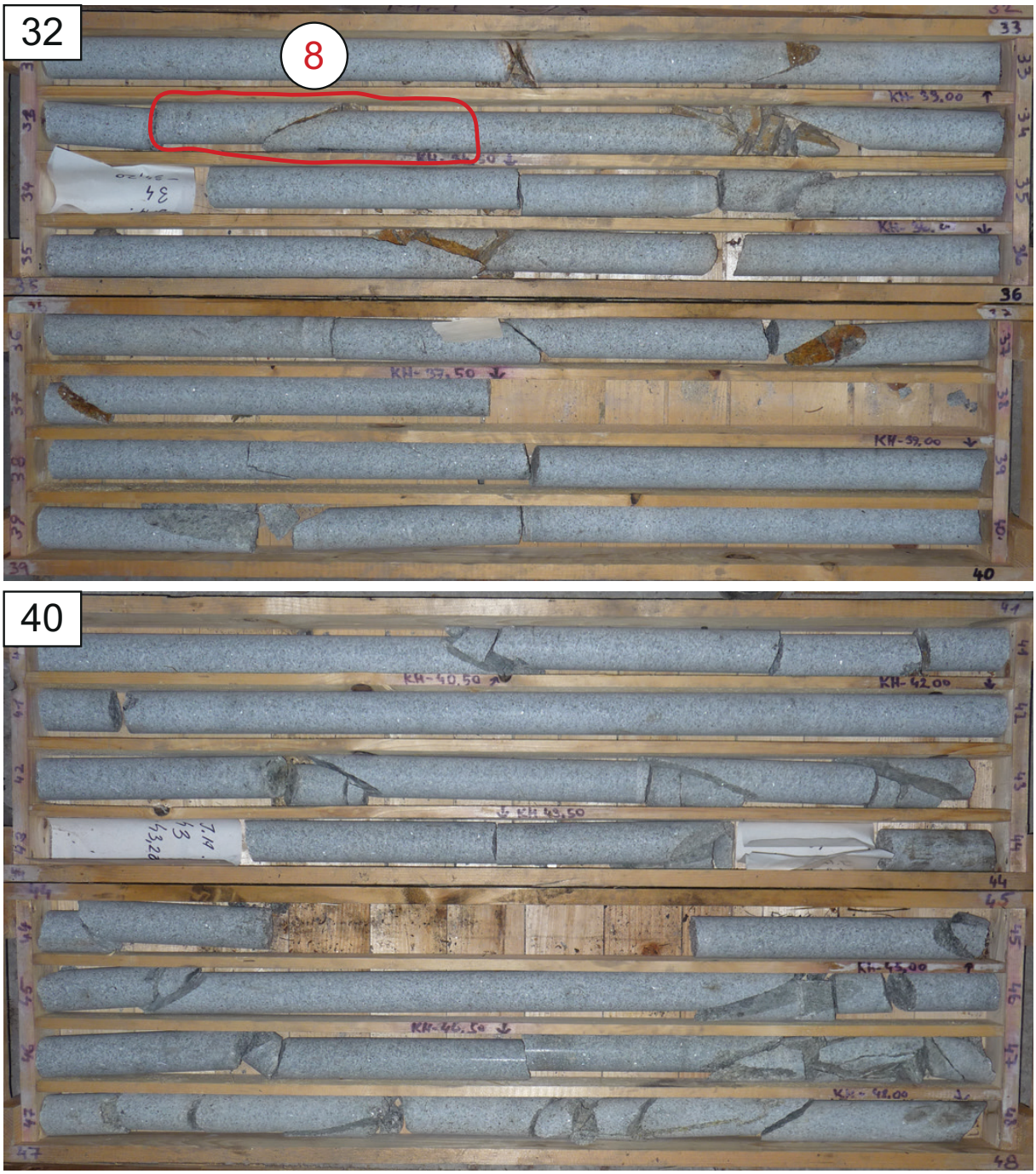

Figure A2 *(continued)*. Position of the borehole core samples within the borehole core. The core with diameter 4.45 cm is stocked by meters. The numbers in top left corner of the photgraphs indicate the upper borehole level (m) of the sequence.

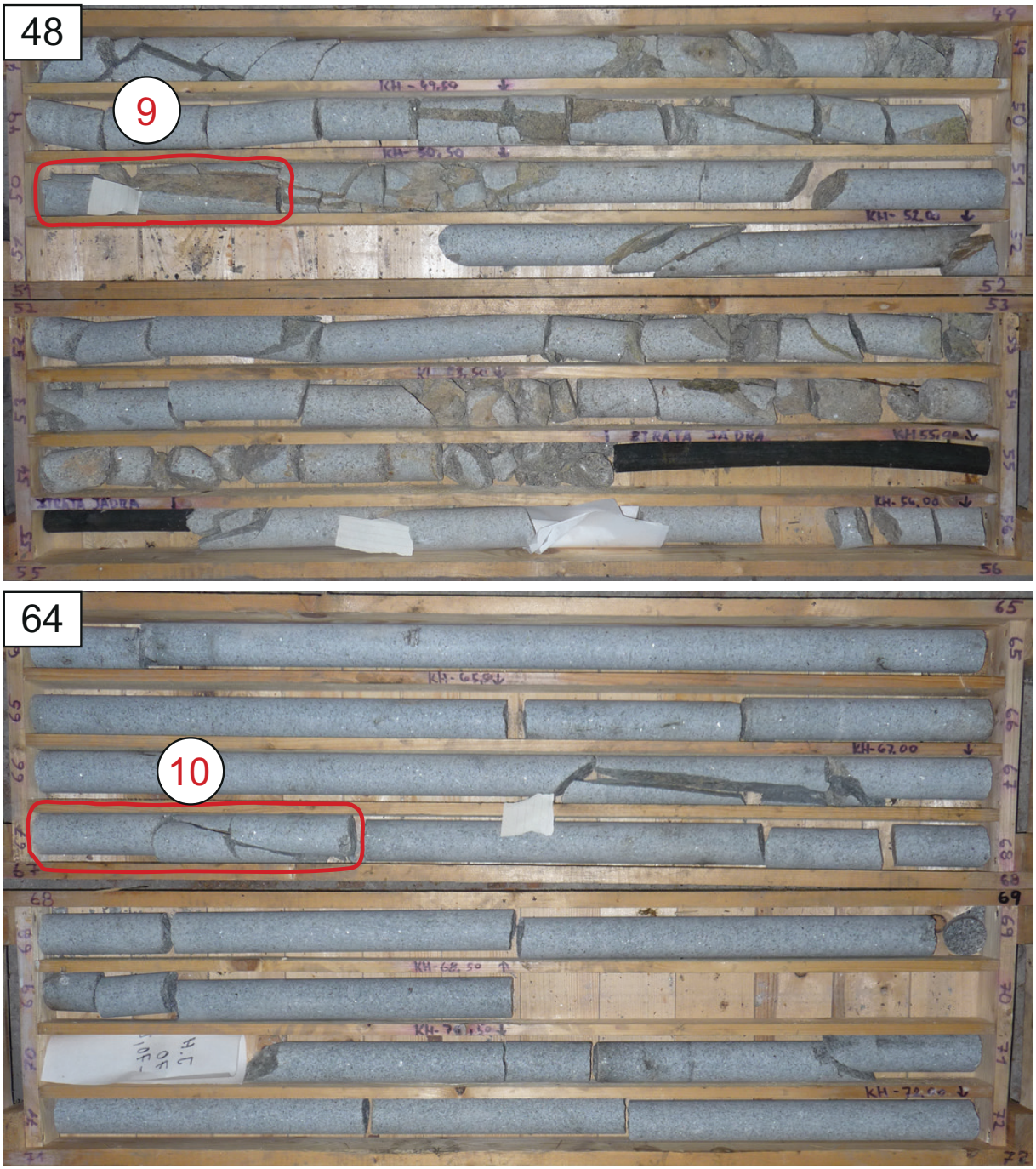

Figure A2 *(continued)*. Position of the borehole core samples within the borehole core. The core with diameter 4.45 cm is stocked by meters. The numbers in top left corner of the photgraphs indicate the upper borehole level (m) of the sequence.

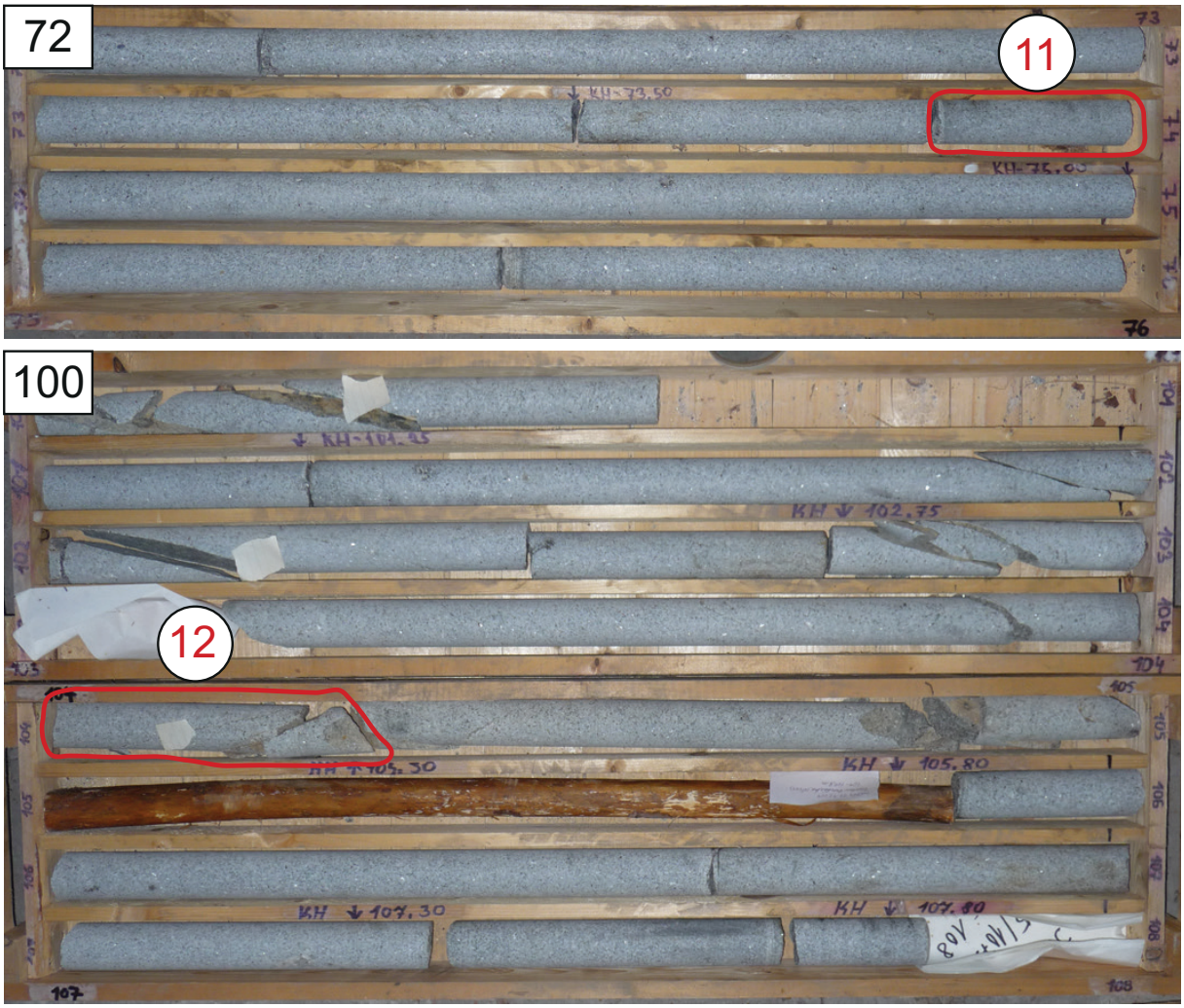

Figure A2 *(continued)*. Position of the borehole core samples within the borehole core. The core with diameter 4.45 cm is stocked by meters. The numbers in top left corner of the photgraphs indicate the upper borehole level (m) of the sequence.

Name	Matrix alteration			Fracture skin				Crack		View		
	Fe-oxide	Chlorite	Clay	Barren	Fe-oxide	Chlorite	Clay	Single	Multiple	A	B	C
1_1	x	-	-	-	x	-	-	-	-	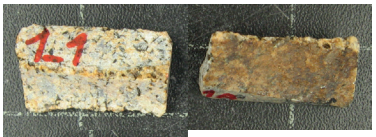		
1_2	x	-	-	-	-	-	-	-	-			
1_3	-	-	-	-	-	-	-	-	-			
2_1	x	-	-	-	x	-	-	x	-			
2_2	x	-	-	-	-	-	-	-	-			
2_3	x	-	-	-	-	-	-	-	x			
3A_1	-	-	-	-	-	-	-	-	-			
3A_2	x	-	-	-	-	-	-	x	-			
3B_1	-	-	-	-	-	-	-	-	-			
3B_2	x	-	-	-	-	-	-	-	-			

Figure A3 *(continued on the following two pages).* Classification and photographs of subsamples for mercury porosimetry. Each line corresponds to one specimen and shows (from left to right) the specimen name, the attributes of the matrix alteration, of the fracture skin and of the macroscopic cracks and finally the photographs (field of view 3 x 2 cm). The class feature is present for symbol "x" and absent for symbol "-". None, one, or more of the features in a class may be present. Where fracture skin, crack(s) or other special feature was present, usually more photographs from different views on the subsample were taken (A, B, C) to document the differences.

	Fe-oxide	Chlorite	Clay	Barren	Fe-oxide	Chlorite	Clay	Single	Multiple
4_1	x	-	-	-	x	-	-	-	-
4_2	x	-	-	-	-	-	-	-	-
5A_1	-	-	-	-	-	-	-	-	-
5A_3	x	-	-	-	x	-	-	-	x
5A_4	x	-	-	-	x	-	-	x	x
5A_5	x	-	-	-	-	-	-	x	-
5A_7	x	-	-	-	-	-	-	-	-
7_1	x	x	-	-	-	x	-	-	-
7_3	x	x	-	-	-	-	-	-	-
7_5	x	x	-	-	x	-	-	-	-
7_7	x	x	-	-	x	x	-	-	-
7_10	x	x	-	-	-	-	-	x	-
8B_1	x	-	-	-	x	-	-	-	-
8B_3	-	-	-	-	-	-	-	-	-

Figure A3 *(continued).* Classification and photographs of specimens for mercury porosimetry.

	Fe-oxide	Chlorite	Clay	Barren	Fe-oxide	Chlorite	Clay	Single	Multiple
9_1	-	-	x	-	-	-	x	x	-
9_2	-	-	x	-	-	-	x	-	x
9_3	-	-	x	-	x	-	x	-	-
9_4	-	-	x	-	x	-	x	-	-
9_5	-	-	x	-	x	-	x	-	-
9_6	-	-	x	-	x	-	x	-	-
9_7	-	-	x	-	-	-	-	x	-
10_1	-	-	-	x	-	-	-	-	-
10_2	-	-	-	-	-	-	-	-	-
11	-	-	-	-	-	-	-	-	-
12_1	-	-	-	-	x	-	-	x	-
12_2	-	-	-	-	-	-	-	x	-
12_3	-	-	-	-	-	-	-	x	-
12_4	-	-	-	-	-	-	-	-	-

Figure A3 *(continued).* Classification and photographs of specimens for mercury porosimetry.

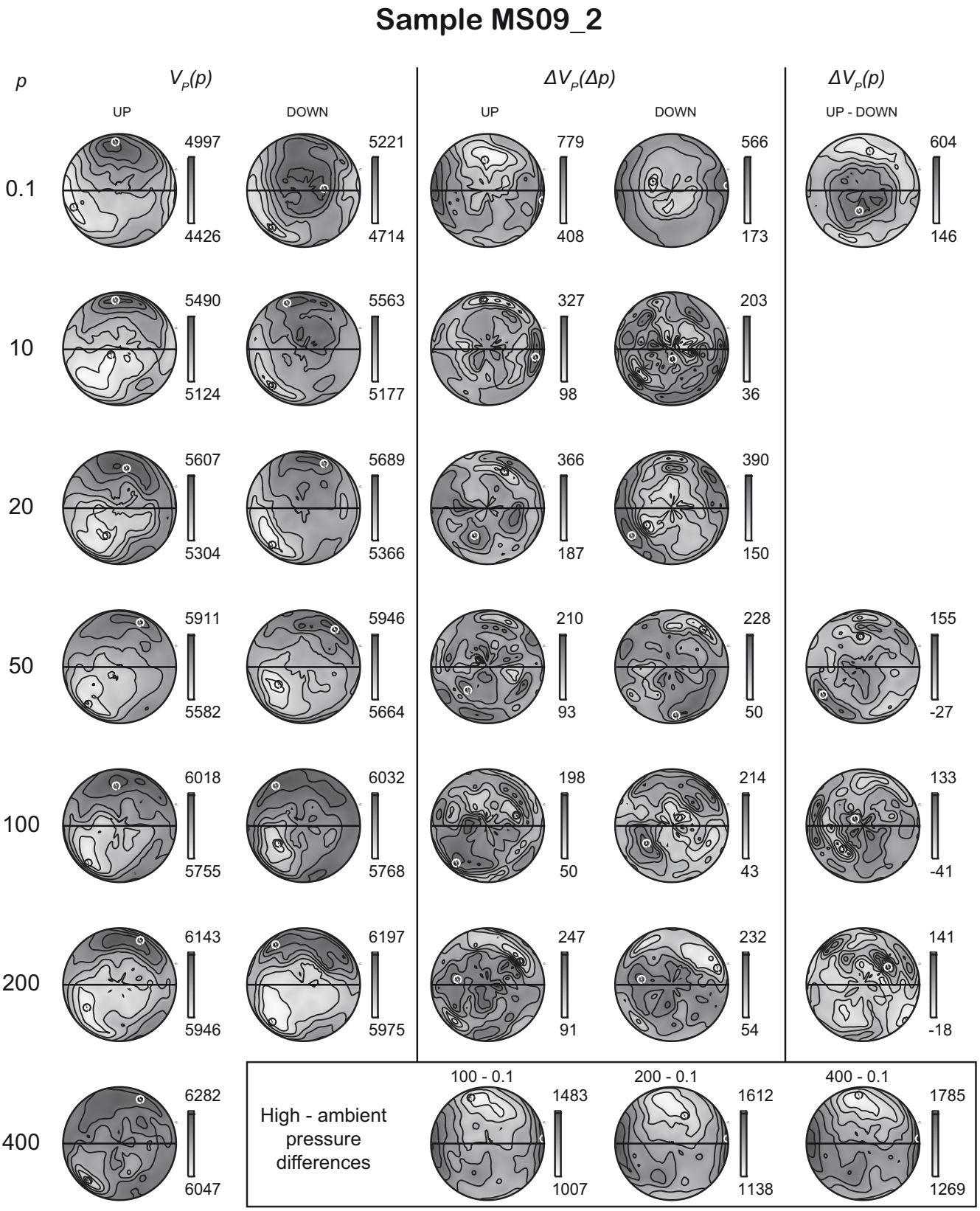

Figure A4 *(continued on the following five pages).* Results of multidirectional P-wave velocity measurements at high confining pressure. P - confining pressure (MPa), $V_p(p)$ - measured velocity (m s^{-1}) at distinct levels of confining pressure, $\Delta V_p(\Delta p)$ - calculated velocity differences (m s^{-1}) between the pressure levels, $V_p(\Delta p)$ - calculated velocity differences (m s^{-1}) between the pressurisation (UP) and depressurisation (DOWN). In the stereonets the horizontal line shows the orientation of the reference fracture and the solid circles are the directions of maximum (white) and minimum (black) velocities. The maximum and minimum velocities are shown above and below the gray scale, respectively.

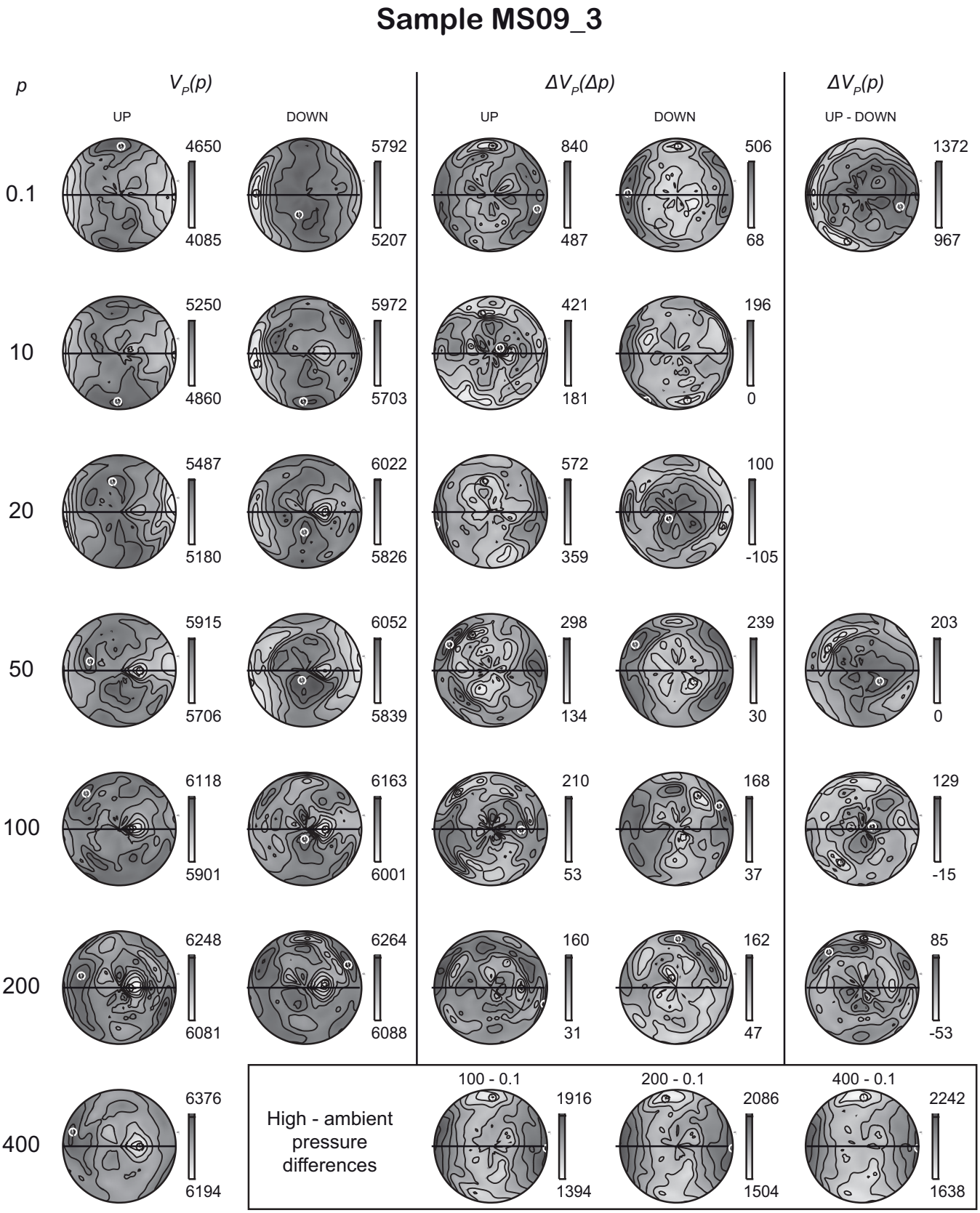

Figure A4 *(continued)*. Results of multidirectional P-wave velocity measurements at high confining pressure. P - confining pressure (MPa), $V_p(p)$ - measured velocity (m s^{-1}) at distinct levels of confining pressure, $\Delta V_p(\Delta p)$ - calculated velocity differences (m s^{-1}) between the pressure levels, $V_p(\Delta p)$ - calculated velocity differences (m s^{-1}) between the pressurisation (UP) and depressurisation (DOWN). In the stereonets the horizontal line shows the orientation of the reference fracture and the solid circles are the directions of maximum (white) and minimum (black) velocities. The maximum and minimum velocities are shown above and below the gray scale, respectively.

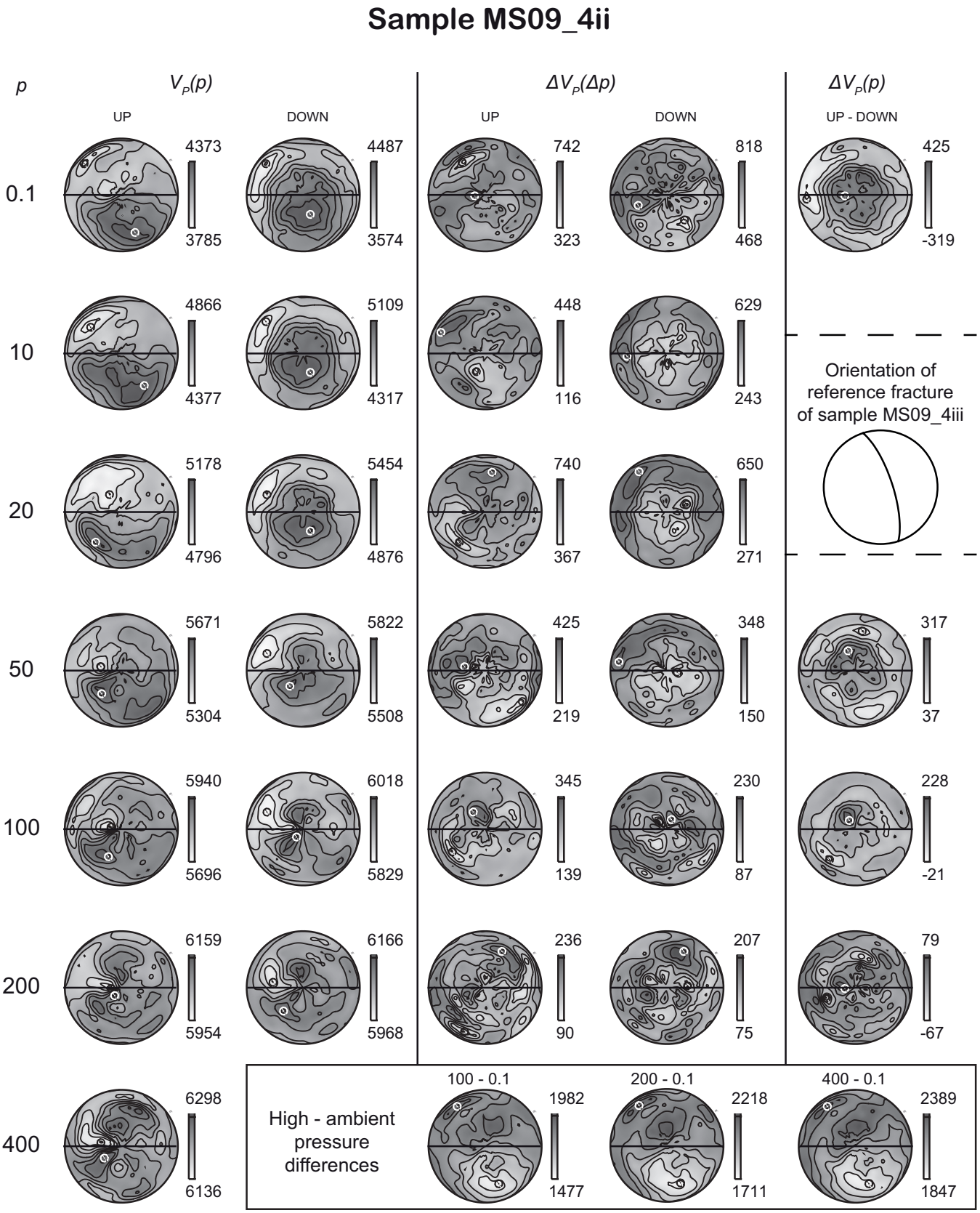

Figure A4 *(continued)*. Results of multidirectional P-wave velocity measurements at high confining pressure. P - confining pressure (MPa), $V_p(p)$ - measured velocity (m s^{-1}) at distinct levels of confining pressure, $\Delta V_p(\Delta p)$ - calculated velocity differences (m s^{-1}) between the pressure levels, $V_p(\Delta p)$ - calculated velocity differences (m s^{-1}) between the pressurisation (UP) and depressurisation (DOWN). In the stereonets the horizontal line shows the orientation of the reference fracture and the solid circles are the directions of maximum (white) and minimum (black) velocities. The maximum and minimum velocities are shown above and below the gray scale, respectively.

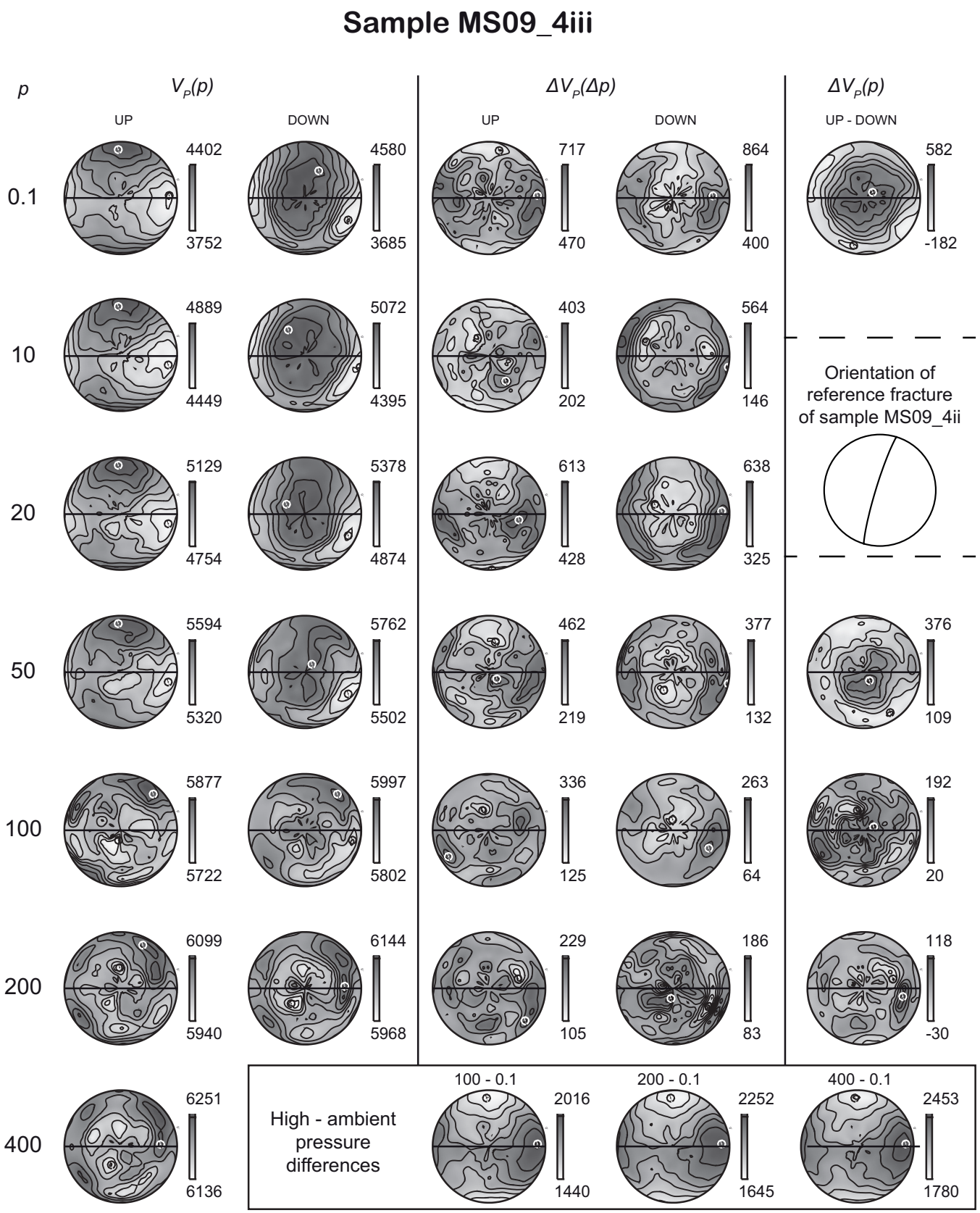

Figure A4 *(continued)*. Results of multidirectional P-wave velocity measurements at high confining pressure. P - confining pressure (MPa), $V_p(p)$ - measured velocity (m s^{-1}) at distinct levels of confining pressure, $\Delta V_p(\Delta p)$ - calculated velocity differences (m s^{-1}) between the pressure levels, $V_p(\Delta p)$ - calculated velocity differences (m s^{-1}) between the pressurisation (UP) and depressurisation (DOWN). In the stereonets the horizontal line shows the orientation of the reference fracture and the solid circles are the directions of maximum (white) and minimum (black) velocities. The maximum and minimum velocities are shown above and below the gray scale, respectively.

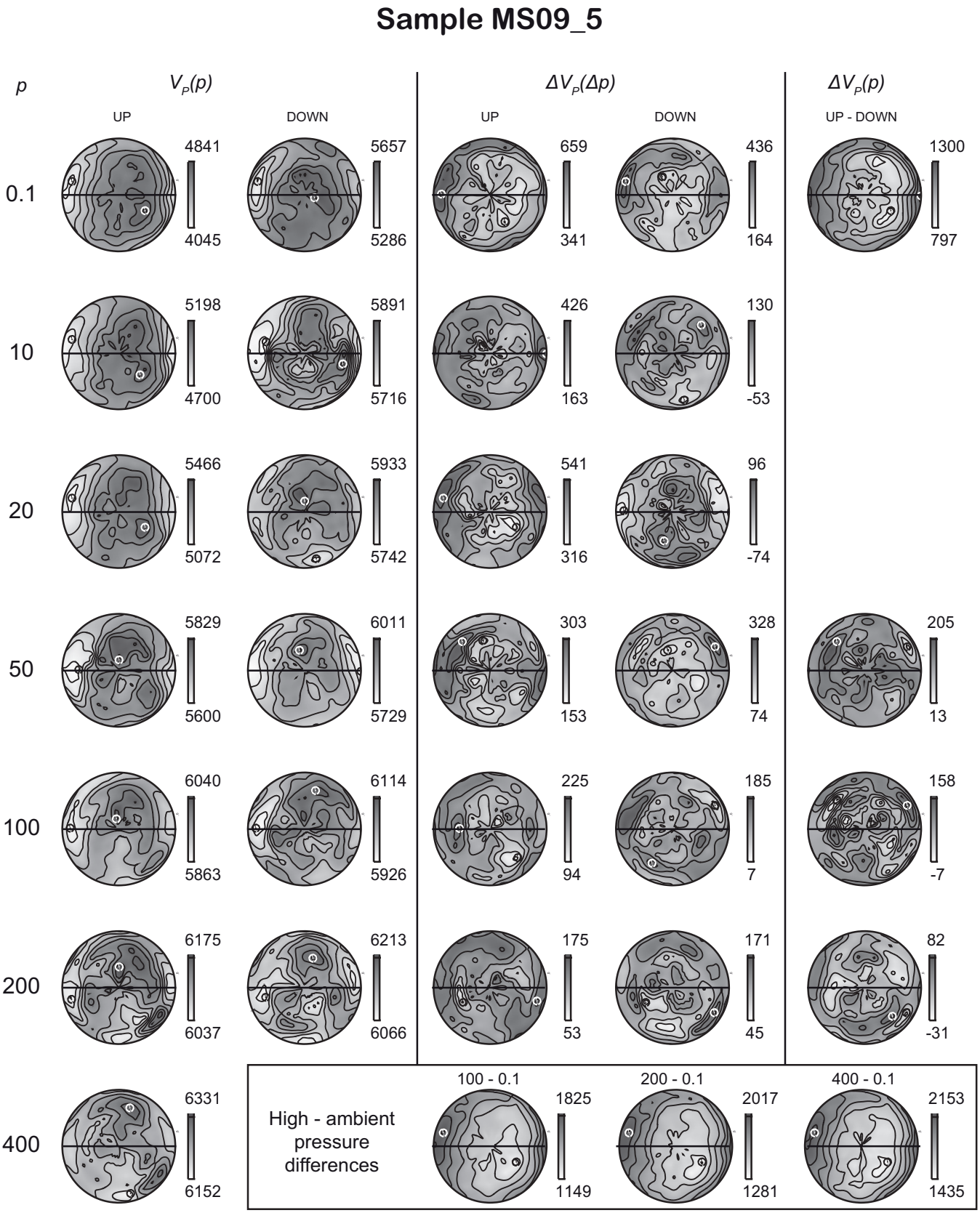

Figure A4 *(continued)*. Results of multidirectional P-wave velocity measurements at high confining pressure. P - confining pressure (MPa), $V_p(p)$ - measured velocity (m s^{-1}) at distinct levels of confining pressure, $\Delta V_p(\Delta p)$ - calculated velocity differences (m s^{-1}) between the pressure levels, $V_p(\Delta p)$ - calculated velocity differences (m s^{-1}) between the pressurisation (UP) and depressurisation (DOWN). In the stereonets the horizontal line shows the orientation of the reference fracture and the solid circles are the directions of maximum (white) and minimum (black) velocities. The maximum and minimum velocities are shown above and below the gray scale, respectively.

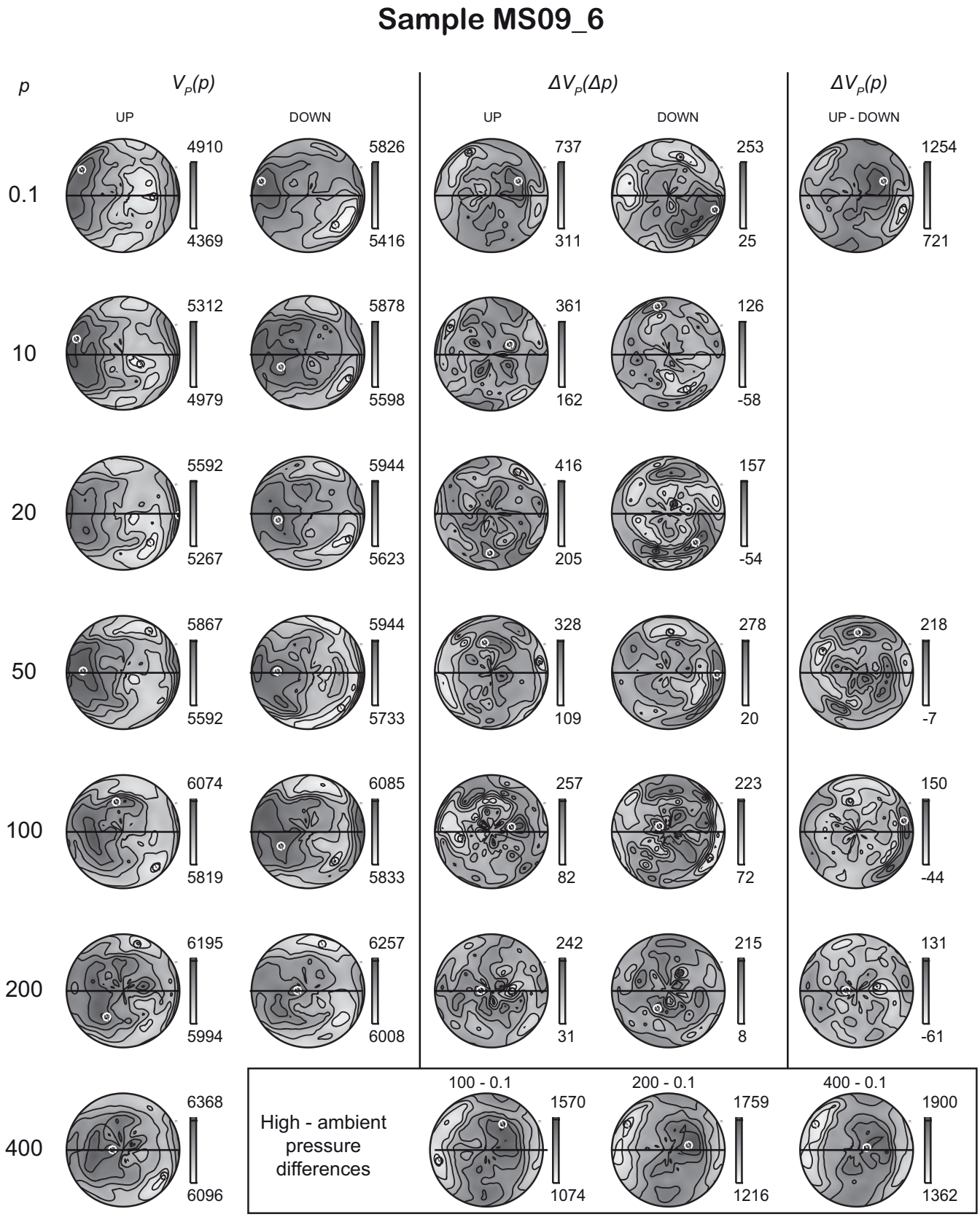

Figure A4 *(continued)*. Results of multidirectional P-wave velocity measurements at high confining pressure. P - confining pressure (MPa), $V_p(p)$ - measured velocity (m s^{-1}) at distinct levels of confining pressure, $\Delta V_p(\Delta p)$ - calculated velocity differences (m s^{-1}) between the pressure levels, $V_p(\Delta p)$ - calculated velocity differences (m s^{-1}) between the pressurisation (UP) and depressurisation (DOWN). In the stereonets the horizontal line shows the orientation of the reference fracture and the solid circles are the directions of maximum (white) and minimum (black) velocities. The maximum and minimum velocities are shown above and below the gray scale, respectively.